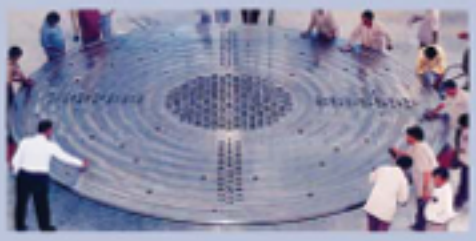

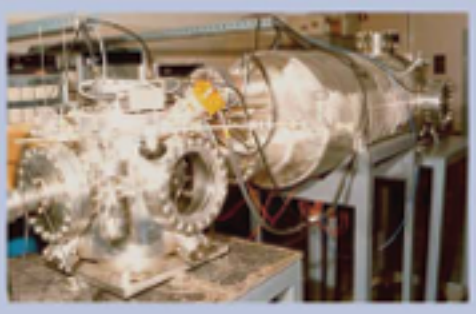

IGC Annual Report 2005

सत्यमेव जयते

Government of India
Department of Atomic Energy
Indira Gandhi Centre for Atomic Research
Kalpakkam - 603 102

IGC

Annual Report 2005

Government of India
Department of Atomic Energy
Indira Gandhi Centre for Atomic Research
Kalpakkam - 603 102

Editorial Committee

Address for Coresspondence
Dr. Vasudeva Rao P. R
Chairman, Editorial Committee
Director, Chemistry Group
Indira Gandhi Centre for Atomic Research
Kalpakkam - 603 102

Phone : 044-2748 0229
Fax : 044-2748 0065
Email : vasu@igcar.gov.in

Published by
Scientific Information & Resources Division (SIRD)
Indira Gandhi Centre for Atomic Research
Kalpakkam - 603 102

Web site : www.igcar.gov.in

Febraury 2006

"Actions today mould our tomorrows"

Indira Gandhi

"... There is a need for a constant interplay between basic sciences, technology and industrial practice if economic progress is to result from the activity undertaken... "

- Vikram Sarabhai

Contents

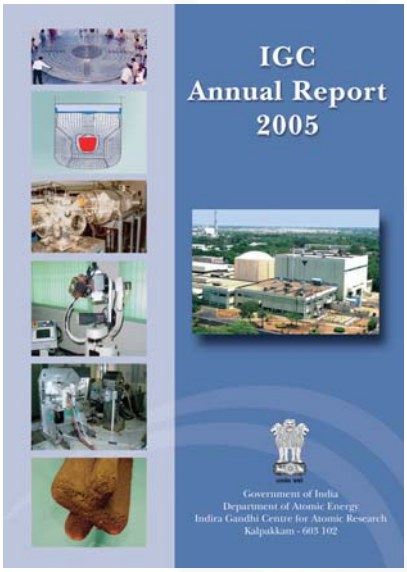

Cover page

Top to bottom
Grid Plate for PFBR, under construction
Mechanical consequences of a simulated core disruptive accident
Time-of-flight mass spectrometer
6-axis mini-robotic arm for remote inspection
Dimond anvil cell based high pressure x-ray diffractometer
Enriched elemental boron deposit
Centre
Aerial view of Fast Breeder Test Reactor (FBTR) complex

Back Cover page

A Fountain in the FBTR complex,
commemorating its twenty years of operation

Editorial

We are very happy to present you the annual report of the Indira Gandhi Centre for Atomic Research for the year 2005. The annual report mirrors the Centre's progress during the period. The significant strides made by the Centre in various spheres of its activities and landmark achievements in many areas have made our task easy. The FBTR reached the milestone of 20 years of successful operation, shining as a good example of the mastery of fast reactor technology. The achievement of 154 GWd/t burn-up in the unique mixed carbide fuel without a single fuel pin failure in the core, and the reprocessing of carbide fuel discharged at 100 GWd/t are other feathers added to the cap of the Centre. The progress in the construction of PFBR adds to the confidence that the PFBR will be commissioned well within the targeted time. The indigenous production of enriched elemental boron, development of manufacturing technology for grid plate and the carefully performed experiments to establish the effect of chloride corrosion on the concrete structures are examples of the multidisciplinary strengths in the Centre which have formed the foundation on which the fast breeder programme is progressing. Buoyed by these successes and the simultaneous progress in the mission oriented R & D programmes, the Centre has raised its targets and is now looking for achieving much higher levels of burn-up, safety and economy in fast reactor systems. In fact, a clear road map emerges from the results of the R & D programmes reported this year. The large number of articles presented in the section on R & D for FBRs as well as the sections on fuel cycle and enabling technologies is an indicator of the thrust of the Centre on taking up programmes with a focus on achieving leadership in fast reactor technology and instilling confidence in policy makers to build on the successes to realize a rapid growth of the fast reactor programme. The basic research activities in the Centre have continued to flourish and support the fast reactor programme. Many new results are reported in physics, chemistry as well as engineering disciplines. The infrastructure facilities have kept pace with the growth of the activities of the Centre.

This is the second issue of the annual report being brought out by the present editorial committee. As in the previous years, we have tried to select the best of the articles submitted by our colleagues, through a transparent and independent review process. We have also tried to make a few changes in the layout and the get-up to make it more appealing to the readers. We have included reports on important events as well as visits of eminent personalities to the Centre.

The emphasis laid on excellence in every activity by Dr. Baldev Raj, Director, IGCAR is reflected both in the contents and appearance of the report, and the Editorial Committee gratefully acknowledges his inputs and guidance. We also thank the authors and also the reviewers who have shared our responsibility with regard to ensuring quality of technical reporting. I am personally grateful to the members of the Editorial committee, especially Dr. K. V .G. Kutty, Shri R. V. Subba Rao, Dr. B. Purniah and Dr. G. Amarendra, for their enthusiastic support at every stage, and for the commitment to adhere to quality and time schedule. I also thank Shri. M. Somasekharan and Shri. M. Ganapathy for their valuable efforts during the printing stages.

We had received many words of appreciation as well as suggestions for improvement from the readers of the last Annual Report. We have tried to meet the aspirations of the readers by emphasizing on quality at each stage of the editing and publication process. We will be grateful to receive any suggestions for further improvement.

Kalpakkam
February 19, 2006

P. R. Vasudeva Rao
Director, Chemistry Group &
Chairman, Editorial Committee

FOREWORD

A large number of significant and a few benchmark achievements have been made in the R & D activities of the Centre pertaining to design and engineering developments, reactor operation, fuel reprocessing, materials, safety, physics, chemistry, instrumentation & control. We have also witnessed a marked improvement in engineering services, administration etc.

The detailed design of major components, systems and structures of the Prototype Fast Breeder Reactor (PFBR) 500 MWe has been completed, with the objective of safety, techno-economic demonstration and indigenous manufacturability. The Preliminary Safety Analysis Report (PSAR), which forms the most important document for reactor construction clearance from the regulatory body, has been updated, reflecting additional design inputs required by the safety committees. The plant layout has been finalised with emphasis on safety, constructability, maintainability and compactness.

Technology development for the manufacture of all the major critical components required for PFBR, has been completed successfully. Control and Safety Rod Drive Mechanism (CSRDM), one of the most important engineered safety components of the reactor, manufactured as a part of technology development and design validation, has been qualified for PFBR, after rigorous testing in air and in hot sodium, representative of reactor conditions. We have gained expertise in steam generator facilities, sodium handling, design and development of sensors, development of structural materials and materials characterisation.

The Fast Breeder Test Reactor (FBTR), the flag-ship of the Centre, has been operating in an exemplary manner with high availability factors. The unique fuel of FBTR has achieved another significant landmark of reaching a peak burn-up of 154,000 Wd/t, without any fuel failure. The PFBR test fuel sub-assembly has reached a burn-up of 59,200 MWd/t, against the target burn-up of 100,000 MWd/t, at the designed linear heat rating (LHR) of 450 W/cm. It is planned to convert the FBTR core from carbide to mixed carbide and MOX fuel gradually. Various important components are being analysed for the extension of the life upto 30 years, as a first step. It is heartening to note that FBTR has attained capabilities to work at high availability factor of more than 80% in successive campaigns during the year 2005.

The Centre has created a new international bench-mark by successfully reprocessing the mixed carbide FBTR fuel, which has undergone a burn-up of 100,000 MWd/t, in the Lead Mini Cell (LMC). Various equipment developed have been subjected to rigorous tests and the experience gained is being utilised for the design of the fast reactor reprocessing plant and also for the demonstration of reprocessing of the oxide fuel.

The Boron Enrichment Plant (BEP) has achieved an enrichment above 65% in ^{10}B, which is the requirement for PFBR. A few kgs of boric acid was produced for conversion into elemental boron. Based on the technology demonstrated, a plant is being set up at Manuguru to produce enriched boron for PFBR.

The Centre has been pursuing basic research in various frontier areas of science and technology and some of them such as radiation damage in reactor materials (D9 and modified D9 steels), applications-oriented superconductivity devices, MEMS ultrasonic transducers for NDT applications etc., find

direct applications for PFBR. We are taking part in setting up of national facilities such as the experimental programme for utilising the INDUS-2 beam line at the Raja Ramanna Centre for Advanced Technology (RRCAT), Indore and materials irradiation beam line at the upcoming medical cyclotron facility at Kolkata.

It is also worth mentioning that as a sequel to our earlier peer review in physical sciences, this year we have carried out peer review of chemical sciences with an eminent panel of experts. The panel has gone through the detailed technical documents, listened to in-depth presentations and visited important laboratories. The panel has suggested valuable recommendations for making our Science R&D more vibrant and relevant for achieving higher impact. We are also taking steps to carry out a similar peer review of our engineering sciences by an expert panel of high repute.

It is a matter of pride that we are taking active part in strengthening the activities related to the Homi Bhabha National Institute (Deemed University), in terms of formulating the curriculum and academic structure. Focussed collaborations have also been made with renowned academic and research institutions like IITs, IISc, SERC, Anna University, FCRI, Sathyabama University, Vellore Institute of Technology etc., for strengthening the various R&D activities and enriching science and engineering education in our universities.

The goals ahead are clear - timely and necessary inputs to the PFBR 500 MWe project, robust reprocessing technology, enhancing the R&D for realising reliable, safe and economical FBRs and the nuclear fuel cycle. We will endeavour to remain at the forefront of basic Sciences, in select areas. We are also chartering a path of achieving significant breakthroughs by harnessing basic sciences for meeting technological challenges. FBR technology is destined to gain more importance and significance. We have not only to continue to march forward at a faster pace, but also to rededicate completely to put in all our efforts in this technology to make it robust. Our merits will be judged, not only by the efforts we put in but, by the results we produce. I am confident that our Centre can achieve better results and can become a bench mark organisation not only in the country but also internationally.

I would like to quote Shri Aditya V. Birla, an eminent industrialist known for his vision, capacity to dream and for delivering the results in a competitive environment. "*Create an environment of Meritocracy: Spot and track nascent talent and create leaders with a rich mix of skills - who have exposure to different functions in the organization. Time and again, the supremacy of the human skill and spirit cannot be over-emphasized. The success or failure of an organization depends on human beings, their talents, their initiatives, their ability to lead and co-ordinate with others and importantly, to work as a competitive team. It also depends on the ability of the organization to motivate them to greater heights and to provide necessary challenges…*". I truly believe that our emphasis on human resources and talents, their mentoring and motivating them to achieve greater heights and creating an environment of individual creativity and providing the necessary challenges with the right synergy are all well-thought out steps in our march towards progress. I believe that our vision is of great value to the nation and our human resources have to continuously grow and match with this mission and vision.

I would like to compliment Dr. P. R. Vasudeva Rao, Chairman, Editorial committee and the members of the committee for putting their best efforts in bringing out the Annual Report, highlighting the significant activities of the Centre in a comprehensive manner

With my best wishes and warm regards,

Baldev Raj
Director

Kalpakkam
February 19, 2006

CHAPTER 1

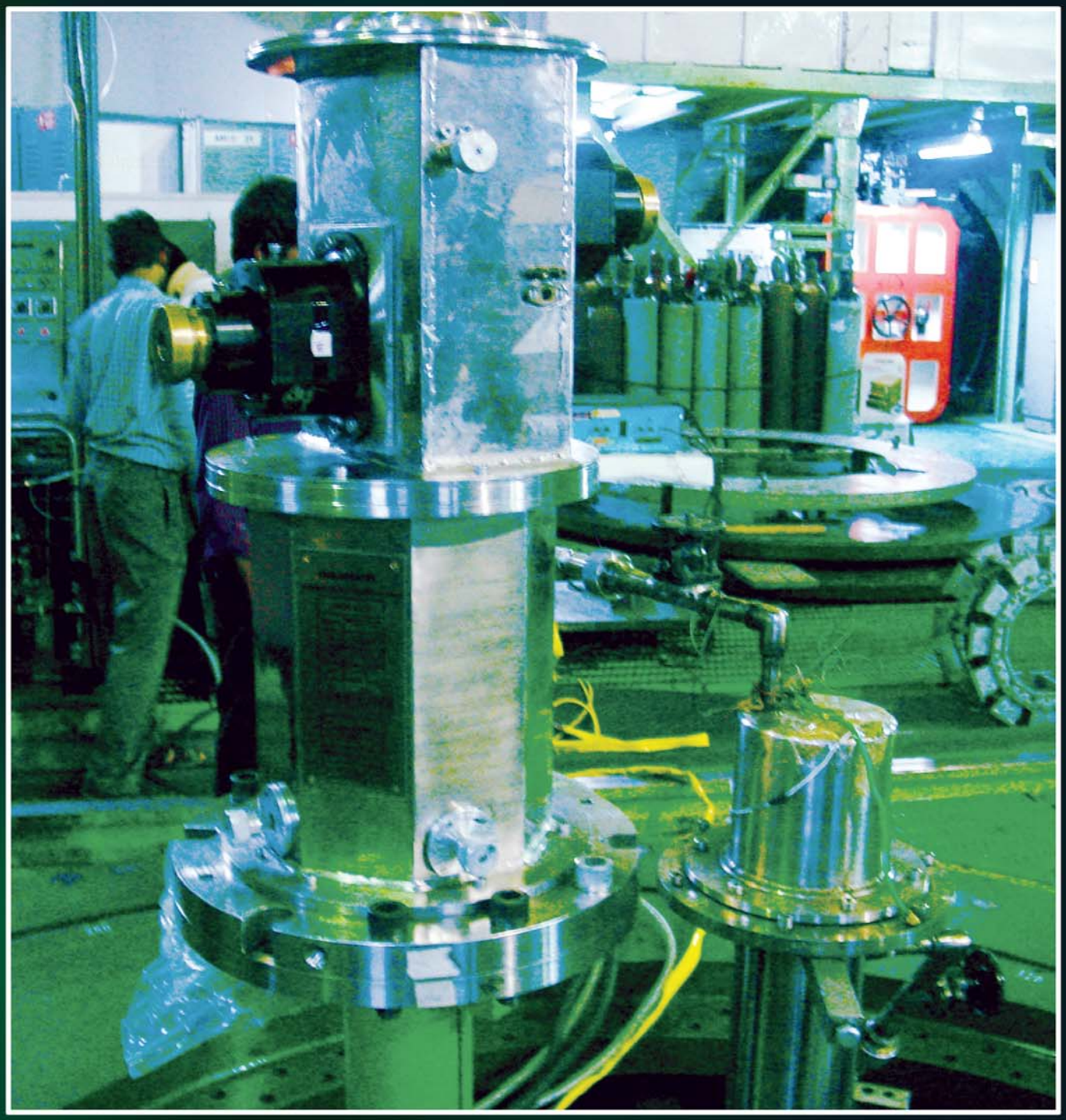

FBTR

1.1 Fast Breeder Test Reactor Completes Twenty Years of Operation

The Fast Breeder Test Reactor (FBTR) turned twenty on 18th October, 2005. Starting with a core of 23 fuel subassemblies rated for 10.5 MWt, the reactor core has been progressively enlarged by adding Mark-I and Mark-II subassemblies. The reactor has completed 13 irradiation campaigns, with the core for the last campaign rated for 16 MWt and having 29 MK-I and 13 MK-II fuel subassemblies, in addition to a Prototype Fast Breeder Reactor (PFBR) test fuel subassembly. Various milestones crossed by FBTR are given in Table 1. The progressive evolution of the reactor power and operating peak linear heat rating are shown in Fig.1.

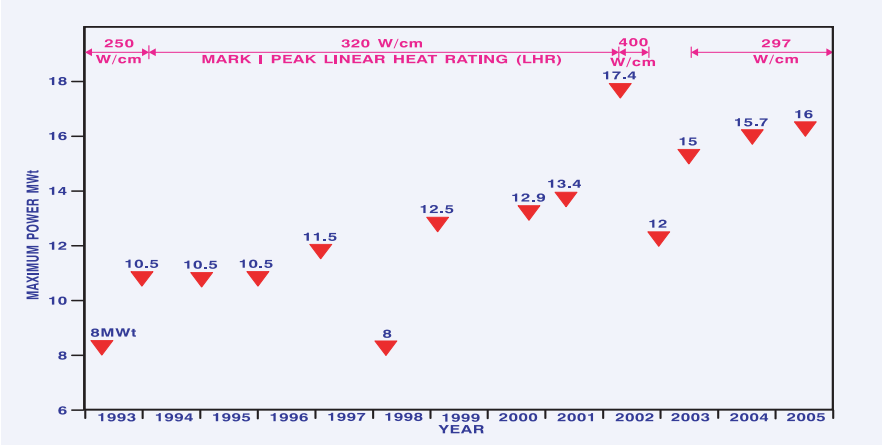

Fig. 1. FBTR power evolution

The performance statistics of reactor operation as on 18th October are summarized in Table 2.

The major challenges faced include reactor vessel deflection due to cover gas convection in the annular spaces at the top, fuel handling incident which warranted in-situ cutting of the guide tube by a special tool developed by BARC (Fig. 2), main boiler feed pump seizure, core cover plate getting stuck, reactivity transients, leaks from the biological shield cooling circuit coils and sodium leak from the primary sodium purification circuit. These affected the reactor availability upto the 9th irradiation campaign. The reactor availability from the 10th campaign onwards has been more than 75%.

As an irradiation facility, Zr-Nb alloys developed indigenously for the PHWR has been irradiated in FBTR and qualified. Fuel of composition simulating the PFBR fuel is at present undergoing irradiation.

The performance of the nuclear systems has been very good. The sodium pumps have been in continuous service most of the time, except during fuel handling, preventive maintenance etc. Availability of the pumps on demand has been excellent- more than 95%. Though occasional problems of high vibration and arcing in the DC generators have been faced in the Ward Leonard drives, the pumps themselves have been trouble free except for occasional increase in oil leaks, warranting replacement of the mechanical seals. Sodium purity is well maintained, with the plugging temperature always below 105°C. Cover gas purity and system integrity are so well maintained that even with the cold traps out of service for three months, the plugging temperatures are below 105°C. So far, 52 fuel handling campaigns have been completed, and all the 46 campaigns after the fuel handling incident of 1987 have been smooth. Integrity tests of the Reactor Containment Building have been carried out 11 times so far, and the leak rate has always been below the permissible leak rate. Visual

Table 1. Milestones of FBTR

18th Oct 1985	First criticality
Nov 89	Sodium valved in into Stream Generator(SG)
Jan 93	Water valved in into SG
Dec 93	Power raised to 10.5 MWt
94-95	Safety Related Engineering Experiments
May 96	MK-I burn-up of 25 GWd/t
July 97	TG synchronised to grid
98-99	Zr-Nb irradiation for PHWR
Apr 99	MK-I burn-up of 50 GWd/t
Mar 2002	Power raised to 17.4 MWt
Sep 2002	MK-I burn-up of 100 GWd/t
July 2003	Start of PFBR Test Fuel Irradiation
Oct 2005	MK-I burn-up of 150 GWd/t

Table 2. Summary of performance statistics

Parameter		Since first criticality
Maximum Power	(MWt)	17.4
Maximum LHR	(W/cm)	400
Maximum bulk sodium temperature	(^{0}C)	444
Operating time		
High Power	h	20,428
Low Power	h	16,490
Total	h	36,918
Thermal energy produced	(MWh)	262748
TG synchronisation time	(h)	5228
Electrical energy generated	MU	5.425
EFPD @ LHR of 320 W/cm	(d)	810
Peak burn-up	(GWd/t)	148.4
Longest operating campaign	(d)	54
Cumulative of four Na pumps operation	(h)	5,45,556
SG operation	(h)	20,428
No. of LOR / scrams		245 / 158

inspection of the reactor vessel internals has been carried out at two-year intervals and reactor internals have been found to be healthy, without much of sodium deposits (Fig. 3). Periodic visual inspection of the primary and secondary piping hanger settings, ultrasonic inspection of the secondary sodium piping and the steam generator shell welds, and liquid penetrant examination of secondary sodium pump supports have confirmed the overall integrity of the sodium systems. The cumulative radiation dose to personnel during the two decades of operation is only 67 person-mSv and the cumulative stack release is 440 Ci of Ar^{41}.

More than 500 modifications have been carried out in the plant to enhance plant safety, availability and for operator convenience. The major replacements include the two sub-systems of Central Data Processing System, neutronic channels, 1-Φ 220 V UPS, station batteries, fire alarm system, nitrogen plant, DM plant and one main boiler feed pump. To avoid the several spurious trips that were originating from the steam-water system, the contact type of feed water heaters were replaced by shell & tube type (Fig. 4). To improve the reliability of the Steam Generator Leak Detection system, triplication of the system in both the loops was taken up, and has been completed for the east loop. For the west loop, the system has been duplicated and triplication will be completed shortly. Augmentation of the

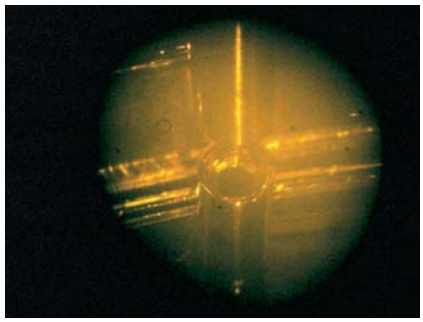

Fig. 3. Siphon Break Pipe and the reflection of its open end in sodium

Fig. 2. In-situ cutting of guide tube on the Reactor (1988)

Unique features of FBTR

- Liquid metal sodium as the coolant.
- Excellent maintenance of the purity of tons of liquid sodium.
- Record performance of electromagnetic pumps for the circulation of sodium.
- High-plutonium monocarbide fuel, used for the first time in the world.
- The burn-up logged by this fuel is an international record.
- The operating temperatures of FBTR heat transport systems are higher than in any other nuclear reactor in India.
- The steam pressure is the highest.
- The turbine is unique in that it is a low power turbine using high temperature, high pressure steam.
- Perhaps the purest DM water among all plants is made in FBTR, arising out of the demand from the once-through steam generators.

Fig. 4. Shell and Tube type rebeaters

ventilation system of turbine building and steam generator building and augmentation of the chilled water supply to the plant are in progress.

Since FBTR has completed 20 calendar years of operation, shortly there will be a Periodic Safety Review by AERB for relicensing the plant. Towards this, residual life assessment of the nuclear system components based on the operational data and physical assessment of the health of the various systems, sub-systems, structures and components by plant walk-through are being undertaken. Due to operation with the small carbide core, the effective life utilized by the nuclear systems so far is only about 3 years. The reactor is hence still left with enough residual life to complete its mission as a test-bed for fast reactor fuels and materials. In the next few years, it is planned to (a) irradiate metallic fuel and vibro-compacted oxide fuel, (b) demonstrate the potential of FBTR as a breeder by breeding U^{233} in thoria blankets surrounding the core and (c) to demonstrate the closing of fuel cycle using several metallic fuel subassemblies.

It may be noted that FBTR is unique in several respects vis-à-vis other nuclear plants in India. It is gratifying to note that FBTR has operated successfully for twenty years, giving rise to these unique performance characteristics, which have given us enough confidence and operational experience to feel that we have mastered fast reactor technology, to embark on the construction of 500 MWe PFBR at Kalpakkam

1.2 Hybrid Core for FBTR

Mixed (U,Pu) oxide (MOX) fuel was considered for FBTR in the 70's at the project design stage. The initial design envisaged 65 fuel subassemblies of MOX fuel with a composition of 30% PuO_2 and 70 % UO_2 , with the latter enriched in U^{235} to 85%, as was used in the French reactor Rapsodie. Since enriched uranium was not available, theoretical studies and limited out-of-pile coolant compatibility tests were carried out for MOX fuel with 74% PuO_2 in the seventies. Poor predicted performance with regard to Linear Heat Rating, poor compatibility of the Pu-rich oxide fuel with sodium and problems in maintaining the O/M ratio and uniformity of phases during fabrication, ruled out the choice of high Pu MOX. Hence the alternative choice of a carbide fuel was chosen and FBTR was made critical with a small carbide core of 23 fuel subassemblies of Mark-I composition (70 % PuC - 30% UC). The core has since been progressively enlarged by adding (U,Pu) carbide fuel subassemblies (SAs) to compensate for reactivity loss due to burn-up.

Towards raising the reactor power to the nominal value of 40 MWt, a core of 76 subassemblies of MK-II fuel (55% PuC - 45%UC) was envisaged in 1995. Subassemblies of this composition were inducted in the peripheral locations of the core in 1996, with a view to progressively phase out the MK-I SA. The present core has 29 MK-I and 13 MK-II fuel subassemblies, in addition to a test fuel subassembly simulating PFBR MOX fuel.

One of the major missions of FBTR is testing of different types of fast reactor fuels. The carbide fuel has now been proven, including its reprocessing and fuel cycle closure. The fuel chosen for the next few power breeder reactors will be MOX, from considerations of cost and ease of fabrication and handling. Recently, there have been studies abroad of high Pu MOX fuel in the context of Pu burning in fast reactors. Reports in open literature indicate that MOX with PuO_2 content to the extent of 45% is compatible with sodium. Hence a study was conducted for the use of MOX with 44% PuO_2 as the driver fuel for FBTR. It is not possible to reach criticality with a full core of MOX with this PuO_2 content, since the core has to be confined within the area covered by the Core Cover Plate, which limits the core size to 85 fuel subassemblies. An alternate strategy of having a hybrid core with MK-I SA at the centre and MOX fuel at the periphery was hence studied

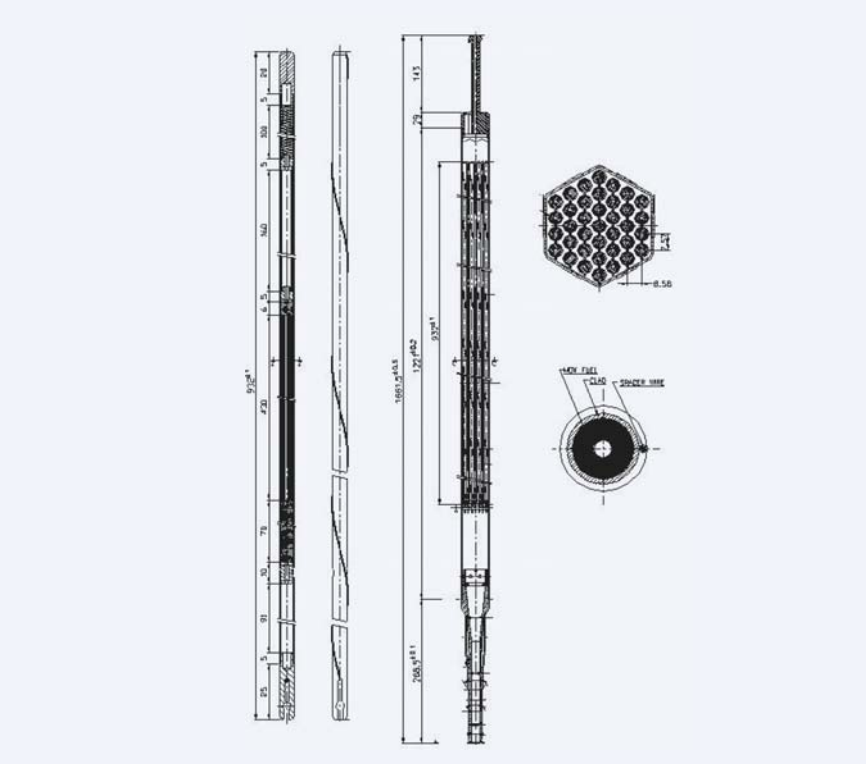

Fig.1. MOX fuel subassembly

and found feasible. The carbide will be the driver fuel and MOX will contribute to increased reactor power.

Fuel-coolant compatibility studies were conducted by RMD, BARC and FChD, IGCAR on several pellets of MOX fuel with 44% PuO_2, at temperatures upto 800°C and times upto 400 h. These studies confirmed good fuel-coolant compatibility. Small volume changes observed in these studies were found to be due to cracking of pellets followed by sodium ingress as well as limited formation of reaction products. Under the sodium purity conditions prevalent in the reactor, the reaction products formed are too insignificant even for detection by XRD analysis. In the event of pin failure, there would be sufficient time for the operators to respond and initiate reactor shut down.
With these reassuring results, the design of the hybrid core has been completed for FBTR. The core will have 27 MK-I and 57 MOX fuel subassemblies, and generate 30.7 MWt with the MK-I operating at 400 W/cm. MOX pins will operate at a peak linear heat rating of 250 W/cm when the central MK-I operates at 400 W/cm. The entire core is designed with only two flow zones- one for MK-I and the other for MOX. This will facilitate fuel management by moving the subassemblies from the outer rings to the inner rings to exploit their full power potential.

MOX subassembly consists of 37 pins of 6.6 mm OD and 5.7 mm ID housed inside a standard FBTR hexagonal sheath (Fig.1). MOX fuel pellets are hollow, with 5.52 mm OD and 1.9 mm ID. Pin and pellet diameters are identical to PFBR fuel design. The clad is of D-9 alloy as in PFBR fuel. To increase the subassembly power, and therefore the reactor power, the fissile column length for MOX pins is increased to 430 mm (as against 320 mm for MK-I pins). The fuel stack will be in line with the B4C column in the control rods when the reactor is in fuel handling state. To limit the dose rate on the grid plate, a bottom axial blanket of depleted UO2, of 70 mm length, has been provided. The fuel pin has been designed for 100 % gas release at a peak burn-up 100 GWd/t.

Though the MOX fuel chosen for FBTR has higher PuO2 content (44%) than the fuel for PFBR (29%), it is expected to provide good feedback on several aspects of the PFBR fuel cycle. The MOX fuel pin and pellets for the hybrid core have the same diameters as PFBR fuel. The clad chosen is also the same as in PFBR. The fabrication and reprocessing routes to be adopted are identical for both the fuels. Therefore the experience with the high Pu MOX fuel in FBTR will be definitely valuable for the PFBR fuel cycle. Due to its higher Pu content, it will also provide conservative feedback on the behaviour of MOX fuel on aspects like fission gas release, swelling, FCCI and failed fuel behaviour.

Provisional safety clearance for the hybrid core has been obtained from the regulatory bodies. Preparation of safety report is in progress. It is proposed to load five MOX subassemblies as lead subassemblies at the end of the 13th irradiation campaign in January 2006. The Advanced Fuel Fabrication Facility, Tarapur, have fabricated MOX fuel pins required for the first charge. The transition to full hybrid core is planned to be completed by the end of the 16th irradiation campaign by end 2007.

1.3 Coupled Neutron Gamma Transport Calculations for FBTR with Hybrid Core, Radial Thorium Blanket and Shields

The performance of the Mark-I fuel in FBTR has been excellent, with the peak burn-up exceeding 150 GWd/t and linear heat rating reaching 400 W/cm. One of the missions of FBTR is the testing of different types of fuels. As a part of this, an alternate strategy of having hybrid core with Mark-I core at the centre and MOX fuel at the periphery was studied. Based on the proposal for hybrid core for FBTR a full 2-D RZ transport calculation including shields, upto the middle of the structural concrete in the radial direction and upto 190 cm in the rotating plug region in axial direction which is almost the middle height of the rotating plug, has been carried out for FBTR. The 2D RZ model is given in Fig.1.

Neutron and gamma distributions in core, sodium, reflectors, neutron shield, detector location, control plug and structural concrete are the most important information from reactor physics point of view. Neutron and gamma distributions have been obtained by 2-D RZ transport calculations using the code DORT and the model extended upto the biological shielding. The cross section sets used were DLC (100 neutron + 21 gamma groups) and IGC-S3 (175 neutron + 42 gamma groups). It is seen that at most of the locations IGC-S3 predicts slightly more flux than DLC. The contour plot of total neutron flux is given in Fig.2. The total neutron flux, fluxes above 0.1 MeV and gamma fluxes at certain locations are given in Table 1. U235 eq. flux in detector location is found to be 6.08*1010 n/cm^2/s and the gamma dose rate in this location 74.3 Gy/h respectively. The total neutron flux and the gamma dose at the middle of the structural concrete is 4.15E*10^3 n/cm^2/s and 2.2E-02 Gy/h respectively. The neutron attenuation produced between the structural concrete beginning and middle is around 500 and for gammas it is

Table 1. Neutron Flux (n/cm^2/s) and Gamma Flux (γ/cm^2/s)Values at 30 MWt

Region	Total Neutron Flux	Fast Flux >0.1 MeV	Gamma Flux
Guide plate	1.30E+14	4.08E+13	2.97E+05
Core Centre	2.96E+15	2.46E+15	2.22E+07
Fuel SA Top	2.59E+13	8.23E+12	4.12E+04
Top of Sodium	1.82E+11	2.65E+09	1.56E+03
Structural Concrete (middle)	4.15E+03	1.18E+02	8.04E+05

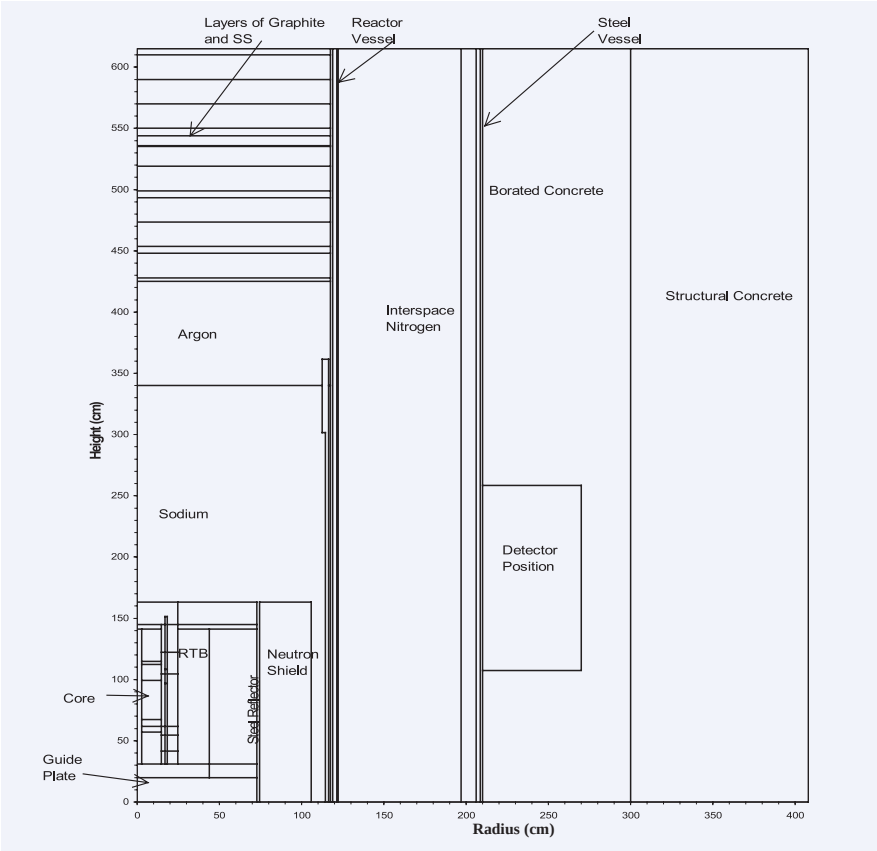

Fig.1. 2D RZ Model of FBTR

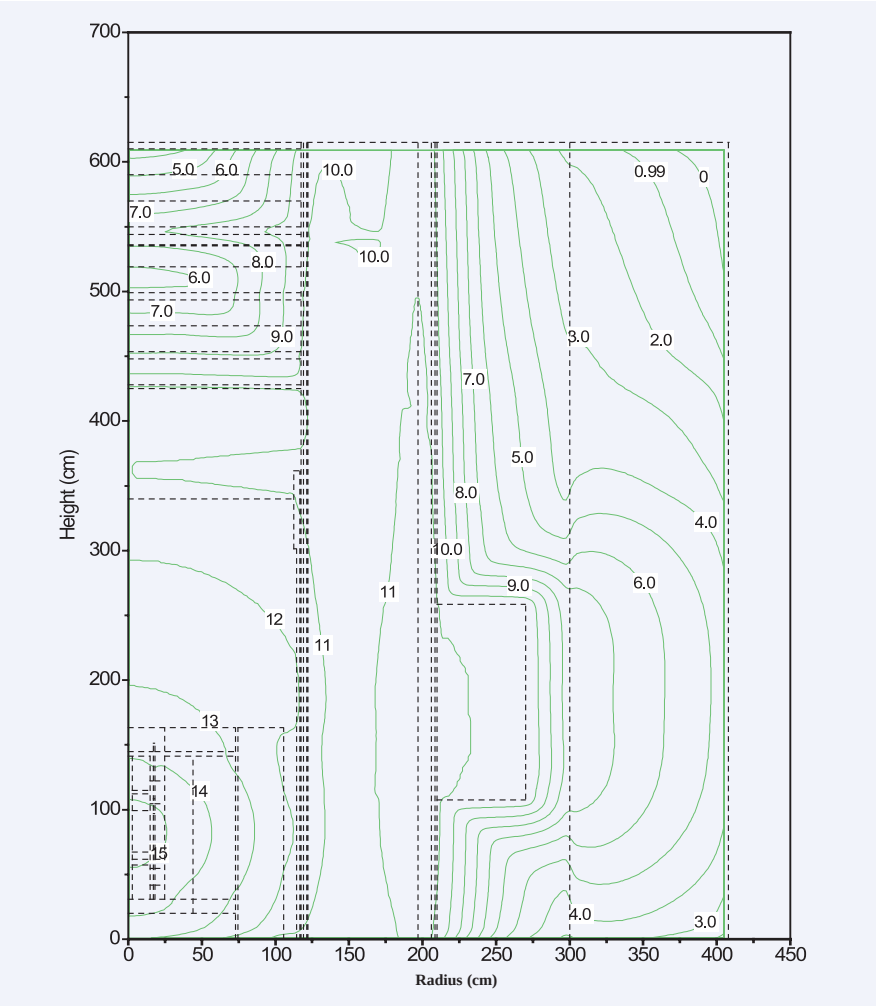

Fig. 2. Neutron flux contours in FBTR (Numbers inside the figure are the order of neutron flux. For example 7 means 10^7 n/cm^2/s).

around 400. The attenuation from the bottom of the rotating plug to 190 cm height in the plug is ~$7.0*10^7$ for neutrons and 10^4 for gammas. A height of 170 cm in the top of rotating plug region which contains mostly steel is not modeled here.

The displacements per atom (dpa) at the core centre for 1 full power year (fpy) is found to be more at the beginning of the Mark-I core and it is continuously decreasing from the MOX core beginning to MOX core end in the radial direction. The dpa at the top of the guide plate is nearly same below Mark-I core (0.36) as well as MOX core (0.33). For 1fpy operation at 30 MWt of hybrid core which corresponds to nearly 2,60,000 MWh the dpa is only 0.36. It is concluded that as far as radiation damage to grid plate is concerned hybrid core is as good as Mark-I core. Similar conclusion is found for helium production in steel of grid plate also.

Heating calculations show that neutron heating, which includes the fission heating, in core contributes more than 97 % of the total heating. Gamma heating contribution is high in the case of steel reflector (94 %) and neutron shield (98 %) after including neutron capture gammas in the gamma heating.

1.4 Dimensional Measurements of FBTR Control Rod Subassembly

One of the FBTR control rod subassemblies that was exposed to 5.0 x 10^{22} nvt fluence has encountered three incidents of dropping of control rod-C during the raising of reactor power. On each occasion, the control rod dropped due to the increase in the lifting force beyond the set limit. It was suspected that this happens when the shoulder of the control rod is about to enter the top stellite track of its outer sheath resulting in the interference of the control rod with the outer sheath. This necessitated detailed Post Irradiation Examination (PIE) of the control rod subassembly. Fig. 1 shows a sketch of the control rod and outer sheath.

The interference of control rod shoulder with its outer sheath might be due to changes in dimensions or/and bending of the control rod or/and outer sheath. Therefore during the PIE, emphasis was given in the determination of following parameters:

1. outside diameters at foot and clad regions of the control rod

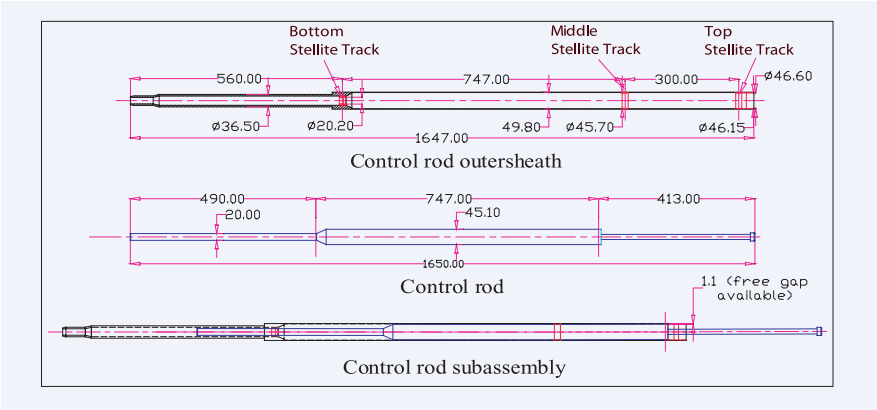

Fig. 1. Schematic of the control rod and outer sheath

2. straightness of control rod with respect to the foot region
3. straightness of the outer sheath with respect to foot
4. inside diameters of the middle and top stellite tracks of the outer sheath

A 'profile scanning device' was designed, fabricated and used for measurements of the outside diameters and straightness of the control rod which was clamped on the in-cell CNC machine table using the T-slots as reference. The device has tenons at the bottom which enables precise horizontal movement along the T-slots parallel to the longitudinal axis of the control rod. The device has a C-frame with three precision dial gauges, two horizontal and one vertical as shown in Fig. 2. The measurement accuracy of device is 0.05 mm. The diameters of the control rod at various locations are found out by comparing the readings of diametrically opposite horizontal dial gauges with the value obtained from a calibration rod. Straightness of control rod is estimated from the longitudinal axis which is reconstructed from the dial gauge readings taken along the length. The horizontal and vertical dial gauge readings are used to re-construct the longitudinal axis of the control rod in two perpendicular planes.

For the determination of the shift in the longitudinal axis of the outer sheath with respect to its cylindrical foot region, a tapered cylindrical mandrel was made and used along with the profile scanning device. The tapered end of the mandrel is inserted into the top hollow region of the outer sheath such that it fits into the middle and top stellite tracks. The axis of the straight portion of the mandrel projecting out of the outer sheath acts as the extrapolated axis of the top two stellite tracks and helps in the measurement and reconstruction of the axis of the outer sheath.

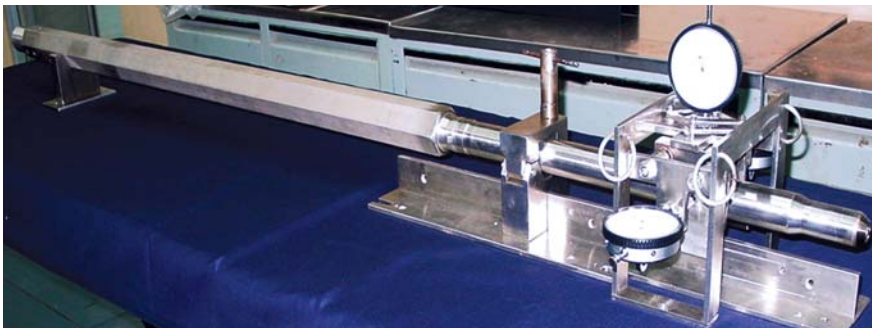

Fig. 2. Profile scanning device

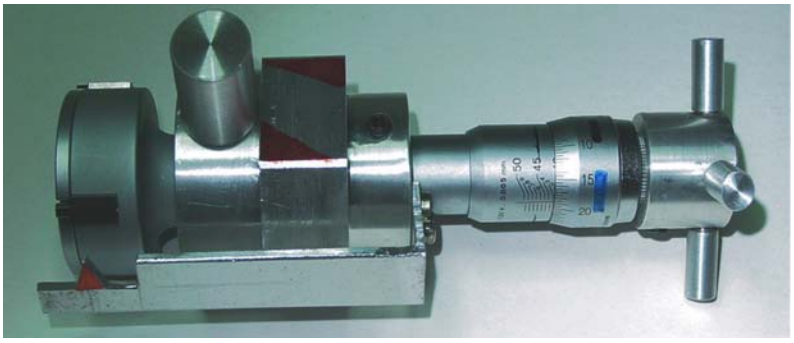

Fig. 3. I.D. Measuring device

Plug gauges with multiple steps were used for measuring the inside diameter of the top and middle stellite tracks. These gauges are based on the principle of 'Go' / 'No Go' gauges. The measurement accuracy of these gauges is 0.07mm. An inside diameter measuring device with a precision three-point contact micrometer was also used for diameter measurements. The measurement accuracy of these gauges is 0.005mm. Fig. 3 shows a photograph of this device.

The diameter of the control rod at various locations along the foot region was found to be

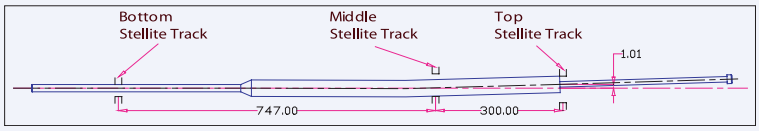

Fig. 4. Shift in the longitudinal axis of the control rod at the shoulder w.r.t. its foot region

within the original tolerance limits. In the middle of the clad region, a marginal decrease (.03 to .15mm less than design lower limit) in diameter was noticed. The shift of the control rod axis at the shoulder region with respect to the foot region was 0.30 mm in one orientation and 1.01mm in the perpendicular orientation. Fig. 4 shows the orientation with the maximum shift.

In the outer sheath, the outside diameter in the foot region and the apex-to-apex distance in the hexagonal region were within the original tolerance limits. Measurements of inside diameters carried out at stellite locations have showed that the ID of the middle and top satellite tracks are within the original manufacturing tolerance limits. The values obtained from the plug gauge and the three-point contact micrometer were found to be in close agreement with each other. The shifts in the axes of the sheath at the top satellite track with respect to the foot region in three orientations are 0.56mm, 0.83mm and 0.56mm. Fig. 5 shows the orientation with the maximum shift.

Fig. 5. Shift in the axis of the control rod sheath at the stellite tracks w.r.t. its foot region

The above results indicate that there is no growth in dimensions in the control rod and outer sheath. The maximum freedom available for the lateral movement of a fresh control rod within the outer sheath at the top satellite track is 1.1mm. However, in case the respective maximum bends of 0.83mm and 1.01mm which are observed in the axes of the control rod and outer sheath happen to be oriented in opposite directions under isothermal or shutdown conditions, there can be an interference of 0.74mm. During the raising of power by withdrawing the control rod, this interference can get compounded due to the temperature gradients in the core that can lead to thermal bowing of the outer sheath and to excessive force between the control rod and outer sheath. Thus, the present dimensional measurements have provided important information on the control rod subassembly.

1.5 Internal Inspection of Reactor Vessel with new Periscope

The technical specification for FBTR operation stipulates biennial visual inspection of reactor vessel internals to assess the extent of sodium oxide deposition on the vessel walls, to ascertain non-plugging of small pipes and to generally examine the internals for any abnormalities. This is carried out with the help of periscope with the illumination provided by the projector. The inspection campaign is carried out with reactor in shutdown state and primary sodium temperature at 180°C.

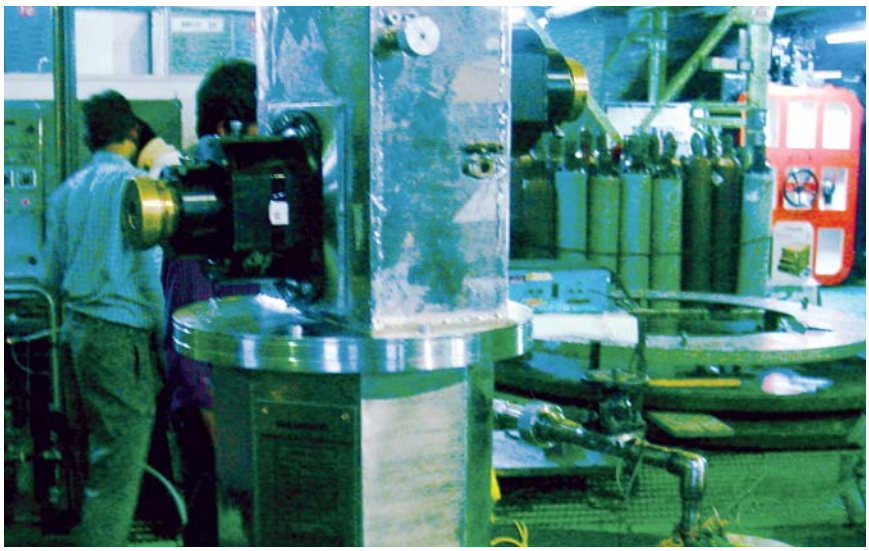

Fig.1. New Periscope installed in pile

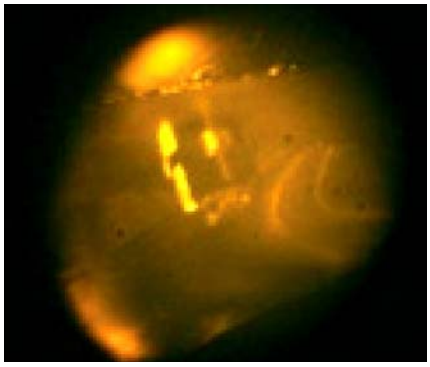

Fig. 2. Bolt of the flow restriction shell attached to the outlet pipe

The inspection so far was carried out with the periscope developed in 1985. This periscope has got some limitations. Its magnification was poor, no zooming facility was available and hence not found ideal for closer examination. The objective prism can only be swivelled from vertical down (0°) to horizontal (90°) in any vertical plane and back swing beyond 90° is not possible to have a view of bottom of rotating plugs. Hence a need for a new periscope was felt with better resolution, zooming facility and a provision to have back swing. The new periscope was designed and developed by DRHR and Spectroscopy Division of BARC and supplied to FBTR.

The new periscope, consisting of a scanning prism mechanism, zoom lens objective, a system of relay lenses and eye piece sub assembly for viewing the objects, has a linear resolution of 0.7mm to 1.6mm depending on the magnification, at an object distance of 2.5m, zooming facility with varying magnification from 2X to 5X and a back swing of 10°. The glass materials used for the lenses are radiation resistant crown and flint glass, which can withstand radiation doses upto 10^8 rads. To prevent the image rotation during viewing when scanning prism is rotated during inspection, a device known as Pechan prism is used in the eye piece assembly. The entire optical assemblies and their drive mechanisms are housed inside a SS tube, which can be installed in the experimental canal in pile. The rotation of objective prism is achieved by bronze pinion gears and the zoom lens movement by screw nut arrangement. The drives for scanning prism and zoom lens are achieved by the drive rods connected by universal couplings. The drive rods can be rotated by the knobs provided at the top of the periscope near the eye piece assembly. To prevent the direct streaming of radiation the optical path was offset with prisms in lead shielding plugs inside the periscope assembly.

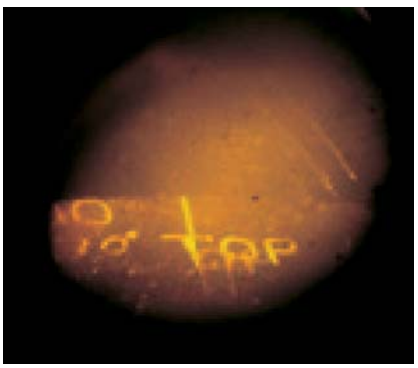

Fig. 3. Marking made during construction

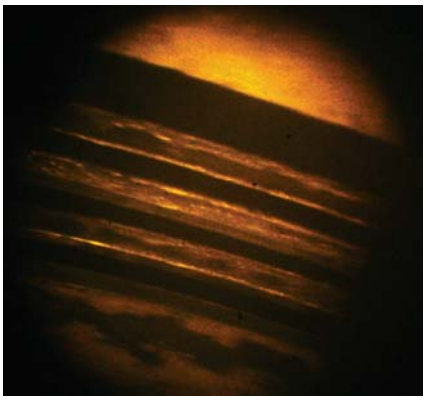

Fig. 4. Thermal shields

After optical alignment and assembly, the periscope was checked in the horizontal condition before despatch from BARC. The new periscope was installed in the pile (see Fig.1) for inspection after a complete mock up installation simulating the pile conditions and checking of the same in vertical condition.

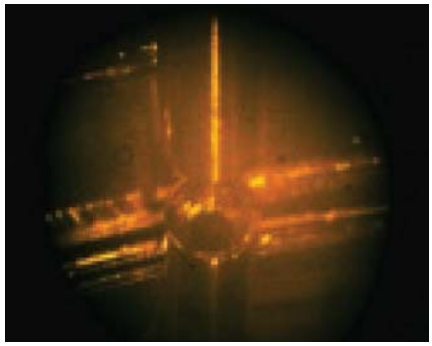

Fig. 5. Siphon Break Pipe and its reflection in sodium

The internal inspection of reactor vessel carried out with the new periscope in Aug. 2005 was satisfactory. The images were comparatively sharper and the resolution was excellent for our purpose. Fig. 2 and 3 showing a bolt of the flow restriction shell attached to the reactor vessel outlet pipe and a marking made during construction are proofs for the better resolution obtained in the new periscope, Fig. 4 and 5 show the clarity of the objects when seen through the new periscope during inspection.

The zooming facility was also useful during inspection. The small pipes are found to be non-plugged and no abnormalities found inside the reactor vessel. The vital reactor vessel internal inspection carried out with new periscope was satisfactory and with an improved illumination, the new periscope will be very useful for future inspection campaigns.

1.6 Thermal Hydraulic Investigations of Plugging Detection in Hybrid Core of FBTR

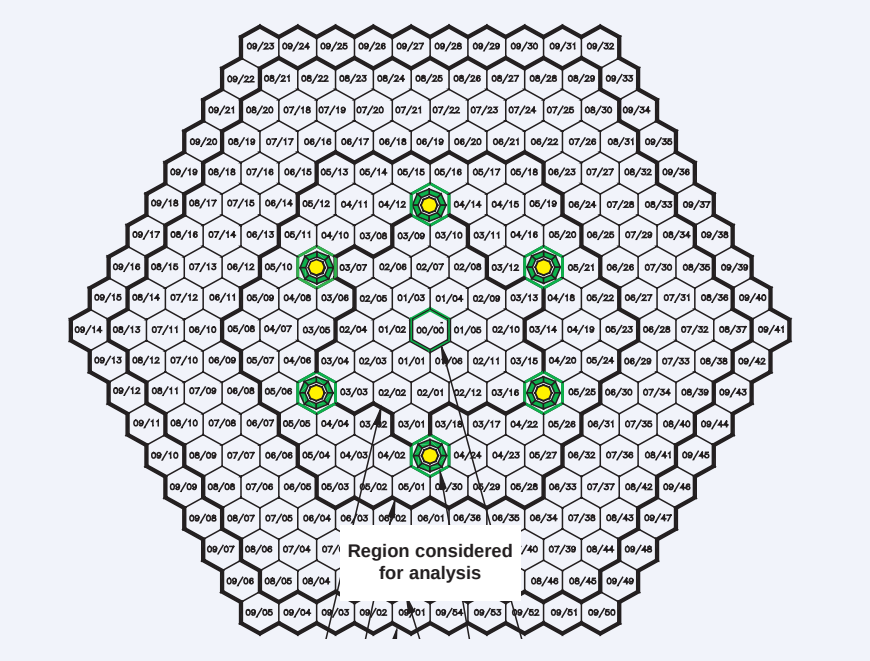

Fig. 1. Proposed hybrid core of FBTR

FBTR is designed for 40 MWt operation. The number of fuel subassemblies (SA) required to achieve this power is about 70. But the reactor has been operating in a smaller core configuration with 70% PuC - 30% UC as the fuel (MK-1). With this small core, a maximum power of 17.4 MWt only could be achieved. To increase the reactor power, it is proposed to add oxide SA surrounding the existing MK-1 carbide SA, leading to a hybrid core of carbide and oxide SA (Fig.1).

The core temperature monitoring system of FBTR has two plates at the bottom of the control plug viz. the fixed plate and the mobile plate (known as core cover plate or CCP). While the thermowells are attached to the fixed plate, the sleeves are attached to the mobile CCP. During reactor power operation, the CCP (hence the sleeves) is moved downwards very close to the SA spout, with a gap of only 15 mm between the spout top level and the sleeve bottom level. This enables the sleeves to effectively guide sodium from the spout to the respective thermowells. During fuel handling operation, when the plug rotation is required, the CCP is moved upwards, such that the bottom of the sleeves is in level with the tip of the thermowells. This position is known as 80 mm position of the CCP. Presently, the CCP is parked at 80 mm position. Due to the difficulties encountered in moving the CCP down, reactor operation is continued with the CCP at 80 mm position, after ensuring that the SA plugging detection is possible even with the CCP at 80 mm position in the current small core. It is essential to verify if plugging detection is possible for the proposed large hybrid core also, with CCP at 80 mm position. With this in view, 3-D thermal hydraulic studies were carried out to understand mixing pattern of sodium streams from various SA below the CCP and to predict the thermocouple readings for normal condition of the reactor as well as for the condition of plugging in SA. The main objective of the

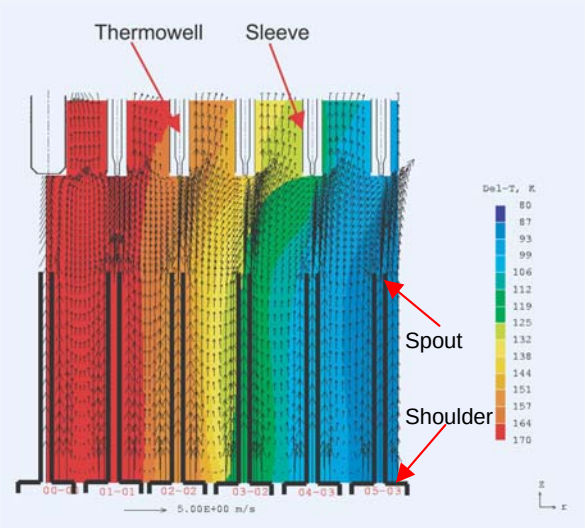

Fig. 2. Flow and temperature in a vertical plane through 04-03 SA (Normal condition)

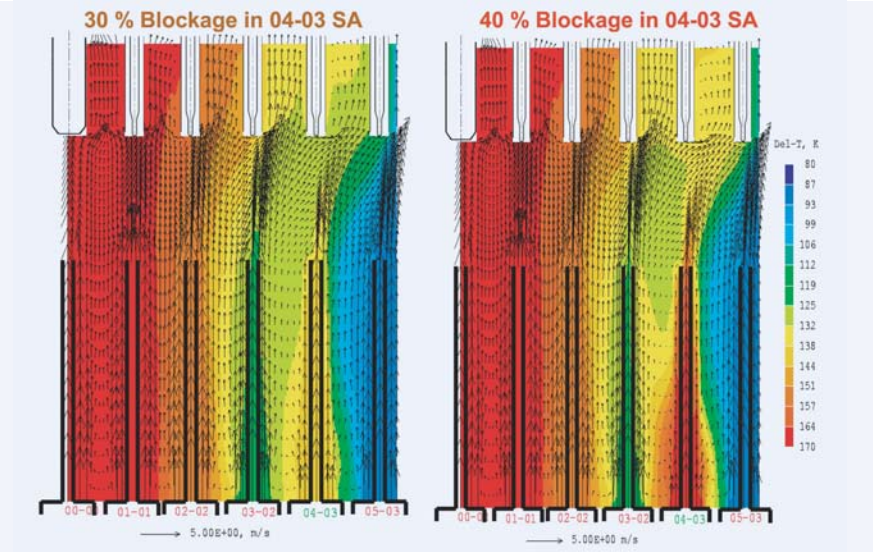

Fig. 3. Flow and temperature in a vertical plane through 04-03 SA as a function of blockage in 04-03 SA

study, thus, is to predict the magnitude of plugging that would lead to a temperature rise of 10 K in the corresponding thermocouple reading and to verify if this magnitude of plugging is acceptable from maximum clad temperature considerations. Detailed parametric studies were carried out with flow reduction in the SA as a parameter.

Based on these studies (Figs. 2 and 3), it is seen that the dilution is the least for all the MK-I SA in the 1st , 2nd and 3rd rings, due to the fact that the flow rate through them is large and they are favorably located in the central part of the core where masking effect is minimum. Temperature dilution is large for oxide SA, as the flow rate through them is less and they are located in the peripheral part of the core where masking effect is large. The maximum value of flow blockage that can lead to a temperature of rise of ≥ 10 K in the thermocouple reading is 10 % for the 2nd ring, 40 % for the 3rd and 4th rings and 30 % for the 5th ring. These values are much less than the permissible blockages (34 % for 1st ring & 51% for 3rd ring) of carbide SA and (55.5 %) of oxide SA in the peripheral rings, indicating that blockage could be detected well in advance, before the clad temperatures reach the allowable values.

1.7 Performance of Electrochemical Hydrogen Meters in FBTR

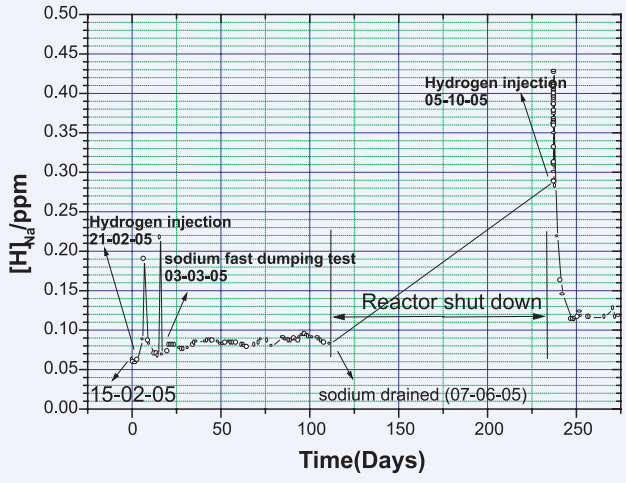

Fig.1. Response of electrochemical hydrogen meter in FBTR in the year 2005

Subsequent to the satisfactory performance of the new electrochemical hydrogen meters (ECHM) based on $CaBr_2$-CaHBr system in the Steam Generator Test Facility (SGTF) and the Sodium-Water Reaction Test (SOWART) facility circuits for on-line hydrogen detection in sodium, another meter of the same design complete with instrumentation for plant adaptation was installed in FBTR east sodium circuit. The response of the meter to hydrogen injections into sodium circuit for its calibration in the plant and the background hydrogen levels measured by it over a period of eight months from February 2005 are shown in Fig.1. The meter was calibrated in FBTR soon after installation by injecting hydrogen three times (40 ppb each time) into sodium circuit. A hydrogen level of 85

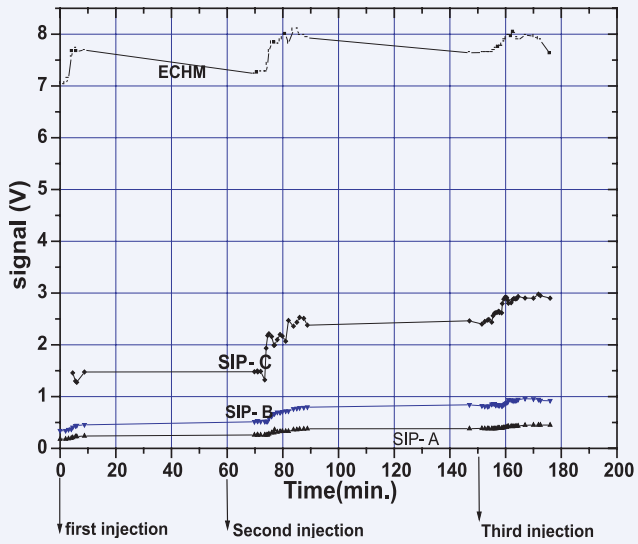

Fig. 2. Response of ECHM to hydrogen injections inphase with SIP detectors in FBTR

ppb was maintained by cold trapping the sodium before calibration. It can be seen that the background hydrogen level in the reactor was varying between 70 and 90 ppb until sodium was drained in June 2005. The Hydrogen Leak Detection (HLD) system was again calibrated during October 2005 when the reactor was restarted. The electrochemical hydrogen meter showed quick response in-phase with Sputter Ion Pump (SIP) based HLD system (Fig.2). After introducing the cold trap into the circuit, the background hydrogen level remained at about 110 ppb.

1.8 Upgradation of Central Data Processing System of FBTR

The application of computers in safety critical applications was pioneered by the fast reactor programme. Fast reactors have a high power density of the order of 500kW/litre in the reactor core and the liquid metal coolant flows through the fuel subassemblies to remove the heat efficiently. Plugging in any one of the fuel subassembly can lead to clad hotspot and fuel meltdown and hence has to be detected immediately to initiate safety measures. This necessitates the monitoring of output temperature of all the fuel subassemblies and the further derivation of mean output temperature. The mean temperature gradient across the core and the comparison of actual temperature rise with the expected temperature rise for every subassembly for early

Fig. 1. New Central Data Processing System of FBTR

warning on plugging. Since many derived parameters from all the fuel subassemblies have to be calculated, the use of computers in safety systems becomes inevitable in fast reactors.

FBTR had in its original design,two TDC 316 computers with 32KB of ferrite core memory and switchover logic to route the output signals. However, the computer system, first of its kind developed by ECIL became obsolete in 1985. Hence, the system was replaced by a dual diverse computer system with one based on PDP-11 and RSX-11M operating system and the other one based on Unipower-30 with VERSADOS operating system. These two computers are also obsolete now and spares are not available. Hence, the Unipower 30 based system has been replaced by three Real Time Computer based systems each exclusively for executing the following functions of FBTR.

1. Subassembly plugging detection - Safety
2. Discordance measurements, fine impulse test of safety logic etc - Safety related
3. Reactor vessel temperature measurement etc - Not related to safety

The RTCs used have been designed and developed in - house for the Intrumentation and Control(I&C) applications of PFBR. VME bus has been adopted as the hardware standard for all the computer systems to be used in PFBR. To minimize inventory and to facilitate maintenance, the same computer system with its family of I/O cards will be employed for all the three categories of I &C systems in PFBR. VME has been chosen the hardware platform as it is in wide use including nuclear and space applications for more than twenty years and is well proven. It is a simple non-multiplexed, asynchronous bus with acknowledgement of every transaction of the bus and is an IEEE standard (P1014). The number of slots (21) is quite adequate for configuring any system.

Motorola MC68020, a 32 bit processor based VME CPU card has been designed and along with it a number of Input / Output Boards also have been developed with self-test features. The boards have been built around VLSI devices and hence the number of interconnections has reduced, thus increasing the reliability. They have been tested extensively for functional as well as environmental specifications. Three computer systems have been configured at FBTR and the software has also been developed indigenously, strictly as per the AERB codes and standards. The computer systems have been commissioned successfully and are performing well thus providing valuable feedback for PFBR I&C design.

CHAPTER 2

Prototype Fast Breeder Reactor (PFBR)

2.1 Consruction Status of PFBR

The Government of India had accorded administrative approval and financial sanction for setting up of the 500 MWe PFBR at Kalpakkam in September 2003. Bharatiya Nabhikiya Vidyut Nigam Limited (BHAVINI), a public sector company under DAE was incorporated for the construction and operation of PFBR. IGCAR is responsible for the design, associated R & D and manufacturing technology, and getting clearance from regulatory bodies.

The detailed design of major components, systems and structures of PFBR has been completed with the objective of safety, techno-economic demonstration and indigenous manufacturability. The plant layout has been finalized with emphasis on safety, constructability and compactness.

The construction of the common base raft for 8 Nos. of Nuclear Island Connected Buildings (NICB) and the outer perimeter wall around the NICB raft have been completed. The construction of peripheral buildings, viz., service building and diesel generator building is in progress. Manufacturing of long delivery mechanical components of Nuclear Steam Supply System (NSSS), viz., main vessel, safety vessel, inner vessel, IHX, sodium pumps, grid plate, shutdown mechanisms, top shield, steam generators and sodium tanks is in different stages of fabrication in Indian Industries. Manufacture of over dimensional components like main vessel, safety vessel and inner vessel is in progress at the site assembly shop at Kalpakkam. The condenser is cooled by once-through system with sea water drawn through a submarine tunnel. The geotechnical investigations for sea water intake has been completed. A mega tender package for turbine generator and associated water - steam cycle equipment is under processing. The sodium service valves and NICB crane tenders are also under processing.

Fig. 1. Construction of PFBR

Fig. 2. Safety vessel fabrication

2.2 Manufacturing Technology Development of Grid Plate

The Grid Plate (GP) is one of the most important components in reactor assembly of the PFBR. It supports Core Subassemblies (CSA) and serves as a pressure plenum for distribution of coolant sodium into the CSA. GP accurately positions and maintains verticality of all CSA, including control rod SA, to facilitate smooth fuel handling operations by controlling the possible mismatch between top of SA and control rod drive mechanisms and fuel handling machine.

The GP is a box type structure of diameter 7m and height 1m and the material of construction is stainless steel 316LN with tight control on the chemical composition for better mechanical properties. It consists of top and bottom

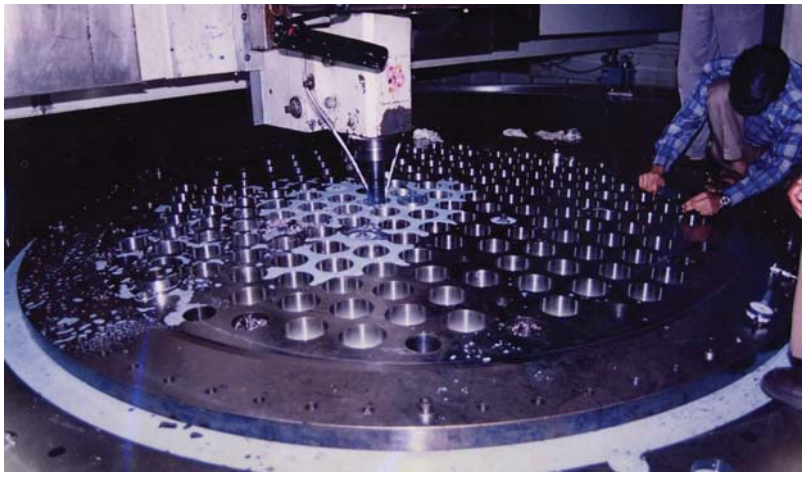

Fig. 1. Machining of top plate in SPM

plates bolted at their periphery through a shell. The plates are perforated in triangular pattern to receive 1758 numbers of sleeves that position the CSA. The GP transfers all the loads coming on it (including its own weight) to the core support structure (CSS). To permit differential thermal expansion between GP and CSS, an annular portion of the bottom of the GP is hard faced. Further to avoid self-welding between CSA and sleeves and facilitate their removal during fuel handling, hard facing is provided at the top and on the inner surface of sleeves at a required depth.

In order to meet the functional requirements and to minimise leakage of coolant sodium from GP, the deviations permitted during the manufacture (tolerances) on the dimensions and geometry of various parts and final assembly of GP are tighter than what are normally specified for other conventional components. Some of the major challenges in the manufacture of the GP include the following.

- Machining of large diameter plates and shell assembly to the required tolerances (for instance, flatness & parallelism tolerances of 0.2 mm over 7 m diameter on mating surfaces of top & bottom plates and shell assembly; position tolerance of ± 0.1 mm on sleeve holes in top & bottom plates, etc.) on dimensions, form, position and orientation to satisfactorily meet all the critical functional requirements.
- Hard surfacing on continuous, large diameter annular tracks in bottom plate and at required depth in the inner surface of sleeves with nickel based cobalt free material with a hardness of around 45 to 50 HRC.
- Heat treatment of large parts with the specified rates of cooling and heating with control on temperature gradient in the parts.
- Establishing safe handling procedure for large diameter thin plates and shell assembly for adoption during the manufacture of prototype.
- The complex assembly of a large number of parts achieving the important requirements on positional accuracy, verticality, concentricity, etc of parts (specified tolerances: verticality of sleeve assemblies is ϕ0.1 mm; concentricity tolerance between sleeve hole in top & bottom plates is Ø0.01 mm; concentricity between axes of plates & shell assembly is ϕ0.01 mm, etc.). The final assembly of the grid plate consists of over 12000 individual parts that are to be precisely assembled and hence the need for establishing a smooth assembly procedure.

All these manufacturing challenges, the first of their kind to be addressed indigenously, require development of robust and sophisticated technology.

With the above primary objectives in focus, the design for the technology development

Fig. 2. Bottom plate after final machining

Fig. 3. Trial assembly of sleeves

of the GP was evolved reflecting all the features of the component and also keeping in view the end use of the developed component for hydraulic and core mechanics experiments. Further, the design was finalised with a view to minimise the cost and duration of technology development in order that timely feed-back from developmental activities is taken in to consideration for the design of the GP for PFBR.

In order to suit the smaller sized core planned for core mechanics experiment, the top plate and shell assembly were made smaller leading to reduced cost of technology development (Fig. 1). The sleeves and bottom plate are of full size, selected in such a way to demonstrate the achievability of the manufacturing and assembly tolerances required for the the require development of robust and sophisticated technology. With the above primary objectives in focus, the design for the technology development of GP was evolved reflecting all the features of the component and also keeping in view the end use of the developed component for hydraulic and core mechanics experiments. Further, the design was finalised with a view to minimise the cost and duration of technology development in order that timely feed back from developmental activities is taken in to consideration for the design of the GP for PFBR.

In order to suit the smaller sized core planned for core mechanics experiment, the top plate and shell assembly were made smaller leading to reduced cost of technology development (Fig. 1). The sleeves and bottom plate are of full size, selected in such a way to demonstrate the achievability of the manufacturing and assembly tolerances required for the prototype and to develop the technology of hard facing continuous and large diameter annular tracks on bottom plate and at required depth on inner diameter in sleeves. Further, the large diameter bottom plate provides the requisite experience needed for the heat treatment of large sized components of the prototype (Fig. 2).

The technology development exercise was undertaken by IGCAR in collaboration with M/s MTAR Technologies, Hyderabad, as the major partner and M/s OMPLAS Systems, Chennai, as the partner in hard facing. As a part of the technology development of the GP, M/s MTAR has specially designed and built a special purpose gantry machine capable of precision machining large components of up to 8m diameter and 1m height and M/s OMPLAS Systems has designed and developed state-of-the-art machines for hard facing by Plasma Transferred Arc (PTA) process using nickel

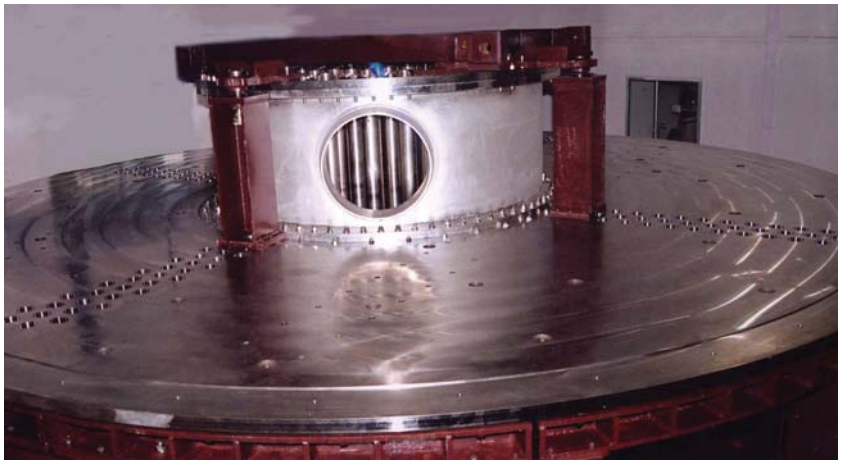

Fig. 4. Assembly of Grid Plate under progress

based cobalt free hard facing material. A large furnace specially designed for the heat treatment of parts of the grid plate has been supplied to MTAR by M/s Precision Controls, Chennai.

With the above facilities in position, the manufacturing technology development has been successfully completed meeting all the design requirements involving machining of large diameter parts to close tolerances, hard facing of items, systematic heat treating of parts for solution annealing, stress relieving and dimensional stabilisation, and achieving the final assembly to the required tolerance levels (Fig. 3 & 4). The timely and more importantly indigenous development of all the technologies involved in the manufacture of the GP augurs well for the FBR project and the importance of successful completion of the development effort would be well appreciated by taking note of the fact that for FBTR, the GP was the only component to be imported due to the then lack of indigenous technology for manufacture. This crucial technology barrier has now been crossed with the indigenous establishment of manufacturing technology for the GP.

2.3 Labyrinths for the Foot of Subassemblies

Labyrinths are provided at the top and bottom of the foot of SA (total 720 nos) in PFBR in order to reduce the sodium leakage flow. The function of top labyrinth is to restrict the total leak flow rate into the hot pool to a maximum of 195 kg/s and the minimum leak flow rate through bottom labyrinth is restricted to 436 kg/s from main vessel cooling considerations. As theoretical calculation for finding out pressure drop across labyrinth is not easy, experimental approach has been adopted to develop labyrinths to suit PFBR requirements. Different labyrinths were designed and tested systematically by varying the parameters like, radial clearance, pitch, depth of the grooves etc. The top labyrinth with a helical groove of circular profile with 0.2mm gap between the sleeve and the labyrinth, pitch of 3.5 mm and the depth of the groove of 1.25mm is recommended for PFBR following the tests conducted in water.

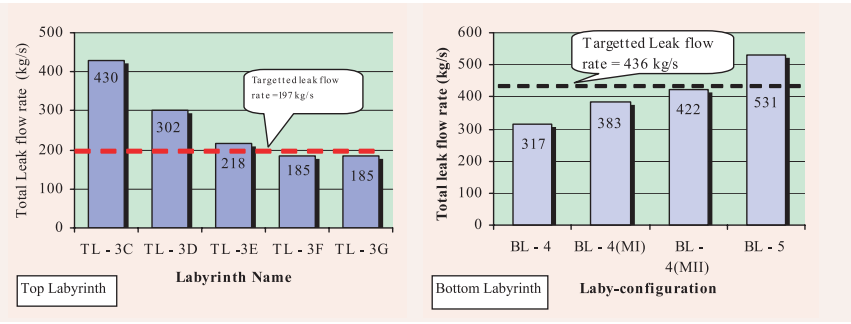

Fig. 2. Total leak flow rate achieved for different configuration of top labyrinth and bottom labyrinths

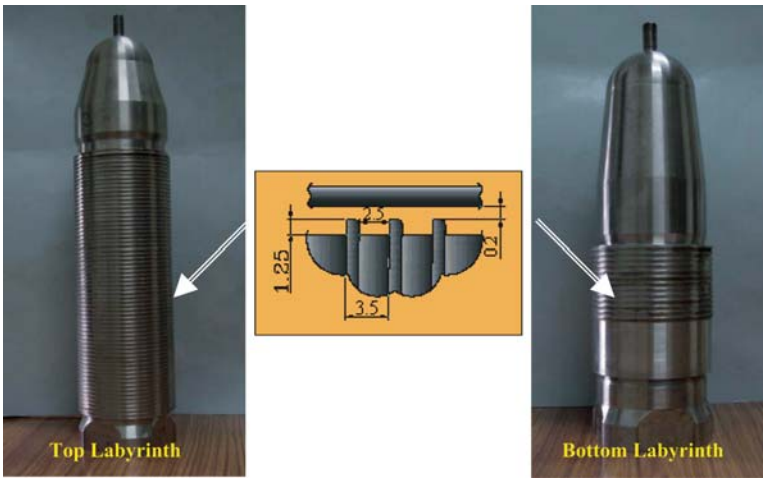

Fig. 1. Top and Bottom labyrinths

Studies conducted on bottom labyrinth in the last year resulted in a geometry which was able to achieve the minimum leak flow rate of 477 kg/s. The profile of the bottom labyrinth was the same as that of top labyrinth with a reduced length and diameter to suit the

grid plate sleeve. The top and bottom labyrinths are presented in Fig. 1. The geometry of labyrinth was reviewed and the maximum allowable length of labyrinth was increased from 50 mm to 80 mm in PFBR. With this modified design, parametric studies were conducted to develop the bottom labyrinth.

The hydraulic tests in water also confirmed the performance of labyrinths to be free from incipient cavitation. Total leak flow rate through the top labyrinth and bottom labyrinth are shown in Fig. 2.

2.4 Gas Entrainment Studies on Scaled Model of Surge Tank

Pressure surges in the secondary circuit of PFBR are possible due to sodium-water reactions in the steam generator or due to the inadvertent closure of isolation valves. In order to protect the components from these surges a surge tank is provided in the hot leg. Argon fills the space above free surface of sodium acting as a cushion in case of pressure surges. The pressure of argon gas in the surge tank is maintained at 0.4 MPa. The entrainment of argon gas in the secondary sodium from the surge tank is undesirable from considerations of heat transfer in the IHX and cavitation in pumps. Hence argon gas entrainment has to be avoided in the surge tank.

Fig.1. Perspex model of Surge Tank

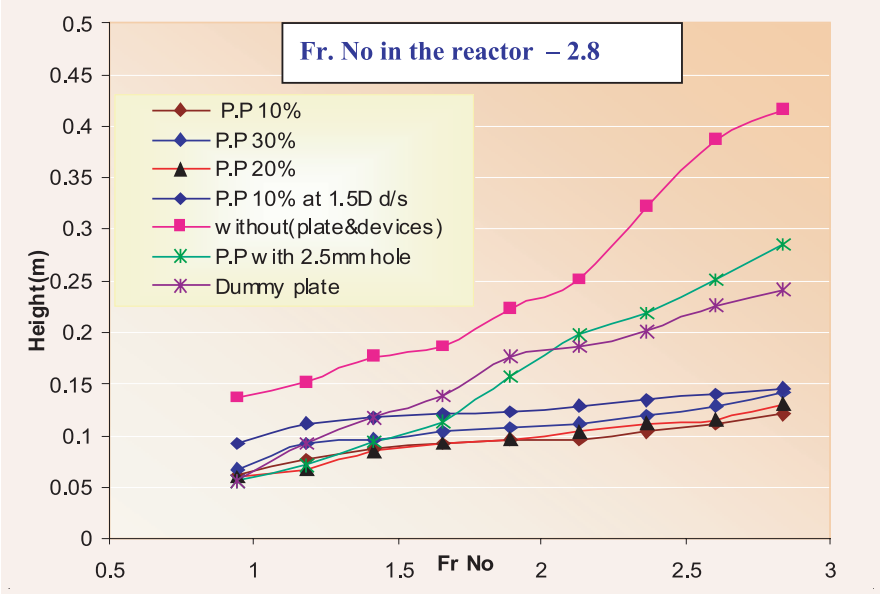

Fig. 2. Minimum height required to avoid gas entrainment from center of outlet nozzle for different Froude numbers

To study mechanisms of gas entrainment in surge tank and to evolve methods to mitigate the same, a small scale model of surge tank respecting Froude (Fr) similarity and by maintaining Re number in the turbulent zone of size 1:12 was selected. It is a full circular 360 deg model with two inlets at the bottom and four circumferentially equi-spaced side outlets which was fabricated using full perspex shell and perspex tubes for outlet nozzles to visualize air bubbles entrainment. The perforated plate (P.P) with a porosity of 10% was fixed above the inlet of the surge tank. Experiments were conducted with DM water at a nominal flow of 24 m^3/h. The flow through the surge tank is measured by two glass tube rotameters. The height of liquid column above the outlet nozzle and the velocity of flow entering the surge tank, determine the onset of gas entrainment. The minimum height of liquid column required to prevent gas entrainment was measured for different flow rates.

Initially, experiments were conducted without devices and the minimum height required to avoid gas entrainment was 415mm (in the prototype it is 4980mm). This would necessitate an increase in the height of the prototype surge tank. To avoid gas entrainment at the minimum level, studies were carried out with different porosities of perforated plates and in combination with devices like stiffening rings. Studies show that, perforated plates alone reduce the height of liquid column by 30% and by 70% when combined with stiffening rings. Fig. 1 shows the gas being entrained in the model during an experimental run.

The minimum level of liquid column to avoid gas entrainment is plotted as a function of flow rate for the various experimental conditions in Fig. 2.

The studies have been able to establish the utility of providing perforated plate and stiffener rings to mitigate the entrainment of gas into the liquid column.

2.5 Comprehensive Failure Modes considered in Structural Design of PFBR

With the use of sodium coolant, it is possible to operate the fast breeder reactor (FBR) at high temperature without pressurising the coolant. This provides significant advantages in terms of high plant efficiency and lower primary loads on the components resulting in thin walled structures. However, sodium which has excellent heat transfer properties poses many challenging structural mechanics problems, originating from thermal stress and thermal shocks, particularly on the components made of austenitic steel which has low thermal conductivity and high co-efficient of thermal expansion. The possible failure modes are identified systematically for 500 MWe PFBR, reflecting the operating experiences accumulated over 300 reactor years worldwide (Fig.1).

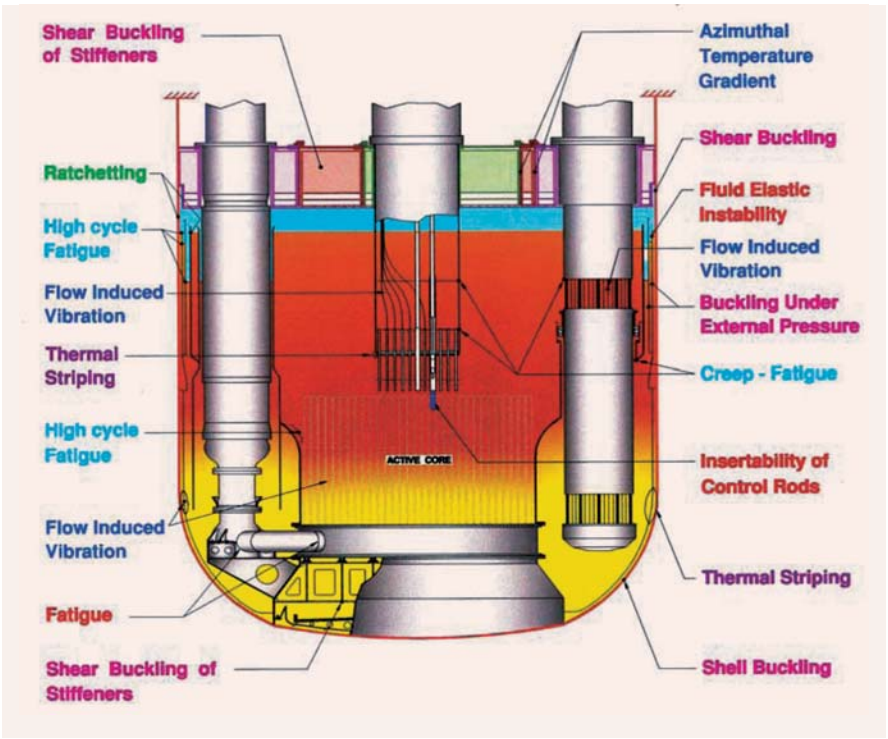

Fig.1. Failure modes considered in structural design of PFBR

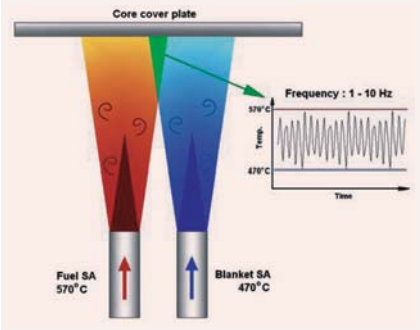

Fig. 2 . Thermal striping phenomenon

Under higher operating temperature over a prolonged period (>40 y) in association with temperature variations following thermal transients, the hot pool components are subjected to creep, fatigue and creep-fatigue interactions which are the main life limiting factors. Apart from these, a few special types of failure modes, viz. thermal striping and thermal ratchetting occur on components when they are subjected to temperature fluctuations caused by thermal hydraulic phenomena. Thermal

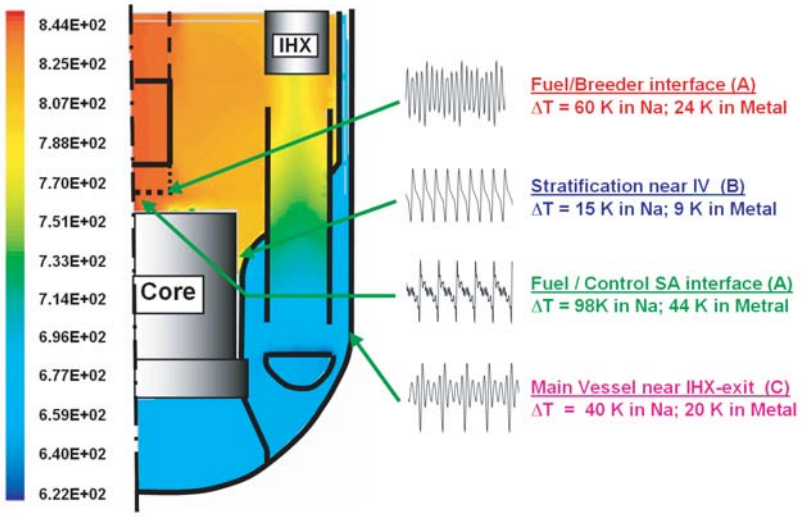

Fig. 3. Thermal hydraulic prediction of temperature fluctuations

striping is a thermal hydraulics phenomenon which causes random temperature fluctuations in the zone where fluid streams of different temperatures co-exist (Fig.2). The predominant frequency of oscillations lies in the range 1-10 Hz. If this phenomenon occurs in the vicinity of the structural wall, the wall will be subjected to high cycle fatigue which may cause crack initiation well before the design life of plant. Such failures have been reported for SPX-1, Phenix and BN 600 fast reactors. PFBR components have been analysed in detail with respect to this phenomenon. For PFBR reactor assembly, the critical locations for thermal striping along with the temperature fluctuations (Dt) predicted by thermal hydraulic analysis are presented in Fig.3. Figure 4 shows the temperature fluctuation limits on the metal wall estimated for the corresponding locations (A, B and C in Fig.3).

The main structural characteristics of reactor assembly components are thin walled large size shell structures supported either at bottom (e.g. inner vessel and thermal baffle) or at the top (e.g. main vessel). Another special feature is the existence of free fluid surfaces which is the source of sloshing phenomena during normal operation. The structural wall surfaces are subjected to random pressure fluctuations which can cause significant displacements of reactor internals by virtue of their high slenderness ratio. These features lead to lower natural frequencies (0.5-15 Hz) and high dynamic response amplifications during seismic and vibration loadings. The seismic loadings decide the minimum wall thickness to guard against buckling of shells and also to control the dynamic displacements within the functional limits specified to ensure (i) smooth insertion of control rods, (ii) acceptable reactivity variations and (iii) prevention of primary sodium pump seizure. In some special cases, the fluctuations due to fluid-elastic instability mechanisms can lead to a rapid damage of the structures (Fig.5). The weir shell in the main vessel cooling circuit of SPX-1 has experienced fluid-elastic instability during its commissioning stage. In PFBR, detailed theoretical analysis and experimental studies on

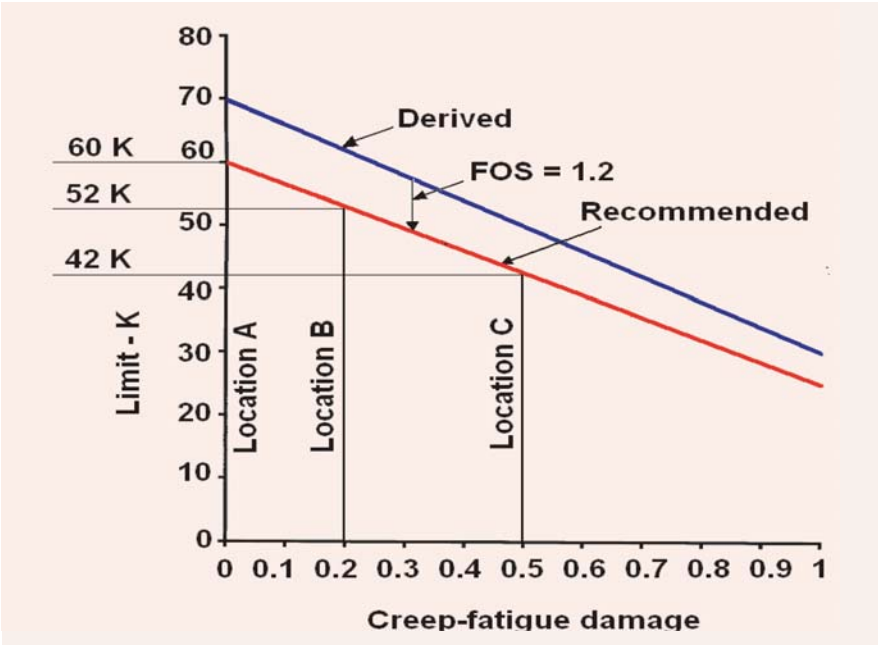

Fig. 4. Acceptable temperature fluctuations

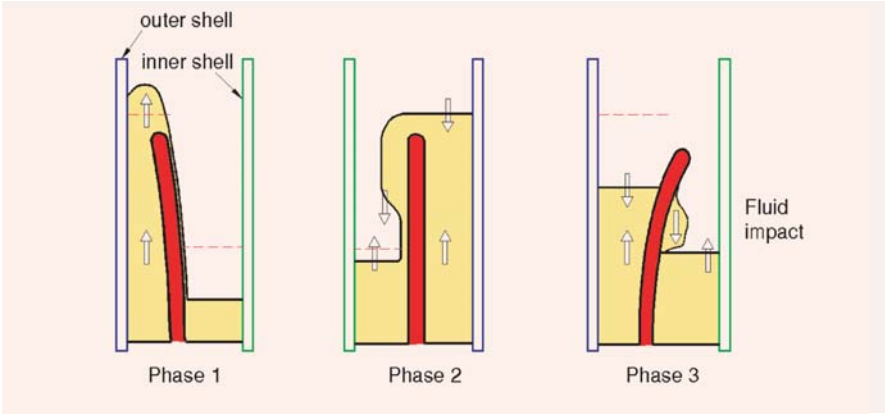

Fig. 5. Fluid-elastic instability of weir shell in main vessel cooling circuit

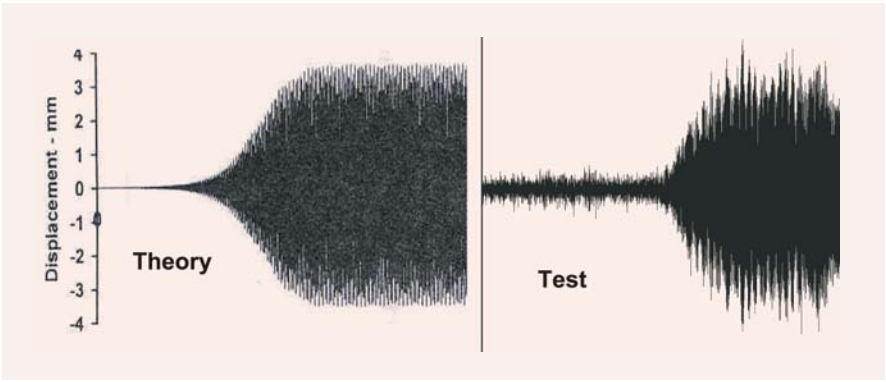

Fig. 6. Dynamic displacement of tip of thermal baffle

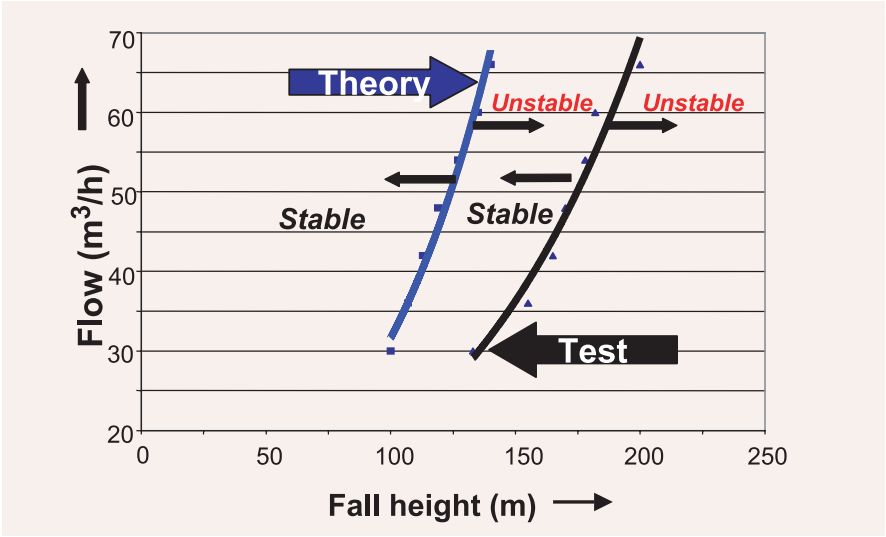

Fig. 7. Instability regime for weir shell

1:4 scale model, have been carried out to preclude the occurrence of vibrations. The displacement time history at tip of thermal baffle and stability map are presented in Fig.6 and Fig.7 respectively.

All the failure modes have been systematically analysed by the application of advanced numerical analysis supported by sophisticated experimental investigations. These investigations are instrumental for the choice of higher operating temperature (820 K) with longer design life (> 40 y) for PFBR and to achieve reliable design with optimum use of expensive materials such as austenitic stainless steels and modified 9Cr-1Mo steel. This has given high confidence of the design under all conditions. Further R&D efforts in these domains are being continued on a larger scale to achieve a robust design for future FBRs with enhanced safety and improved economy.

2.6 Ensuring the Structural Integrity of Main Vessel by Temperature Monitoring

The Main vessel is an important component of the fast reactor which holds the entire primary sodium of 1150 t along with other structural loads such as core, grid plate, and core support structure. The primary sodium pool is divided into hot (820 K) and cold pool (670 K) by the inner vessel. Due to the temperature difference of 150 K, heat is transferred from hot pool to cold pool through the inner vessel. The radial distance between inner vessel and main vessel is only about 300 mm in the upper part of the inner vessel. In the absence of any cooling for the main vessel, the temperature of the main vessel would reach the hot pool value of 820 K. This means that the main vessel, made up of austenitic stainless steel SS316LN is to be analysed for high temperature failure modes including creep effects. The French design code RCC-MR has provided a creep cross-over curve (Fig.1) as per which the main vessel is to be maintained at ~723 K or below so as to have negligible creep effects for the design life of 40 years or even more. Hence the upper part of main vessel has to be cooled. In order to ensure the structural integrity, availability of main vessel cooling system needs to be ensured. Since it is difficult to directly measure the flow, an indirect method of flow prediction in the cooling circuit by main vessel temperature measurement has been investigated.

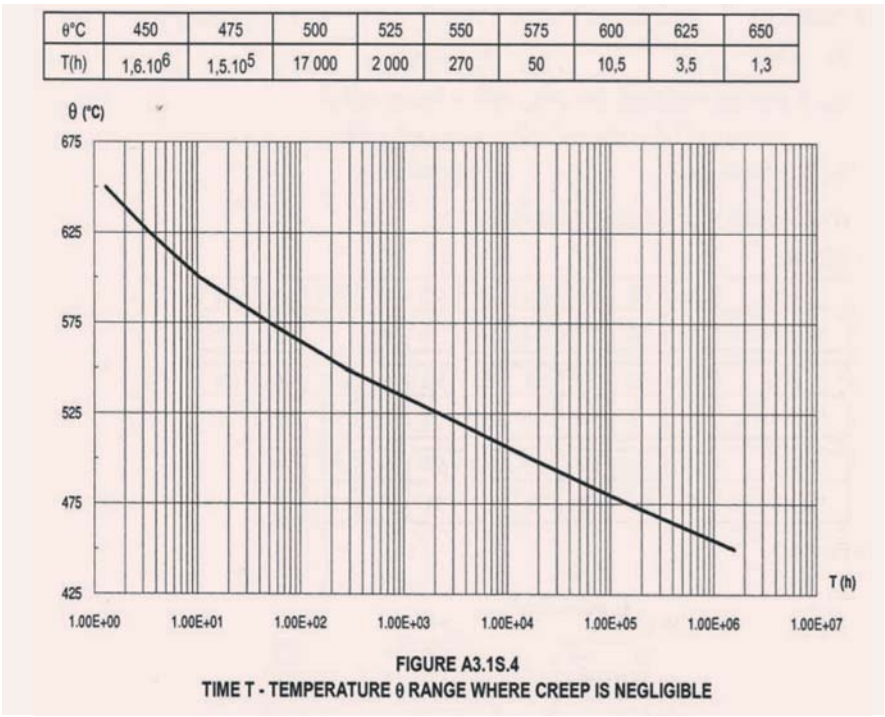

Fig. 1. Creep - cross over curve for material SS 316 LN

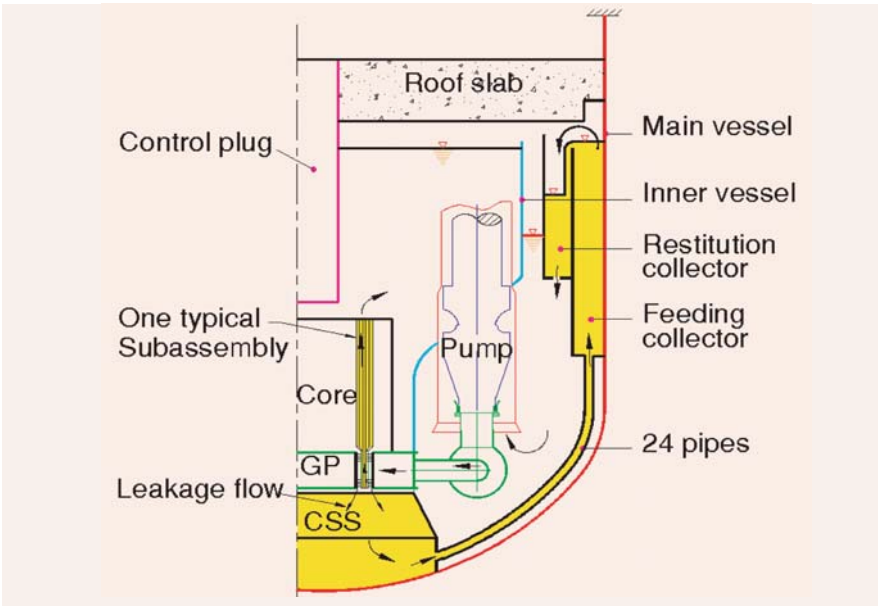

Fig. 2. Schematic view of main vessel cooling system

The Main vessel cooling system consists of two thermal baffles attached to the inner side of main vessel (Fig.2). Cold sodium at 670 K from grid plate is led into core support structure via labyrinths provided at the feet of the subassemblies. From core

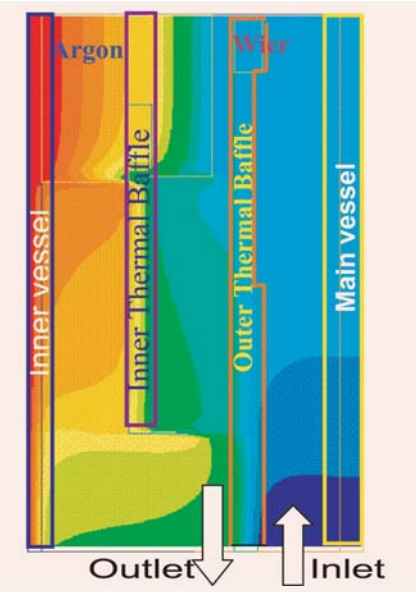

Fig. 3. Temperature distribution in main vessel cooling system

support structure the flow is guided to the feeding plenum through pipes. The pressure inside the grid plate drives the flow through the core as well as through the main vessel cooling system. As the majority of sodium flows through the core, the grid plate pressure is governed by core flow. So the main vessel cooling flow is high at higher power and low at lower power. The assumption of "core flow proportional to power" leads to a temperature difference of 150 K between hot and cold pools at all loads. At low power operation, reduced flow goes to the cooling circuit. The flow rate during full power operation is 400 kg/s and at 20% load it is 80 kg/s. Hence, the main vessel coolant requirement is controlled by the low power operation.

The main vessel temperature has been predicted for various cooling flow rates using the computational fluid dynamic code, PHOENICS. Typical temperature distribution in the cooling circuit for a coolant flow rate of 80 kg/s is depicted in Fig.3. The value of maximum main vessel temperature as a function of coolant flow rate is depicted in Fig.4. It is clear that the minimum flow rate required to maintain the main vessel temperature below 723 K is 55 kg/s. Also, the main vessel temperature exhibits a strong dependence on the coolant flow rate if the flow rate is less than 160 kg/s, which is much higher than the minimum required flow. Thus there is adequate margin in the coolant flow rate and continuous monitoring of main vessel temperature can be used to assess the coolant flow rate.

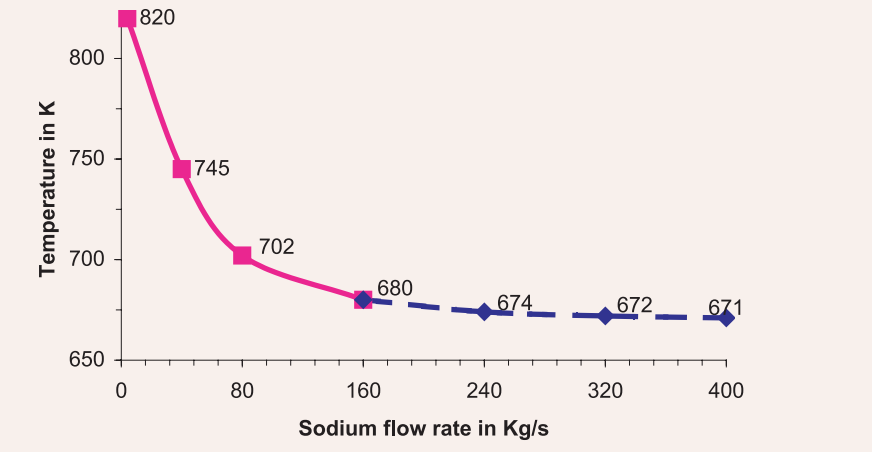

Fig. 4. Main vessel maximum temperature for various flow rates

2.7 Heat Transfer Studies on the Modified Core Catcher of PFBR

In PFBR, the core catcher is provided as an in-vessel core debris retention device to collect, support and maintain in sub-critical configuration, the core debris generated from fuel melting due to certain postulated Beyond Design Basis Events (BDBE). This also acts as a barrier to prevent settling of debris on main vessel and keeps its maximum temperature within the acceptable creep range. Experimental studies are being carried out at the Safety Engineering Division for validating the numerical models, which are used for the analysis of full-scale PFBR core catcher assembly. Experiments have been carried out in water to understand natural convective heat transfer and fluid flow in and around the core catcher assembly. Two types of chimney configurations, with some changes in overall assembly, were taken up in phases to understand their effect on heat removal capability. The schematic of the earlier and

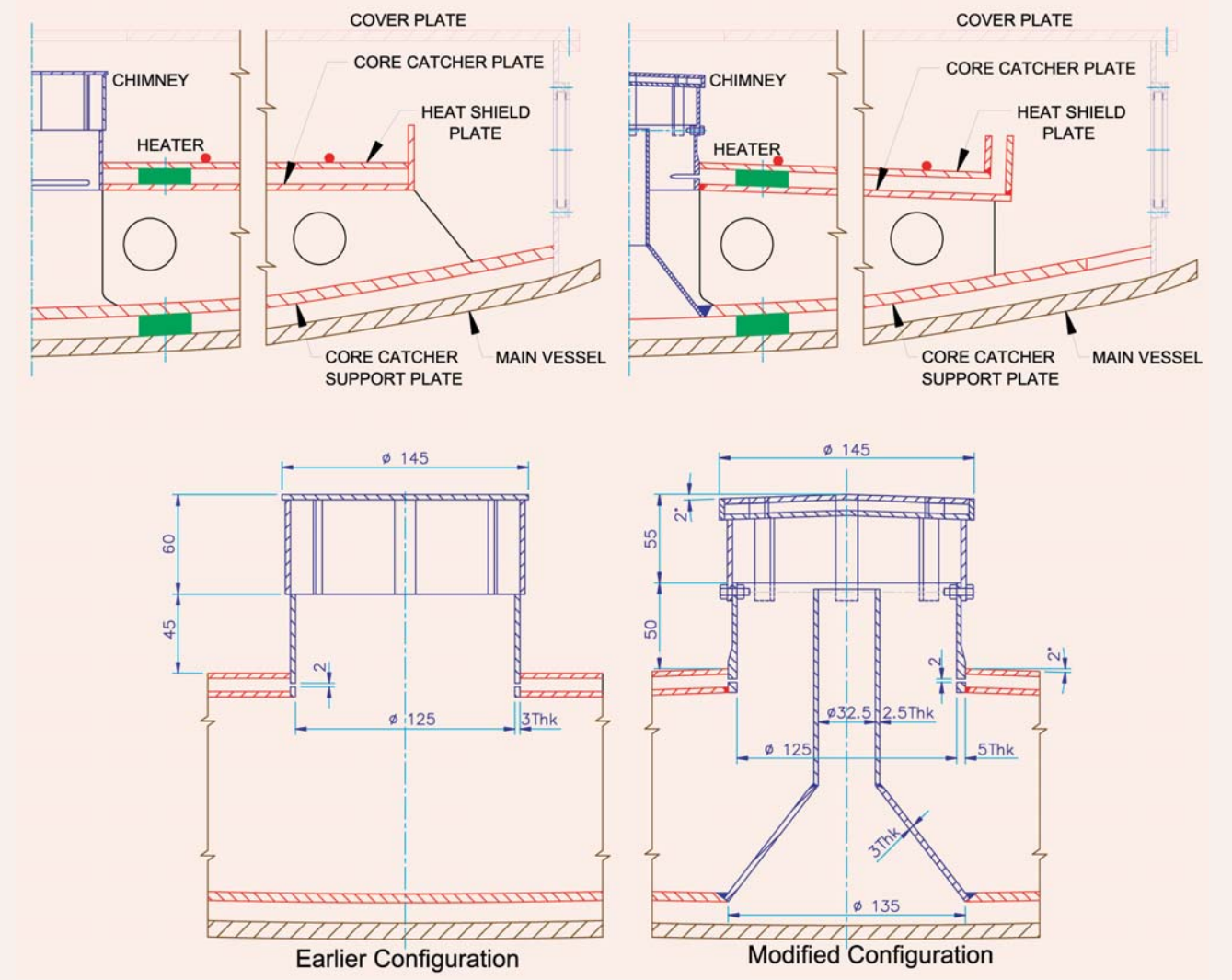

Fig. 1. Details of the earlier and modified core catcher assemblies

modified experimental setup and details of both the chimneys are shown in Fig.1. As compared to the earlier configuration, in the modified one, flow path was further enhanced with addition of an inner chimney connecting the fluid zone below the core catcher support plate to the upper coolant zone through a smooth and guided tubular path. Slopes are also provided on the chimney head, core catcher plate (CCP) and heat shield plate (HSP). A peripheral rim is added on the HSP and equally spaced rectangular slots have also been added on the periphery of the modified core catcher support plate (CCSP) giving entry path to the surrounding fluid.

Both experimental and numerical studies have been carried out to understand the influence of the modified experimental setup. The experimental temperature distribution over the HSP has been used as the boundary condition for the numerical analysis of the system through the FLUENT code. Velocity fields are obtained to assess the impact of both geometries on the flow pattern and overall heat transfer characteristics. In brief, the results and observations of the system for both the experimental set-ups at a steady state temperature of 328 K are highlighted here.

A detailed parametric study has been done for both the earlier and modified configurations. Figures 2a and 3a show the velocity field vectors at the chimney and figures 2b, 3b show the same at the side zones of the cavity for the earlier and modified case respectively. For the earlier configuration, the velocity vector plots confirm strong

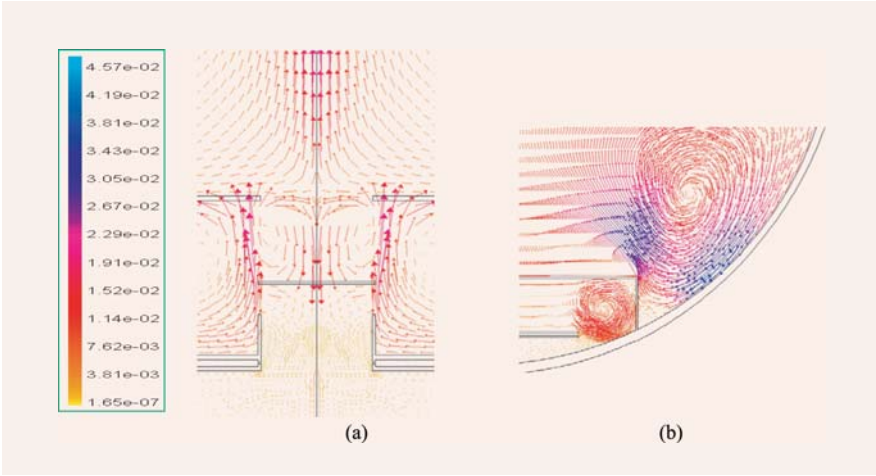

Fig.2. (a) and (b) Velocity field (m/ s) vectors at chimney and side zones of cavity for the earlier configuration

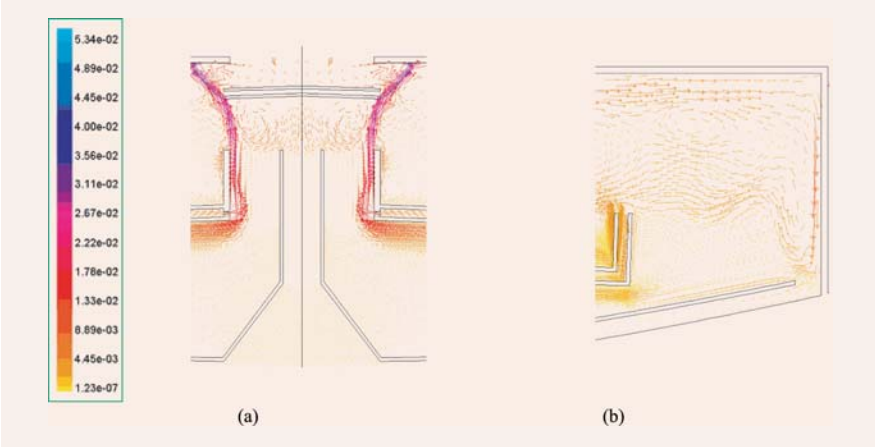

Fig.3 (a) and (b) Velocity field (m/ s) vectors at chimney and side zones of cavity for the modified configuration

re-circulating flow above HSP. In the zone below the cover plate and the main vessel a strong closed cell with a maximum velocity of fluid 2.3 cm/s occurs at the peripheral zone of CCP as shown in Fig. 2b, and transfers the heat through the cylindrical side wall to the bulk fluid. The hot fluid rises above the leading edge of the plate until it reaches near the bottom of the cover plate, then it flows downward after being cooled by natural convection transferring heat through the cover plate to the bulk fluid above it. In the chimney region, fluid moves upward with very low velocity of magnitude of order 10^{-4} m/s and mixes with the high circulatory fluid above HSP, which in turn avoids stagnancy in the region below CCP. As seen in figure 2a, very close to the opening in cover plate and above the top lid of the chimney, flow reversal takes place with two circulatory loops. In the bulk fluid above cover plate, fluid rises in the central region with the velocity of order of magnitude 10^{-2} m/s and transfers the heat from mixing zone through the free surface. After losing the heat to the surroundings the bulk fluid gets cooled and slides through the vessel wall back to the cover plate top and again takes the heat from it and moves upward in the cellular structure. The flow path is completed as the colder fluid is entrained to the ascending flow at the center of the cavity. It is clearly seen in the velocity fields that the fluid remains almost stagnant in the lower-most part of the cavity.

For the modified configuration, fluid below the cover plate and HSP moves in a closed cell with the lower velocity compared to earlier configuration with a maximum velocity of 0.9 cm/s. The fluid does not roll in the strong circulatory single roll, but moves towards the peripheral zone of the CCP as seen in Fig. 3b. It transfers heat through the wall and cover plate to the bulk fluid above and around it. The fluid enters in the gap between HSP and CCP with a higher velocity and allows the fluid movement in that region by forcing the fluid in the chimney zone. In the chimney region as shown in Fig. 3a, the fluid moves upward with a higher velocity of the order 10^{-2} m/s compared to earlier configuration and mixes with the fluid above the HSP. The fluid below CCP is displaced by the fluid movement from side zone improving the cooling capability of the cavity fluid. The fluid enters through the outer peripheral zone to the space between the main vessel and CCSP and circulates through the inner chimney configuration and mixes with the main fluid at the outlet of

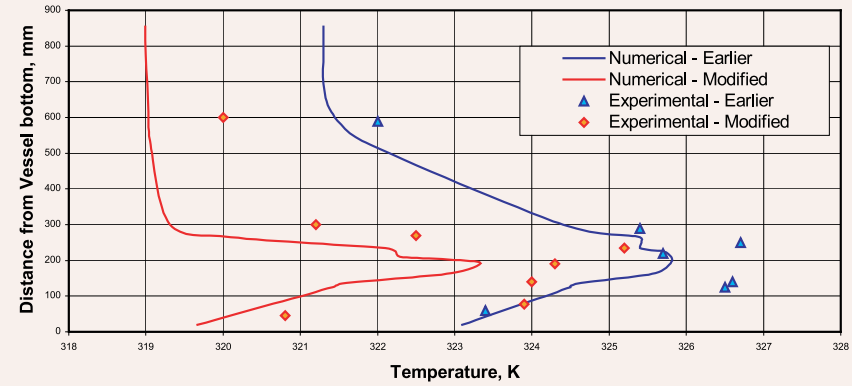

Fig. 4. Comparison of axial temperature profiles at heat shield plate temperature of 328K

the chimney as shown in Fig. 3a. Hence a further reduction of temperature of the outer peripheral region to the cavity takes place.

Figure 4 shows the comparison of axial fluid temperature profile obtained both experimentally and numerically along the depth of the cavity for both the configurations discussed earlier. It can be clearly seen that for the earlier case, the maximum temperature is around 326 K whereas in the modified case it is around 323 K. Higher temperature gradient is also seen for earlier one, in the confined zone compared to the modified configuration. Experimental heater power to achieve 328K steady state conditions over the HSP was 8 kW and 9 kW respectively for the earlier and modified cases, confirming the enhanced heat removal for the latter. Numerical results are generally in good agreement with experimental data in most of the region except in the confined zone where it is under-predicted. The reason for the same is being investigated. However, the results confirmed the enhanced heat removal capability for the modified core catcher set up with annular chimney configuration.

2.8 Ultrasonic Inspection Methodology for Support Shell Weld of Core Support Structure in the Main Vessel of PFBR

An innovative ultrasonic test methodology has been developed for in-service inspection of the shell weld of the core support structure in the main vessel of PFBR. Fig.1 shows the cross-sectional view of the core support structure showing the shell weld, which is immersed in sodium. The inspection of this weld requires special methodology to be developed because of the restricted accessibility to the weld, curvature of the main vessel and ultrasonic beam skewing that occurs at the K type weld used for joining the main vessel to the support shell plate.

The developed methodology involves inspection from the outside surface of the main vessel at point 'a', shown in Fig. 1, using normal beam ultrasonic transducer. Because of the presence of curvature in the main vessel, the ultrasonic beam enters the weld overlay at an angle α to the support shell structure (Fig. 1). Further, because of the presence of columnar grains in the austenitic stainless steel weld overlay and the K weld, ultrasonic waves get skewed and enter the support shell structure at an angle β (Fig. 1). Beyond this point, ultrasonic wave propagates in the support shell structure at an angle β and gets reflected every time it encounters the plate surface. When the wave encounters any defect or

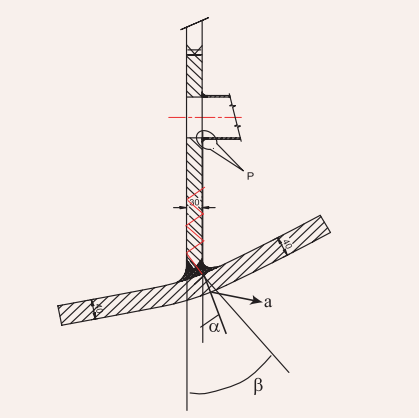

Fig. 1. Cross-sectional view of the core support structure showing the support shell weld

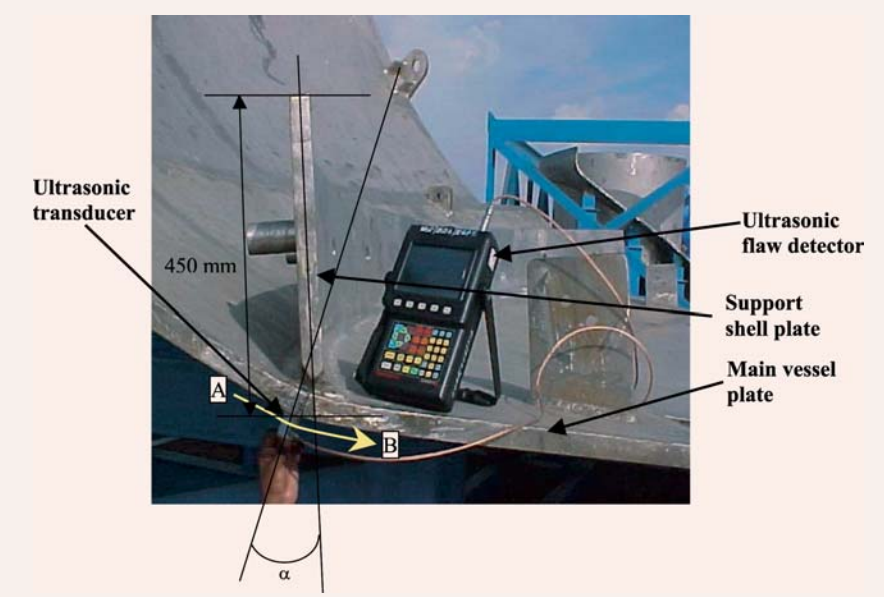

Fig.2. Experimental setup for the inspection methodology showing the transducer location in the close-up view of support shell.

interface in the shell plate, it is reflected from the defect or interface and picked up by the same transducer. By changing the location of the transducer, angles α and β can be changed and hence defect at any location including in the shell weld of the core support structure can be detected.

The above methodology has been successfully demonstrated on the main vessel sector mock-up, fabricated as part of the technology development programme of PFBR. Figure 2 shows the experimental setup used for the developed inspection methodology showing the ultrasonic transducer location in the close-up view of support shell. In order to carry out studies for establishing the sensitivity of the proposed methodology, notches of dimensions 10 % and 30 % of wall thickness were made at a simulated location 350 mm away from the outer surface of the main vessel, in the support shell plate of the main vessel sector mock up. Ultrasonic signals were acquired at an interval of 10 mm by moving the transducer along the path AB (Fig. 2) to carry out the inspection at different angles of ultrasonic wave propagation. The ultrasonic testing, using this methodology, indicated that the defects on both sides of the plate could be detected reliably with 28 dB reserved gain in the flaw detector. Fig. 3 shows a typical ultrasonic signal from a 9 mm deep notch at 350 mm away from the outer surface of the main vessel, demonstrating the potential of the developed methodology for inspection of the shell weld of the core support structure of PFBR. Further, in order to simulate the defects in the shell weld of actual main vessel, a 30 mm thick stainless steel plate was welded at the top of the shell plate of the main vessel sector mock up using a K-type weld. Notches of dimensions 10 % and 30 % of wall thickness were made in this weld and successfully detected.

The developed methodology has the advantage that inspection at multiple angles of ultrasonic wave propagation can be achieved just by moving a single normal beam ultrasonic transducer along the curved surface of the main vessel. Multiple angle beam inspection would ensure the detectability of defects of any orientation.

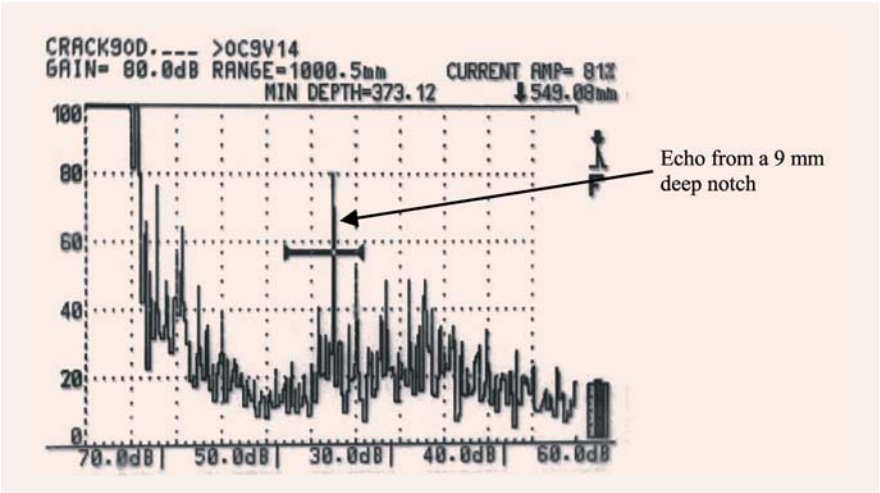

Fig. 3. Ultrasonic signal corresponding to a 9 mm deep notch at 350 mm away from the outer surface of the main vessel ($\alpha \approx 35^0$ and $\beta \approx 50^0$).

2.9 Enriched Boron Production

Pellets of Enriched Boron Carbide, B_4C, containing 65 atom% of ^{10}B isotope (in boron), is to be used as the absorber rod pellets in Control and Safety Rods (CSR) and Diverse Safety Rods (DSR) in PFBR. The boron carbide is produced in the following steps: a) Enrichment of Boron b) Production of elemental boron and C) Production of boron carbide.

Boric acid enriched in ^{10}B to 65% was produced at the Boron Enrichment Plant at Separations Technology and Hydraulics Division (ST&HD). The first product withdrawal campaign was successfully completed during April, 2005. The product solution was then dried to powder form using an evaporator drier system after carrying out trial experiments with depleted boric acid solution so as to minimize the losses from 30% to 5% in the operation. The drier was operated at different air velocities and temperatures to fix the optimum conditions. The tray drier and enriched boric acid product crystals are shown in Fig. 1 and 2 respectively.

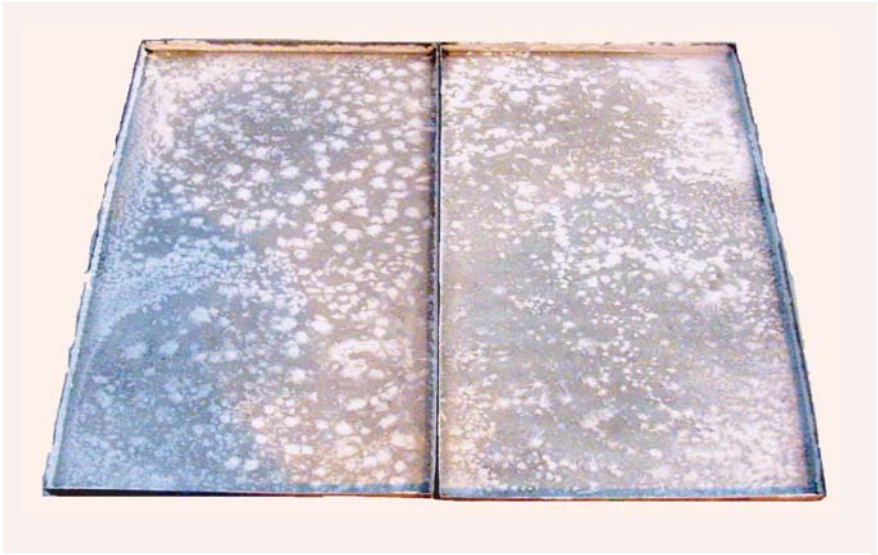

Fig. 2. Crystals of enriched boric acid in the tray of the drier

The facility is being augmented for enrichment to 90% in ^{10}B in order to meet the future requirements. This is being done based on the experiments carried out using fine resin (having particle size of 0.075mm to 0.150 mm) which shows superior ion exchange characteristics compared to the normal size (0.3 mm to 1.2 mm) resin. The augmented facility consists of two streams of ion exchange columns each having process ion exchange columns and a regeneration column. The mathematical modeling of the augmented facility was carried out to establish the advantage of using fine resin in the plant, and the results are encouraging.

Fig. 1. Tray drier

In parallel, a facility to demonstrate the feasibility of production of elemental boron from boric acid by electrowinning process is being operated at the Fuel Chemistry Division. Elemental boron was produced through electrowinning from potassium

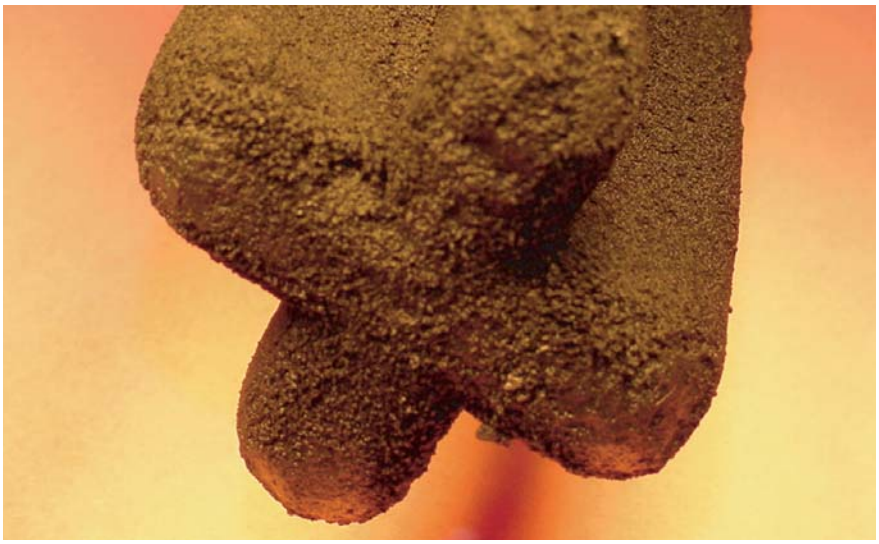

Fig 3. Enriched elemental boron deposit

fluoborate (KBF_4) dissolved in a mixture of molten potassium fluoride and potassium chloride. The characteristics of the electrodeposited boron (raw boron) as well as the processed boron were studied. The chemical purity, specific surface area, distribution of sizes among the particles and X-ray crystallite size of these boron powders were investigated. The morphology of these deposits was examined using scanning electron microscopy (SEM), while the chemical state of the matrix as well as the impurity phases present in them were established using X-ray photoelectron spectroscopy (XPS). The ease of oxidation of these powders in air was investigated using differential thermal analysis coupled with thermogravimetry. From the results obtained in this study it was established that elemental boron powder with a purity of 98 % could be produced using the above process. The major impurities were found to be boric oxide, fluoride, chloride, iron and carbon. About 2.5 kg of elemental boron was produced during this year.

The first batch of enriched boric acid received from the enrichment plant was converted to KBF_4. About 800 g of enriched elemental boron was produced by the electrowinning technique. (Fig. 3) The electrodeposited boron was processed and about 700 g of enriched elemental boron meeting all the technical specifications is ready for conversion to high-density boron carbide pellets for PFBR control rod applications.

2.10 A Revised Physics Design of Control and Safety Rods with the Reduced Requirement of Enriched B_4C

The absorber rod (AR) systems in PFBR consist of nine Control and Safety Rods(CSR) and three Diverse Safety Rods (DSR). These rods are located in the third and sixth hexagonal rings. During normal operation, the CSRs are partially inserted and the DSRs are parked above the core. The two systems independently are capable of achieving cold shutdown of the reactor in any eventuality. Presently 65% B-10 enriched B_4C is planned to be used as the control material for the CSR of PFBR. A study was

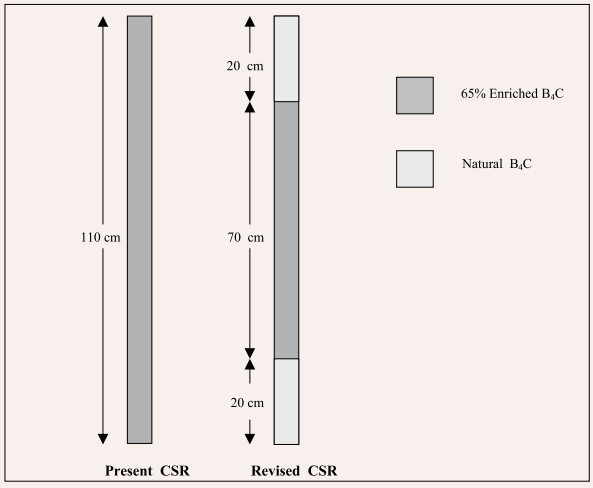

Fig. 1. Schematic Comparison of the Present and the Revised CSR

conducted to establish that upto 20 cm replacement of enriched B_4C by natural B_4C in the top and bottom sections of AR reduces the AR worth only by a few percent. This reduction is acceptable from safety considerations and considerable savings in enriched B_4C is achievable.

It is planned to replace a CSR after every 3 cycles (2 years) of operation due to the irradiation life limitation of the D9 hexcan and clad. But from the worth reduction point of view, the CSR can last for about 5 cycles. Thus further savings in enriched B_4C annual requirement is possible by increasing the residence time of CSR. A study was also carried out to investigate whether it is possible to increase the residence time of CSR inside the reactor.

The CSR design will be improved in two phases. In phase-1 it is proposed to replace the top and bottom 20 cm section of CSR with natural B_4C and the remaining portion by 65% enriched B_4C pellets. Since D9 is retained as the hexcan material, the residence time of CSR in the reactor is not changed. Fig. 1 gives the schematic representation of the present and the proposed CSR in phase-1. The DSR system design is not changed.

The integral worths for various AR in/out cases and the shutdown margins of new CSR are compared against the corresponding cases calculated using single enrichment CSR. The results are shown in Table 1. It is shown that in the revised design there is about 6% reduction in the total AR worth. It was found that neutron absorption capability of natural boron (20% B-10) is half of 65 % B-10 enriched boron. Thus the effectiveness of CSR with different lengths of insertions is reduced only marginally. It is found that in case of a stuck CSR or DSR, adequate shutdown margin is present for the fresh core (which has maximum reactivity).

In phase-2, along with the changes made in phase-1, D9 material in the hexcan will be replaced with ferritic steel to increase its life to 5 cycles. The life of the cladding is determined by the maximum capture rate it can withstand. The capture rate can be controlled by the amount of enriched B_4C used. From Superphenix experience, the maximum capture limit of control rods of PFBR is taken as 1.2×10^{22} capture/cm^3 . This capture rate is reached in 3 cycles for the present uniformly enriched CSR. With natural B_4C section in the bottom, this limit is also reached in 5 cycles.

Presently phase-1 changes are suggested for implementation and have been approved by the safety committees. With the changes made in phase-1, the savings in initial enriched B_4C inventory is 36 % for CSR and 28 % for all AR. This reduction translates to a very large economic gain, as the cost of the material in one CSR is about Rs.40 lakhs excluding fabrication cost. Thus total saving in initial core is Rs. 1 crore and Rs. 20 crore over the reactor life.

Table 1 . AR Insertion Worth with Present and Revised CSR (Fresh Core)

Description	Present CSR	Revised CSR
	Δk/k (pcm)	Δk/k (pcm)
All Rods In	14528	13939
All CSR In	10110	9524
All DSR In	3983	3875
8 CSR In and 1 CSR Stuck	8266	7808

2.11 Ion Simulation of Radiation Damage

Radiation induced dimensional changes of the core components like fuel cladding and wrapper of a fast reactor, limit the long residence time needed for achieving high fuel burnup. Hence there is considerable interest in developing radiation resistant alloys for use as reactor structural materials, and a programme on charged particle simulation of radiation damage

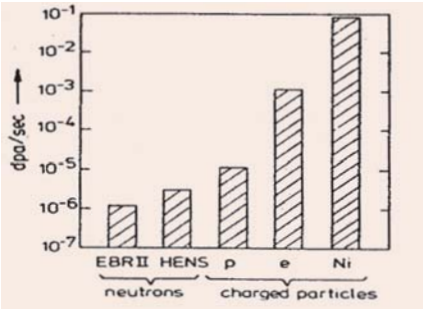

Fig. 1 Damage rates attainable with different bombarding particles

behavior of materials has been initiated. One of the important activities envisaged is connected with the development of D9I alloy for PFBR with a target burn up of 150000MWd/t.

The ideal method of investigating radiation damage effects relevant to in-reactor service condition is the irradiation of the material in a test reactor under identical conditions. However, obtaining a high damage of 100 dpa corresponding to a fast neutron fluence of 10^{23} n/cm^2 requires very long irradiation times, up to a few years, in a high flux test reactor. Damage rates attainable with different bombarding particles are shown for comparison in Fig. 1. As seen in the figure, the damage rate created by heavy ions like Ni is several orders of magnitude higher than that by neutrons, and hence Ni ion bombardment can yield very fast data under controlled conditions of temperature, flux and irradiation environment. The study of void swelling in D9 alloy was undertaken using 5 MeV Ni ions from the 1.7 MV Tandetron accelerator following the ASTM Code E-521-89 which summarises the standard procedure for ion simulation of neutron damage .Due to the large difference in the defect production rate, the peak swelling temperature during ion irradiation is higher than that for neutron irradiation. Since the earlier studies have shown that void swelling behaviour obtained from ion and reactor irradiation are similar at their respective peak swelling temperatures, the swelling measurements were made as a function of temperature in order to find out the peak swelling temperature under ion irradiation, in the range of 573K-1023K. The irradiations were carried out using a high temperature irradiation setup designed and developed for this purpose. A temperature stability of ± 2°C was maintained using a temperature controller. Damage rate employed during the irradiation was 7 × 10^{-3} dpa/s and the beam was scanned in order to achieve beam homogeneity across the sample surface. Prior to irradiation with heavy ions, the samples were implanted with 30 ppm of helium to simulate the helium production in reactor structural materials by the (n,α) reaction. The void swelling in irradiated samples were determined using step height method. During ion bombardment, the specimen was masked so that part of the sample was irradiated while the other region was protected from the beam. As the irradiated region swells, the surface becomes elevated and a step forms at the boundary of the masked and bombarded regions. A measurement of the step height provides the total integrated swelling that has occurred

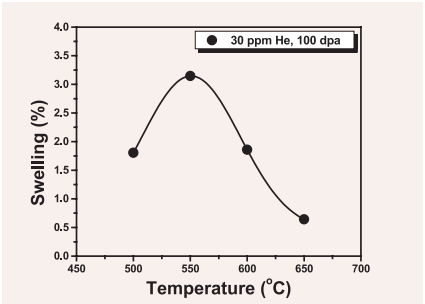

Fig 2. Void swelling in D9 alloy as a function of irradiation temperature.

along the path of the bombarding ion. The step height was measured using a surface profilometer,from which the integrated swelling rate was estimated. The void swelling in D9 alloy as a function of irradiation temperature is given in Fig.2 . The peak swelling temperature during ion irradiation is 550°C. Normalizing for the temperature shift arising from the difference in the damage rate, the peak swelling

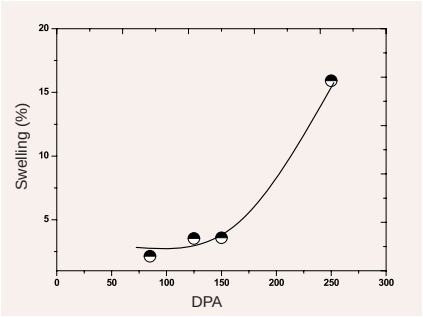

Fig 3. Dose dependence of void swelling in D9 alloy

temperature is estimated to be 435 °C for n-irradiated D9.

Void swelling as a function of irradiation fluence was also studied. The main interest was to determine the onset of the linear swelling regime. The irradiations were carried out at 550°C (peak swelling temperature) to various doses from 85 dpa to 250 dpa using 5MeV Nickel ions. Swelling as a function of dose (Fig. 3) shows a qualitative resemblance to the expected behavior, with a low swelling regime, a transient region and a linear swelling regime. However the percentage swelling in the linear regime was much less than the 1%/dpa usually observed in neutron irradiation. The lower swelling rate found in the case of ion irradiation may be attributed to the effect of injected interstitials.

These initial studies, using the experimental setup have clearly demonstrated the feasibility of utilizing heavy ion irradiation for simulating the displacement damage which occurs in fast reactor structural materials.

2.12 Tribological Studies on Materials of PFBR: Friction and Wear Testing on 316LN and Colmonoy-5 in Sodium

In the PFBR, the critical components of reactor operating mechanisms like Control and Safety Rod Drive Mechanism, Diversified Safety Rod Drive Mechanism, Transfer Arm and Primary sodium pump etc. have friction and wear between moving parts in the presence of sodium at high temperature. This friction and wear may lead to mechanical failure. To study these aspects, a tribometer was designed and fabricated for in-sodium testing of specimens.

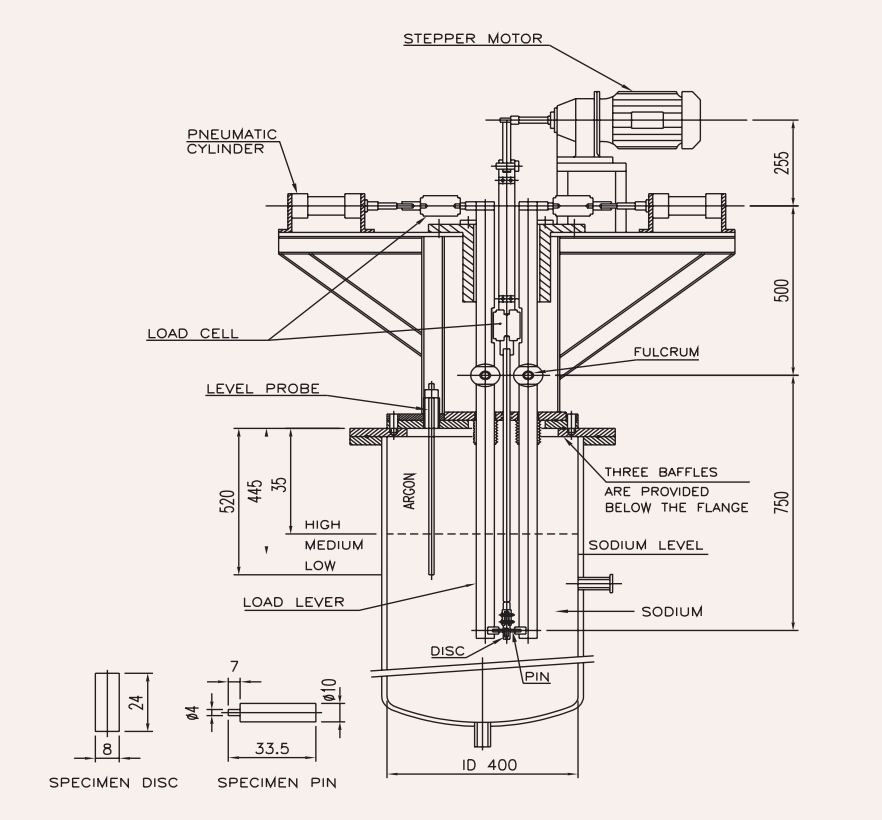

Fig 1. Tribometer in sodium vessel of SILVERINA

The tribometer is a reciprocating type where sliding friction of the specimens is studied. It consists of two load levers with pneumatic cylinders, central reciprocating lever that is accelerated by a stepper motor, cam and connecting rod. The static specimen (pin) is put in the specimen holder of load lever. The reciprocating specimen (disc) is put in the specimen holder of the reciprocating lever. The pneumatic cylinders are operated by air. The load on pneumatic cylinder and reciprocating rod are measured by load cells. The tribometer is inserted in test pot-3 of SILVERINA sodium loop as in Fig 1.

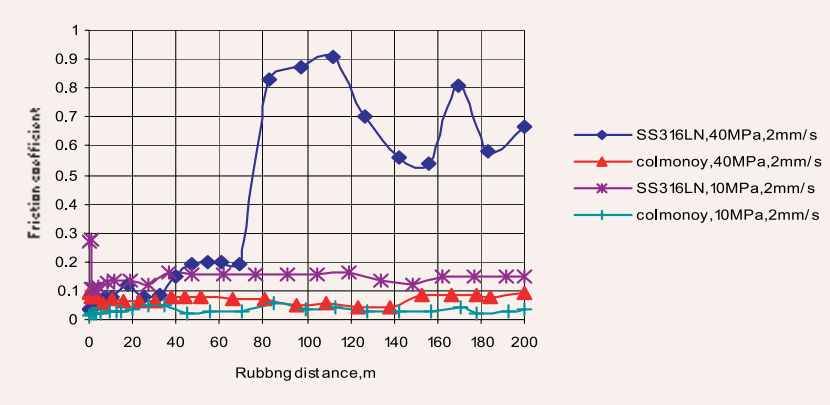

Fig 2. Static friction coefficient of SS316LN and Colmonoy-5 in sodium at 550 °C

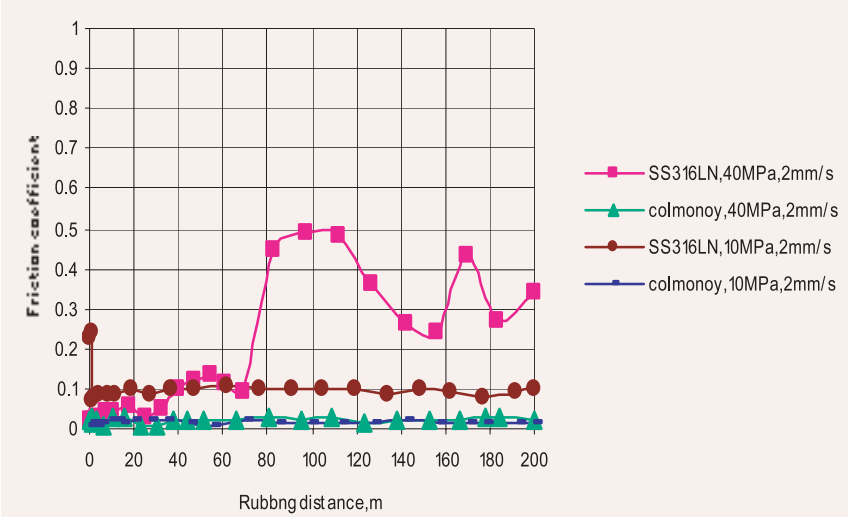

Fig 3. Dynamic friction coefficient of SS316LN and Colmonoy-5 in sodium at 550 °C

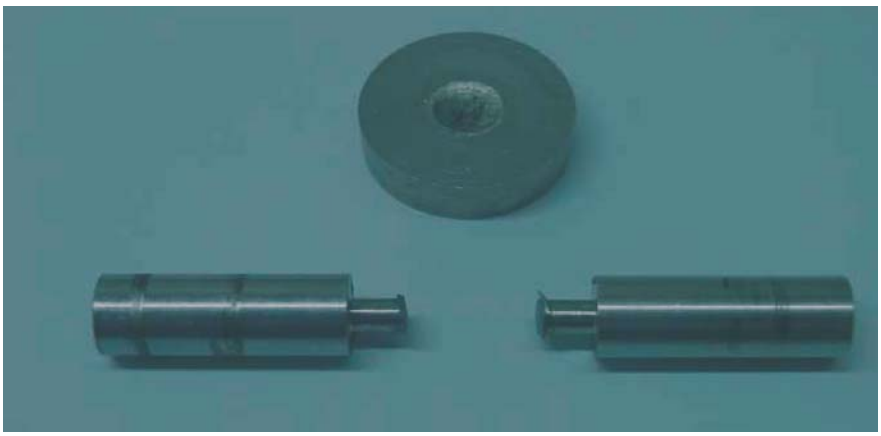

Fig 4. Pin and Disc used in tribometer

In the first stage of experiments, SS316LN and colmonoy-5 hard facing alloy were chosen for testing. Tests were carried out at 823 K in flowing sodium. The variation of static and dynamic friction coefficients with sliding distance are shown in Figs. 2 and 3. The results show that friction coefficients in sodium are higher for the stainless steel than for the hard facing alloy which can be attributed to the difference in their hardness. The friction coefficients of SS316LN are initially less and then rise to a higher value due to surface roughness consequent to wear. The results obtained are comparable to those reported in other in-sodium wear studies. The reported dynamic friction coefficient in sodium for stainless steel is 0.7 to 0.9 and for the hard facing alloy about 0.2. Wear damage was found to vary from specimen to specimen in the case of colmonoy-5 deposit. This is due to variation in dilution of the deposit from the stainless steel substrate. For PFBR design, the dynamic friction coefficient for SS316LN is 0.5 (max.) and for colmonoy-5 0.05 (max.). The pin and disc used in the tribometer are shown in Fig. 4.

2.13 Development of Sodium Resistant Concrete

Sodium resistant concrete is used as the floor finish in the Steam Generator Buildings (SGB) of Fast Breeder Reactor based power plants, where hot sodium spillage may take place. Sodium reacts violently with normal concrete damaging the surface. To protect structural concrete, a sacrificial layer, which is less aggressive with liquid sodium, referred to as sodium resistant concrete has been developed. The thickness of this sacrificial concrete layer is arrived from the liquid sodium-concrete interaction studies.

Water and silica content in the normal concrete are prime factors for sodium interaction. Sodium interaction with normal concrete takes place by penetration and exothermic reaction. To reduce silica content, coarse and fine aggregates of limestone are used in the sodium resistant concrete. To reduce water content, water is restricted to 191 litres/m^3. To maintain strength, the water to cement ratio is limited to 0.58, resulting in cement content of 330 kg/m^3. To improve workability of the mix, chemical admixture is used. Table 1 gives the composition of the sodium resistant concrete mix. Test blocks (Fig. 1) of 600 mm x 600 mm x 300 mm size with a top cavity of 300 mm x 300 mm x 150 mm were prepared using the sacrificial concrete mix.

Table 1. Sacrificial Concrete Mix Proportion by Weight

Cement	Water	Fine Aggregate	Coarse Aggregate	Admixture super plasticizer
1	0.58	2.547	3.817	0.7% by weight of cement

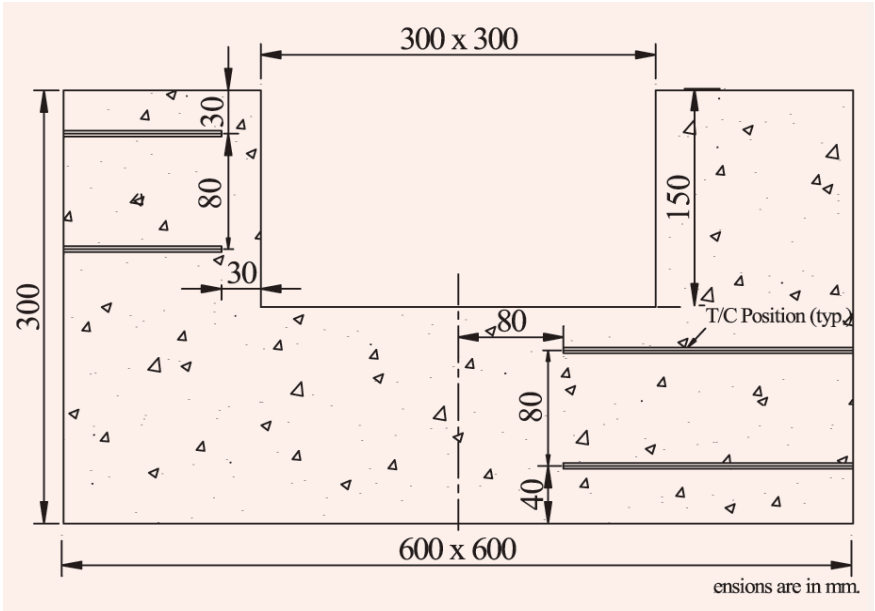

Fig. 1: Test Concrete Block

Fig. 2: Impact Echo Testing

Mechanical properties are evaluated before sodium pouring test using destructive and non destructive tests. Base line data are evaluated using Impact Echo Technique (Fig. 2) and Schmidt Hammer (Fig. 3) Tests.

A sodium pouring facility, whose schematic is as shown in Fig. 4, is used to conduct the tests. Each block was exposed for 30 minutes to about 12 kg of liquid sodium (~ 120 mm liquid column, Fig. 5) at 550 °C in open air, after which sodium was sucked back from the cavity of the concrete block into the same sodium tank used for pouring. On-line monitoring of temperatures was carried out at strategic locations of the

Fig. 3. Schmidt Hammer Test

sodium pool and concrete block. Color videography was employed for taking motion pictures of various time dependent events like dumping and suction of liquid sodium, appearance of flame, formation of smoke, cracking of concrete surface and release of water through cracks or pores. During the test period, the mass of the concrete block was continuously recorded with the help of a PC based weighing machine. After removing sodium from the cavity and cleaning the surfaces, non-destructive examinations such as Schmidt Hammer and Impact Echo testing were carried out on each concrete block at the same locations where data were taken earlier at pre-exposed stage. Rebound hammer tests were conducted for all the four blocks.

The statistical analysis of Schmidt Hammer data revealed that block II has undergone damage to the extent of 16 %. The average reduction of rebound hammer number is attributed to the combined effect of decrease in compressive strength and hardness of the concrete after sodium exposure. But all other blocks have suffered no detectable degradation. The measurement of mass before and after sodium exposure indicated that loss of mass occurred for all the four blocks varying from 0.6 to 2.4 % due to release of water.

Chemical analysis for sodium monoxide was carried out in the samples collected by core drilling of the cavity floor of each block. A typical depth profile of sodium monoxide concentration for block 2 is shown in Fig. 6. From a detailed evaluation of the results of

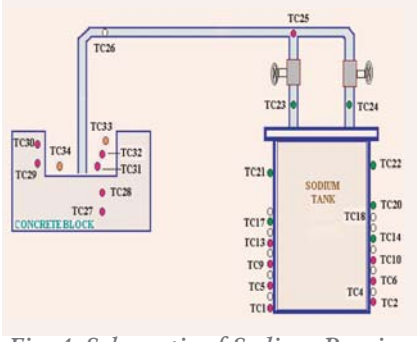

Fig. 4. Schematic of Sodium Pouring Facility

chemical analyses of all the blocks, it is concluded that bulk penetration of sodium into the concrete has not taken place beyond 30 mm. However in some local spots, the sodium penetration is as high as 50 mm.

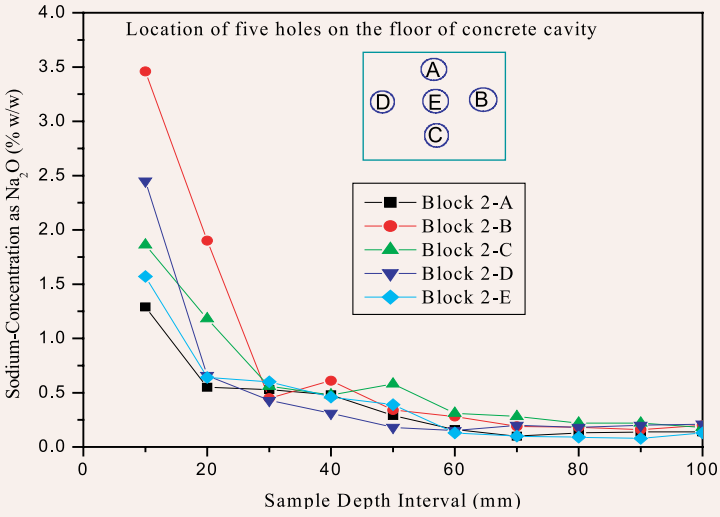

Fig. 6. Sodium Penetration in Test Concrete Block 2

Fig. 5. Sodium Exposure on Test Block

Cylindrical core samples were obtained from the sodium exposed concrete cavity and tested for compressive strength and longitudinal Ultrasonic Pulse Velocity (UPV). These are compared with test results of samples obtained from concrete cubes used as standard reference. The average reduction in UPV and compressive strength were 7 % and 29 % respectively indicating a marginal degradation in mechanical properties of sodium - exposed concrete. Based on this and the sodium penetration results, 50 mm thickness of sacrificial concrete layer is recommended for the FBR power plant.

2.14 Microstructure, Microchemistry and Long Term Diffusion Behavior of Chloride in PFBR Concrete Structure

The entry of seawater into the PFBR construction site during Tsunami, entailed a detailed study on the extent of chloride ingression into the concrete that had been laid and its consequences on the subsequently built layers. It was necessary to assess whether the chloride content in the newly built concrete would be below the allowable limit of 0.6 kg/m^3 (as per IS: 456-2000), even after 150 years. The studies consisted of microstructural and microchemical features of different concretes, cured under different simulated conditions, and samples from the raft of PFBR which was exposed to the sea water. The study also included prediction of redistribution profiles of chloride in the concrete structure up to 150 years and an assessment on the reliability of the estimated concentration profiles.

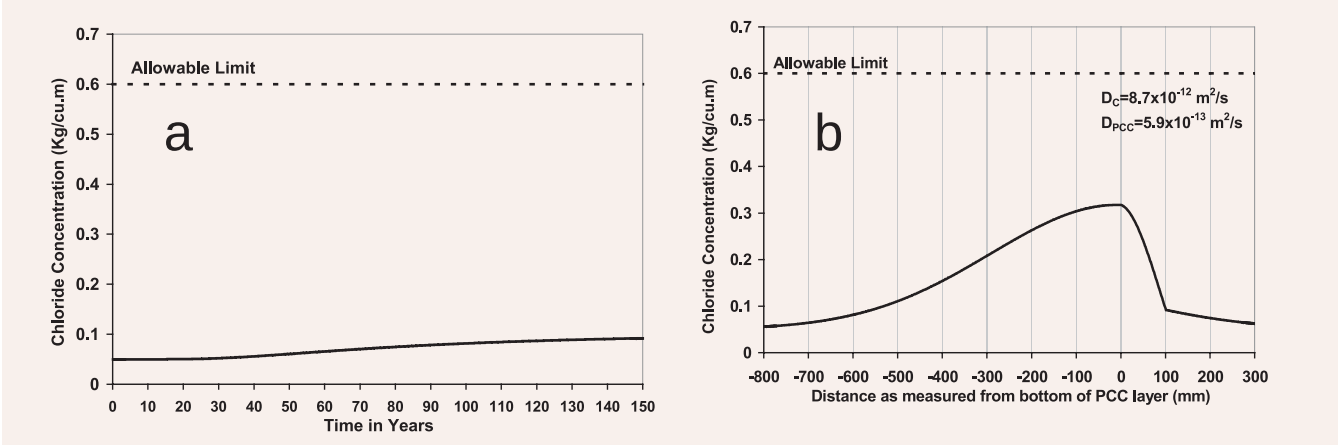

Fig 1. Chloride concentration profile in concrete as a function of (a) time at the surface of PCC (b) depth after service life of 150 years

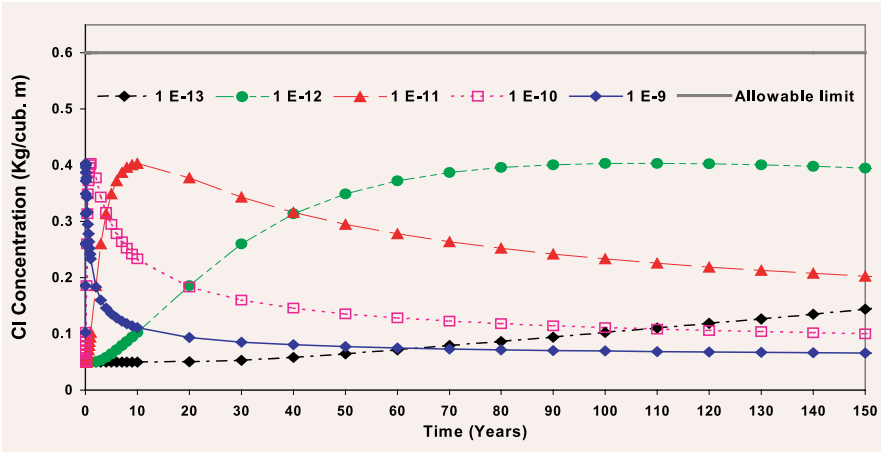

Fig 2. Calculated chloride concentration profiles as a function of time at surface of PCC (100mm above the Pour-P2 concrete) for different 'D' values

The chloride ingression was measured at different depths and reported by BHAVINI. The chloride level in the freshly built layers consisting of 100 mm of Pulverised Coal Combustion (PCC) type concrete (with 30% fly ash) followed by normal structural concrete was 0.05 kg/m^3. However, it was necessary to ascertain that any increase in chloride concentration in the structural concrete due to diffusion from the underlying layers, would be within the permissible limit even after 150 years.

Since redistribution of chloride within the structure occurs essentially by a diffusion process, one-dimensional diffusion equations were set up with appropriate initial and boundary conditions and solved using numerical methods to obtain the chloride concentration as a function of distance and time. The required

inputs on initial concentrations of chloride and diffusion coefficients (D) of chloride in concrete (D_C) and in fly ash containing concrete (D_{PCC}) were taken from a BHAVINI report and the literature on similar type concrete respectively. The predicted chloride concentrations show the chloride concentration to be always well below the allowable limit on the surface of fly ash concrete (Fig. 1(a)) and also in the entire concrete structure even after 150 years (Fig. 1(b)).

The D values reported in literature ranged from 10^{-13} to 10^{-11} m^2/sec, representing various types of concrete, exposure conditions, and testing methods. The concentration profiles evaluated by analytical method, at a distance of 100mm above the pour-P2 concrete using the above range of D values (Fig. 2) show the concentration to always remain below the permissible level of 0.6 Kg/m^3, for even a 'D' value as high as 10^{-9} m^2/sec. A scenario giving rise to such high D value is examined below.

SEM/EDS analysis on the cement region of a concrete block (150mm cube) that was mixed using normal water but cured in seawater for 20 days, showed a typical microstructure of an inhomogeneous dispersion of aggregates of different shapes and sizes, the binding medium of hydrated cement paste (Fig.3 (a)) and an interface transition zone (IFT) between cement and aggregates. During curing, water reacts with tricalcium silicate mineral to form the porous hardened cement paste, and chloride species exist predominantly within the pores of the cement phase. Chloride concentration measured by Proton Induced X-ray Emission (PIXE) on specimens from different depths of this block is shown in Fig. 3(b). It is seen that the net intensity of chlorine at the surface of the block and up to a distance of 35-40 mm is higher than that at larger distances or at the center of the 150mm block. The D value obtained by fitting the above chloride concentration profile is ~1.8 x $10^{-9}$$m^2$/s, which is higher than values reported for cured concrete ~ 10^{-13}-10^{-11} m^2/s. This experiment shows that a high value of D can be obtained in a concrete that is exposed to seawater during the initial stages of curing, which is attributed to the undeveloped pore system in the wet concrete, in the initial stages of hydration of cement. However, in cured concrete structures such high rates of diffusion are not expected during service.

These studies lead to the conclusion that chloride content on the surface of the PCC layer would always be below the allowable limit.

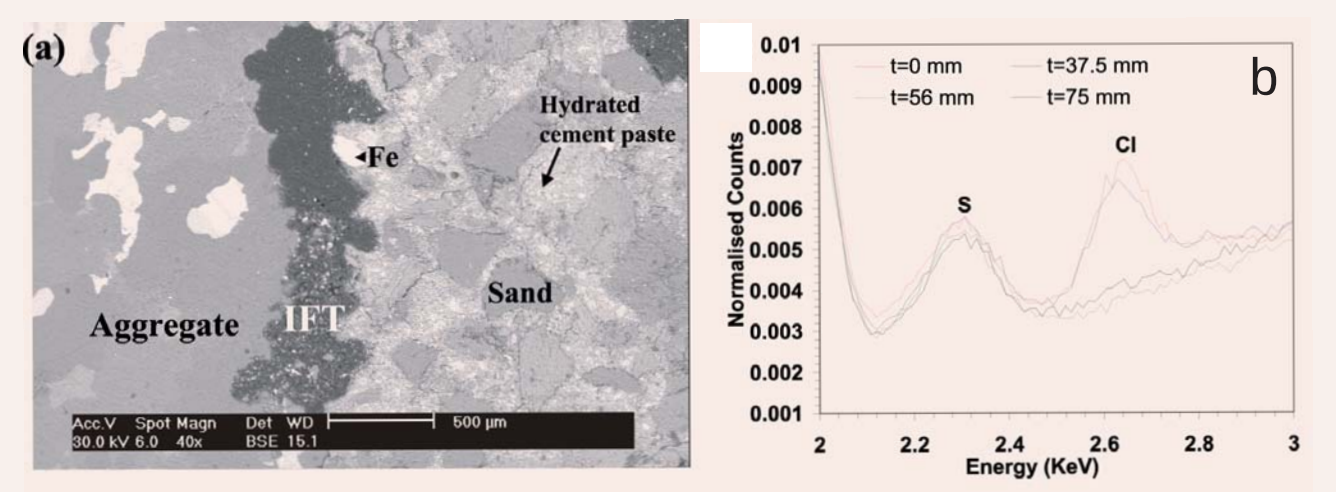

Fig 3. (a) Microstructure of a typical concrete structure (IFT-Interfacial Transition Zone) (b) Chloride profile by PIXE analysis of specimens from different depths of the concrete block cured in seawater (t = depth from surface).

2.15 Development and Characterisation of a $Ni_{50}Fe_{37}Co_{13}$ Soft-magnetic Alloy for Application in Diverse Safety Rod Drive Mechanism

The Diverse Safety Rod employs a driving mechanism, called DSRDM that incorporates a temperature sensitive electromagnetic switch (TSMS), the function of which is to cut off the energising current supplied to the electromagnet of DSRDM, once the sodium temperature crosses the Curie temperature. The de-energisation of the magnet results in the drop of the Diverse Safety Rod (DSR) into the reactor core. In this regard, the choice of the candidate material for the electromagnetic switch is rather crucial as well as limited, from the point of view of ensuring a Curie temperature of about 625°C, which is set by design considerations. The Curie point of this sensor material depends on the chemical composition and it is necessary to optimise the chemical composition and thermo-mechanical processing to achieve the required Curie temperature. Based on calibration data relating the chemical composition to Curie temperature and the variations found in the vacuum induction melting route, the ingots were prepared with cobalt in the range 12 to 15% (Ni - 50% and Fe - balance).

These laboratory ingots were subjected to X-radiography to identify and locate the casting defects. Gas holes were found in the ingots. Though pouring was done in a very thin stream to reduce the porosity, the presence of porosity could not be completely eliminated. Also extensive cracking of the ingot was noticed in the ingots forged using pneumatic hammer. Therefore a systematic study was undertaken and the thermo-mechanical processing route was optimised to obtain sound products. Figure 1 shows the successfully forged alloy which shows the expected hot worked structure and equiaxed grains. The radiography of the hot worked piece did not show any porosity indicating that the pores got self-welded during hydraulic press forging. The press forging reduced the cracking and also resulted in a good microstructure. Differential scanning calorimetry was employed to obtain the Curie temperature and it was found that the alloy with $Ni_{50}Fe_{37}Co_{13}$ compositions resulted in required Curie temperature in the range 620 - 630°C. This alloy with a Curie temperature of 616°C was forged based on the optimised thermomechanical processing and the sensor components fabricated are shown in Fig. 2. These components are now being functionally tested in the furnace.

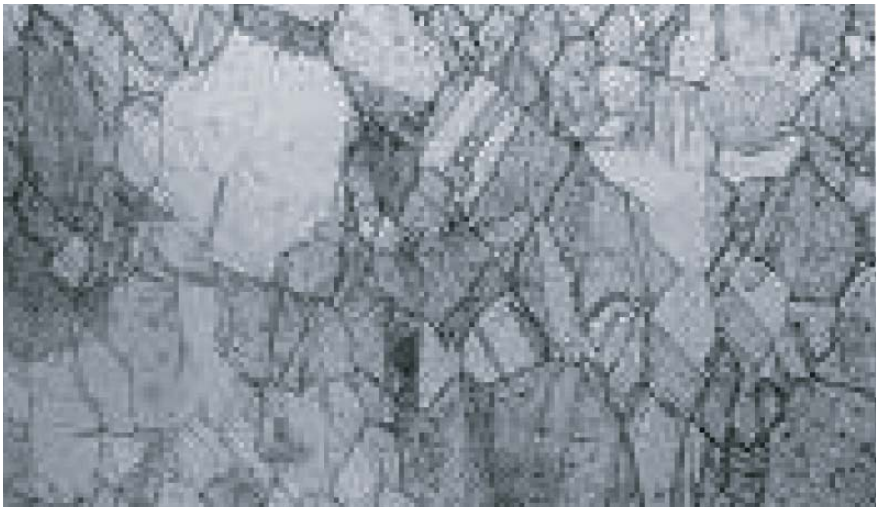

Fig. 1. The hot worked microstructure (50 X)

Fig. 2 . The sensor components

2.16 Indigenous Development of Grade 91 (Modified 9Cr-1Mo) Steel Electrodes for PFBR

The material chosen for fabrication of steam generators of PFBR is Grade 91 (modified 9Cr-1Mo) steel. To ensure that the welding electrodes for fabrication of PFBR steam generators are available indigenously, a development programme was taken up with Indian welding consumables manufacturers. During the design of steam generators, it was envisaged that both gas tungsten arc and shielded metal arc welding processes would be employed for fabrication. Accordingly, specifications for Grade 91 filler wires and coated electrodes were finalized. These specifications are in consonance with and as stringent as the corresponding AWS/ASME or ISO specifications. Included in the specifications are a minimum requirement of toughness, matching of composition of core wire for the coated electrodes and Reference Temperature - Nil Ductility Transition (RT_{NDT}). For indigenous development, all potential Indian electrode manufactures were invited. Based on the results of chemical analyses and impact tests of coupons supplied by them, two electrode manufacturers were selected. The electrodes and the weld joints produced by them were subjected to extensive testing as per quality assurance plan drawn up and it was seen that they met all the mandatory requirements (as shown in Table 1). This work represents a successful import substitution effort.

Table 1. Comparison of major properties of the weld metals deposited using indigenously developed electrodes meeting the requirements of PFBR specifications. Mechanical tests were carried out after the specified post - weld heat treatment at 1013 K for 3 h.

	Specified	Manufacturer 1	Manufacturer 2
YS at ambient temperature (MPa)	415 (min.)	669	748
UTS at ambient temperature (MPa)	585	770	800
%elongation at ambient temperature	16	18.4	17.3
YS at 798K (MPa)	313	498	505
Charpy V-notch impact energy at 298 K (J)	45	59	50
RT_{NDT} (K)	To record	268	268
Diffusible hydrogen content (ml/100g weld)	4.0	3.7	3.2

2.17 Thermal Hydraulic Experiments in SAMRAT Model

SAMRAT is a 1/4 scale model of the PFBR primary sodium circuit. Various thermal hydraulic studies were carried out which are discussed below.

Gas Entrainment Studies

The phenomenon of gas entrainment in fast reactor hot sodium pool may create reactor operational problems. Suitable techniques are required to be developed to mitigate this problem. Gas entrainment being a very complex phenomenon, can be studied in a better manner through experimentation. Water model tests are a proven technique to study this phenomenon. Earlier, studies were carried out in SAMRAT model and the presence of entrapped air bubbles was observed at 40% of nominal flow rate. It was also observed that turbulence at the

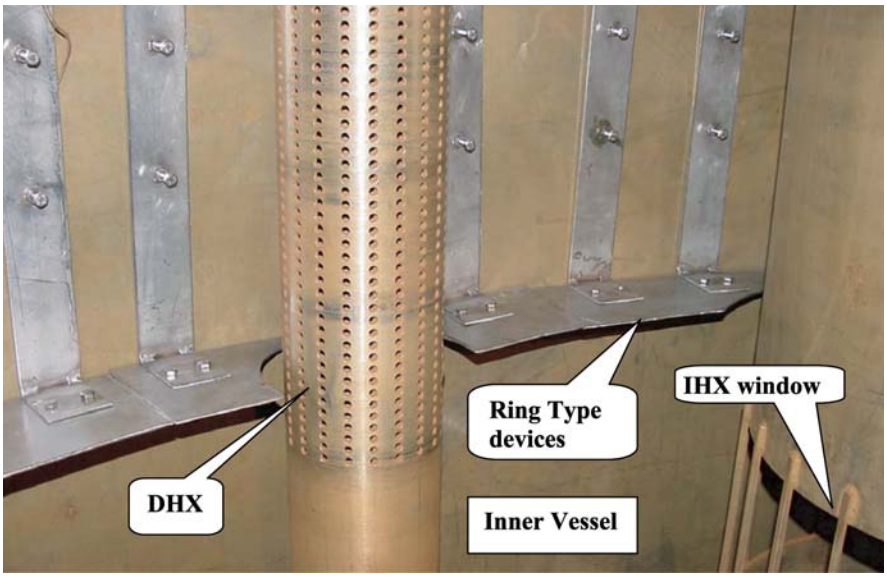

Fig. 1. Ring type device assembled with Inner Vessel of the model

free surface is the major cause for gas entrainment. To reduce the turbulence at the free surface, ring type devices were designed. These devices were fixed at the inner vessel just above the IHX window as presented in Fig. 1. The experiment was conducted with this configuration and it is seen that the free surface turbulence is reduced very much. The path of the entrained bubbles was traced by an underwater camera. The videographs obtained from the underwater camera reveal that air is getting entrained from the loop also. Further investigation is being carried out to eliminate any chance of air entrainment from the loop.

Dilution studies of coolant sample exiting from core top

The coolant sample collected through the sampling tubes located at the bottom of the control plug is fed to the Failed Fuel Identification Module (FFIM) for identification of the particular failed fuel Subassembly (SA). It is important to know the amount of dilution of the coolant sample exiting from the particular SA by the coolant of the neighboring SA before reaching the sampling tubes. An experiment was carried out using conductivity probes to estimate the dilution at nominal flow rate. The dilution phenomenon was simulated in the model by Reynolds number (Re) similitude. To maintain the Re similarity, the flow rate requirement in model is very high. So the experiment was conducted at lower flow rates (Re distortion in the model is 1/10 and 1/18). Theexperiment was conducted by sending low conductivity DM water to the normal SA and tap water was sent to the SA designated as the failed fuel SA. Prior to the study, conductivity probes were fixed at the receiving end of the sampling tubes. Initially the conductivity of tap water was measured by the probes as a reference value. Then the model was filled with DM water and the conductivity of DM water was monitored continuously. The conductivity shown was constant against time but when the jet of tap water struck the probes, a sudden increase in conductivity was observed. This is illustrated in a real time plot presented in Fig. 2. The presence of dilution is confirmed once the conductivity values become less than the reference value. It was observed that at lower value of Re (Model distortion: Re/18), the coolant is diluted by 5 - 6% before entering to the sampling sleeve but at higher Re (Model distortion: Re/10) the coolant is not diluted.

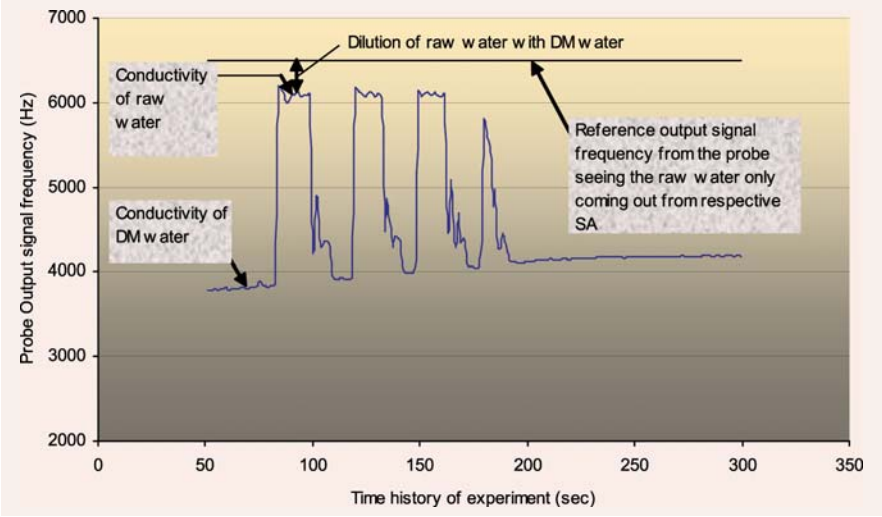

Fig. 2. Real time plot of conductivity probe output at Re/18 distortion in model

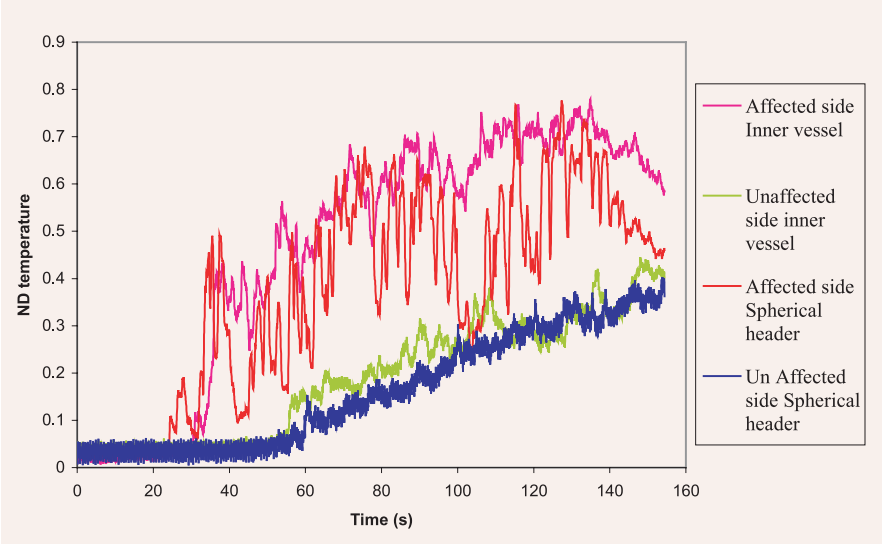

Fig 3. Normalised temperature plot for the immersed components inside the cold pool

Simulation of secondary pump trip studies in scale model

In the event of one secondary pump trip, the reactor has to operate with only one secondary loop. In this case, the corresponding two affected IHX's will not transfer heat to the secondary side and hot sodium enters the cold pool. Due to the mixing of the hot and cold streams, the main vessel and inner vessel will be subjected to temperature fluctuation. This can affect the structural integrity of these vessels due to induced thermal stresses. The study was conducted in SAMRAT using water to assess the temperature evolution in the cold pool with a simulated secondary pump trip. Studies were conducted with a Re distortion of 25. The flow required in the model was 577.15 cu.m/h. The study was carried out using hot and cold water with hot water entering through the top of the IHX at 70 ^{0} C into the cold pool directly and the cold water temperature being 36^0 C. The thermocouples located in the pool sensed the temperatures around the immersed components.

Based on the data obtained from the experiment, dimensionless normalised temperatures were calculated by taking the ratio of the difference of instantaneous temperature and cold temperature to the maximum possible temperature difference.

Fig-3 shows the normalised temperature versus time plot for the inner vessel and pump spherical header at affected and unaffected locations.

From the plot it can be seen that the maximum normalised temperature for Inner Vessel(IV) is 0.78 at the affected side as compared to 0.43 for the same component at the unaffected side. Similarly for pump spherical header the maximum normalised temperature is 0.77 and 0.39 respectively for the affected and unaffected side.

These data are used to validate the code for the estimation of the actual temperature gradient for the components immersed inside the hot sodium pool of PFBR.

2.18 Sodium Testing of Prototype DSRDM and Prototype DSR

The second shutdown system of PFBR consists of three absorber rods, called Diverse Safety Rod (DSR)s, and the respective drive mechanisms, called Diverse Safety Rod Drive Mechanism (DSRDM)s in addition to sensors, control logic etc.

As the failure of the C & DSR to perform the intended function has safety implications, its design, manufacturing and operation have to be qualified before clearing for use in the reactor. One Prototype DSRDM (P-DSRDM)and Prototype DSR(P-DSR) were fabricated and are being tested in Engg. Hall-III.

Qualification testing consists of performance testing and endurance testing. The performance of DSRDM along with DSR was checked in air, in argon at 200°C, and in sodium

Fig. 1. Pin with Longitudinal Marks

at 200°C, 300°C, 400°C, 500°C, and at 550°C. The performance testing was carried out with 30 mm misalignment between the axes of electro-magnet (EM) and the head of the DSR sheath.

Air testing was carried out in a special rig on Large Component Test Rig. DM Water was used as working fluid in the dashpot in earlier air testing experiments. For carrying out testing in argon and in sodium, the mechanism was initially assembled in a vessel, called inner vessel, and the prototype DSR was mounted at the lower end of vessel. The inner vessel with the mechanism was lowered into a 1.0 m dia × 12.6 m long sodium vessel.

The tests carried out are : - Measurement of Torque (translation torque and support rod torque), measurement of friction between fixed and mobile assemblies, measurement of translation characteristics, measurement of EM minimum holding current, measurement of EM response time, measurement of leak tightness and fast drop test

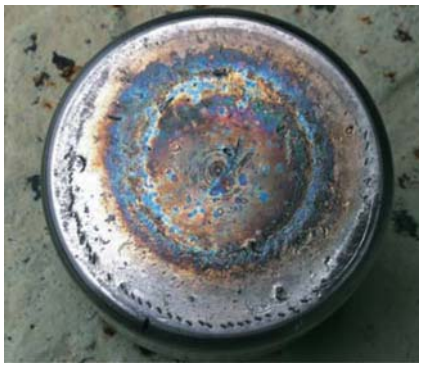

Fig. 2 : Armature Top Surface with regular Cuts

Results of the performance tests are given in Table-1. It is found that the results are satisfactory.

Table 1. Performance Test Results of DSRDM along with DSR with 30 mm misalignment

	Testing in Argon	Testing in sodium at				
		200°C	300°C	400°C	500°C	550°C
Maximum friction force (N)	23.75	32.75	32.5	30.25	25	24.5
Maximum translation torque (kg-cm)	46	52	54	50	52	52
Electromagnet minimum holding current (A)	0.75	0.75	0.75	0.75	0.75	0.75
Free fall time (for drop height of 1075 mm)#	-	-	560	540	540	540
Braking time (for drop height of 1075 mm)#	-	-	240	200	240	240

Results of acoustic measurement method

After successful completion of performance testing, endurance testing for SCRAM operations and translation cycles was taken-up. After 115 cycles of Type - 1 translation cycle operations, it was found that DSR could not be lifted by DSRDM.

P - DSRDM and P - DSR were taken out of TV-1 and sodium cleaned. The following observations were made: longitudinal marks on the pin of universal joint (refer Fig. 1), regular cuts of uniform shape on the armature top surface (refer Fig. 2), scoring marks on the translation tube of DSRDM and on the handling head of DSR stationary sheath, scoring marks on the handling head of DSR sheath (refer Fig. 3 & 4)

Fig. 3:Handling Head of DSR Stationary Sheath

Different postulates were made regarding the probable cause of malfunction. Root cause analysis was carried out, based on the various trials and visual observations, to find out the exact cause of the malfunction. The following two deficiencies are found in the system of DSRDM and DSR.

- The clearance provided between the pin and the colmonoy bushes in universal joint of DSR is inadequate

- The handling head of DSR (material: SS) is rubbing against the chrome plated translation tube of DSRDM. In addition, a sharp edge is provided in the handling head.

The following modifications were carried out:-

- The clearance between the pin and colmonoy bushes was increased.
- The load on the universal joint was reduced by modifying the drive line
- The ID of the handling head of DSR was hard faced with Colmonoy. The sharp edge is rounded.

After modifications, it is proposed to carry out functional testing, in the sequence as indicated above, before resuming the endurance testing. Functional testing is in progress.

Fig. 4 . Scoring Marks on the Handling Head

2.19 Acoustic Technique for Drop Time Measurement of PFBR Diverse Safety Rod

In PFBR there are 3 Diverse Safety Rods (DSR), in addition to the normal control rods to shut down the reactor. During a reactor SCRAM, the electromagnet holding the DSR gets de-energized and the DSR falls under gravity into the reactor core and at the end of the free fall, it is decelerated by a sodium dashpot and is brought to rest. Development of a system for measuring free fall time and total travel time of DSR is in progress. The free fall time is the time elapsed between the instant at which the electromagnet de-energizes and the instant at which dashpot action is initiated. At the end of the free fall, the DSR hits the top end of the dashpot and generates a shock signal. Similarly at the end of braking time (deceleration in dashpot) another shock pulse is generated. By measuring the time delays between the step transition of the electromagnet signal and the above shock signals, free fall and braking times can be estimated. Feasibility of using high frequency accelerometers for measuring the shock pulse produced, was studied during

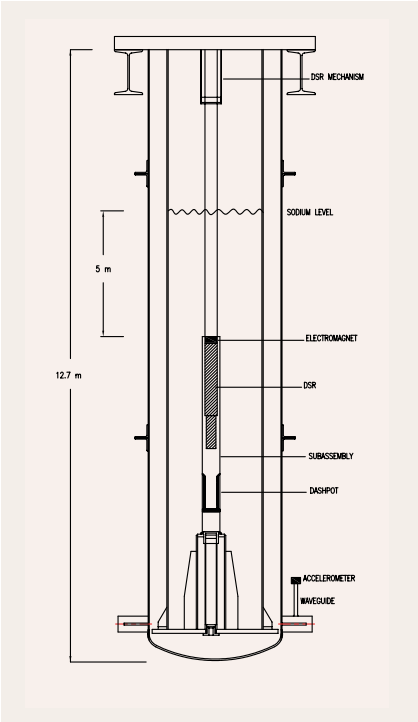

Fig. 1 Test Vessel

the performance testing of DSR drive mechanism in sodium at 550°C (reactor condition). An earlier test was carried out in water. The accelerometer sensor mounted on the SS wave-guide welded to the test vessel in Hall III showed very good response to the shock pulse generated. Experiments were carried out for different drop heights of the DSR in sodium and the free fall and braking times were measured.

The test setup is shown in Fig. 1. The test vessel was ~12.7m height and ~1m dia. The free level of sodium (550°C) in the test vessel is maintained at 5m above the top of the subassembly. The subassembly was mounted on the sleeve arrangement as shown in Fig-1. For raising and dropping the DSR, the DSR is connected to the mechanism called DSRDM (Diverse Safety Rod Drive Mechanism). During the normal

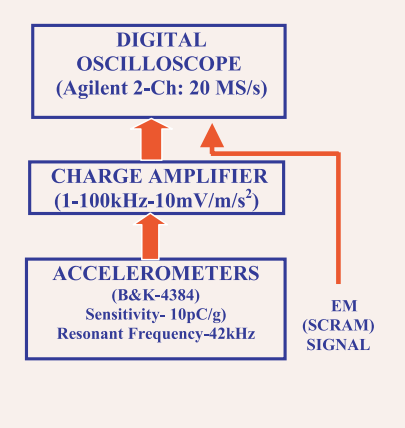

Fig. 2. Instrumentation schematic

operation of the reactor, the DSR is held inside the subassembly at 1075 mm above the dashpot bottom. After receiving the SCRAM signal, an electromagnet holding the DSR is de-energized and the DSR falls into the dashpot. Experiments were carried out to measure the drop time / total travel time of DSR.

Figure.2 shows the instrumentation schematic for the measurement. The shock signal generated during the dropping of the DSR into the dashpot is sensed by the accelerometer. The output of the accelerometer after conditioning and amplification was fed to a digital oscilloscope. Along with accelerometer signal, The electromagnet (EM) de-energizing signal was also fed to the oscilloscope.

The EM signal and the acoustic signal were captured in real time. During dropping of the DSR, the EM signal exhibits a step transition as shown in Fig-3. The dropping of DSR into the dashpot l generates a shock signal as shown in Fig-3. The sudden rise in signal obtained from the accelerometer is used for the detection of free fall time, braking time (in the dashpot) and the total drop time. The time delay between the dropping edge of EM signal and the rising edge of acoustic signal gives the free fall time. The time delay between the rising edge and peak value of the acoustic signal gives the braking time and adding the free fall and braking times gives the total drop / traveling time of DSR.

Initially the DSR was kept at a fall height of 300mm. The acoustic time signal and SCRAM signal were continuously monitored and recorded. The EM holding the DSR was de-energized and the DSR was allowed to fall under gravity into the dashpot in the subassembly. From the recorded time signal, the free travel time of the DSR in sodium, braking time in the dashpot and the total drop time were calculated. The experiment was repeated by varying the drop height from 300mm to 1075mm (reactor condition). Free fall time, braking time and total drop time were calculated for various drop heights of DSR.

The EM signal and accelerometer time signal, for the maximum fall height (1075mm) is shown in Fig. 3. For the maximum fall height of

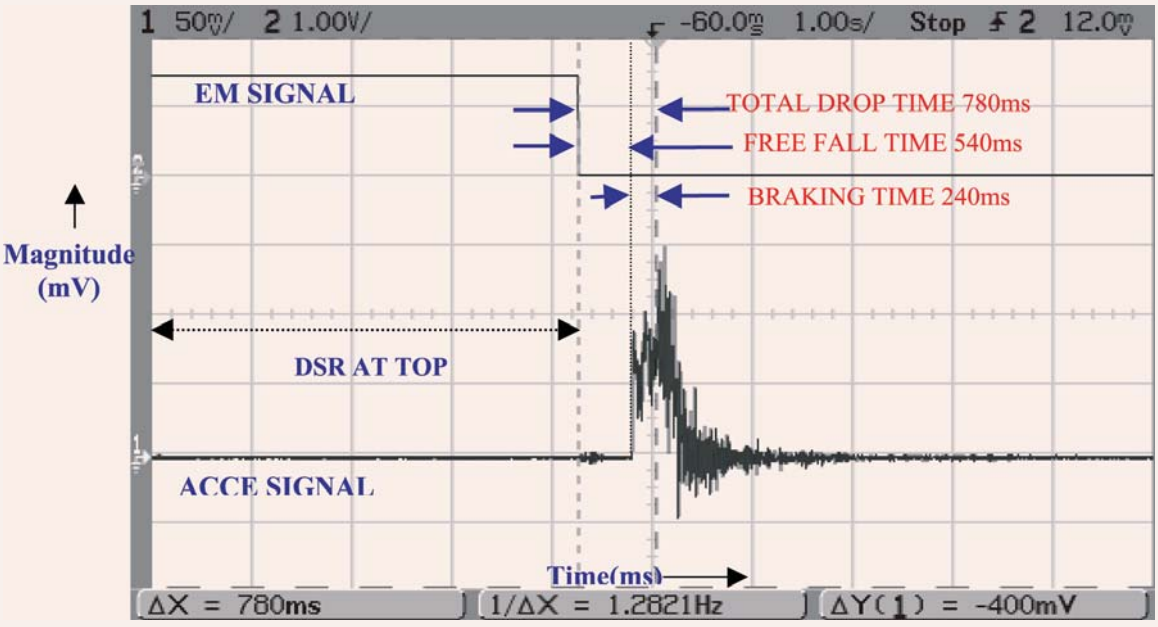

Fig. 3 Acoustic signal for a drop height of 1075mm (550°C)

1075mm, the free fall time is observed to be 540ms, the braking time is 240ms and the total drop time/travel time is 780ms in liquid sodium. The accelerometer mounted on the SS waveguide has shown very good response to the shock pulse produced during the impact of the DSR in the dashpot.

For the drop height of 1075mm in sodium at 550°C, the measured total drop time/traveling time of the DSR is 780ms, is less than the allowable time of 1s. During the test in water the free fall time of DSR is observed to be 690ms, braking time 380ms and total drop time is 1070ms. The difference in total travel time is due to the difference in buoyancy and viscous forces of water and sodium. From the experimental results, it is concluded that acoustic measurement technique can be used to determine the drop time of DSR in PFBR.

2.20 Sodium Testing of Eddy Current Flow Meter for PFBR Primary Sodium Pump

The Eddy current flow meter (ECFM) is proposed to be used in the Primary Sodium Pump (PSP) of the PFBR for pump flow measurement. ECFM is an electromagnetic device, which can be used for flow measurement of non-magnetic liquid metals at different operating temperatures.

The flow sensor consists of three coils wound on a former made of pure iron / ferrite stainless steel. The middle primary coil is excited with a constant current (200mA) source at constant frequency. The two secondary coils are wound symmetrically on either side of the primary coil on the same core. Due to the magnetic flux generated by the primary coil, secondary coils will have induced voltages. When this flow meter is inserted in flowing sodium, the magnetic field interacts with sodium and produces additional eddy currents. Flux induced due to these eddy currents will oppose the main flux linking the upstream secondary coil while aiding the main flux linking the downstream coil thereby causing imbalance in the voltages in the secondary coils. The difference between the two secondary coil voltages forms the signal output and is proportional to relative sodium velocity.

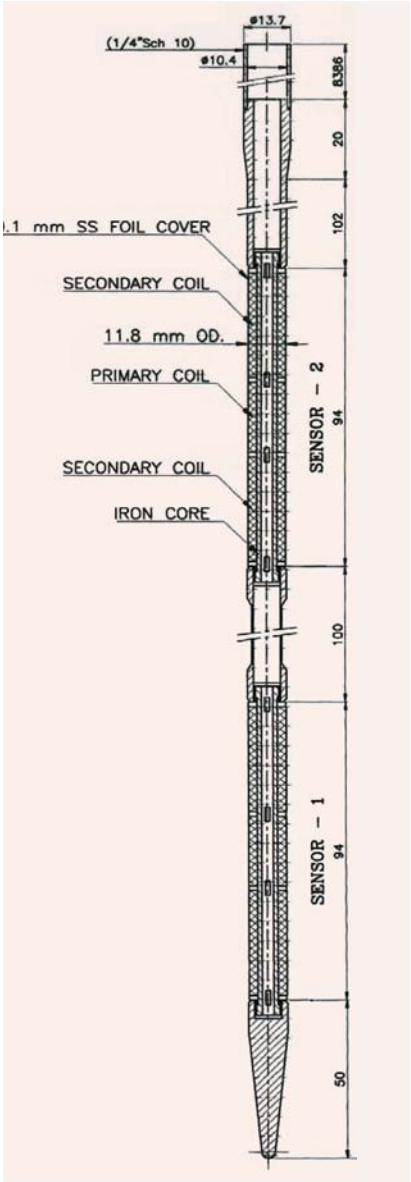

Fig 1. Details of ECFM

A probe type ECFM suitable for operation up to 823 K was designed and constructed. Fig.1 shows the details of the probe. Each probe consists of two independent flow sensors. Both sensors are of same length and diameter.

Each sensor consists of a magnetic core on which the primary and secondary windings are wound. For studying the suitability of core material, one sensor was made with soft Iron and another one with SS410. The outer diameter of sensor is 11.8mm and the length of probe with both sensors together is 456 mm.

Each sensor consists of one primary and two secondary windings made of SS sheathed MgO insulated copper and Nichrome conductor cables of outer diameter 0.5mm. The

total number of primary windings on each sensor is 200 turns and the total no. of secondary windings is 300 turns.

Salient features of sensor:

Bobbin material	:	Midhani soft Iron and SS410
Primary exciter coil	:	MgO insulated SS sheathed Copper conductor with O.D 0.5mm
Secondary exciter coil	:	MgO insulated SS sheathed Nichrome conductor with O.D 0.5mm
Exciter current	:	200 mA
No. of primary turns	:	200 turns
No. of secondary turns	:	300 turns
IR Value	:	> 20 MOhm

Sodium Testing in 500 kW loop:

Sodium testing was carried out in the existing 500kW sodium loop. The test section location in the 500kW loop is as shown in the Fig. 2.

Sodium testing of ECFM was conducted in two phases. In the first phase Fe-Ni tube was used as the shield material and in the second phase SS 410 was used as the shield material. This shield material helps in concentrating the magnetic flux in the probe region.

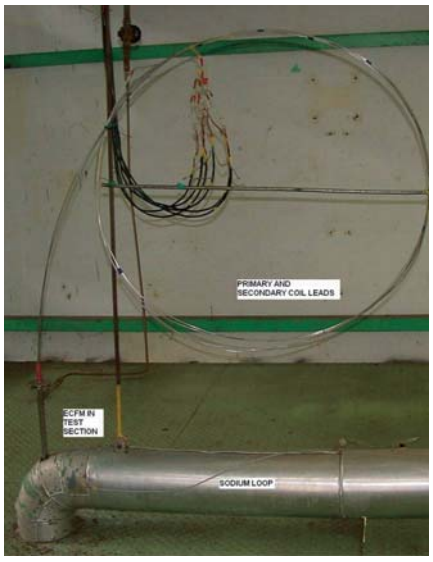

Fig 2. Test section in 500 kW loop

A. Phase-I Testing (with Fe-Ni as shield material)

Testing at different sodium temperatures from 250°C to 500°C for various flow rates:

With sodium temperature at 250°C, primary excitation current at 200mA, 433Hz, secondary outputs were recorded for flow rates from 30 m^3/hr to static condition. To check the repeatability of the output, the flow rate was raised from 0 m^3/hr to 30 m^3/hr. Outputs S1, S2, S3, S4 were recorded. Reference permanent magnet flow meter output (RF1) was also recorded. Accuracy of this flow meter is 2%.

The ratios (S2-S1)/(S1+S2) and (S4-S3)/(S3+S4) give the flow through the ECFM after temperature compensation. Testing was repeated with different temperatures of 300°C, 350°C, 400°C, 450°C, 500°C. Readings were recorded in PC using a data logger.

B. Phase II Testing (with SS410 as shield material)

1. Testing at different sodium temperatures from 250°C to 500°C for various flow rates:

With sodium temperature at 250°C secondary outputs were recorded for flow rates from 30 m^3/hr to 0 m^3/hr. Repeatability of the output was checked. This testing was repeated with different temperatures of 300°C, 350°C, 400°C, 450°C, 500°C. and readings were recorded.

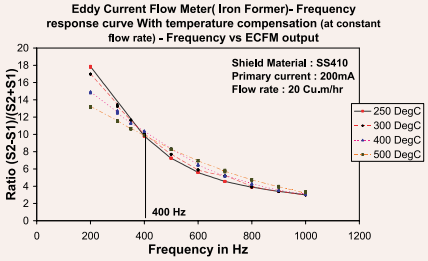

3 a. Frequency vs ECFM output with temperature compensation for different temperatures (iron former).

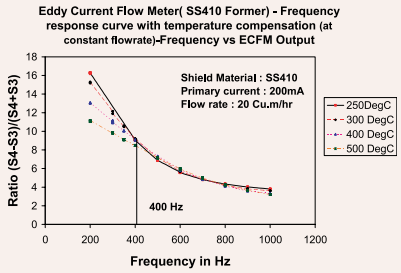

3 b. Frequency vs ECFM output with temperature compensation for different temperatures (SS410 former).

2. Frequency response at sodium temperatures from 300°C to 500°C for constant current at different frequencies from 200 Hz to 1000Hz for a flow rate of 20 m^3/hr.

This test was done to select the primary excitation frequency of sensor for an optimum output. At 250°C for a constant flow rate of 20 cum/hr and for different frequencies from 200Hz to 1000Hz, secondary outputs were recorded. This test was repeated for sodium temperatures of 300°C, 400°C, 500°C. Fig.3a & Fig.3b show the frequency vs ECFM output with temperature compensation for different

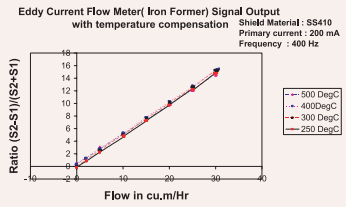

Fig 4a. Flow rate Vs Temperature compensated output at different temperatures for iron former.

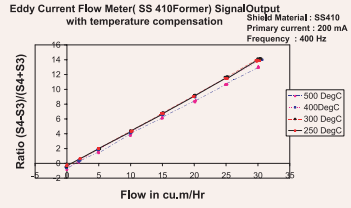

Fig 4b. Flow rate Vs Temperature compensated output at different temperatures for SS410 former.

temperatures for iron and SS410 former.

3. Testing at different sodium temperatures from 250°C to 500°C for constant current at a frequency of 400Hz for various flow rates:
Based on the above test the operating frequency was selected as 400Hz for iron former and 433Hz for SS410 former and testing was done at different temperatures of 250°C, 300°C, 400°C, 500°C at 400Hz for different flow rates.
Fig. 4a & 4b show flow rate vs. temperature compensated output of ECFM at different temperatures for iron and SS410 formers.

The sodium test results indicate that both the type of sensors i.e iron and SS410 formers can be used for flow measurement of PFBR primary pump. Two types of shield materials Fe-Ni alloy(in Phase-I) and SS410 (in Phase-II) were tested and found that SS410 alloy is a suitable shield material. Test results have good repeatability and the temperature error is $\pm$ 2% for sodium operating temperature from 200°C to 500°C.

2.21 Poolside Spent Sub-Assembly Inspection Bench for PFBR

A prototype special purpose inspection bench has been developed at IGCAR to carry out the dimensional measurement / profilometry and visual examination of spent sub-assemblies (SA) at the spent fuel storage pool of PFBR. The main purpose of dimensional measurement / profilometry of the spent SA is to evaluate the extent of irradiation-induced deformation like bow, bulge across the faces, and elongation of the hexagonal SA wrapper. The bench is designed in such a way that all moving components except the measuring probes, are kept above the storage pool eliminating the need for expensive underwater compatible components.

The inspection bench is in essence, a 4-axis (X, Y, Z & θ) programmable manipulator having three mutually perpendicular translational motions (X, Y & Z) and a rotary motion (θ), driven by stepping motors. Motion along the X-axis is divided into 2 independent stages namely X1 & X2 for taking measurements across the hexagonal faces. All parts that are exposed to the pool water are fabricated from corrosion resistant steel (AISI 304). The SA is inspected in a vertical condition underwater in the storage pool of PFBR. The X1, X2, Y and θ motions lie in the horizontal plane and are used to measure the deformation across the faces of hexagon and the motion along the Z-axis is used for measurements along the length including the elongation of SA wrapper. A single LVDT is used as a simple touch probe to register the co-ordinates of points on the six faces around the sub-assembly at a particular cross section. These co-ordinates are used to reconstruct the hexagonal profile at that cross section. The inspection head will begin measurements at the lowest possible point on the SA forming the datum and the inspection head will establish the bow "zero" from the hexagonal features at that datum. The probe head will be traversed up along the sub-

Fig. 1. Poolside spent sub-assembly inspection bench

assembly (along the Z-axis) at user-defined intervals to get the profiles of various cross sections of the sub-assembly. Profiles of the various cross sections of the SA are integrated using standard modeling software to get a 3D wire frame model of the SA. From the wire frame model, the extent of deformations such as bulge across the faces & corners, bow & elongation of the SA are determined. The bulge across the faces can be measured with an accuracy of 0.1 mm, and the rest with 0.2 mm.

The SA is located on a base which has the calibration standard plus the auto-aligning mechanism. The calibration standard is provided to conform to the geometry of the outer envelope of a standard SA and the standard will be characterized to ±0.005 mm to calibrate the LVDTs prior to the inspection campaign. The calibration standard is located on the auto-aligning mechanism at the bottom of the storage pool.

A radiation resistant under-water camera is integrated into the system for visual examination of the SA including identification of numbers on the SA wrapper and any observable defects on the surface. The camera will be able to inspect all surfaces of the SA with a suitable motorized zoom. The dimensional measurement and visual inspection of the SA can be carried out in tandem or independently.

Translational and rotary motions are achieved using stepping motors and drives through reduction gear trains. X1, X2 and Y axes are fitted with precision linear scales and Z and θ axes are fitted with incremental encoders. These feedback devices provide the respective coordinates of surface points when the LVDT touches the surface and trigger the data acquisition. A motion control system is provided to control all axes using a PC based controller and dedicated motion control software with a user friendly GUI. The PC-based software enables the user to control and program the speed and direction of the motion along X, Y, Z & θ axes. The inspection system also has a handheld pendant for manual operation of each axis with a provision for auto-acquisition of positional data during dimensional measurement. Fig.1 shows a photograph of the inspection bench.

The inspection bench has been tested for all the functionalities and is being validated extensively in air and water.

2.22 Validated Code Development for the Transport and Deposition of Activated Corrosion Products in LMFBR

The safe operation and maintenance of any process industry aims at minimum occupational hazard to the personnel involved. This becomes more stringent in the case of nuclear industry through minimizing the radiation burden. In the case of Liquid Metal Fast Breeder Reactors (LMFBR), it has been observed that the major radiation contribution to the maintenance personnel during normal operating conditions is due to the activated corrosion

Table 1. Comparison between the estimated and measured deposition density (AMTL-1)

Surface Concentrations (Bq/cm^2)			
^{54}Mn	HL-1	HL-2	CL-02
Measured	74	65	148
Calculated	70	87	111
^{60}Co			
Measured.	740	185	296
Calculated.	1996	296	740

Table 2. Details pertaining to the operation of FBTR that are considered in the computation are listed

Period	Max. Power level (MW)	No. of FSA	Flow rate ($m^3 h^{-1}$)
1990-92	1.0	23	200
1993-94	10.2	24	380
1995-96	10.5	25	375
1996-97	11.5	26/27	440
1998-99	8.0	28	300
1999-00	12.5	29	460
2000-01	13.0	31	500
2001-02	17.4	33	540
2002-02	17.4	35	620

products deposited along the primary sodium circuit. Among these corrosion products, ^{54}Mn and ^{60}Co are the prominent ones, with half-lives of 313 days and 5.27 years respectively. These nuclides are produced through the (n, p) reaction with the ^{54}Fe and ^{60}Ni present in the core cladding material. Subsequent to their production, the transport and deposition involve two stages. In the first stage, the activated products diffuse in SS and get released through the clad surface into the liquid sodium. In the next stage, they are transported along the primary loop with subsequent deposition.

These processes are modelled using the solution and precipitation and semi- infinate cladding approximation. The resultant diffusion equation is solved exactly. This is valid for the diffusion through cladding, as the diffusion lengths of ^{54}Mn and ^{60}Co are much smaller than the clad thickness. Based on this model, a computer code has been developed and validated.

In this code, the partial differential equation for mass conservation in one dimension is solved numerically using the upward finite difference method. The source terms for the PDE are supplied by the diffusion equation from the model.

Initially the code has been validated with data of AMTL-1, a Japanese test loop. The results are shown in Table-1. Agreement within a factor two is considered reasonable. For ^{54}Mn, the agreement between measured and calculated values is quite satisfactory. The computed results of ^{60}Co are in conformity with the general trends observed in experiments and the deviation is essentially due to the sensitivity of the input parameters.

Subsequently, the code was adapted for the FBTR. The estimation was considered for the reactor operating period beginning May 1990 during which the reactor was raised to the power level of 200kW. The campaigns from that period include shutdown. The details required for the code include flow rate, plugging

Table 3. Comparison between the estimated and the measured deposition density of activated corrosion products in FBTR

Location	Ratio: Estimated/ Measured	
	^{54}Mn	^{60}Co
IHX outlet	0.75	0.2562
IHX Pump	0.78	0.4882
Pump-Inlet	0.87	0.9359
Pump-outlet	2.45	0.9300

temperature, and temperatures in the core, RV outlet, and the IHX outlet. The details of the flow rate of sodium, the number of fuel sub-assemblies and the maximum operating power during this period involving different campaigns are listed in Table-2.

The primary loop was divided into about 225 cells. The production and release is considered only in the core regions while deposition is computed along the entire flow zones. The code was run for the real time operation of the reactor for the 100 GW days burn-up. The estimated surface deposition density for both nuclides compare well with the measurements made as shown in Table-3.

A similar code for the case of PFBR has been completed. The flow path was divided into about 130 cells. The code is being run with the envisaged operational campaign involving 8 months of full power and 20 days shut down for a continuous period of 15 years.

2.23 Fabrication of Axial Shield Model for PFBR

The shielding block is used for PFBR shielding experiments at APSARA to study neutron transfer through single shield material. This assembly comprises of sub-assemblies like outer casing, inner casing and seven hexagonal cans and shielding pins assembly. The shielding materials consist of SS 316 LN pellets, Boron carbide pellets and graphite capsules stacked in SS tubes of size 36 mm OD and 2 mm thick. Seven SS tubes were inserted into the hexagonal sheaths termed as a hexagonal can. Hexagonal cans and blocks were housed in the inner casing and closed with end plates. Provision was made in the inner casing to fill sodium. Finally the inner casing was placed inside the outer casing.

Outer and inner casings were made of carbon steel. The machining of grooves required for welding in 49 numbers. of end closers, drilling accurately with close tolerance in the enclosure to assemble seven SS tubes were a critical jobs. Machining of four carbon steel blocks with sloping faces on either side were carried out successfully.

Fig. 1. Axial Shield Model for PFBR

40 kg of sodium at 150^0C was filled in the boxes by Sodium Facilities division. Finally the outer case was machined to suit with the inner casing. Controlling distortion in welding of four sub-assemblies was achieved successfully.

The overall size of the outer casing is 1190 x 498 x 500 mm. Total weight of the model is 2.5 t. All the weld joints were subjected to Liquid Penetrant Inspection and the inner casing was subjected to pneumatic test as per ASME SEC VIII-DIV.1.

CHAPTER 3

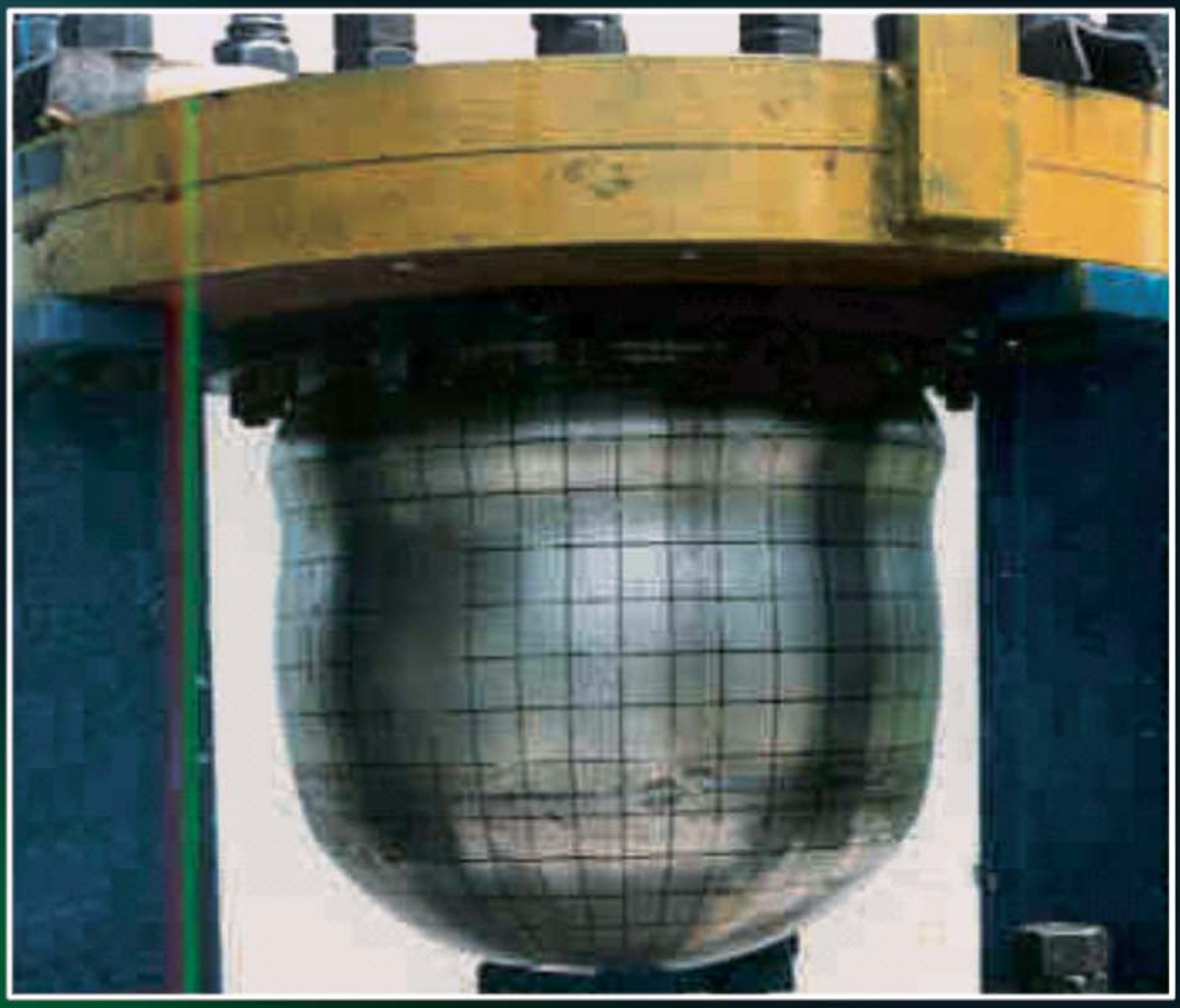

R&D for Fast Breeder Reactors

3.1 Experimental Validation of FUSTIN: The Code for Fast Transient Fluid Structure Interaction

A core disruptive accident (CDA) is a very low probability event (< 10^{-6}/reactor year) considered as a 'beyond design basis event' in a fast breeder reactor (FBR). It is postulated that loss of core flow caused by primary sodium pump trip in association with failure of both the shutdown systems on demand is an initiating event. The sequence of events in a CDA are (i) temperature rise of fuel, clad and coolant resulting in coolant boiling, fuel melting and slumping, (ii) formation of vapourised fuel, coolant and structural materials, called core bubble at high pressure and temperature, (iii) automatic neutronic shutdown of reactor due to fuel dispersal caused by core bubble pressure and (iv) release of mechanical work by pressure energy stored in core bubble. Based on the reactor physics analysis with pessimistic assumptions, a mechanical energy release of 100 MJ is considered for the design of the 500 MWe PFBR. Subsequently, analysis is carried out to determine the strains in the main vessel and its internals, sodium slug impact at the top shield bottom and sodium release to the reactor containment building (RCB). Analysis of a CDA calls for sophisticated modeling features for the treatment of large distortions in the fluid domains, strong geometrical and material non-linearities in structures, fast transient fluid structure interaction, sodium slug impact on the top shield, shock wave propagation, interactions between the moving interfaces of various fluids and automatic rezoning of finite element mesh. Addressing all the above complexities, a computer code FUSTIN has been developed in-house based on the Arbitrary Lagrangean Eulerian (ALE) formulation for fluids and convected co-ordinate formulation for structures. Fig.1 shows the numerically predicted core bubble expansion at a few discrete intervals during CDA.

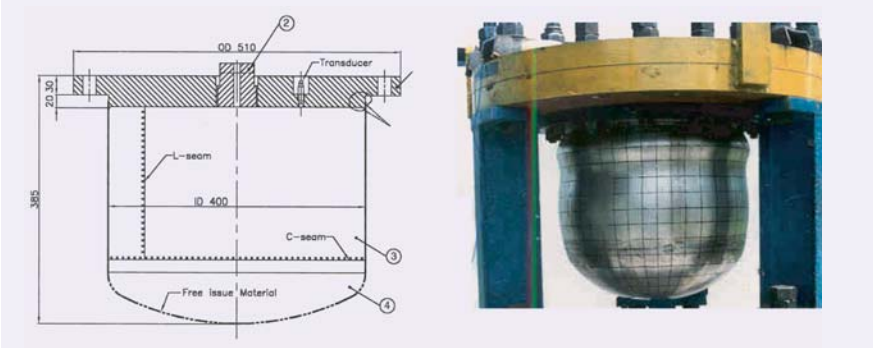

Fig. 2. Dimension details of a typical TRIG-2 test vessel and test setup

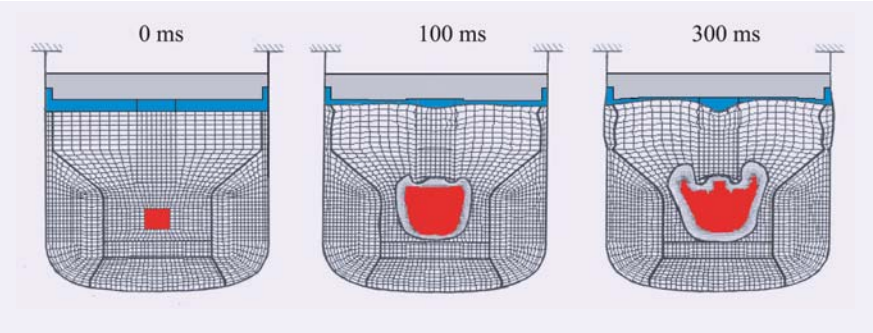

Fig. 1. Simulation of mechanical consequences of CDA in PFBR-Reactor Assembly

FUSTIN has been extensively validated using international benchmark problems viz. MANON (France), COVA (UK), CONT (UK), MARA (France) and TRIG (India) series. TRIG tests were conducted at the Terminal Ballistic Research Laboratory, Chandigarh, specially to generate data for validation. TRIG consists of 3 test series: TRIG-1 on simple cylindrical shells filled with water to characterise the low density explosives (LDE) developed by TBRL, TRIG-2 on 1/30th scale, main vessel models without internal components to understand the loading scenario and also to generate data for validating the FUSTIN code, and TRIG-3 on 1/13th scaled down mockups to quantify the effects of internals. Tests conducted on 1/13th scaled down models of reactor assembly help to ensure the

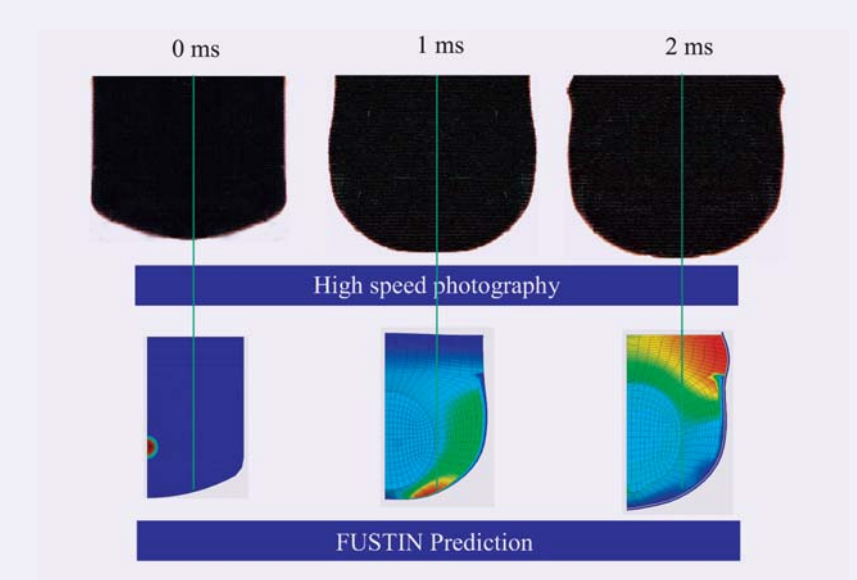

Fig. 3. Transient pressure and its effects on vessel deformation during CDA

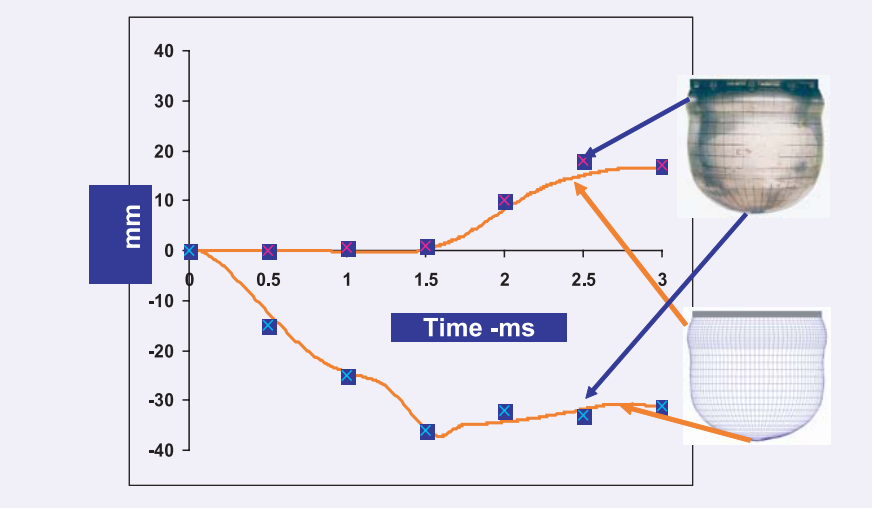

Fig. 4. Vessel displacements predicted by FUSTIN

structural integrity of intermediate heat exchangers and decay heat exchangers as well as to estimate liquid sodium leak through the top shield penetrations.

The validation of FUSTIN code is done using the TRIG-2 test results. The TRIG-2 test vessel is geometrically similar to the main vessel, scaled down by 1/30 with the top supported rigid cover. The dimensions are indicated in Fig.2 along with the test setup. Fig.3 shows the high speed photography of a typical test at three discrete times viz. 0, 1 and 2 ms and the respective predictions by FUSTIN. Fig.3 also shows the evolution of transient pressure within the vessel. During the first phase which lasts about 1 ms, the bottom portion of vessel undergoes radial bulging and downward motion and the top portion is subjected to high axial tensile stress. It is worth to note that the top portion shrinks slightly while the bottom portion moves down due to the Poisson's effect. During the subsequent phase (1 - 2 ms), the upper portion of the vessel undergoes local radial bulging in association with a slight upward motion of the bottom portion. This complex accident scenario has been numerically simulated. The prediction of vessel deformation history by FUSTIN is found to be excellent as seen in Fig. 4.

With extensive numerical and experimental investigations, the structural integrity of the primary containment has been demonstrated with a high level of confidence under CDA loadings.

3.2 Assessment of Thermal Ratchetting in Fast Breeder Reactor Assembly Components

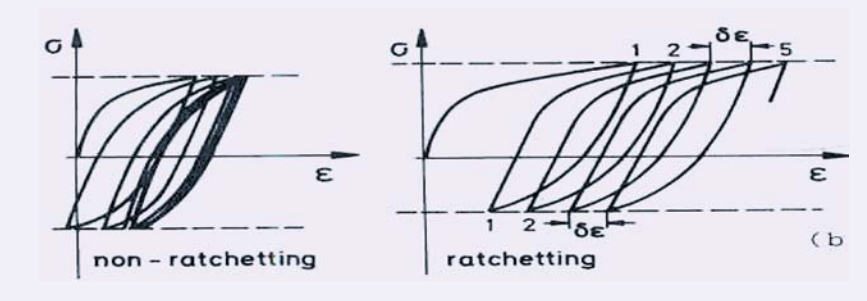

Fig. 1. Material behaviour under cyclic loads

In fast reactor assembly, if the metal parts are subjected to cyclic loads, particularly with the presence of primary stresses, the structures may shakedown (undergo stress/strain cycling without any progressive plastic strain growth) or ratchet (stress/strain cycling with incremental strain growth). This is illustrated in Fig.1. Among the many failure modes, ratchetting is one of the critical failure modes to be considered in the structural design of fast breeder reactor components, particularly when they are subjected to cyclic thermal loadings. The main vessel, subjected to cyclic variation of axial temperature gradients accompanied with steady mechanical load due to its own weight along with core, the internals and sodium, develops about 30 MPa primary stress and undergoes ratchetting deformation. Under ratchetting, the vessel in the vicinity of the sodium free level undergoes progressive strain growth at the end of each thermal cycle during safety grade decay heat removal operations. The strain growth which is in the form of local denting / bulging, should not exceed certain limits, i.e. the radial deformation should not exceed ± 15 mm, for the smooth movements of in-service inspection devices being developed. Ratchetting can reach this limit after a few cycles (10-20). Hence this problem has been analysed critically by detailed inelastic analysis in conjunction with experimental investigation.

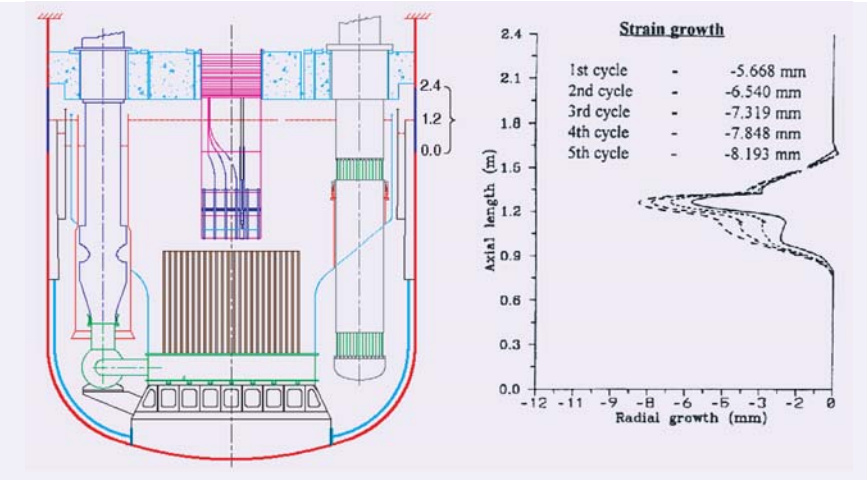

Fig. 2. Stabilised radial growth in the main vessel due to ratchetting

As far as numerical simulation is concerned, the mechanism of ratchetting is a complex thermo-mechanical phenomenon to be simulated which calls for a coupled constitutive material model involving both metallurgy and mechanics. For this, a '23-Parameter Viscoplastic Model' based Chaboche theory has been employed after thorough validation. The viscoplastic analysis indicates that the stabilized radial deformation (~8 mm) is less than the specified limit (Fig.2).

Considering the complexities involved in the analysis, an extensive experimental programme has been taken up at Structural Mechanics Laboratory (SML). Ratchetting phenomenon is simulated on a cylindrical shell made of SS 316 LN which represents the main vessel. Fig.3 shows the test set-up, where the sodium is simulated by hot air and argon by water. The test set-up has a device which can generate hot air and water jets in the close proximity so that when they impinge on the vessel, they can produce sharp axial

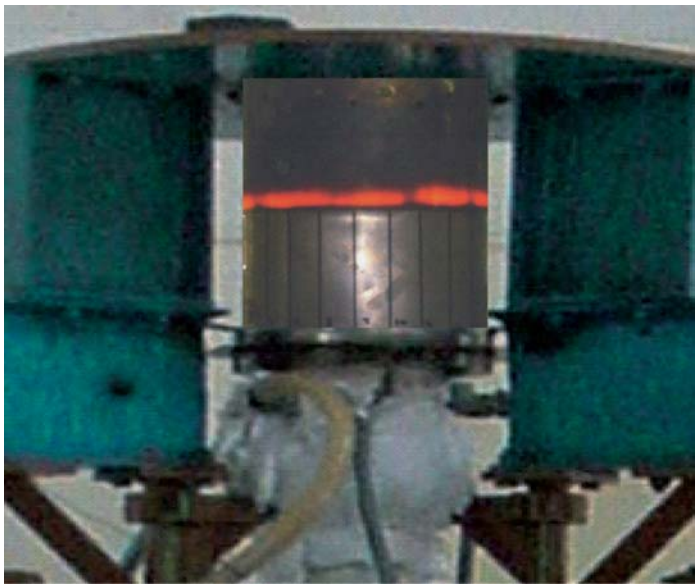

Fig. 3. Simulation of ratchetting in the 1/40th scale model of main vessel

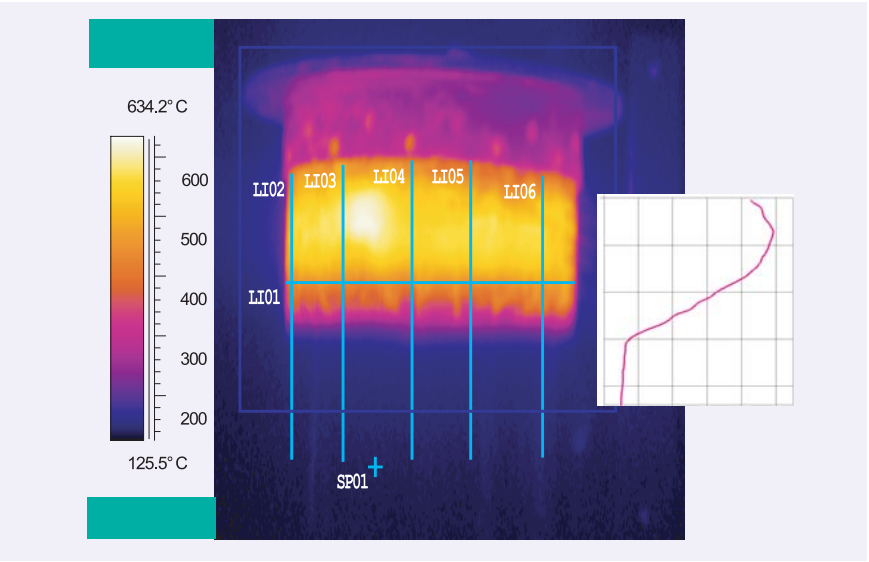

Fig. 4. Thermal imaging display of moving axial temperature gradients

temperature gradients. The gradient is made to oscillate axially to simulate the moving temperature gradient as in the case of sodium free level. An infrared thermal imaging system is used to map the moving thermal gradients and vertical thermal profiles in the region of interest (Fig.4). The maximum temperature is ~923 K, and the temperature distribution along the circumferential direction is found to be nearly uniform.

Based on state-of-art analysis and experimental simulation, it is demonstrated that the ratchetting strains developed in the main vessel are within the acceptable limits.

3.3 Thermal Hydraulic Analysis of Spent Fuel Subassembly during Transportation from FBTR to Reprocessing Facility

Irradiated fuel subassemblies (FSA) of FBTR are removed from the reactor core after achieving the required burn-up, and at 160W decay power, they are sent to the reprocessing facility for extracting the fissile material. During transportation, the FSA will be loaded inside a leak tight pot filled with argon gas. The pot containing the irradiated fuel will be loaded inside a lead shielded cask. The cask has been designed to carry one FSA. The removal of decay heat from the spent FSA is important, which would otherwise lead to fuel pin clad failure due to the high temperature. The temperature distribution in the FSA, pot and cask was estimated assuming natural convection in the cask. The analysis was carried out using the PHOENICS 3.5 fluid dynamics package. The objective of the analysis is to see if any forced cooling of the pot is required during transportation.

The thermal hydraulic analysis was carried out to determine the maximum temperature of clad. The active height of the fuel is 320mm. Only radial heat transfer has been considered. The analysis was carried out in three steps. First the temperatures of the cask, pot and FSA sheath were found out. For this, a 180° symmetrical sector of the cask loaded with FSA and pot was modeled. The entire assembly is modeled in the horizontal position, as the pot would be transported in this position. The air inside the cask is assumed static. The K-ε model with buoyancy effect is used. The heat flux on the FSA sheath surface is 3014 W/m^2. Heat transfer to the ambient as well as within the cask is by radiation and natural convection. The natural convective heat transfer coefficient and the ambient temperature are the boundary conditions at the outer surface of the cask. Conduction and radiation heat transfers are considered in the annular space between the pot and the FSA sheath. The temperatures of the FSA sheath, pot and cask were obtained by running the solver for momentum and energy. This completes the first part of the analysis. The second step of the analysis is to determine the individual fuel pin clad temperature. The FSA consists of 61 fuel pins of 5.1mm diameter and 531.5mm length. To obtain the temperature profile within the FSA, a 60°symmetrical sector of the FSA sheath with five rows of fuel pins is modeled. The fuel pins with a volumetric heat generation of 4 x 10^5 W/m^3 is the heat source. The FSA sheath temperature with emmisivity of 0.2 is the other boundary condition. Only radiation and conduction heat transfer between the fuel pins is considered. The radiative heat transfer between the fuel pins of alternate rows is also accounted for in this model. The emissivity of fuel pin surfaces with sodium deposits was taken as 0.2, while the emissivity of the remaining stainless steel surfaces was taken as 0.6. The temperatures of the fuel pin clad in all the five rows are thus obtained. The third step of the analysis is to evaluate the average temperature and the

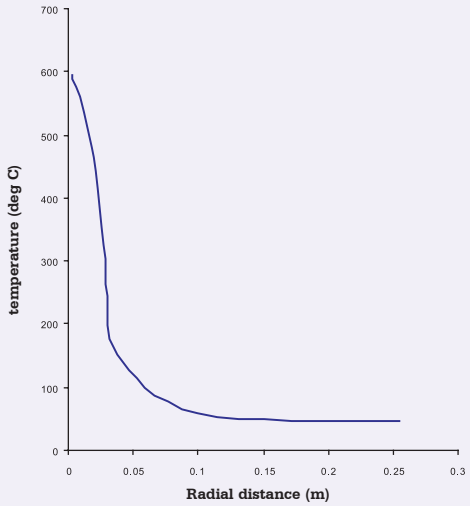

Fig. 1. Radial temperature profile at the middle of the FSA.

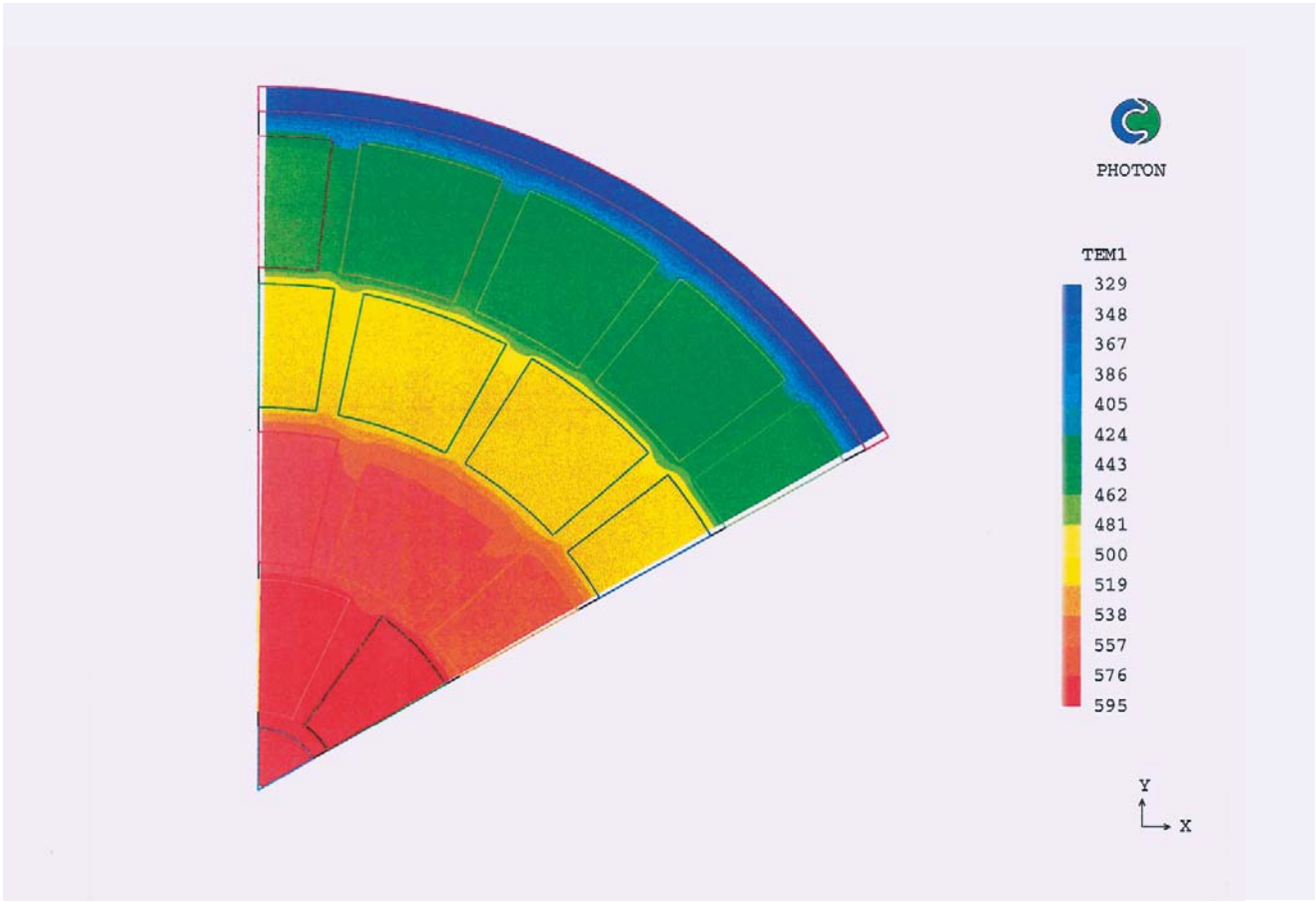

Fig. 2. Temperature contour in a symmetrical sector of FSA.

corresponding pressure of argon in the pot. For this, the FSA sheath, pot and cask were modeled in r-z coordinates. Radiation and natural convection are considered in the space between pot and cask. The temperature of argon gas at 11 grid points in the annular space is obtained from the result file. The volumetric average gas temperature is finally calculated. The corresponding absolute argon pressure is also calculated using the ideal gas equation.

After the first step of the analysis, the maximum temperatures of the FSA sheath, pot and cask were found to be 329, 190 and 48°C respectively. Fig.1 shows the radial temperature profile at the middle of the FSA. The FSA sheath temperature of 329 °C as obtained after the first analysis was provided as the boundary condition in the second part of the analysis. The maximum temperature of the central fuel pin clad without forced cooling was found to be 595°C. Fig.2 shows the temperature contour inside the FSA. The bulk temperature of Argon in the space between the FSA sheath and pot was estimated to be 94°C after taking both conduction and radiation heat transfer between the FSA sheath and pot. The corresponding gauge pressure in the pot is estimated to be 0.17 bar. Since the values obtained for the central fuel pin clad temperature and the argon pressure in the pot are below the permissible limit of 700°C and 0.4 bar respectively, it can be concluded that at this decay power, forced cooling is not required during transportation of the spent FSA.

3.4 Thermal Hydraulic Investigation of Decay Heat Removal System

Heat continues to be generated due to the radioactive decay of fission products, even after reactor shutdown. This heat, referred to as 'decay heat' has to be removed continuously to ensure that the temperatures of structural components and sodium are within safe limits even under a worst design basis events like a station blackout. In the PFBR, this is carried out with the help of a passive system called Safety Grade Decay Heat Removal System(SGDHRS). This takes heat directly from the hot pool and releases it to air without any external power supply requirements.

SGDHRS consists of four totally independent circuits with two diverse designs (Type-A and Type-B). Each circuit consists of a sodium to sodium heat exchanger (DHX) and a sodium to air heat exchanger (AHX) connected by an intermediate sodium circuit. In order to get natural circulation flow in the intermediate circuit, the AHX is located at a higher elevation (42 m) compared to the DHX. A tall air stack provides the driving force for the natural convection airflow through the AHX.

Both types (A & B) of circuits are designed with one-dimensional models and their heat removal capacity is confirmed with detailed multi-dimensional analysis using the general purpose CFD codes PHOENICS and STAR-CD. The DHX (type-B) is a 'U' tube type two-pass heat exchanger. Intermediate sodium enters

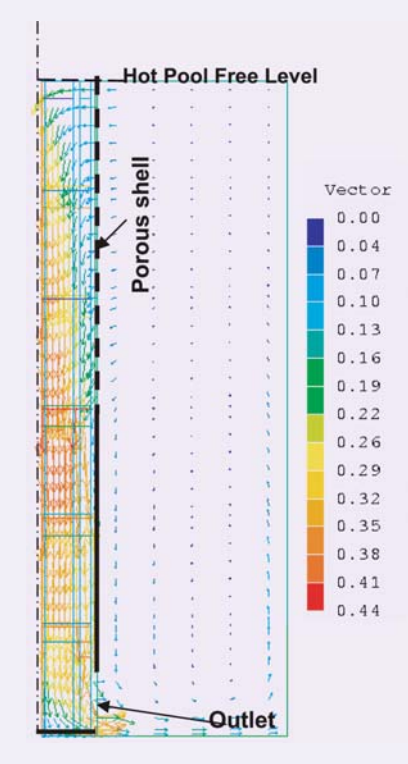

Fig. 1. Sodium flow distribution in DHX-B

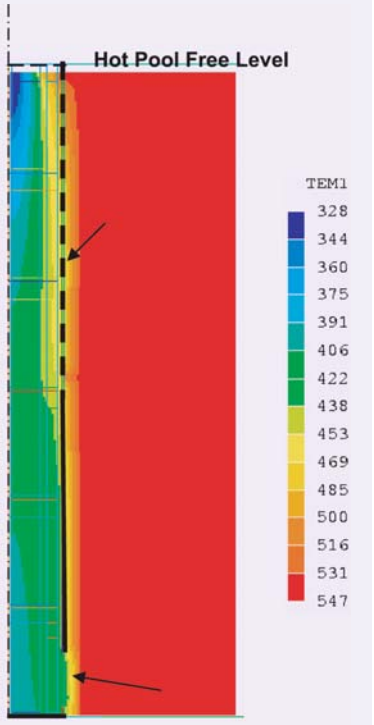

Fig. 2. Temperature distribution in DHX-B

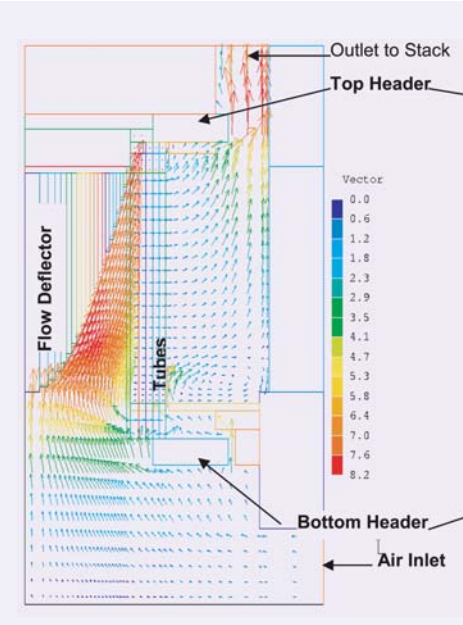

Fig. 3. Flow distribution in AHX

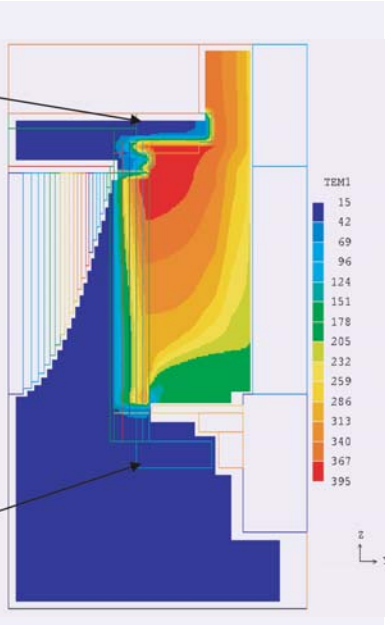

Fig. 4. Temperature distribution in AHX

inner legs of the tubes and comes out through the outer legs. Primary sodium flows over the tubes. Primary sodium flow and temperature distributions in the DHX are shown in Fig. 1 and Fig. 2 respectively.

The AHX (type-B) is a vertical tube type heat exchanger with sodium flowing inside the tubes and air flowing over them. Air flow and temperature distributions are shown in Fig. 3 and Fig. 4 respectively. Similar analyses are carried out for type-A DHX and AHX also. With these studies it is confirmed that each circuit of SGDHRS can remove the 8 MW with hot pool at 820 K with sufficient margin.

3.5 Studies on Sodium - Graphite Interaction

Graphite is one of the candidates for thermalising fast neutrons in order to monitor their flux at the detector location on the cover plate of a fuel sub-assembly in the fast reactor. Since graphite will be positioned on the top of the fuel pellet stack, it would come into contact with liquid sodium in the event of a cladding rupture. Chemical interactions between liquid sodium and graphite need to be considered prior to the final choice of graphite as the thermalizer material. Although graphite does not react with pure sodium to form a stable compound, it is reported to form intercalation compounds with oxygen rich sodium at 470°C resulting in the expansion of its lattice by about 60 %. Industrially manufactured graphite is known to have occluded gases (viz. oxygen and nitrogen) and the quantity of these occluded gases depends upon the density of the graphite. Presence of the occluded oxygen can also result in the formation of these intercalation compounds. To understand the effects of chemical compatibility between high purity sodium and commercial graphite, graphite samples of different densities were equilibrated with liquid sodium at 550°C and the integrity of the graphite specimens were investigated by radiography. Feasibility of removing the occluded gases from the graphite samples by vacuum degassing at elevated temperatures was also investigated and the degassed samples were also employed for studying their chemical compatibility with liquid sodium.

1(a) Before degassing & immersion in Na

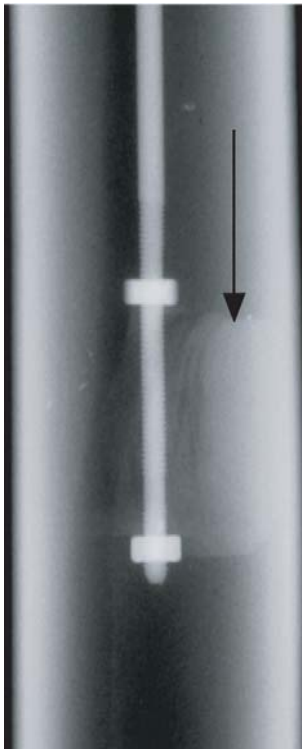

1(b) Degassed & heated in sodium at 550°C for 24 h

Fig. 1. (a) Digitized radiographic images of the graphite pellet of density 1.70 g/cc before degassing & immersion in Na (b) after degassing & heated in sodium at 550°C for 24 h (1(a) shows the intact pellet ; in 1(b), the arrow shows the broken pellet sticking with the guide rod).

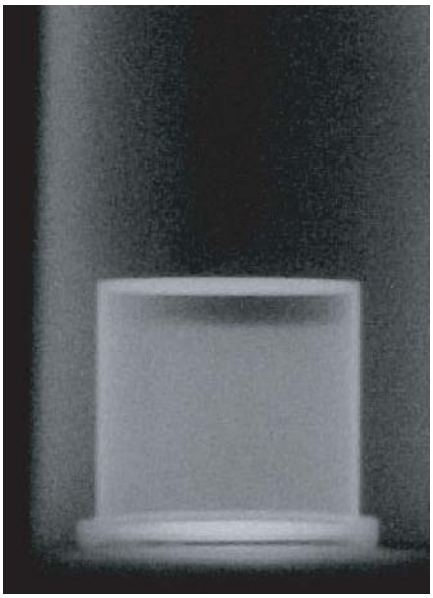

2(a) after 120 h

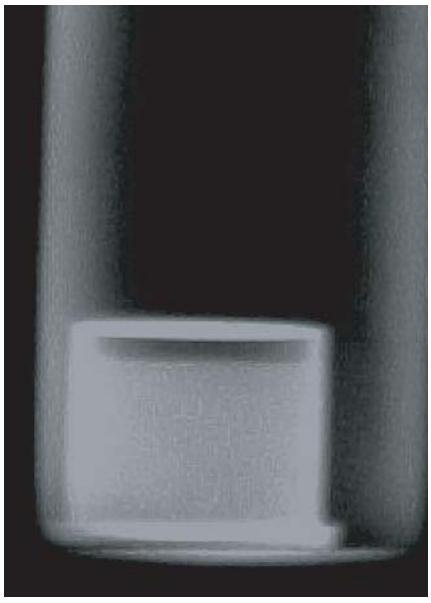

2(b) after 240 h

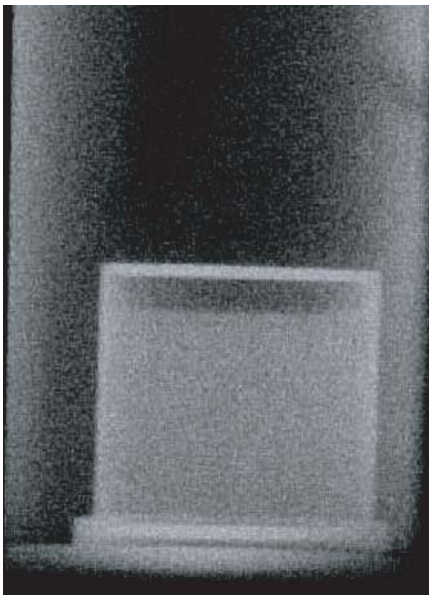

2(c) after 360 h

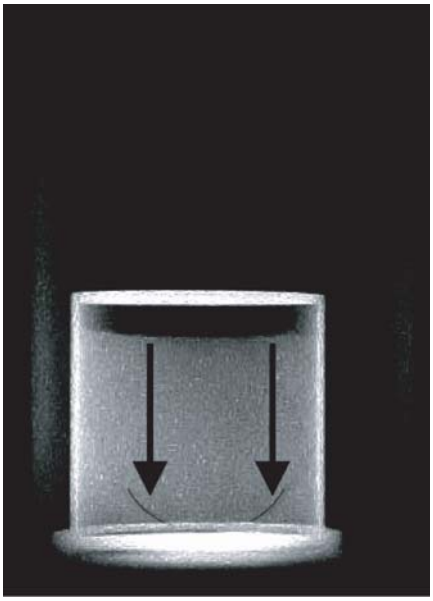

2(d) after 480 h

Fig. 2. (a-d) Digitized radiographic images of the encapsulated graphite pellet of density 1.84 g/cc heat-treated at 550 °C after degassing at 1000°C for different durations (In 2(d), the arrows indicate the cracks in the graphite rod).

Graphite specimens of different densities (1.7, 1.8 and 1.84 g/cc - total metallic impurity content < 500 ppm) in the form of rods were employed for the chemical compatibility studies. Two different degassing conditions were employed to study the removal of the occluded gases: 1) under a vacuum of 10^{-4} torr at 650°C and 2) under a vacuum of 10^{-4} torr at 1000°C. Analysis of the occluded gas in the as-procured as well as the degassed graphite samples were carried out to study the effectiveness of the degassing conditions. The analytical results showed that for the samples treated under a vacuum of 10^{-4} torr at 650°C, the occluded oxygen reduced by nearly 50 % in graphite samples of density 1.84 g/cc density (610 ppm) while it remained nearly the same in samples of lower density (400 ppm). On degassing at 1000°C, concentration of occluded oxygen reduced in all samples although complete removal could not be achieved. Concentration of nitrogen was 290 ppm in the as-procured graphite sample of density 1.84 g/cc while it reduced to ~ 15 ppm on degassing at 1000°C. The as-procured samples of densities 1.7 and 1.8 g/cc had ~ 15 ppm of occluded nitrogen in them. All these results indicated that the extent of removal of occluded gases depended upon the density of the graphite samples and the chosen degassing conditions. The results also indicated that the complete removal of occluded oxygen would not be feasible under the chosen conditions.

Interaction of the as-procured as well as the degassed graphite samples with sodium was studied by taking the sample in the form of a rod and directly immersing it into high purity liquid sodium taken in a stainless steel vessel followed by heating the assembly to 550°C. In addition to these experiments, the graphite samples which had been degassed at 1000°C under vacuum were equilibrated with high purity sodium by

encapsulating the sample in a 316L stainless steel capsule with dimensions to be in the same proportion as those in a typical PFBR fuel pin. The capsule also had pin holes for effecting a restricted sodium entry so that conditions in a typical failed fuel pin could be simulated. After a designated period of heating in sodium at 550°C, the experimental assembly was cooled to room temperature and the integrity of the graphite sample was assessed by radiography.

The experimental results indicated that the as-procured graphite samples of density 1.7 g/cc disintegrated while directly immersing in sodium and heating for 24 h at 550°C. Graphite samples of densities 1.7 and 1.8 g/cc which were degassed at 1000°C and heated at 550°C by directly immersing in sodium also lost their integrity after 24 h (Fig. 1), while the sample with 1.84 g/cc when subjected to identical experimental conditions was intact till 144 h. Subjecting the latter sample to the chosen experimental conditions for a period > 144 h resulted in the loss of its integrity. Experiments carried out by encapsulating the graphite samples followed by immersing and heating them in sodium showed that they were intact up to a duration of 240 h irrespective of their densities (Fig. 2). Beyond this duration, encapsulated samples also failed. These results show that the samples disintegrate irrespective of the degassing process and even after an encapsulation indicating that graphite cannot be used in sodium systems.

3.6 Experimental Evaluation of Pool Fire Suppression Performance of Sodium Leak Collection Tray in Open Air

In the event of sodium leakage from heat transfer circuits of fast breeder reactors (FBRs), liquid sodium catches fire in ambient air leading to production of flame, smoke and heat. One of the passive fire protection methods involves immediate collection of the leaking sodium into a sodium hold-up vessel (SHV) covered with a sloping cover tray (SCT) having one or three drain pipes and one vent pipe. As soon as the liquid sodium falls on the sloping cover plate under gravity, it guides the sodium through drain pipes into the bottom tray in which self-extinction occurs due to oxygen starvation. This sodium fire protection equipment called leak collection tray (LCT) works without the intervention of an operator and an external power source. A large number of LCTs are strategically arranged under the sodium circulating pipe lines in the FBR plants to serve as passive suppression devices.

Fig. 1. Experiment on a typical Leak Collection Tray

The PFBR leak collection tray made up of 5mm thick mild steel, consists of a 250 kg capacity SHV (lower part), of 1200 mm × 500 mm × 500 mm and a SCT (upper part), with two sloping plates forming a 20^0 V - shaped cover on SHV . The overall size of the SCT is 1200 mm × 1000 mm × 280 mm and out of the 280 mm height, 170 mm is with 20° slope. The upper part is provided with three drain pipes on the centerline of SCT, one at center and the other two at 400 mm distance on either side of it. The drain pipes are of 50 NB

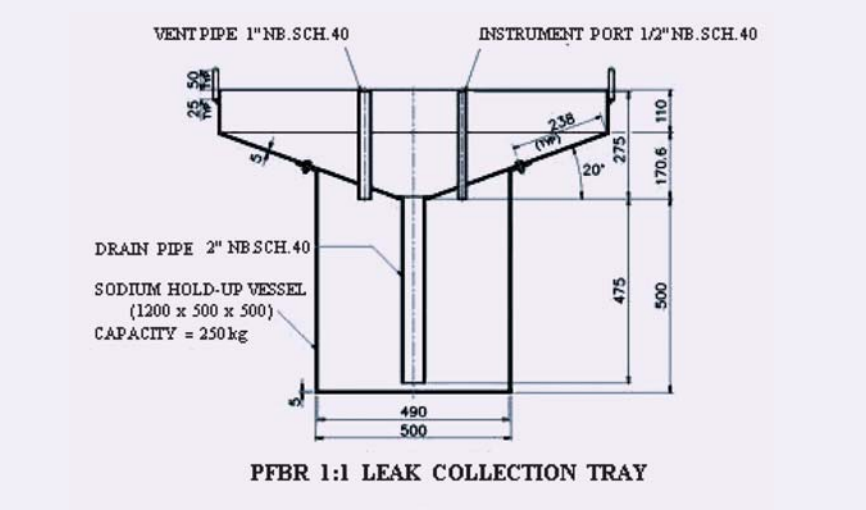

Fig. 2. Schematic sketch of LCT

and extend up to 20 mm above the bottom surface of the holdup vessel. One vent pipe of 25 NB and instrument port of 15 NB is provided on the sloping surface of the SCT. The SCT is firmly fixed to the holdup vessel with fasteners and gasket to prevent air entry into the system. The photograph of the LCT is given in Fig1. and schematic sketch is given in Fig 2.

Sodium leakage in the steam generator building of PFBR is classified into three categories based on the extent of leak and frequency of occurrence (Table 1). The leak collection trenches in the PFBR SG building are suitably compartmentalized and design provisions have been made to collect the leaked sodium into a tank through pipe lines with fusible plugs. However, for category 2 leaks, the compartments are sized to retain all the sodium that leaks within itself also.

In SED four tests with 40 kg sodium at 550^0 C (MS-1 to MS-4) were carried out. Out of these four tests, two (MS-1 and 2) were conducted with LCT having three drain pipes and rest with one pipe. In each experiment, nearly 40 kg of hot liquid sodium at 550 °C was discharged on the LCT in the open air. Continuous on-line monitoring of the temperature at strategic locations (~ 28 points) was carried out. Colour videography was employed for taking motion pictures of various time-dependent events like sodium dumping, appearance of flame and release of smoke through vent pipes. After self-extinction of the sodium fire, the LCT was allowed to cool overnight in an argon atmosphere. Solid samples of sodium debris in the SCT and SHV were collected by a manual core drilling machine. The samples were subjected to chemical analysis for determination of unburnt and burnt sodium. The sodium debris removed from SCT and SHV were separately weighed. The important observations are given in Table 2.

Table 1. Classification of sodium leakage

Amount of leak	Frequency of occurrence	Category
Up to 2 t	> 10^{-2}/reactor year	2
2 t – 10 t	<10^{-2}/reactor year > 10^{-4}/reactor year	3
10 t – 140 t	<10^{-4}/reactor year > 10^{-6}/reactor year	4

Table 2. Summary of important test results

Main Parameters	Test Number			
	MS-1	MS-2	MS-3	MS-4
Sodium collection efficiency(%) in SHV	31	63	96	88
Smoke release fraction (% mass)	21.4	6.5	0.6	5
**Smoke reduction factor	2.0	6.5	75	9
Combustion efficiency (%mass)	61	25	4	10
*Pool fire suppression factor	1.2	3.2	18	7

*** Typical combustion efficiency of open sodium pool in ambient air = 73 %**
****Typical sodium release fraction of open sodium pool in ambient air = 42 %**

Sodium drained into the SHV to the extent of 88 to 96 % for LCT with one drain pipe whereas the LCT with three drain pipes exhibited a low collection efficiency of 31 to 63 % due to freezing of sodium, resulting in plugging of drain pipes. This can be explained by the fact that for the fixed mass of hot liquid sodium dumped on LCT, the sodium is distributed into three drain pipes during gravity driven draining from upper SCT to lower SHV leading to lower draining rate per drain pipe than LCT having one drain pipe. As the draining rate decreases, freezing rate of hot sodium in each drainpipe

increases due to conductive heat transfer from the slowly flowing sodium to the pipe, thereby reducing the sodium temperature below its melting point in the vicinity of the pipe tip.

The large amount of sodium that remained on the surface of SCT had undergone prolonged burning in open air, thereby increasing combustion and smoke release fraction for the LCT with three drainpipes. Hence it is inferred that the LCT with one drainpipe gives better performance in passively suppressing sodium pool fire than that with three drainpipes.

Optimization of the LCT is planned to be carried out based on more experimental and theoretical model studies.

3.7 Investigation of Hydrogen Explosion in Steam Generator Building

Secondary sodium at 798 K flowing on the shell side of the steam generator is used to generate steam in FBRs. Failure of tube in the steam generator may lead to sodium water reaction which produces heat and other reaction products, viz., NaOH, Na_2O, NaH and hydrogen. These reaction products cause corrosion and erosion of steam generator shell leading to a hole/crack on it. Through this opening, hydrogen, one of the reaction products enters the steam generator-building. To ensure the integrity of the building structure from a possible explosion due to this accidental release of hydrogen, easily breakable vent panels are to be provided. The steam generator building volume is vertically divided into 5 separate compartments floor-wise. Pressure rise in any of the compartments will be communicated to the whole volume through a grilled opening provided at each floor for ventilation of the steam generator building.

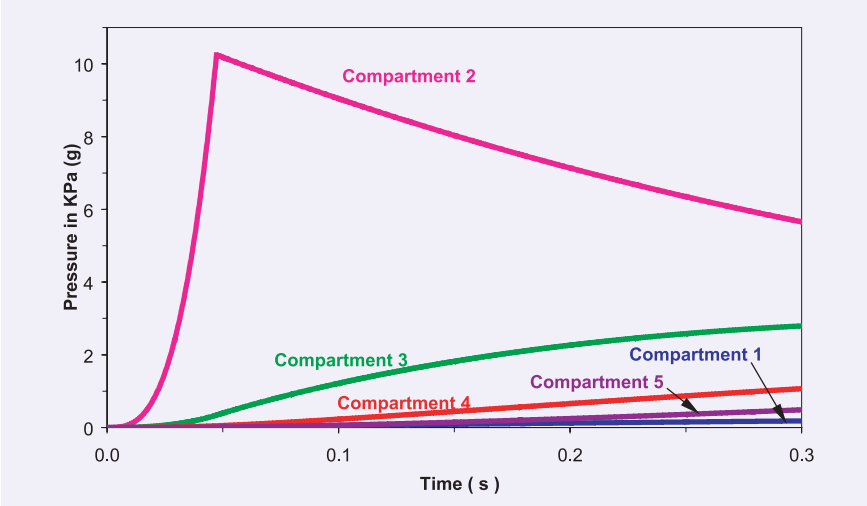

Fig. 1: Pressure rise due to hydrogen vapor cloud explosion

Hydrogen explosion in the steam generator building is a low probablity event because care has been taken at the design and fabrication stage to reduce the possibility of a sodium water reaction. Selection of modified 9Cr-1Mo material for tubes to avoid stress corrosion cracking and elimination of tube-to-tube weld to avoid leak through welds etc., are some of the salient design features. On detection of sodium water reaction by the leak detecting system, isolation valves on the steam side as well as on the water side isolate the steam generator and prevent further reaction. So the possibility of hydrogen explosion can only be analyzedkeeping in mind that this is a fictitious case.

Two sceraries are envisaged. In the first case, it is assumed that the hydrogen leak is accumulated until the concentration reaches the lower limit of explosion and is ignited. With the assumption of local volume of burning and using the acoustic approximation, the wave front pressure at any location can be determined. If the local concentrated volume is small compared to the steam generator building volume, then the method of passing

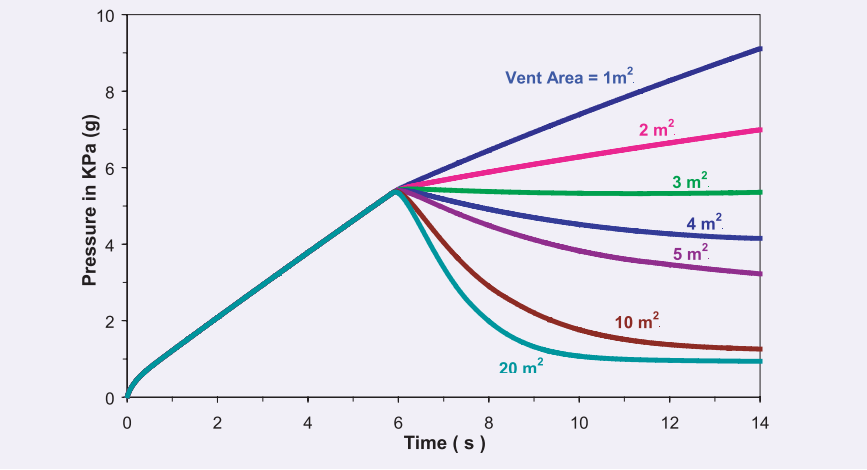

Fig. 2. Pressure rise due to hydrogen burning

shock wave pressure can be used for the approximation of pressure values in the volume far away from the local explosive mixture volume. The maximum pressure peak obtained is given in Fig.1. Here the pressure peak is reduced by the flow of a certain amount of air to the adjacent compartment, which pressurizes the other compartment. The assumption of hydrogen filling in the entire volume of the compartment that reaches the stoichiometric condition and then burning may not be a realistic situation, because, the jet of hydrogen contains traces of sodium. Sodium when comes in contact with air burns immediately which will lead to continuous burning of hydrogen. Hence a scenario of continuous burning of hydrogen is considered for vent area estimation.

In the second case, hydrogen generated as the result of a design basis leak (13 kg/s) for sodium water reaction is assumed to be discharged as a jet in air. The air available in the compartment aids the combustion of hydrogen. Under this transient condition, the equation for conservation of energy and species are solved numerically. The partial pressures of reactants at the end of every time step is taken for determining the pressure developed inside the steam generator volume. For various vent areas the calculated pressure transients are plotted in Fig. 2. It can be seen from the figure that for vent area greater than 4 m^2, the pressure reduces after the vent opening. Since hydrogen explosion in the steam generator building is a very rare event it is decided to have a vent panel of 4 m^2 area.

3.8 Development of Chemical Decontamination Technique for Fast Reactor Primary System Components

The major source of contamination of the primary circuit of sodium cooled fast reactor other than fuel pin failure is the activated corrosion products. Among the important activated corrosion products, ^{54}Mn is the major contributor to the radioactivity burden as it is preferentially released from the core surface and migrates to the cold leg. At the operating temperatures, this radionuclide penetrates into the structural material owing to its high diffusion coefficient in stainless steel.

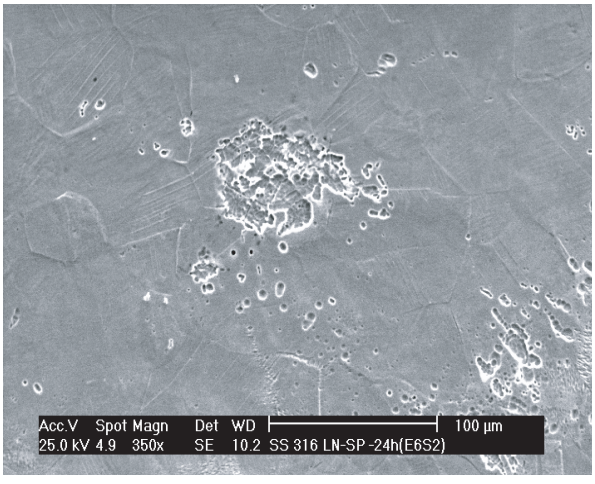

Fig. 1. SEM Microstructure of SS 316LN in DC1 for 24 h

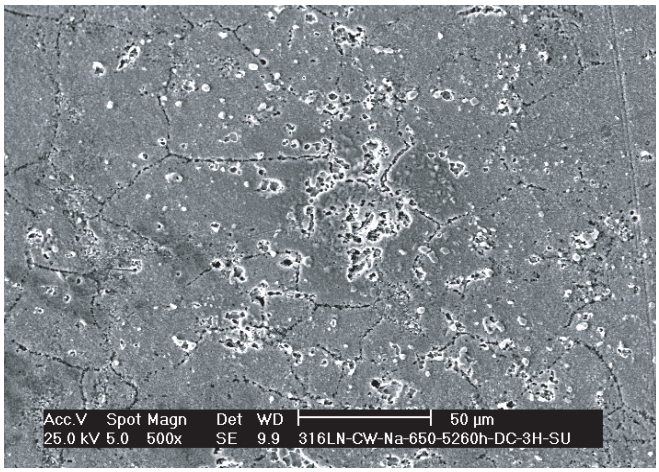

Fig. 2. SEM micrograph of Na exposed specimen in DC1 for 3 h

This renders component decontamination procedures difficult and removal of a few micron thick layers from the metal surface is required to achieve a fairly good decontamination. A knowledge of the diffusion coefficient of the radio-isotope of interest (^{54}Mn) in structural and clad materials helps in estimating the extent of material removal for good decontamination of the component. Hence the diffusion coefficient of ^{54}Mn in AISI type SS 316LN was determined using tracer technique. The penetration profile indicates the extent to which the material is to be removed from the surface for effective decontamination. Decontamination is required prior to maintenance where components are reused and also for components prior to disposal. The selection of a decontamination technique for primary components of fast reactors requires knowledge about the type of contaminant and their operation history. The present study was taken up at Chemistry Group to develop a suitable chemical decontamination technique for those fast reactor components, which can be reused. In these studies, a chemical decontamination process using a mixture of H_2SO_4 and H_3PO_4 is applied to AISI type SS 316LN, which is the candidate structural material for PFBR. The requirement of the process is its ability to remove the contaminant without impairing the mechanical property of the structural material. To study the effect of the decontamination formulation on the chemical removal of the surface layer thereby getting rid of the radioactive species without modifying the microstructure and hence the mechanical properties of the material, a number of commercially procured AISI SS 316LN rectangular sheet specimens were exposed to various compositions of H_2SO_4 and H_3PO_4 at 333 K for 6 to 24 h with continuous argon purging. Pitting of the specimen surface was observed to increase with increasing H_2SO_4 content and longer exposure time as shown in Fig. 1. To simulate the conditions of the primary components of fast reactors, which are in sodium service, decontamination experiments were carried out with specimens equilibrated in sodium at 923 K for several thousand hours. The sodium exposed specimens, cleaned free of sodium were treated in the decontamination formulation of H_2SO_4 and H_3PO_4 as described above. The different compositions used

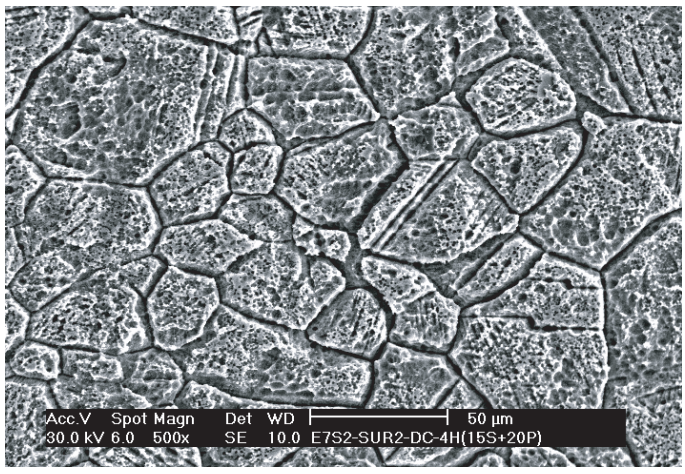

Fig. 3. SEM micrograph of Na exposed specimen in DC2 for 4 h

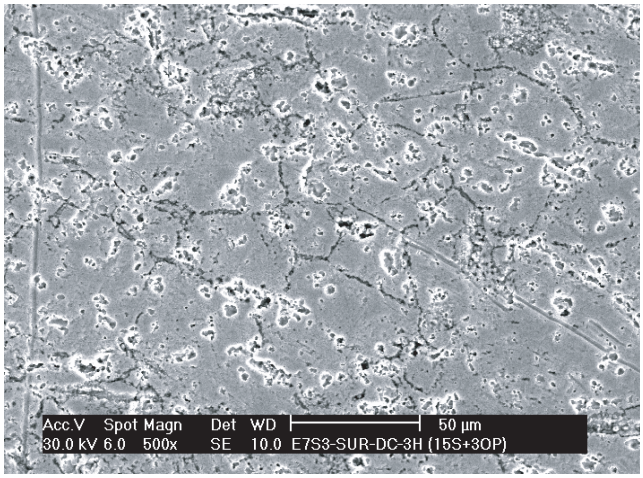

Fig. 4. SEM micrograph of Na exposed specimen in DC3 for 3 h

were (i) 12.5 gL^{-1} H_2SO_4 and 30 gL^{-1} H_3PO_4 (DC1), (ii) 15 gL^{-1} H_2SO_4 and 20 gL^{-1} H_3PO_4 (DC2) and (iii) 15 gL^{-1} H_2SO_4 and 30 gL^{-1}. H_3PO_4 (DC3). The surface of the specimens was characterised by SEM. It was observed that the specimens exposed to a typical composition of 12.5 gL^{-1} of H_2SO_4 and 30 gL^{-1} of H_3PO_4 revealed no appreciable structural degradation except signs of slight pitting corrosion as shown in Fig. 2. Exposure to higher H_2SO_4 content (DC2) revealed grain boundary attack as shown in Fig. 3 which could lead to decohesion of the grains. However, for the same H_2SO_4 content as in DC2 with increase in H_3PO_4 concentration (DC3), grain boundary attack is minimized and mild pitting corrosion is observed as shown in Fig. 4. It was also observed that pitting corrosion was predominant in sodium-exposed specimen than in non-exposed specimens for the same composition of the acid and for the same duration of exposure in the specific decontamination formulation. This is due to the fact that on exposure to sodium for a long duration of time, the initially austenitic surface gets depleted in nickel and chromium and tends to become ferritic in nature, which is highly prone to corrosion attack by the acid. Considering the fact whether the component is for reuse or not and also considering the operation history of various components, it can be stated that one single composition of decontamination formulation cannot be applied to all types of components. A suitable composition of the correct decontamination formulation needs to be chosen depending on the requirement, to achieve a higher decontamination factor and also to retain the mechanical integrity of the material.

3.9 Development of Environmental Gamma Dose Logger (EGDL) using State of the Art Technology

Each nuclear power plant site is required to be provided with an environmental monitoring network consisting of several monitoring stations around the power plant (i) to ensure that the radiation levels in the site boundary are within the regulatory limits and (ii) to provide early detection of excess release in case of an untoward incident. The data from these stations along with the site meteorological data provide a quick estimate of the source term, an obviously vital information for the emergency response/management. Further, the data also provides a measure of validation for the computer codes used for atmospheric dispersion modeling, especially regarding site characteristic input parameters.

As part of the Continuous Environmental Radiation MOnitoring Network at Kalpakkam (CERMON), eight numbers of commercially available Gamma Tracers have been procured and installed at various locations and the data being archived regularly. These units are hermetically sealed battery operated instruments that can work under field conditions reliably. However, the units have to be sent to the suppliers for replacement of batteries,

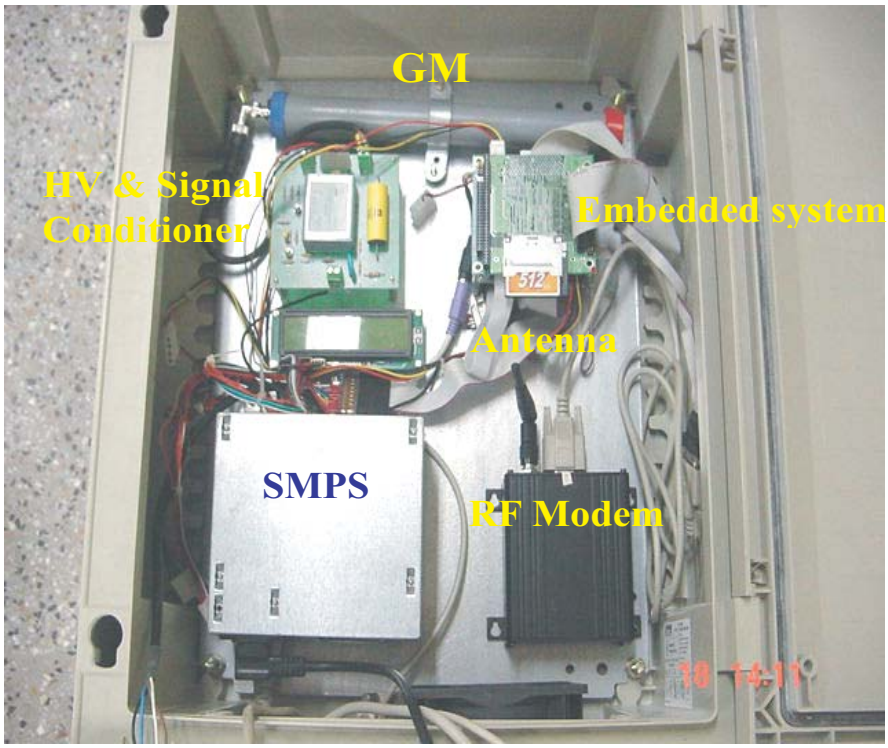

Fig. 1. Environmental Gamma Dose Logger

Fig. 2. Typical CERMON Station

detector and maintenance etc. A state of art Environmental Gamma Dose Logger (EDGL) based on an embedded system with energy compensated GM as a detector was developed at RSD. The same has been incorporated in the CERMON network.

The EGDL system is shown in Figs. 1 and 2. The system is based on the energy compensated halogen quenched GM model 7807 of M/s LND. The 500V operating voltage of the GM is derived from a DC-DC converter working on a 12 volts dc input. The on-line data is displayed on a 16x2 LCD module with real time information and dose rate. The data archival in the field is in a compact flash card and real time data access is through RF communication. The battery-operated unit is convenient to be installed in locations where mains power is not available. The measuring range is 20nGy/h to 100mGy/h. Two units of mains operable have been installed at two locations. The acquired raw data of counts is converted to engineering units to give the dose rate. The counts are validated, processed and written in appropriate files in the specified format using software coded in VB. The software performs various tasks such as engineering conversion, derivation of averages for 15 minute, 1 hour, standard deviation, minimum and maximum values with real time stamp besides archiving the data in a compact flash card. The flash card can be very easily retrieved from the field for data transfer in the central facility. The typical data for a day at hourly average storage is about 2kB and a flash card capacity is 512MB.

In addition, a real time point to point data link has been established using a high performance wireless modem. The operating frequency is 2.4 GHz in the ISM band; this frequency-hopping spread-spectrum module is capable of providing reliable wireless data transfer between any types of equipment, which uses an asynchronous serial interface. The main advantage of this modem is that it can be configured using AT modem commands to meet the requirements of an application. A network of gamma measuring systems using data links through Ethernet, GSM modems and RF links has been planned for implementation.

Novel features of this indigenous development are

- ❖ The hardware is designed around readily available embedded systems
- ❖ The software is totally developed in house and modifications can be done easily.
- ❖ The system has all the features of a commercial system with easy data archival/ transfer using compact flash cards.
- ❖ Real time access to data through RF link.

3.10 Biomarkers of Radiation Quality and Dose-rate

Biological dosimetry is a method of measuring the amount of ionizing radiation received by an individual using biological material. This type of dosimeter is useful when an individual is accidentally exposed and no physical dosimetry is available, or if the reading from a physical dosimeter is in dispute. However, occupational workers engaged in the nuclear industry are usually exposed to chronic low doses from gamma radiation or alpha particles (nuclear reprocessing), the effects of which are very different from exposures received in accidental conditions. Radiation protection requires estimation of risk factors for such exposures. This involves determining a realistic Dose and Dose-Rate Effectiveness Factor DDREF, a measure of the diminished biological effect on reducing dose-rate; and an accurate Relative Biological Effectiveness (RBE) factor, a measure of how damaging a given type of radiation is when compared to an equivalent dose of X or gamma rays.

Biomarkers of Alpha Exposures: High LET radiations such as alpha

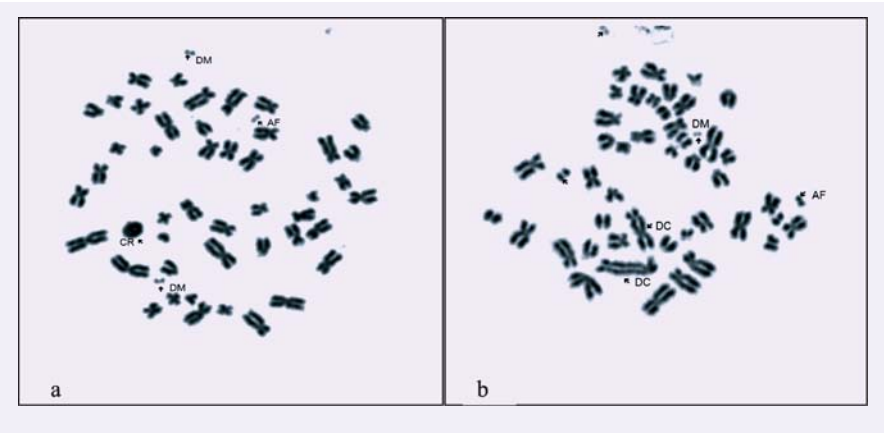

Fig. 1. a. Metaphase containing centric ring (CR) and double minutes (DM)-signatures of alpha exposure. b. Metaphase containing multiple aberrations such as dicentrics (DC), acentric fragments (AF) and DM

particles produce closely spaced energy depositions and thus chromosome breaks. At equal doses, high LET radiation is much more likely to produce multiple breaks and cluster damages within a given chromosome than gamma rays, and hence can serve as "fingerprints" of radiation quality for determining RBE.

Heparinised whole blood collected from healthy individuals was exposed to various concentrations of radon gas for 3 hours in a shaker incubator maintained at 37°C. Radioactivity content of the radon gas was estimated using a Lucas cell. Control samples were sham exposed. Chromosome preparations were made from the whole blood cultures using standard procedures. Metaphase spreads were captured and aberrations such as dicentric chromosomes, excess acentric fragments, centric and acentric rings, double minutes, chromatid breaks etc., induced by radon exposure in blood lymphocytes were scored (Fig.1 a & b). Regression analysis showed a significant increase ($P< 0.005$) in dicentric yield with increasing concentrations of radon. Yields of dicentrics, acentric fragments, centric and acentric rings and double minutes were found to be distributed in a non-Poisson manner.

DDREF: Since DNA damage and repair at high dose rates are different from those produced at low dose rates, a dose-response curve which is constructed for high dose rate exposure may not be useful for estimating doses due to low dose-rate exposures. It has been shown that the spectrum of mutations induced at the hypoxanthine guanine phosphoribosyltransferase (*HPRT*) locus can serve as an indicator of dose-rate and radiation quality. In order to measure the mutant frequency at the *HPRT* locus, a T lymphocyte cloning assay has been established at IGCAR.

Lymphocytes isolated from blood samples of normal healthy individuals were exposed to varying doses of gamma radiation (1- 4 Gy) at low (0.0014 Gy/ min) and high (0.85 Gy/ min) dose-rates in vitro. From this study, it was observed that the dose dependent increase in *HPRT MF* significantly differs at low and high dose-rates. Regression analysis of the *HPRT* mutant frequency and slopes at high and low dose-rates respectively yielded a DDREF value of 3.4 (Fig.2). This study showed that for very low dose-rate exposures typically encountered by occupational

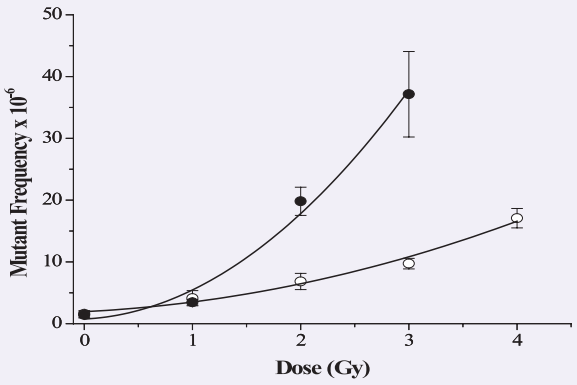

-●- High dose-rate (0.85 Gy/min), -○- Low dose-rate (0.0014 Gy/min)

Fig. 2. Dose response curves for HPRT mutant frequency in blood lymphocytes exposed to high and low dose-rate of gamma radiation giving rise to a Dose Dose-Rate Effectiveness Factor (DDREF) of 3.4.

workers, DDREF factors can exceed the ICRP recommended value of 2.

Further, analysis of the mutation spectrum at the HPRT locus revealed specific signature events to differentiate low and high dose-rate exposures. Genomic DNA obtained from each mutant colonies were amplified using the multiplex Polymerase Chain Reaction (PCR) technique. The mutation spectrum obtained at low dose-rate showed a significantly higher induction of partial deletions (compared to the high dose-rate) exposure suggesting that the mutation spectrum can be used to characterise unknown human exposures.

The above studies are aimed to develop simple and accurate assays to estimate risk factors and "fingerprints" of specific radiation exposures.

CHAPTER 4

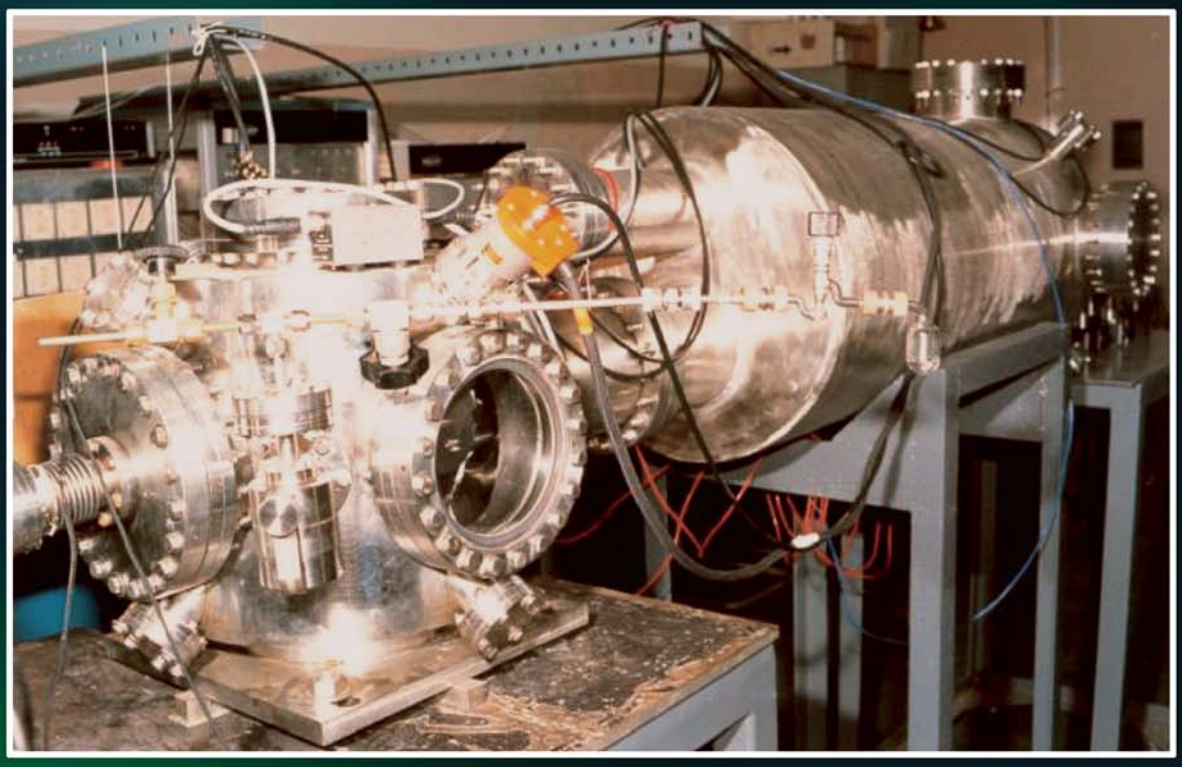

Fuel Cycle Activities

4.1 FBTR Fuel Reprocessing - 100 GWd/t Burnup Fuel Reprocessed

Reprocessing of the 100 GWd/t burnup FBTR mixed carbide fuel has been successfully demonstrated in the Lead Mini Cell (LMC). This facility, commissioned in late 2003, has reprocessed carbide fuels of progressively increasing burn-up, that is, 25, 50 and 100 GWd/t. With the demonstration of very high burnup high-Pu bearing mixed carbide fuel, an important milestone in closing the fast reactor fuel cycle has been reached.

In LMC, the single pin chopper, dissolver, centrifuge and banks of centrifugal extractors and strippers were operated and maintained remotely, and all the systems have performed satisfactorily. The auxiliaries like master slave manipulators, in-cell crane, sampling and analytical systems extended cohesive support. The fuel subassemblies disassembled at the post-irradiation examination cells into individual pins, were loaded in a specially designed magazine and transported in a special α-tight container inside a shielded cask, to the LMC. At the LMC, the magazine was transferred into the shielded containment box in α-tight mode. The estimated β,γ activity of these pins ranged from 14 Ci/pin to 150 Ci/pin.

The dissolver operation in LMC has generated data on the dissolution of mixed carbide fuel rich in Pu, at various burn ups. Tracking the carbon present in the dissolver solution and solvent extraction runs conducted so far aided in finalising the dissolution parameters. Hull monitoring was done with an HPGe detector and the hull losses were estimated to be very low Figs. 1and2 show typical operations in the fuel pin chopping and hull removal.

The dissolver solution was clarified using the air turbine operated centrifuge. The mechanical performance of the unit improved and the frequency of breakdowns reduced after the components were modified based on vibration analysis. The equipment performance has been extremely satisfactory. Remote maintenance was carried out without any problem. Modification of operating and idle running procedures to keep the unit healthy, aided in reducing the frequency of maintenance.
The raffinate losses were less than 0.1%. Operation of the three cycles of solvent extraction has established low raffinate losses and high Pu recovery. Uranous addition in the stripper has decreased the Pu content in lean solvent.

As a modification, the introduction of a spacer plate in the stationary bowl of the centrifugal extractors in the extraction and stripping chambers of the first cycle centrifugal extractors has helped in improvement of performance.

The decontamination factors for ^{106}Ru and ^{137}Cs were better than 10^3 and 10^4 respectively in

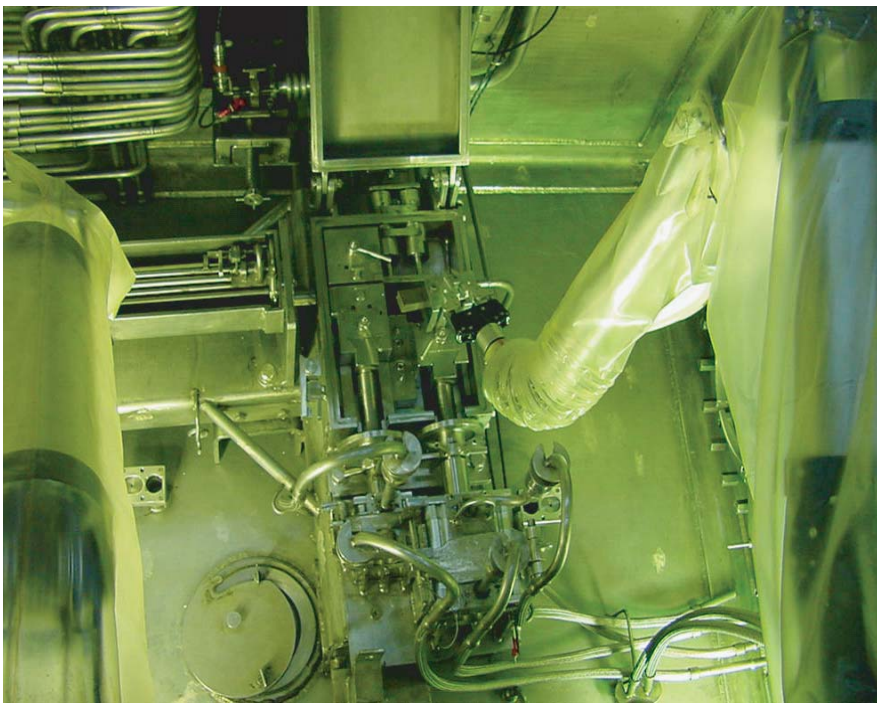

Fig. 1. Remote removal of cutting blade holder of chopper

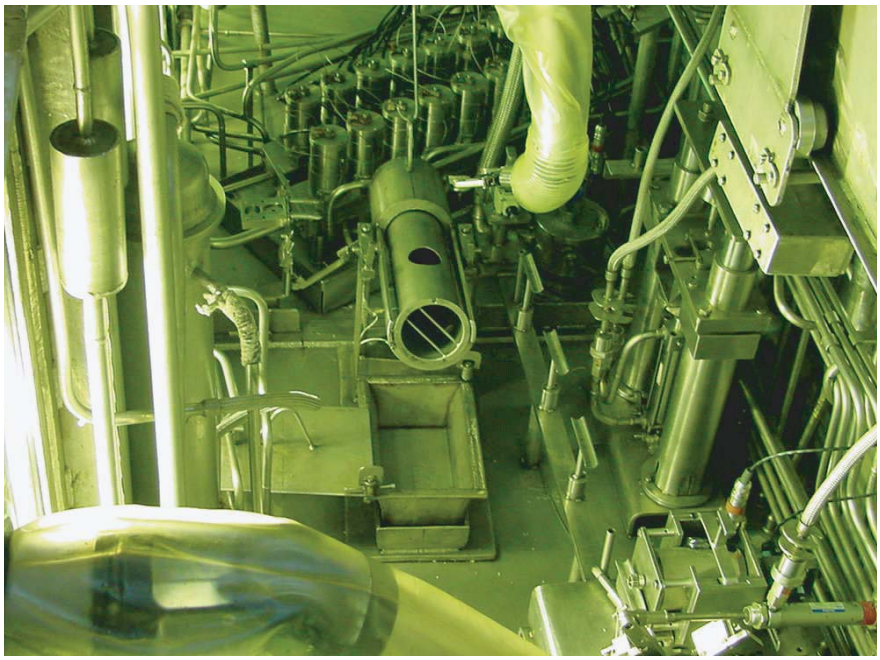

Fig. 2. Dissolver basket tilted to remove the hulls

first cycle . While the first cycle solvent did not show any appreciable increase in DBP content with burnup up to 50GWd/t, it increased significantly during the 100 GWd/t campaign. The Ru content in the strip product also increased compared to the previous campaigns. Heavy organic formation and plugging problems cropped up resulting in maloperations during start-ups. These were identified and rectified.

The problem in the electrolytic partitioner was identified to be due to the degradation of electrodes. Also the uranium to plutonium ratio was not sufficient enough to get satisfactory separation. Hence partitioning based on direct oxalate precipitation was adopted successfully. The Pu product meets the specification with respect to permissible levels of U; the uranium product needs further treatment. Batch precipitation process was continued with satisfactory results.

The operation in U and Pu reconversion facility was quite smooth and incident free Pu was also recovered from heavy organics and ammonium carbonate strip solutions generated during the solvent treatment.

All the instrumentation systems for the measurement and data acquisition of process parameters; logic control systems in chopper, dissolver, centrifuge, and centrifugal extractors; interlock systems for liquid transfer, sampling and exhaust & off-gas systems performed as per the design specifications. The working of all the radiation monitoring instruments and fire alarm systems were satisfactory and were as per the technical specifications. The functioning of Radiation Data Acquisition System(RADAS) and its data acquisition from Continuous Air Monitors(CAMs), criticality monitors and stack monitors were satisfactory.

The reprocessing of different burn-up fuels has thrown up a lot of process challenges in the chemical process, mechanical operations and maintenance. This valuable experience has given enough confidence to the plant designers and operators for undertaking the design, construction and operation of reprocessing plants of robust design, higher capacity and complexity. Close monitoring of the process, equipment as well as fissile material were easily possible in the LMC, as it is a compact facility.

4.2 Thermal Properties of High Plutonium Bearing Mark-I Carbide and Advanced Nitride Fuels

Hyperstoichiometric uranium-plutonium mixed carbides, having the compositions of $(U_{0.3}Pu_{0.7})C_{1+x}$ and $(U_{0.45}Pu_{0.55})C_{1+x}$, designated as Mark-I and Mark-II respectively are being used as fuels in FBTR for the first time. Besides the monocarbide MC (M=U+Pu), the Mark-I fuel contains 5-20 wt.% and Mark-II fuel contains 5-15 wt.% sesquicarbide. The Uranium-plutonium mixed nitride $(U_{0.45}Pu_{0.55})N$ is also a high plutonium containing advanced fuel being considered as a candidate for future FBRs. Heat capacity of the fuel is an important thermodynamic parameter, which is needed to model the fuel behaviour as well as to derive the thermal conductivity of the fuel from the measured thermal diffusivity data. In the literature, heat capacity data are not available for the mixed carbides of Mark-I and Mark-II compositions as well as $(U_{0.45}Pu_{0.55})N$. The Enthalpy increments of Mark-I and $(U_{0.45}Pu_{0.55})N$ fuel samples have been measured for the first time by using a high temperature differential calorimeter (Model HT 1500 of M/s. SETARAM, France), in the temperature range 1021-1759 K and 1025-1775 K respectively employing the inverse drop calorimetric method. The measured enthalpy increments of Mark-I fuel and the mixed nitride were fitted to polynomial functions in temperature, by the least squares method, from which the heat capacity and other thermodynamic functions have been derived. The fit equations for the enthalpy increments obtained for Mark-I and $(H_T^0 - H_{298}^0)$ $(U_{0.45}Pu_{0.55})$ N are given below as equations (1) and (2) respectively.

The error in the enthalpy

$$H_T^0 - H_{298}^0 / \text{J mol}^{-1} = 33.9569(T/K)+15.9028*10^{-3}(T/K)^2 -40.4126*10^4(K/T)-10182 \quad \text{--- (1)}$$

$$H_T^0 - H_{298}^0 / \text{J mol}^{-1} = 39.0543(T/K)+9.1005*10^{-3}(T/K)^2 -38.3847*10^4(K/T)-11166 \quad \text{--- (2)}$$

increments from our measurements has been determined to be 2-4%. The standard deviation for the fit is 782 J mol^{-1} and 434 J mol^{-1} respectively.

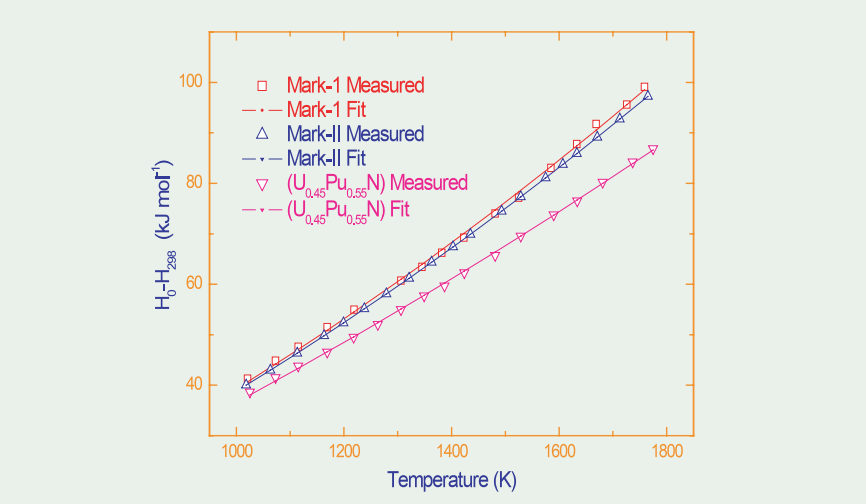

Fig. 1. Enthalpy of Mark-I, Mark-II and $(U_{0.45}Pu_{0.55})N$ fuel materials

In Fig. 1, the experimental enthalpy increment data of Mark-I, Mark-II fuels and $(U_{0.45}Pu_{0.55})N$ are plotted against temperature along with that of the fitted values. In Fig. 2, the heat capacity data of Mark-I, Mark-II fuels and $(U_{0.45}Pu_{0.55})N$ fuel are plotted against temperature. It can be seen from the Figs. 1 and 2 that the enthalpy increments as well as the heat capacity of Mark-I mixed carbide are higher than those of Mark-II mixed carbide fuel which in turn are much higher than those of the mixed nitride of the same composition with respect to uranium and plutonium. The trend is to be expected in view of the fact that the heat capacity of Pu_2C_3 is higher than those of U_2C_3 and those of UN and PuN are lower than those of the respective carbides.

The carbide and nitride fuels , besides being radioactive, are very sensitive to oxygen and moisture. In carrying out the measurements on such fuel materials, the major challenge is to maintain an ultra-high-pure atmosphere to avoid oxidation of the samples, while

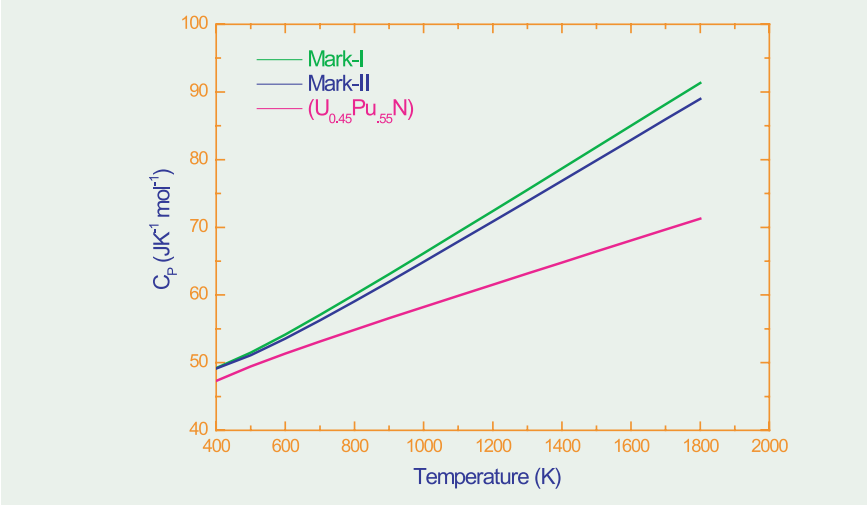

Fig. 2. Heat capacity of Mark-I, Mark-II and $(U_{0.45}Pu_{0.55})N$ fuel materials

maintaining a negative pressure with respect to the ambient in the glove box. It was achieved by incorporating the calorimeter in a leak-tight glove box having a carefully controlled inert atmosphere whose oxygen and moisture contents were maintained below 10 vpm each during the measurements as well as sample handling.

4.3 MOX Fuel-Coolant Chemical Interaction Studies

A hybrid core with MOX-44%PuO_2 is being considered for FBTR. High-plutonium MOX fuel is expected to be less compatible with the sodium coolant than the conventional MOX fuel used in power reactors. In the event of a fuel pin failure, liquid sodium comes in direct contact with the MOX fuel, leading to the formation of the voluminous reaction product sodium urano-plutonate (Na_3MO_4; M = $U_{1-x}Pu_x$). This compound, due to its lower density compared to the fuel, increases the fuel volume and the stress level of the clad which can further increase the size of the initial leak or cause a secondary crack. As the defect size increases due to fuel-coolant interaction, fuel and fission products can get released into the coolant, which manifests as a Delayed Neutron Detector (DND) signal. The formation of Na_3MO_4 is thermodynamically favoured at the operating conditions, when sufficient oxygen is available. Out-of-pile experiments were carried out at the Chemistry Group to characterize the chemical compatibility of MOX-44% PuO_2 with sodium coolant. Prior to taking up MOX pellets, the reaction between UO_2 and sodium was undertaken. Two annular UO_2 pellets (5.5mm OD) from BARC were equilibrated in excess liquid sodium containing about 1000 wppm oxygen at 773 K for 24 h. The excess sodium was

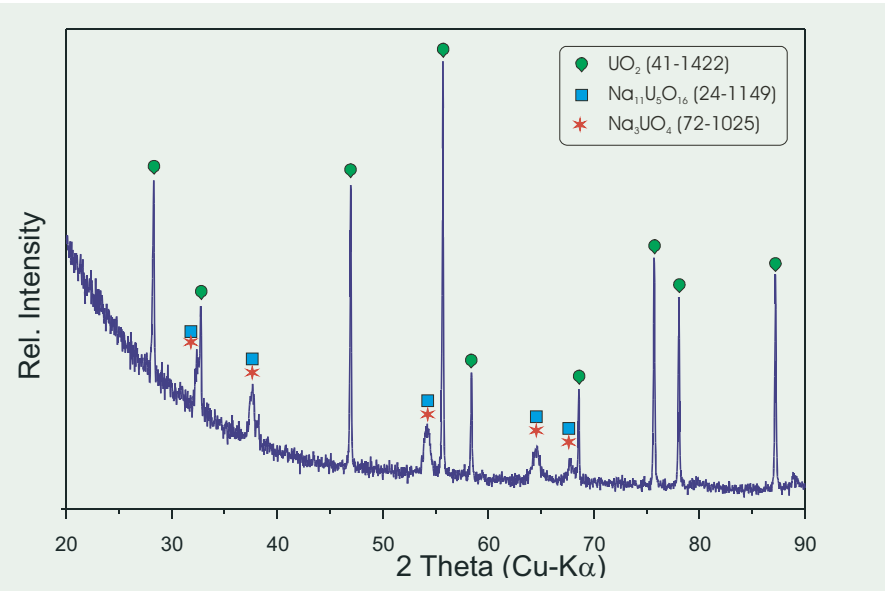

Fig. 1. XRD pattern of the product obtained on (UO_2+Na) equilibration at 773K. The sodium uranate lines are identified along with those of unreacted UO_2.

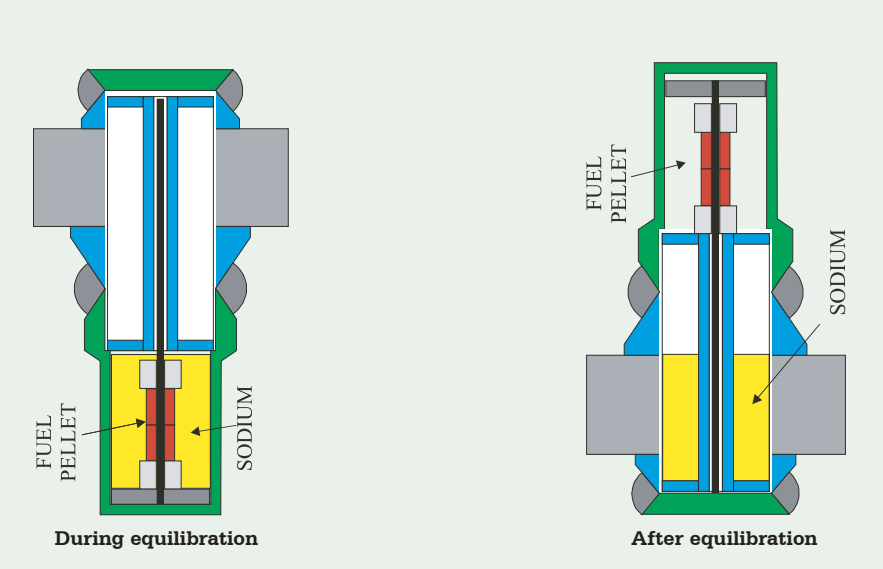

Fig. 2. The equilibration vessel with MOX pellets and sodium during equilibration. At the end of the equilibration, the vessel was immediately inverted to drain the sodium surrounding the MOX pellets.

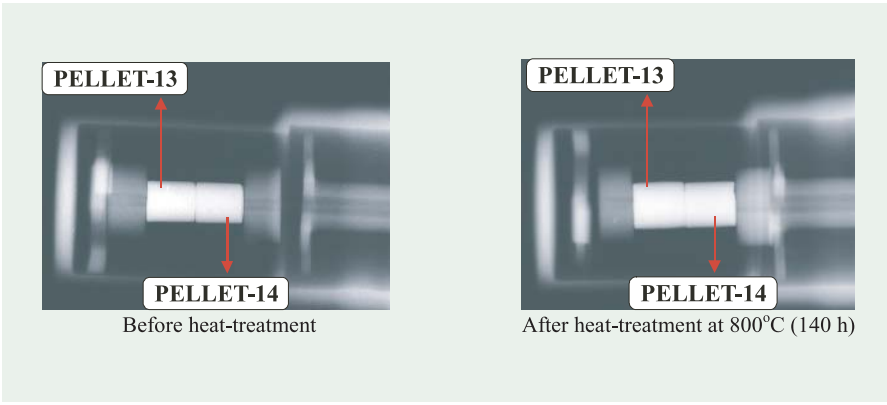

Fig. 3. The X-radiography of the equilibration vessel before and after equilibration. The MOX pellets are indicated.

distilled off at 623 K by resistance heating. The residual sample in the crucible and the chocolate brown vapour deposit at the colder regions of the distillation vessel were sampled in a Lindemann capillary tube for XRD owing to the moisture sensitive nature of the samples. Initial XRD patterns (Fig. 1) corresponded to the sodium uranates Na_3UO_4 (a_o=4.78 Å) and $Na_{11}U_5O_{16}$ (a_o=9.543 Å). The same samples re-measured after 24 h indicated disappearance of certain peaks. The final pattern is close to Na_3UO_4 (a_o=4.78 Å), which is the expected reaction product with UO_2. These capillary samples were also analyzed at BARC and the results were confirmed.

Experiments were conducted to study the swelling behaviour of fuel pellets exposed to liquid sodium. Towards this, annular UO_2 pellets (5.5mm OD) from BARC and sodium were assembled in a specially designed equilibration capsule with 'Conoseal' fitting to avoid welding and cutting open the capsule after each experiment. The design incorporates the requirement that liquid sodium be drained at 973 K from the fuel pellet side. This is to ensure absence of any possible mechanical interaction of sodium metal on the fuel pellet while cooling.

A trial run was carried out with UO_2 before attempting work with MOX. The capsule containing UO_2 and sodium was equilibrated at 973 K inside an inert atmosphere glove box for 92 h after which the sodium was drained from the UO_2 pellet chamber at the same temperature. The samples were furnace cooled. The radiographic results for this capsule indicated no swelling of the pellets, which is in conformity with literature reports.

A similar experimental set-up was adapted for carrying out experiments with MOX-44%PuO_2 pellets. In this case, 100 ppm of oxygen was added to liquid sodium. The equilibration was carried out at 1073 K for 140 h inside an inert atmosphere glove box. At the end of 140h the hot experimental assembly was inverted to drain sodium from the MOX pellet chamber (Fig.2). High sensitivity radiography of the pellets was carried out in two different orientations 90° apart (Fig.3). Dimensional measurements of the fuel

pellets were made from the radiographs.

From the results, it was observed that the average diameter/height increase is 11% for pellet-13 and 9% for pellet-14. The relative volume increase for pellet-13 and pellet-14 were 37% and 29.5% respectively. It can be shown that $(\Delta W/W)\% \approx 0.21\ (\Delta V/V)\%$. The estimated percentage volume swelling using the literature data is 23% for MOX-44%PuO_2 of O/M 2.000 at 1173 K. From the above studies, it is concluded that the experimental observation of swelling for MOX-45%PuO_2 is in accordance with the estimate reported in literature. The product Na_3MO_4 being isomorphous with Na_3UO_4, was identified by XRD in an independent experiment involving UO_2 equilibration in sodium.

4.4 Supercritical Fluid Extraction Studies on Plutonium

Supercritical fluids possess low viscosity, high diffusivity and high density, making their penetration easy through the pores of a sample matrix to extract the components of interest. Hence they provide faster, cleaner and more efficient extractions without generating a secondary solvent disposal problem unlike the conventional solvent extraction methods, an important advantage especially in the case of radioactive wastes. This becomes possible because the extracting supercritical fluid escapes as a gas under atmospheric conditions after the extraction and hence there is no burden of secondary liquid radioactive waste generation. Among many possible candidate materials, the inexpensive carbon dioxide is the widely used supercritical fluid for its convenient critical temperature and pressure. The non-polar nature of supercritical carbon dioxide (Sc-CO_2) is modified with a modifier like methanol to extract polar compounds. The metal ions are extracted by using Sc-CO_2 modified with an appropriate ligand in the modifier.

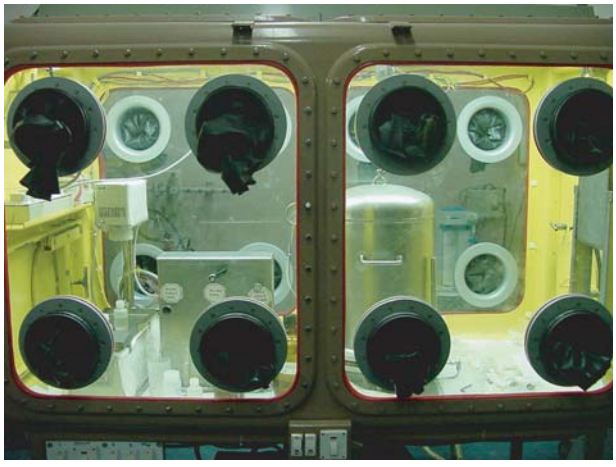

Fig.1 Supercritical Fluid Extraction Facility inside a Glove Box for the Recovery of Plutonium from Waste

The extraction of uranium nitrate from a tissue paper matrix, silicone oil from urania microspheres of the sol-gel process and a separation study of uranium from thorium were completed maintaining the Supercritical Fluid Extraction (SFE) system outside a glove box or fume hood. However, the extraction study of actinides like plutonium, americium etc., need a fully dedicated SFE instrument accommodated in a glove box system which is a mandatory requirement for handling radioactive materials.

SFE facility in glove box

Since the study involved a high-pressure system with radioactive handling, certain special safety features were incorporated in the glove box (Fig .1a). The glove box is to be maintained under a negative pressure but an accidental burst of the carbon dioxide from the extraction vessel at a high pressure during a run can destroy the negative pressure environment of the glove box. This may release radioactive contamination to the atmosphere. Hence a secondary container with a provision for automatic

switching-off of pumping, is incorporated to contain such a pressure burst, and only to release it slowly and safely later. Since an inflammable solvent, methanol, is used as a modifier in the glove box, a methanol sensor has been incorporated along with its annunciation system to avoid any fire hazard. The system pressure line is incorporated with appropriate non-return valves to avoid back flow. Among the various components of the SFE, the extraction vessel in the oven, Back-Pressure Regulator(BPR) and the sampling system are maintained inside the glove box while the two reciprocating pumps function from outside.

Actinide extraction

Initial studies with a mixture of thenoyltrifluoroacetone (TTA) and hexafluoroacetylacetone (F_6AcAC) in methanol modified Sc-CO_2 system established the complete extraction of plutonium (Pu(IV) nitrate) from a teflon matrix. SFE methods were developed using Sc-CO_2 modified with octyl(phenyl)-N,N'-dibutyl carbamoylmethyl phosphine oxide (OϕCMPO) in methanol for the complete removal of plutonium i.e. Pu(IV) from glass and stainless steel matrices and about 88 % from a simulated tissue paper waste. The study using Sc-CO_2 modified with OϕCMPO yielded near complete extraction of trivalent americium (> 99%) from a simulated tissue paper waste and also resulted in near complete extraction (> 99%) of plutonium from tissue paper after stabilizing its oxidation state at +3 using ferrous sulphamate. Experiments are in progress to achieve the complete extraction of Pu(IV) from tissue paper waste.

The investigations to establish the complete extraction of actinides such as uranium, plutonium and americium from tissue paper waste and various other possible matrices are expected to achieve a minimum liquid waste generation which will reduce the waste management requirement of nuclear industry and various other applications possible in the fuel reprocessing cycle.

4.5 Jet Entrainment Facility for the Preparation of Urania Microspheres

The preparation of fuel in the form of microspheres using sol-gel methods and subsequent vibro-compaction of these microspheres in the clad is one of the candidate routes to be used in future for the fabrication of FBR fuel pins. To achieve smear densities in the range of 80% TD in these sphere-pac fuel pins, at least two fractions of spheres having different sizes are required for packing. It is known from theory that the size of the larger spheres should be 1/7 of the fuel pin inner diameter to obtain maximum packing efficiency and that the smaller spheres should have a diameter larger than 1/7 of the larger spheres to obtain a stable packed column. Thus, for the test fuel pins proposed for FBTR, having a diameter of 6 mm inner diameter, a coarse fraction of spheres of size 750-800 μm and a finer fraction of 100-150 μm are needed. Generally, the coarse fraction will be the mixed oxide of uranium and plutonium and the fine fraction will be UO_2. Both the coarse and the fine fractions are prepared by internal gelation process using hexamethylene tetramine as the gelating agent. The coarse fraction is prepared in the conventional gelation set up by carrying out the gelation in a column of silicon oil maintained at 363 K. The fine fraction of microspheres cannot be prepared using the

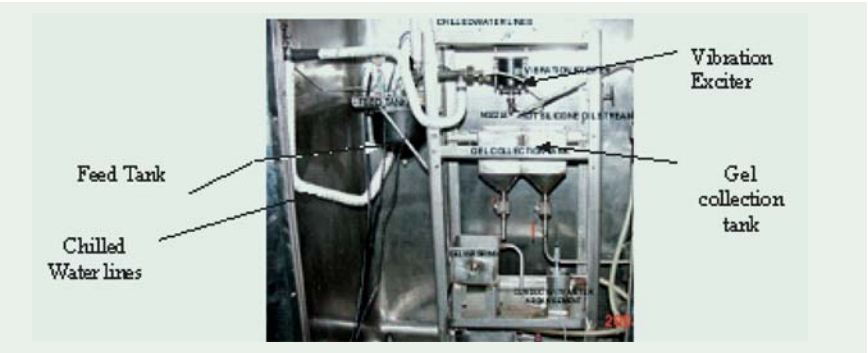

Fig. 1. Jet-entrainment facility

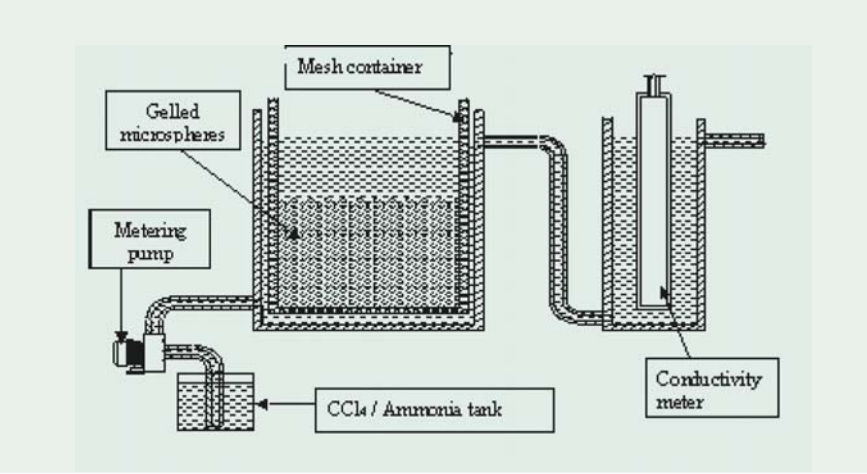

Fig. 2. Gel washing set-up

conventional gelation set-up as the lighter droplets will start floating above the silicon oil column. Further, it will lead to coalescence of broth droplets, which will eventually lead to the formation of microspheres larger than what is required. Therefore, a jet entrainment facility was set up and has been used for the preparation of the fine fraction of urania spheres.

The jet-entrainment set-up is shown in Fig. 1. It consists of a double walled feed tank, a dispersion device containing a 0.2 mm ID stainless steel capillary, an oil-tank of about 40 litres capacity, a collection tank, a vibration exciter cum power oscillator, a pressure indicator cum controller, a gel-collection tank, a gel washing set up and an online electrical conductivity measuring setup. The temperature of the silicone oil in the oil-tank is maintained at 85 ° C using an on-off temperature controller. The silicone oil is pumped into a ½" tube whose dispersion end is flattened so that the width of the aperture is around 1 mm. The silicone oil dispersed through this aperture forms a jet of silicone oil. The linear flow of the oil is maintained above 1.5 m/s to prevent the dispersed droplets from coalescing with one another. The mixture of uranyl nitrate, hexmethylene tetramine and urea from the feed tank is dispersed in the form of droplets, through a vibratory nozzle, on to the jet of hot silicone oil stream for gelation. Each droplet is carried away by the oil jet preventing the next droplet from coalescing with it. The design of the gel collection tank ensures that the residence time of the gelled microspheres in the hot oil is minimum. Parameters such as the pressure of the feed tank and the frequency of the vibrator were optimized to be 1500 mm H_2O and 3700 Hz respectively through calibration runs.

Gelation experiments were performed using the above facility under the optimized conditions. The gelled spheres were washed with CCl_4 and ammonia using the washing set-up shown in Fig.2. The washed spheres were subjected to various heat treatment steps viz. drying at 373 K and calcination at 573 K in air, reduction at 1073 K in Ar+8% H_2 atmosphere and sintering in argon atmosphere at 1673 K. The sintered microspheres are shown in Fig. 3. The density of the sintered microspheres was measured using a helium pycnometer to be 10.49 g/cm^3 (96% TD). The tap density of the sintered microspheres was 6.53 g/cm^3 (59.6% TD). The sintered micro-spheres were then sieved using 100 mm and 150 µm mesh. The percentage yield of the microspheres obtained in the sieve range 100 - 150 µm was 50%.

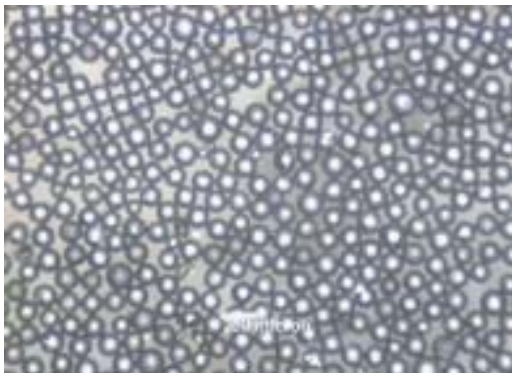

Fig.3. Sintered UO_2 microspheres (100-150 mm)

4.6 Laser Mass Spectrometric Studies on Rare Earth Doped UO_2 towards Direct Determination of Burn up of Nuclear Fuel

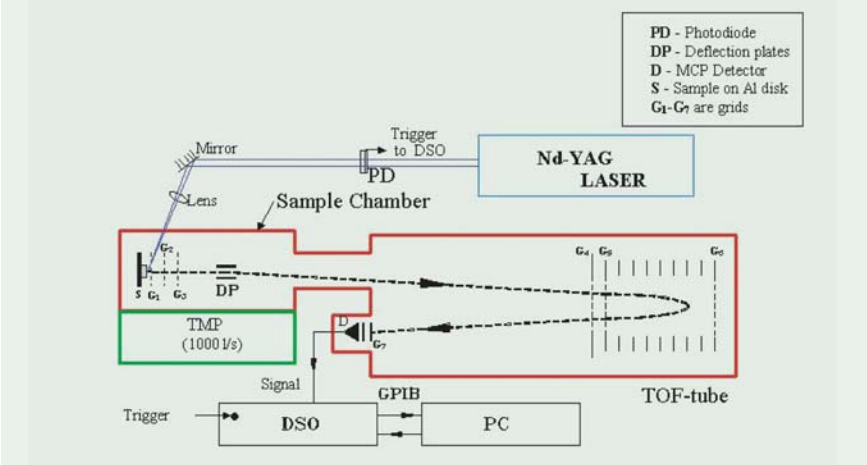

Fig. 1. Schematic of in-house developed Laser-Mass spectrometer facility

A laser mass spectrometric system containing a home-built reflectron time-of-flight mass spectrometer (RTOF-MS) was used to study the UO_2 system doped with lighter rare earths (La, Ce, Sm, Nd), both in solid and liquid samples. Unit mass base line separation is obtained for all the rare earth isotopes. Preliminary results indicate that this method has potential for the direct burn-up determination of irradiated nuclear fuels and to study the distribution of solid fission products in irradiated pellets.

The experimental facility used is schematically shown in Fig. 1. It employs a nano-second Nd-YAG laser as the heat source for the evaporation / ionization of the material. The mass analysis is done by the RTOF-MS, which ensures a high mass resolution. A microchannel plate (MCP) detector is used in the equipment. The signal from the MCP is fed to a digital storage oscilloscope (DSO). The whole system (the ultra-high vacuum chamber and the RTOF tube) is pumped by a turbomolecular pump (TMP). The kind of simultaneous evaporation carried out here is not possible in a conventional mass spectrometric method where resistive heating generates the ions, whereas here an 8-ns laser pulse is used. Also, all the ions formed are measured simultaneously unlike in a conventional scanning mode. A photograph of the facility is shown in Fig. 2, and a typical mass spectrum obtained is given in Fig. 3.

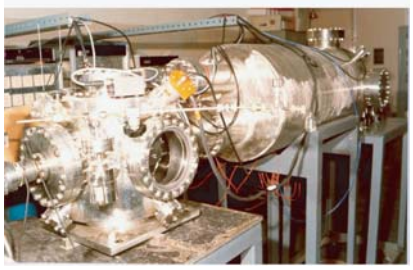

Fig. 2. The RTOF-MS System

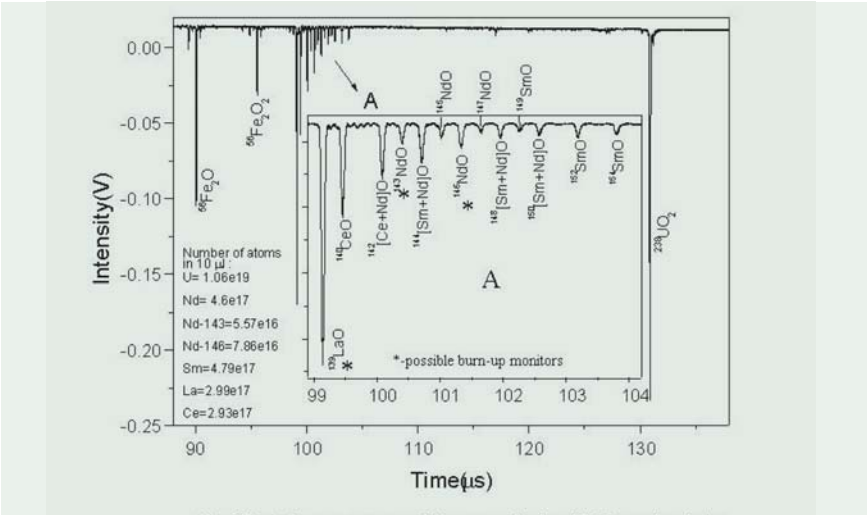

Fig. 3. Typical mass spectrum of light rare earths doped UO_2 sample solution

4.7 Modeling of Aqueous Density and Mean Ionic Activity Coefficients for Nitric Acid

Density and mean ionic activity coefficients are important parameters for solvent extraction modelling and simulation. For inter-conversion of molar concentrations to molal concentrations and vice-versa, the density of nitric acid solution is required. Coefficients for the density equation as a function of acid concentrations were computed by robust regression of data available in the literature. Fig.1 shows the excellent agreement between experimental values (points) and the modelled values (line).

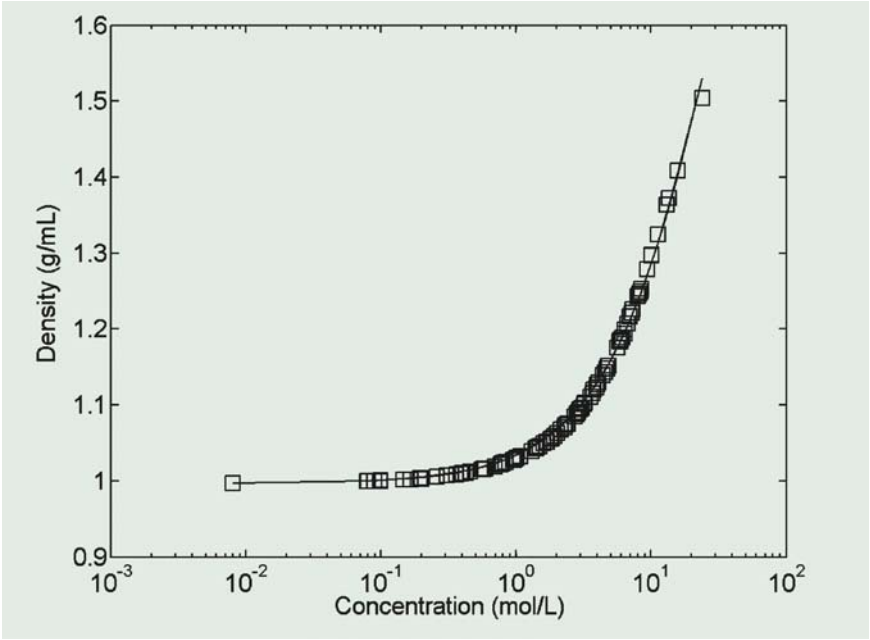

Fig. 1. Comparison of density of aqueous HNO_3 solutions at 298.15 K.

For the mean ionic activity coefficients of nitric acid on molal scale, the upper limit of the previously applicable models is only 28m. The popular thermodynamic models available in the literature are valid only up to 6m concentrations. This limit is easily exceeded for aqueous solutions of interest to reprocessing. We could model the activity coefficient of nitric acid in the ultra high concentration ranges such as 200 m (~20 kmol/m^3) with a fair accuracy. Fig.2 shows the excellent agreement between the literature values and the modelled values (line).

This model is useful for solvent extraction systems with high nitrate salting strengths also

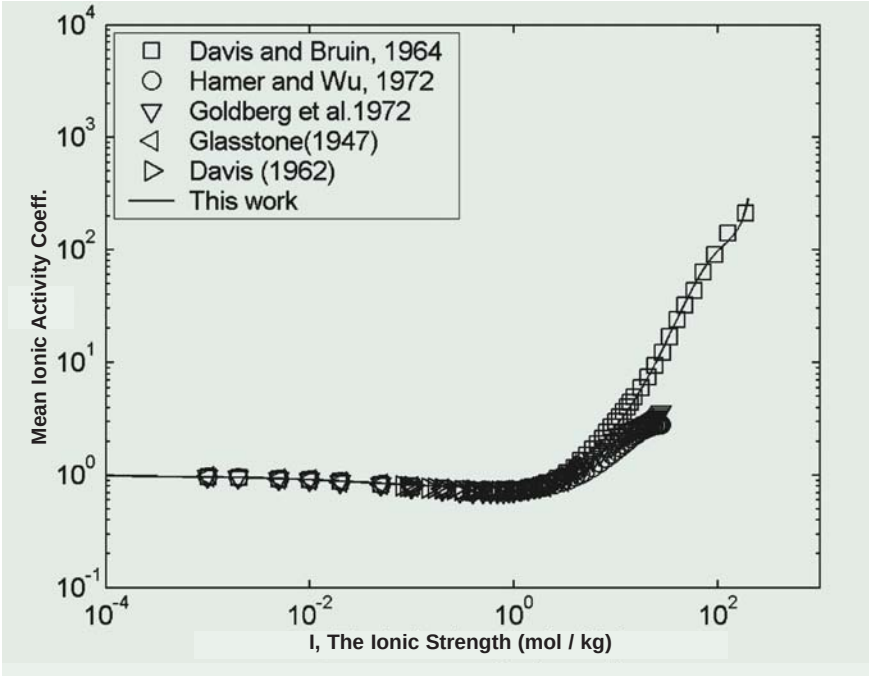

Fig. 2. Comparison of the calculated activity coefficient of nitric acid with the data in the literature.

4.8 Remote Maintenance Experience with Hot Cell Gadgets

In the LMC, a host of hot cell equipment are deployed such as Master Slave Manipulators (MSMs), in-cell crane, sampling systems, capping-decapping systems etc. Apart from their utility for the remote operation and maintenance of the chopper, the centrifuge, and the centrifugal extractors, they were used for sampling, aliquoting and high active analysis.

The articulated arm manipulator of 8 kg capacity with Remote Removable Tonnage (RRT) and the 50 kg in-cell crane were very useful in trouble-shooting without any a breach in the cell (Fig. 1). Some of the important experiences are highlighted below.

1) Fuel Pin Spacer Wire Entanglement

The spacer wire is helically wound over the fuel pin, one end welded to the front end of the fuel pin and other end inserted into the groove of the tail end. Initially the fuel pin is fed into the chopper from the front end of the pin. After the first piece of the fuel pin is chopped, the spacer wire gets unwound from the pin and goes beyond the reach of the cutting tool and will not be cut in successive cutting as it gets entangled somewhere in the chopper box, leading to an undue force in the feeding mechanism of the drive. This in turn trips the system, thus preventing further chopping. Viewing with a CCTV, with the aid of the master slave manipulator, the entanglement of the spacer wire was removed remotely.

After analyzing the root causes of the problem, it was decided to cut the fuel pin from the tail end, in the subsequent campaigns, which enhanced the spacer wire cutting. Also, modifications have been carried out on the design of gripping and stationary tools for positive cutting of the spacer wire in the Demonstration Fast reactor fuel Reprocessing Plant (DFRP).

2) Choking of Dissolver Chute

Due to paucity of space in the LMC, a large space could not be provided for the chopped pieces to fall freely into the dissolver. Due to this the chute got choked.

Various methods, were tried to remove the choke remotely with the aid of the master slave manipulator, but finally a flexible shaft with a guide suitable to the dissolver limb was made and inserted from the top of the dissolver limb. The flexible shaft was inserted into the chute by the manipulator. By pushing the flexible shaft back and forth, the choke was removed.

Thus the MSM proved as a useful aid in solving the problems of remote maintenance.

3) Modification in Centrifugal Extractor

During the operation of the Centrifugal extractor (CE), it was found that the efficiency of the extractor needed further improvement. Towards this, modifications were carried out on the extractor. This modification involved removal of the rotating bowl and the rotor assembly with the aid of the master slave manipulator, in-cell crane, pneumatic wrench, and special gadgets. A spacer plate of thickness 3 mm was tightened to the end of a specially designed tool, then it was inserted into the stationary bowl and rotated remotely by the manipulator so as to match the stationary bowl vanes with the grooves of the spacer plate. With the assistance of the manipulator, the tool was unscrewed from the spacer plate and removed, placing the plate in the stationary bowl. In this way all the plates were placed successfully.

During the above remote operation, a lot of challenges such as mismatching of vanes with the plate and falling down of a nut to the stationary bowl etc., have been overcome by using special gadgets remotely by the manipulator.

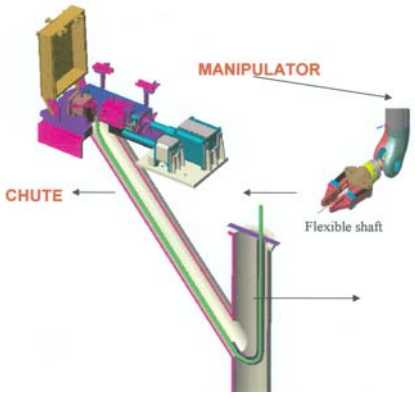

Fig. 1. Articulated arm manipulator

4.9 Fibre Optic-Aided Spectrophotometry for On-line Monitoring of Plutonium in Process Streams of Reprocessing Plant

The reprocessing of spent nuclear fuels needs information regarding the oxidation states and concentrations of uranium and plutonium in process solutions for safe and efficient process control. This information guides the operator to continuously adjust the process parameters to optimize quality and the yield of heavy metal products. To meet these essential requirements in the plant, a Fibre-Optic aided Spectrophotometric (FOS) method has been developed at the Reprocessing Group. This method is a useful analytical tool for the detection and determination of various oxidation states of uranium and plutonium. The procedure and instrumentation have been adapted for remote operation with the necessary shielding and automation. Experience during the reprocessing of FBTR fuel in LMC established the usefulness of the FOS technique for the determination of oxidation states and concentrations of uranium and plutonium in the various process streams. Encouraged by these results, the Reprocessing Group has taken up a comprehensive programme for the indigenous development of the total instrumentation and automation in collaboration with CAT, Indore and ECIL, Hyderabad. With this instrument it will now be possible to follow chemical and electrochemical reactions *in situ*. With the deployment of this technique in nuclear fuel reprocessing plants, the sampling of highly radioactive solutions will be avoided resulting in real time analyses with almost nil man-rem exposure and without generating any radioactive waste.

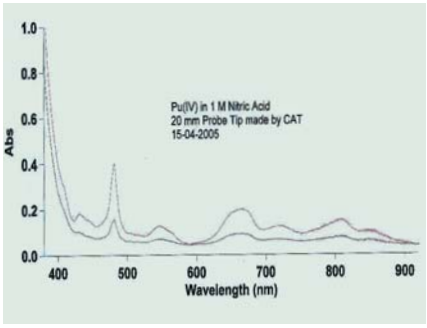

Fig. 1. Absorption spectra of Pu(IV)

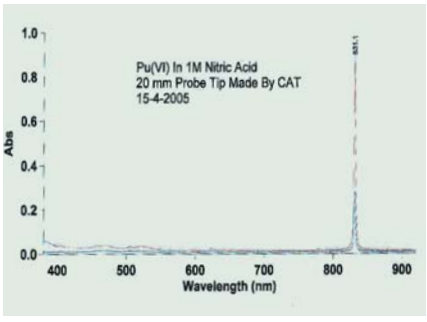

Fig. 2. Absorption spectra of Pu(VI)

The initial milestones, namely, fabrication of opto-mechanical tips of various path-lengths and development of complete dip type fibre optic probe of 80 mm path length and three-meter long fibre optic cable have been achieved. The performance of this probe and tips were found to be very satisfactory. Figs.1 and 2 show the absorption spectra recorded for Pu (IV) and Pu (VI) using the new opto-mechanical tips developed indigenously at CAT, Indore. Figs. 3 and 4 show the plots of calibration for uranium (VI) in aqueous and organic media using the same tips. These tips are now deployed and routinely used for the determination of plutonium in aqueous and organic samples.

In order to establish the feasibility for on line monitoring of Pu (VI) in the first cycle raffinate, a prototype of the equipment to be used was made in glass and tested. With this assembly and a probe of 80-mm path length, it was possible to achieve a detection limit of < 10 ppm for Pu (VI).

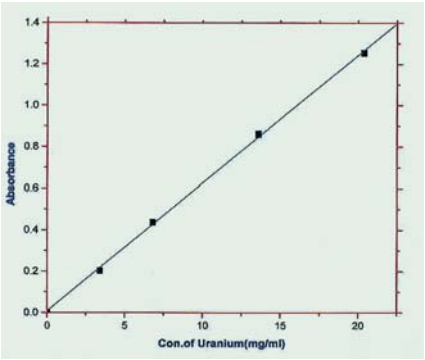

Fig. 3. Calibration curve for U(VI) in acid

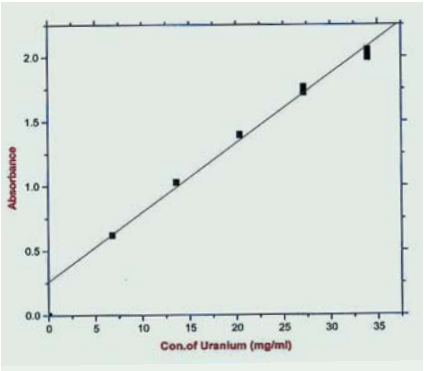

Fig. 4. Calibration curve for U(VI) in TBP

4.10 Studies on $MgCl_2$- NaCl- KCl Electrolytes for Pyrochemical Reprocessing of Oxide Fuels

Pyrochemical reprocessing methods are more suitable than the conventional aqueous methods for reprocessing the short cooled, high burn-up fast reactor fuels because of their ability to withstand high levels of radioactivity. Though the Russian process of oxide electrowinning reprocessing of oxide fuels is well known, it had been established in Fuel Chemistry Division that a novel method of electrorefining is possible for UO_2. In the Russian method, 2CsCl-NaCl is used as the electrolyte, and the temperature of operation is 973 K. The important advantage of our salt is that it is very much cheaper than the highly expensive CsCl. Also the melting point of this salt mixture is below 673 K and hence, the temperature of operation could be brought down by about 200^0. There is an added advantage that the fused high purity electrolytic grade $MgCl_2$ is a by-product from the zirconium sponge production at the Nuclear Fuel Complex, Hyderabad.

Fig. 2. Cathode deposit of UO_2

Generally $MgCl_2$ is not a preferred electrolyte salt because of its easy vulnerability to electrochemical decomposition. But in this case, this salt mixture could be successfully used utilizing its sustained stability in the decomposition potential region of uranium and plutonium oxychlorides. It was established that electrorefining of the UO_2 fuel pellets could be carried out in the 50% $MgCl_2$-30% NaCl-20% KCl salt as well and that the reduction behaviour of UO_2Cl_2 was similar to that in 2CsCl-NaCl. The separation factor of Ce was determined in the electrorefining process in which the UO_2-CeO_2 pellet was used as the anode and 50% $MgCl_2$-30% NaCl-20% KCl as the electrolyte. A schematic of the electrolytic cell is shown in Fig.1. The electrolyte salt was contained in a high density graphite crucible. Sintered UO_2-CeO_2 pellets lying at the bottom of the graphite crucible acted as the anode. The electrorefining experiments were carried out at 773 K with a potential of nearly 0 V between the working electrode and the Ag/AgCl reference electrode. Crystalline deposit of UO_2 (Fig.2) was obtained on the cathode. The purity of the crystalline UO_2 deposit was found to be >99.8 %. The deposits were dissolved and analysed for its Ce and U contents using potentiometry as well as by the technique of High Performance Liquid Chromatography(HPLC). The method for simultaneous determination of U and Ce by HPLC was developed for the first time. The separation factor for Ce was computed from the results and was found to be in the range of 60 - 100.

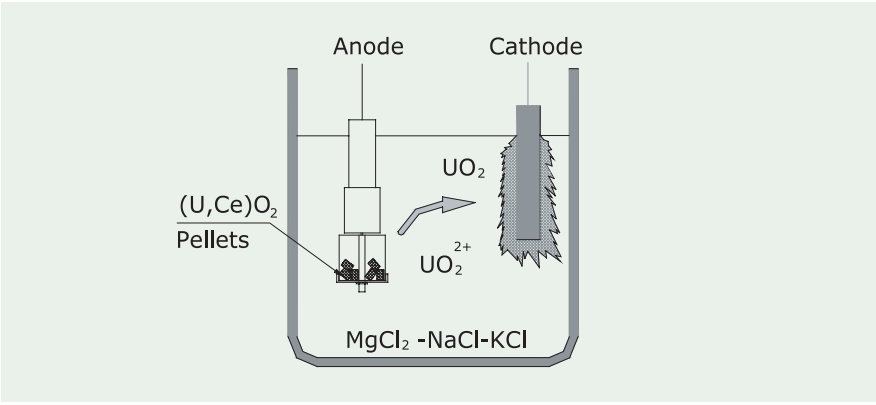

Fig. 1. Schematic of electrorefining cell

4.11 Superheated Emulsion Technique for Alpha Activity

A fast screening Superheated Emulsion Technique (SET) has been developed for measuring the alpha activity in an aqueous solution. Nucleation of superheated liquid droplets dispersed in a polyacrylamide gel medium serves as a sensitive means for detection of alpha particles. The interaction between alpha particles and superheated liquid droplets triggers bubbles and the number of bubbles nucleated could be related to the alpha activity. In view of the fact that the alpha particles have short ranges (~ 40 microns), it is felt necessary to have superheated liquid droplets in the closest vicinity of the alpha emitting radionuclides to detect alpha events quantitatively. The novel method developed involves (i) selective extraction of the alpha emitting radionuclide from an aqueous solution into an organic phase by solvent extraction (using TBP), (ii) dissolution of the organic phase in a low boiling liquid (Freon-12) and (iii) dispersion and immobilization of the mixture as fine droplets in a polymer matrix (polyacrylamide gel). The bubble nucleation due to alpha decay is recorded at 333 K using an indigenously developed image analyzer (Fig. 1).

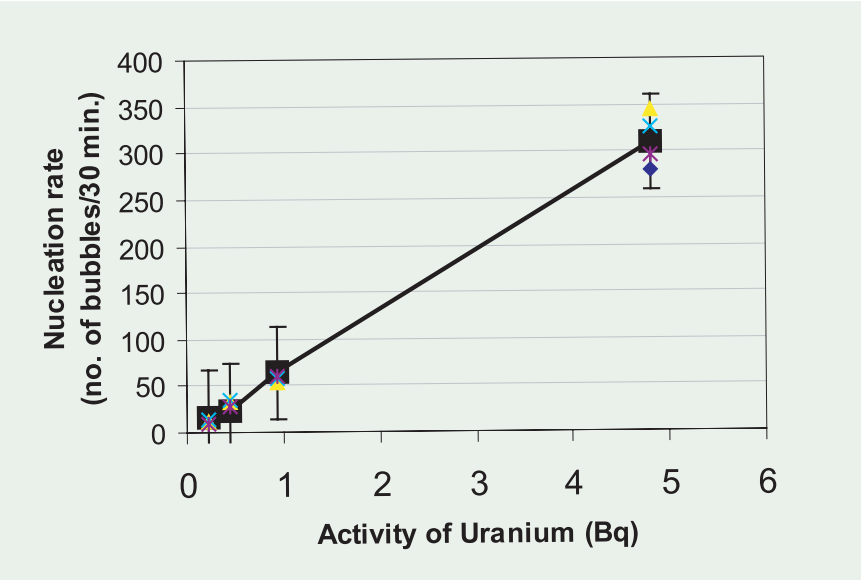

Fig. 2. Bubble nucleation rate Vs uranium activity

The measured bubble nucleation rate for various activity levels of uranium is shown in Fig. 2. The alpha detection efficiency of this technique is observed to be about 3%.

The inherent ability of SET in discriminating alpha events from beta and gamma events makes it a potential competitor to the conventional methods (which are time consuming and cumbersome). It is observed that the estimation of uranium in aqueous solution could be made within a few hours and hence, this can supplement the existing conventional techniques. This technique also promises to be a rapid method for the estimation of uranium in liquid effluents as well as in environmental and bioassay samples.

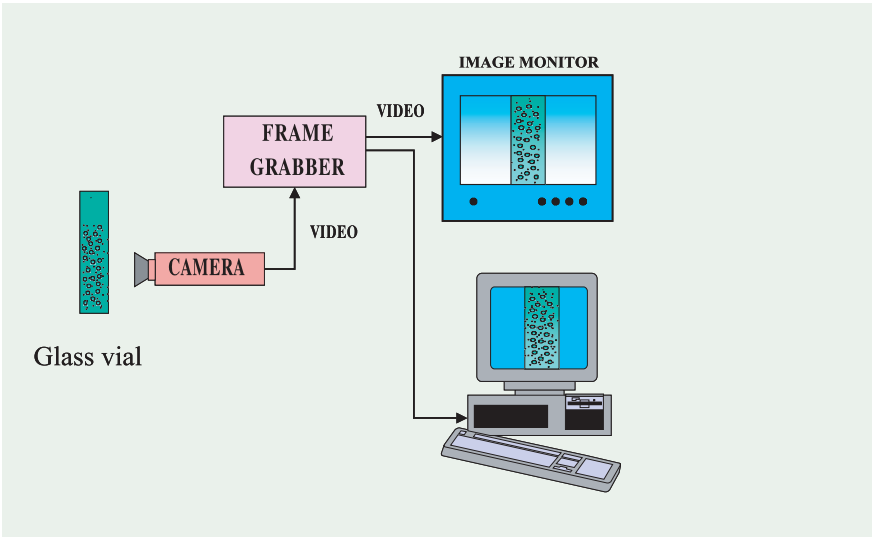

Fig. 1. Image analysis system for measuring the bubble nucleation

4.12 Membranes for Removal of Nitric Acid from Effluents

Reprocessing of Fast Reactor Fuel generates wastes containing Cs, Sr, minor actinides and fission products in 4N nitric acid. Removal of nitric acid is an important step in treating the High Level Liquid Waste (HLLW) arising from reprocessing operations. R&D related to the development of the process for the removal of nitric acid from these wastes were taken up to achieve these separations using different techniques like membranes, crown ethers attached to hydrogels or resin and ion exchange chromatography.

Towards the above, experiments were conducted with commercially available polyamide Reverse Osmosis (RO) membrane. The experimental set up comprises a feed tank, feed pump RO membrane, collection tank and inter connecting piping. The schematic diagram of the set up is shown in Fig 1. Nitric acid of different concentrations varying from 0.1N to 4N from the feed tank was fed to the RO unit and the product analyzed for the concentration of nitric acid. The results are shown in Fig.2. It can be seen that the membrane is able to remove nitric acid efficiently. The stabilization time is about 20 minutes after which nitric acid starts appearing in the product stream.This study has shown the feasibility of use of a commercially available RO membrane for the removal of nitric acid from effluents.

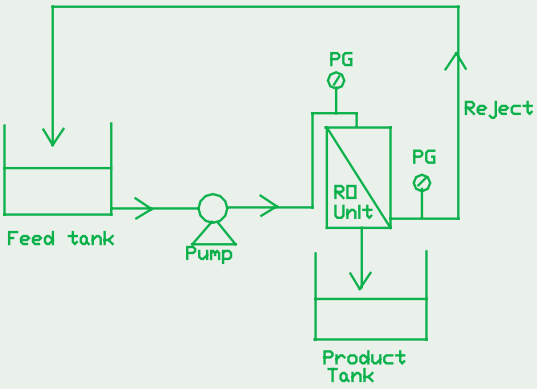

Fig. 1. Schematic diagram of RO Membrane setup

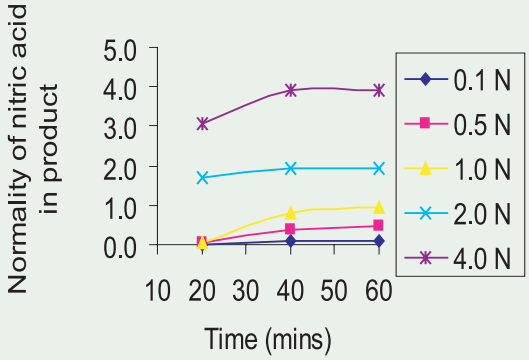

Fig. 2. Variation in concentration of nitric acid at the outlet of the membrane at different feed concentrations from 0.1N to 4.0N

4.13 Corrosion Investigations using Nitric Acid Loop

The conventional AISI type 304L stainless steel (SS) used for the reprocessing plants is presently evaluated as per ASTM A262 practice C (HUEY test). The test is also recommended by the United States Nuclear Regulatory Commission (USNRC) for evaluating the materials intended for nitric acid service in reprocessing plants [USNRC Regulatory Guide 3.37, 1975]. It is an accelerated test involving boiling nitric acid of 65% concentration, and the experiments are conducted by immersing the test coupon for five times of 48 h periods in the solution. The major drawbacks of this test procedure are that the specimens are tested in highly concentrated medium in static condition, the total test period is shorter, and it is specific to the evaluation of intergranular corrosion. Comprehensive corrosion assessment of AISI type 304L SS by ASTM A262 practice C test is difficult, taking into consideration the ranges of concentration of nitric acid used, temperature of operation, impurities and redox chemicals present, and the metallurgical

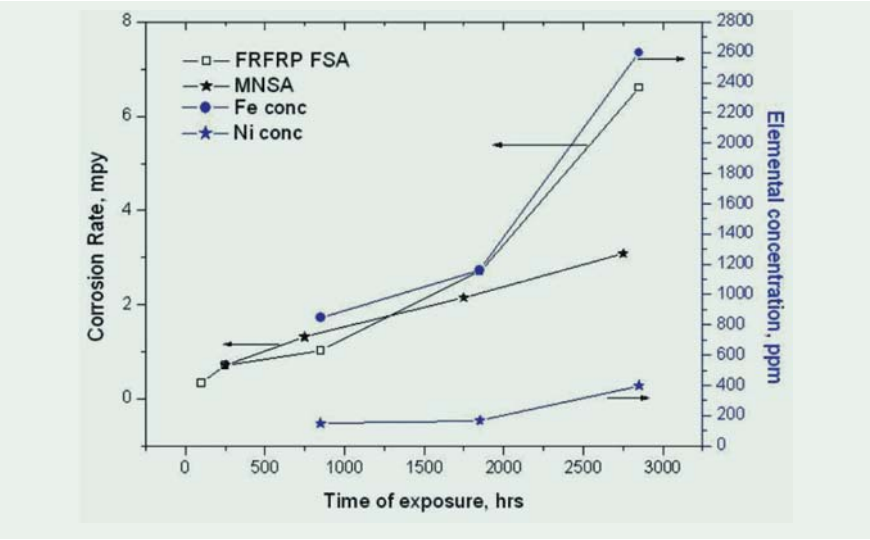

Fig. 1. Corrosion rates obtained for two grades of 304L SS, and chemical analyses of loop acid, after 2850 h operation (FSA = FRFRP solution annealed; MNSA = MIDHANI NAG SS).

state of the materials used in the reprocessing plants. This motivated the design of a dynamic nitric acid loop made of AISI type 304L SS, with flowing nitric acid at different temperatures to evaluate the corrosion performance of materials used in reprocessing plants. A loop has been and designed with a 350 litre capacity for evaluating the corrosion performance over long operating periods under simulated plant conditions. Corrosion resistance of the materials used in different metallurgical conditions, namely, cold-worked, solution-annealed, sensitized, varied alloy composition etc. would be evaluated in this loop in flowing nitric acid of a known concentration at different flow velocities (up to 1.55 m/sec) and temperatures (313, 333, 353 and 380 K, and in vapour phase). The data generated over a long period of exposure (up to 10,000 h) would be used to arrive at an acceptable corrosion rate of AISI type 304L SS used for applications in nitric acid service. The availability of such reliable and useful data will be helpful in predicting the remnant life of the components used in the reprocessing plants by developing suitable analytical and modelling tools of the corrosion processes.

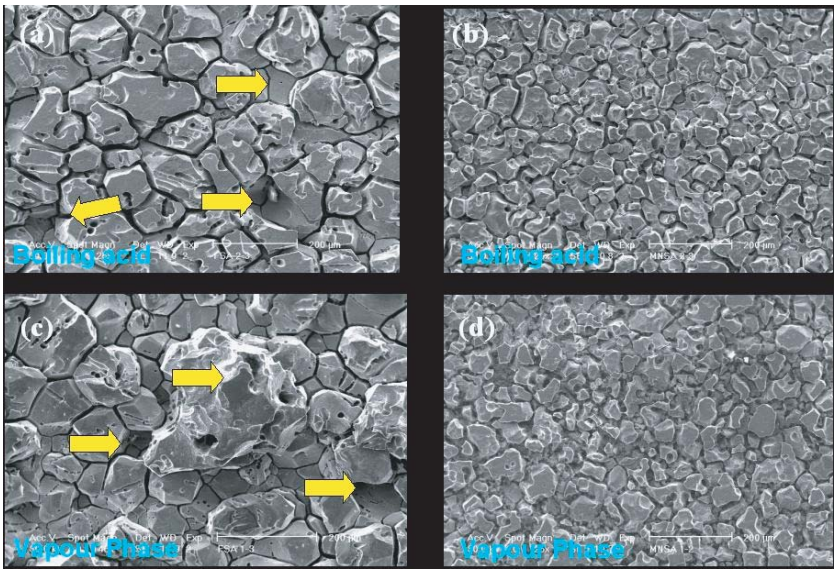

Fig. 2. SEM micrographs showing grain boundary corrosion and grain dropping for FRFRP solution-annealed SS, (a) and (c), and grain boundary corrosion for NAG SS, after the second 1000 h campaign.

Currently the loop is operating with flowing 6 N nitric acid at 1.25 m/s velocity, and AISI type 304L SS samples of solution-annealed, sensitized (923 K/ 1 h) and welded conditions, used in fast reactor fuel reprocessing plant (FRFRP), are being tested. In addition, the indigenously developed nitric acid grade (NAG) type 304L SS from MIDHANI, Hyderabad, in solution-annealed condition is also tested. The loop has successfully completed 100 h, 250 h, 500 h, 1000 (first) h and 1000 (second) h campaigns of operation. Results obtained after 100 h, 250 h, 500 h, 1000 (first) h and 1000 (second) h of operation indicated that the samples showed marginal corrosion rates (< 5 mils per year) up to 80°C of testing. However, at boiling and vapour phase conditions significant corrosion rates were obtained. The normalized corrosion rates for solution annealed FRFRP and NAG SS at boiling condition is shown in Fig. 1.

The chemical analyses of the nickel and iron present in the loop acid after the campaigns are also depicted in the figure. It can be noticed that the normalized corrosion rate of the FRFRP solution annealed 304L SS is below 8 mils per year (mpy) while that of NAG 304L SS is below 4 mpy. The chemical analyses indicated that the iron content of the loop acid is continuously increasing to 2600 ppm as the duration of operation increased. The nickel content was almost steady around 400 ppm and a tendency to saturation is noticed. Nondestructive testing of the samples using eddy current and ultrasonic methods did not reveal any significant defects on the surface of the samples that were investigated. Examination of the tested samples by scanning electron microscopy (SEM) showed grain boundary attack for all samples, and the samples tested in vapour phase condition showed significant grain dropping on the surface (Fig. 2). The results indicated the following : (i) intergranular corrosion with grain dropping is the mode of corrosion, (ii) normalized corrosion rates are below 8 mpy, (iii) the corrosion rate of NAG SS is better than that of conventional SS, and (iv) the attack is marginal for detection by NDT methods. Presently, the loop is operating with samples for a third 1000 h campaign, and the testing will continue for more 1000-hour operations up to 10,000 h in the future.

4.14 Geotechnical Characterization of Kokkilamedu Site

To characterize the Kokilamedu site for locating the Fast reactor fuel cycle Facility (FRFCF), detailed site-specific geotechnical investigations along with the seismic refraction survey were carried out.

Boreholes were drilled in a 30m X 30m grid for all safety related structures as per USNRC guidelines and at least one borehole was proposed for other major buildings. The depth of bore holes was 40m for safety related structures and 20m for other non-safety related structures. The location of the bore holes along with the seismic refraction survey profile is shown in Fig.1. Besides bore hole investigations, cross hole tests, pressure meter tests, permeability tests in rock core and overburden soil, chemical analyses of soil and water samples from bore holes, lab tests on soil samples and rock cores were proposed. This investigation provides the necessary information for establishing broad design parameters related to the site and its characteristics.

To decide the founding level and to design the foundations of civil structures, the subsurface strata information

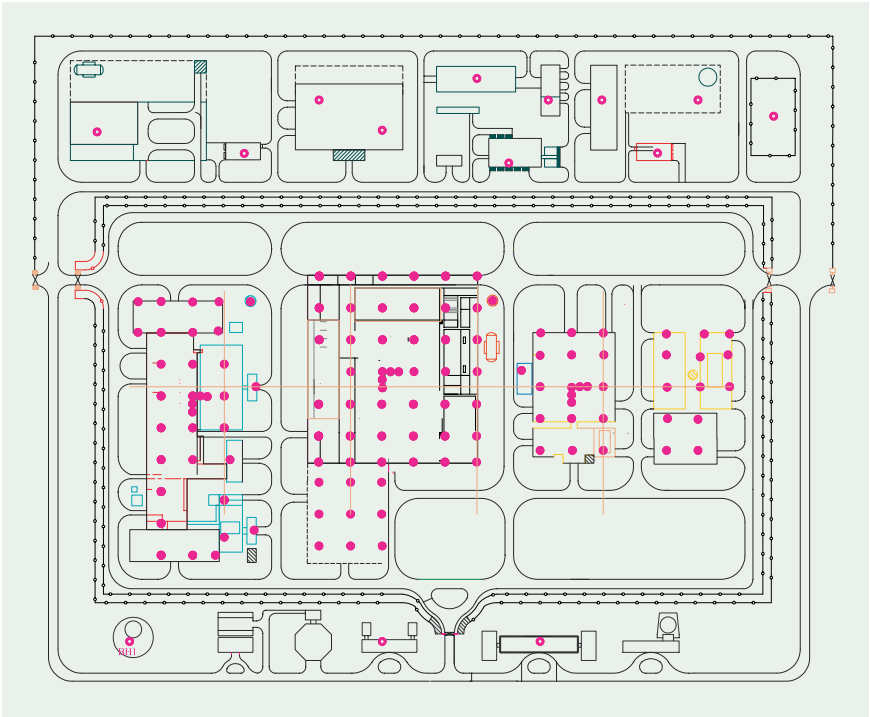

Fig. 1. Bore hole plan and seismic refraction traverse

Fig. 2. Photograph showing typical rock core sample.

including rock topography is essential. A continuous seismic refraction survey along five traverses was carried out at the Kokkilamedu site to decipher the subsurface stratigraphy including rock topography and its quality. The refraction survey was conducted along five traverses of lengths varying between 225m and 555m. Of these traverses, one central profile of length 555m was conducted in the north-south direction. The remaining four cross-traverses of length 225m each were taken perpendicular to the central profile.Cross-traverses were aligned in the east-west direction.

The detailed geotechnical investigations revealed that the site consisted of a top layer of loose to dense sand with a standard penetration

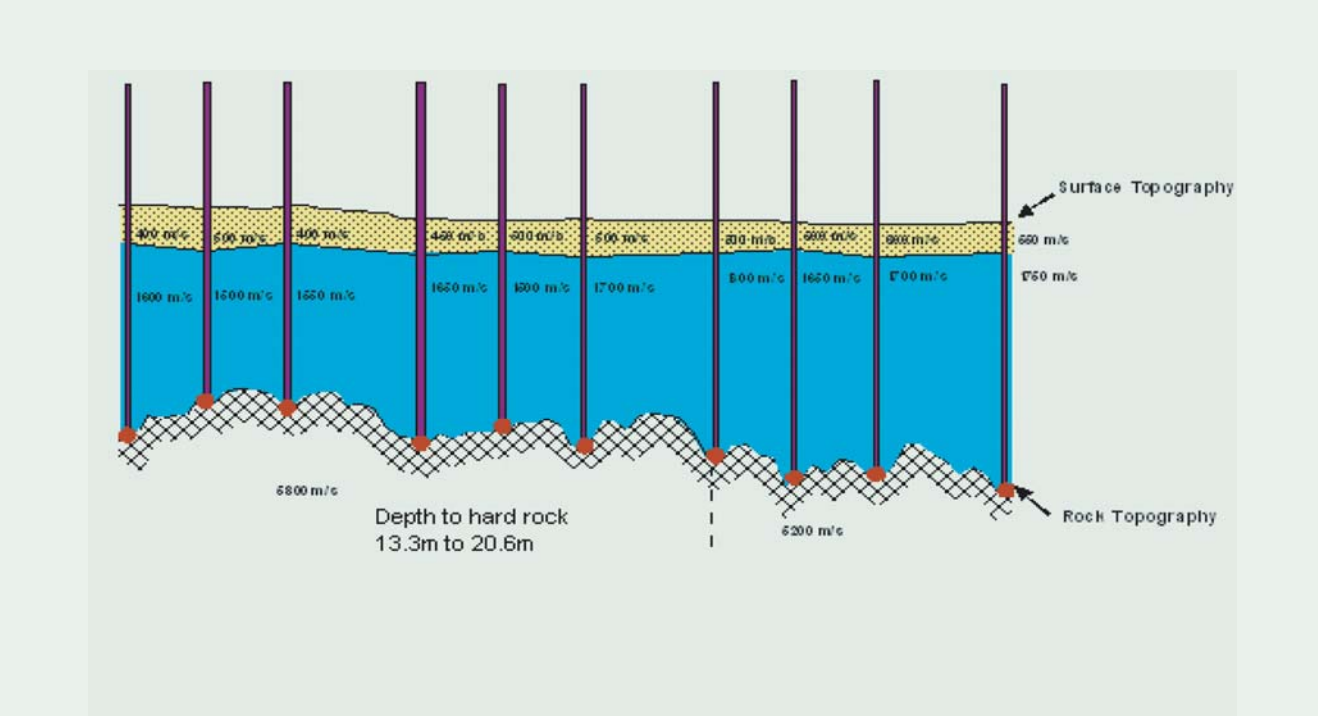

Fig. 3. Depth section along central profile

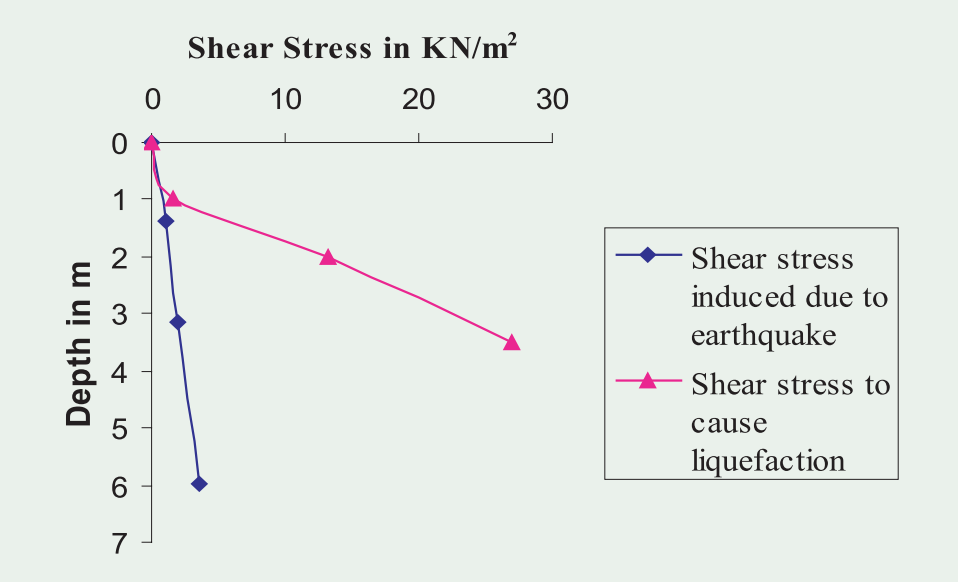

Fig. 4. Variation of cyclic shear stress due to earthquake and the stress required to initiate liquifaction.

resistance varying from 2 to 61. The thickness of this layer was 3.5 to 7.6m. This layer was followed by medium to stiff clay of thickness varying from 1.9 to 4.5m. A layer of weathered rock was encountered below this clay layer and its thickness ranged from 5.5 to 10.85m. The standard penetration resistance of the weathered rock layer was more than 100. Bed rock (compression wave velocity greater than 2000 m/sec) was encountered at a depth of 15m to 20m below the ground level. The rock quality designation (RQD) of the rock core varied from 50 to 100 which indicated the quality of rock as good. A typical photograph showing the rock core sample is shown in Fig. 2.

Results of the refraction traverses revealed that the subsurface comprises three layers. The top layer was interpreted to be loose sand. The second layer matched with saturated sand /weathered rock. The third layer was inferred to be granite gneiss rock. The compression wave velocity of the top layer varied from 300 m/sec to 950 m/sec and its thickness in general was evaluated to be between 2m and 4m except below one cross-traverse where the same was found to be 9.6m. The compression wave velocity of saturated sand ranged from 1500 m/sec to 2000 m/sec. Compressional rock velocity varied between 4400 m/sec and 5800 m/sec. This order of wave velocity for granite gneiss indicates good quality of rock. (The typical compression wave velocity of sound granite gneiss rock varies from 4000m/sec to 6000m/sec). Bed rock was encountered at 11.2 to 20.6m below ground level in seismic refraction survey. A typical section showing the subsurface profile along the central traverse is shown in Fig.3. Generally a rock core sample with an RQD more than 50% can be compared with the compression wave velocity obtained from the seismic refraction survey. The RQD value obtained from geotechnical investigation varied from 50 to 90 which indicated that compressional wave velocity of bed rock obtained from seismic refraction survey and RQD value of rock cores obtained from site specific geotechnical investigation were matching. The results of the refraction survey did not reveal any fault or major shear zone which might pose foundation problems.

Since the top sandy layer is susceptible to liquefaction (a phenomenon in which the cohesion-less soil looses its shear strength during vibratory motion under saturated condition), liquefaction analysis was carried out for the top sand layer (having varying

thickness in different locations with a maximum of 7m) with the observed standard penetration resistance value. The ground water table was assumed at the ground level for liquefaction analysis. The variation of the average shear stress induced due to a design earthquake and shear stress (stress produced due to cyclic loading like earthquake) required to initiate liquefaction were plotted along the depth, for different locations.
A typical graph for a location is shown in Fig.4. From these graphs, the cyclic shear stress to initiate liquefaction was found to be more than the shear stress due to the earthquake. The factor of safety against liquefaction varied from 1.21 to 4.66. As per the IAEA Safety Series No.50-SG-S8 - Safety Aspects of Foundations of Nuclear Power Plant - the factor of safety against liquefaction should not be less than 1.1, which suggests that the site studied is safe against liquefaction.

The possibility of liquefaction in the sandy layers and the presence of clay layer is a major factor in deciding the type of foundation. The geotechnical investigations at the site and seismic refraction survey revealed the presence of good quality rock, at a reasonable depth of 15 to 20 m. The site is not likely to liquefy as there is an adequate factor of safety against liquefaction. Further, the results of the refraction survey did not reveal any fault or major shear zone. Hence the foundation of the safety related structures can be at appropriate depths depending on the safety classification of the building. Thus, from the geotechnical investigation carried out, it is concluded that the site is suitable for the establishment of the FRFCF.

4.15 Current Status of the Demonstration Fast Reactor Fuel Reprocessing Plant (DFRP)

After the successful campaign of the 100 GWd/t burnup FBTR fuel reprocessing at the LMC, the fine-tuning of the design of important equipment such as chopper, dissolver, centrifuge and centrifugal extractors has been completed. The conceptual design of the in-cell cranes has been completed and the drawings have been released for fabrication. The titanium dissolvers and titanium electrolyzers are being fabricated. The fabrication of centrifugal extractors and sampling systems is in an advanced stage of completion.

Fig. 1. Equipment and piping erection in the DFRP cell

The experience in LMC operation was utilized to update the process flowsheet and the liquid transfer systems. This has aided in fine-tuning the piping engineering.

The design of the Head End Facility (HEF) to dismantle the FBTR and PFBR fuel subassemblies has been completed. This is intended to aid in dismantling the PFBR fuel subassembly so that it is possible to demonstrate the reprocessing of power reactor mixed oxide fuel.

The Atomic Energy Regulatory Board (AERB) has constituted a Project Design Safety Committee for review. It is planned to start the commissioning activity by 2007. Fig. 1. shows a typical construction activity.

CHAPTER 5

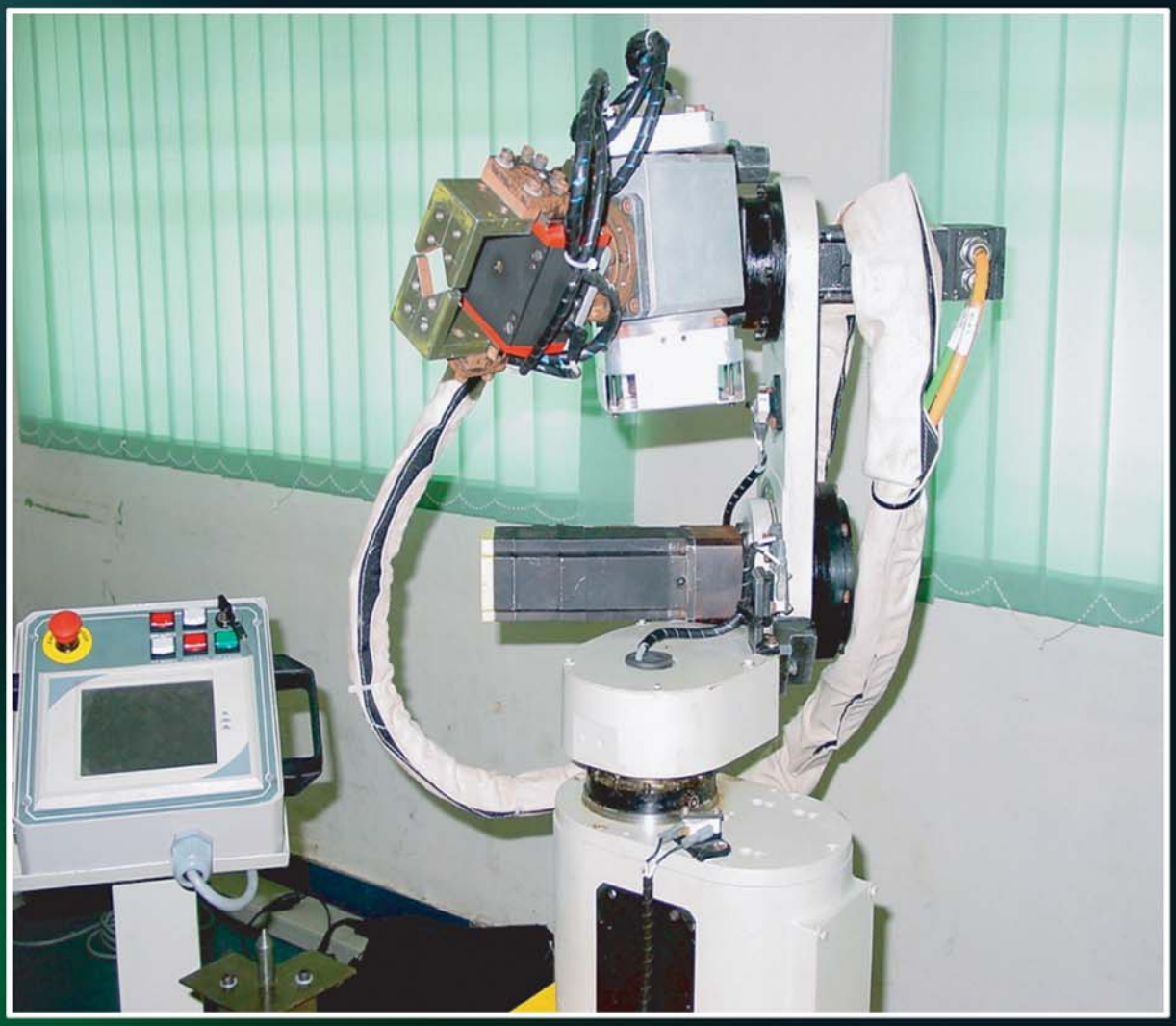

Enabling Technologies

5.1 Studies on Low Cycle Fatigue and Creep-Fatigue Interaction in Modified 9 Cr-1 Mo Steel

The high temperature components of PFBR are subjected to temperature gradient induced thermal stresses, which are cyclic in nature as a result of start-ups, shutdowns and transients. Furthermore, steady state loading at elevated temperatures in combination with cyclic loading leads to creep-fatigue interaction (CFI) damage. Therefore, resistance to low cycle fatigue (LCF) and creep-fatigue interaction are important criteria in the design of these components. Modified 9Cr-1Mo ferritic steel has been chosen for the steam generator components owing to its beneficial attributes such as a high thermal conductivity and a low thermal expansion coefficient in addition to a good compatibility with liquid sodium. Fatigue tests were carried out on an extruded pipe of 30mm wall thickness at a constant strain rate at different strain amplitudes at 873K. Creep-fatigue interaction tests were conducted by introducing hold-at-peak-tension and in peak compression for periods in the range 1 min to 10 min at 873 K.

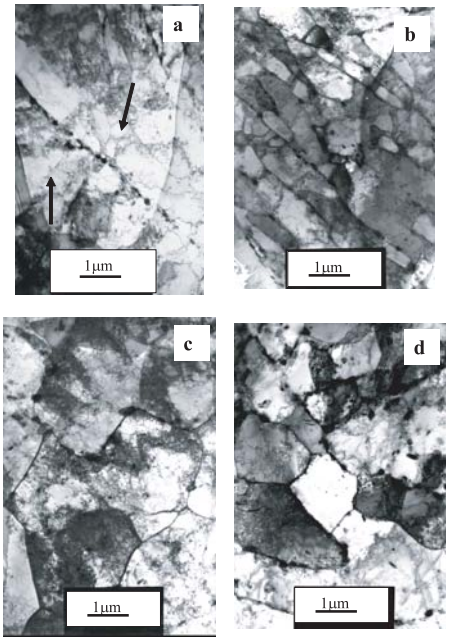

Fig. 2. Microstructural changes occurring in a fatigue tested sample during (a) continuous cycling shows a highly heterogeneous microstructure with ill-defined cell structure (b) introduction of 1 minute tension hold leads to more well-defined cells (c) increased duration of hold of 10 minute in tension leads to a well-defined equiaxed sub-grains configuration and (d) 1 minute compression hold gives well defined sub grain

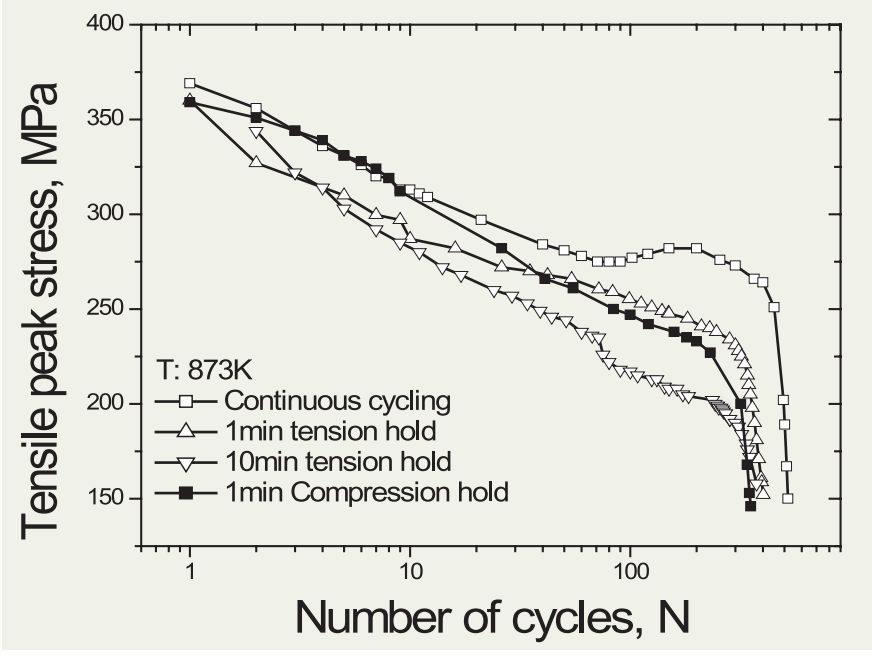

Fig. 1. Cyclic stress response as a function of hold time in tension and compression peaks

The alloy observed in general, exhibited continuous cyclic softening typical of high strength materials. The overall cyclic stress response is lower in hold time tests compared to continuous cycling (Fig. 1). Detailed transmission electron microscopy of the samples tested to various fractions of

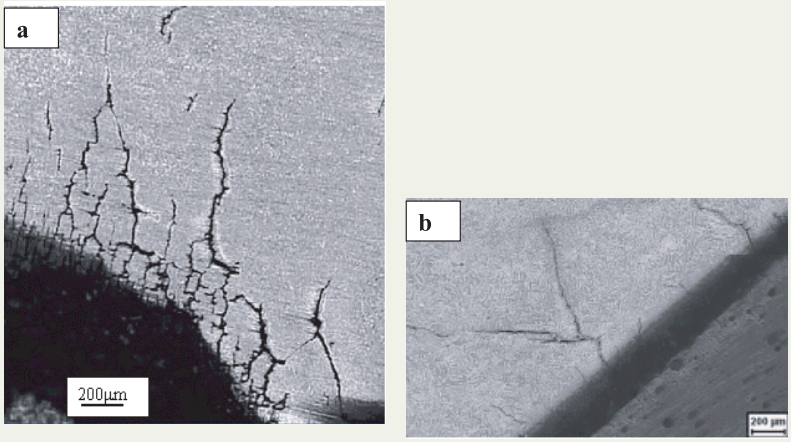

Fig. 3. Optical metallograph of the longitudinal section of a fatigue tested sample depicting secondary cracks under (a) 1 minute compression hold (b) 1 minute tension hold

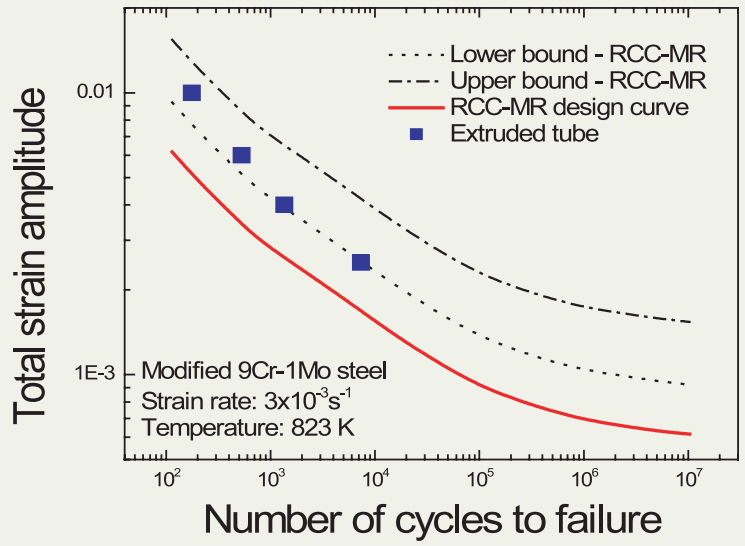

Fig. 4. Comparison of data with RCC MR code at 823 K

fatigue life indicated that at room temperature, the cyclic softening is attributed to the annihilation of dislocations while at 873 K, it is ascribed to the formation of cells and coarsening of the carbide precipitates. The substructure formed during continuous cycling without the introduction of hold is highly heterogeneous (Fig. 2(a)). The introduction of one minute tension hold during cycling resulted in more well-defined cells (Fig. 2 (b)). On increasing the tension hold time, dislocation substructure assumed the configuration of well-defined equiaxed sub-grains (Fig. 2(c)). The decrease in fatigue strength (decrease in cyclic stress response) with increase in hold time (reduced frequency of testing) can be attributed to the rearrangement/annihilation of dislocations and coarsening of carbides with increase in testing time. Unlike under one minute tension hold, the one minute compression hold developed well defined sub-grains (Fig. 2(d)). The fatigue life decreased with the introduction of hold and application of a one minute compression hold period resulted in a far more deleterious effect on the fatigue life than application of a one minute hold under tension. Optical microscopy conducted on the longitudinal section of the tested samples (1 minute tension and 1 minute compression), showed multiple crack initiation sites and oxidation assisted crack initiation and propagation (Fig. 3). It has been found that oxide layer spalls off during tension hold due to compressive stresses on them whereas the oxide layer cracks during compression hold due to tensile stresses. The data generated in IGCAR is compared with the best fit curve derived from the RCC-MR code for this steel at 823 K in Fig.4. All the data lie above the lower bound curve and thus it indicates the RCC-MR curve can be safely used for design purposes.

5.2 Low Cycle Fatigue Properties of Indigenous Modified 9Cr-1Mo Steel in Sodium Environment

In LMFBRs, the secondary sodium transfers heat to the steam generators to raise steam for running turbines. In this process, the tube sheet experiences low cycle fatigue (LCF) conditions. Hence, the use of liquid sodium as a heat transfer medium for LMFBRs necessitates the assessment of the compatibility of structural materials, and the influence of long-term exposure to sodium on the creep, low cycle fatigue and creep-fatigue interaction (CFI) properties. To evaluate the LCF and CFI properties of modified 9Cr-1Mo steel, a fatigue test chamber has been developed in-house . The specimen is enclosed within a miniature primary bellow surrounding which, a secondary bellow is provided for safety. Sodium temperature is maintained within ± 2K of the test temperature and the sodium velocity was maintained at 2 m/s in the test chamber. The oxygen level in the loop is maintained at less than 2 ppm. LCF tests on modified 9Cr-1Mo steel at 823 K and 873 K have been conducted at a constant strain rate of 3×10^{-3} s^{-1} employing strain ranges varying from ±0.4 % to ±1.0%.

The fatigue life of modified 9Cr-1Mo steel produced indigenously has been evaluated in flowing sodium. The fatigue life data in sodium are compared with that in air obtained under identical testing conditions at 823 K (Fig.1). The results show that the LCF life of modified 9Cr-1Mo steel in a sodium environment is significantly higher, compared to that obtained in an air environment. A few tests have also been conducted above the upper temperature of end use for this material at 873 K (Fig.2). At this temperature also, there is a significant improvement in LCF life for the tests conducted in a sodium environment. The lack of oxidation in the sodium environment is considered to

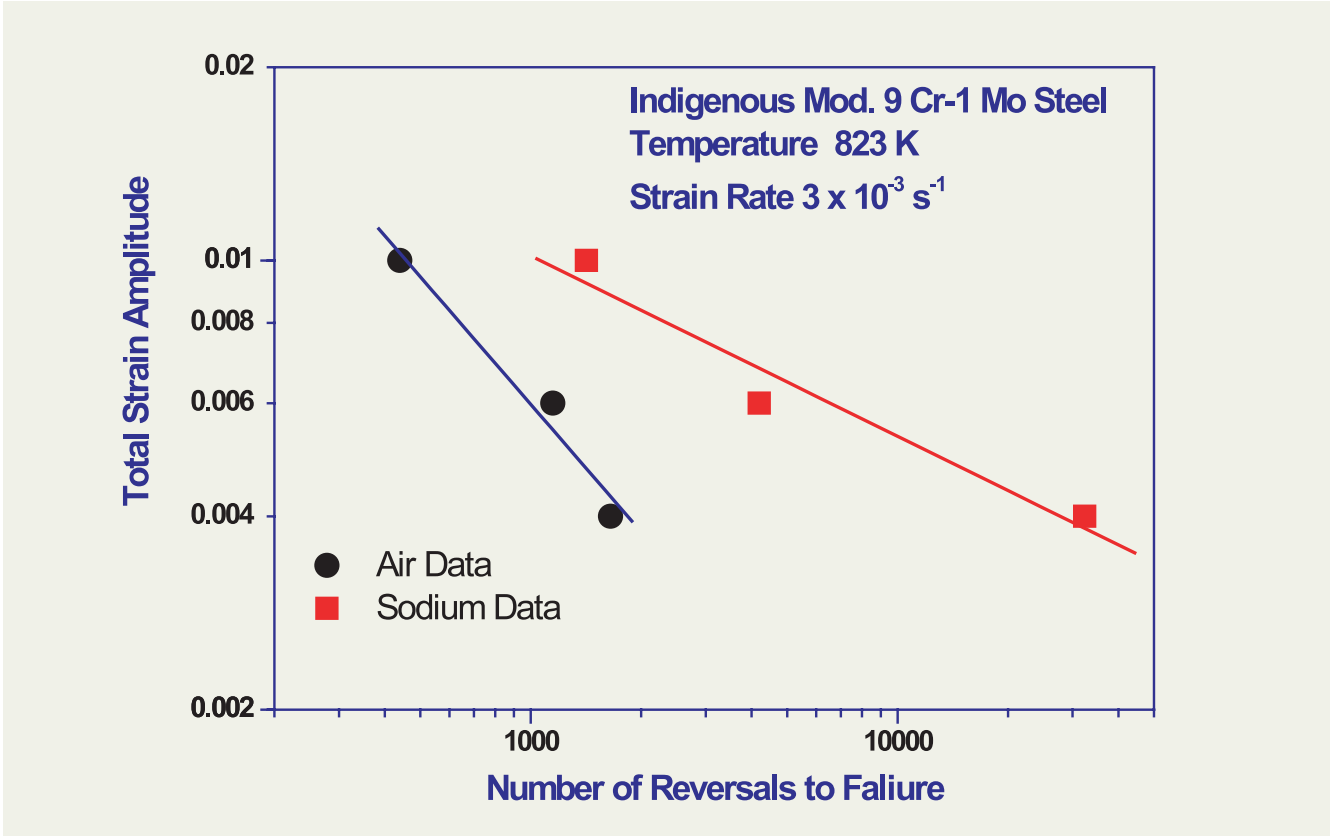

Fig. 1. Strain-Life Plot at 823 K

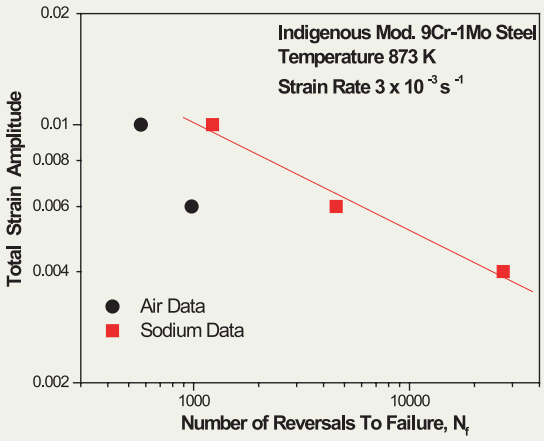

Fig. 2. Strain-life plot at 873 K

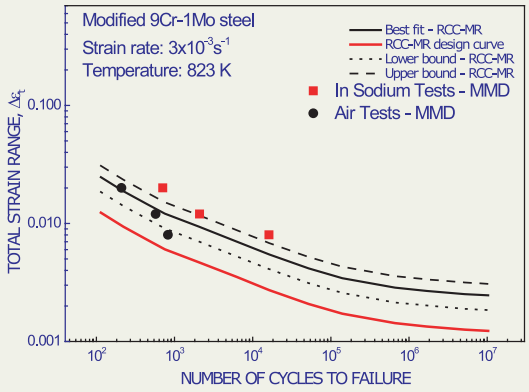

Fig.3 Comparison of data with RCCMR codes

be responsible for the delayed crack initiation and consequent increase in fatigue life. It must be pointed out that the LCF life at lower strain ranges (close to the HCF regime) is dominated by crack initiation. Since crack initiation in fatigue usually starts from the surface, the lack of oxidation in sodium environment delays crack initiation, with a consequent increase in life. Therefore, the beneficial effect of sodium is more predominant at lower strain ranges.

The data generated in the Mechanical Metallurgy Division in a sodium environment, is compared with the data provided in the RCCMR code for modified 9Cr-1Mo Steel at 823 K in figure 3.The data pertaining to sodium tests lie above the upper bound curve of the air data. These results clearly indicate that design against LCF with air data is conservative.

5.3 Thermal Stability of Modified 9Cr-1Mo Ferritic Steel Using Drop Calorimetry Studies

High chromium ferritic steels are the preferred structural materials for the core of metal-fuelled fast reactors, in view of their good neutron irradiation swelling resistance, fairly adequate mechanical properties and corrosion resistance. A study on the physical metallurgy of ferritic steels is interesting both on the basic and applied fronts. The presence of (i) precipitation reactions upon thermal ageing and their significant impact on subsequent mechanical properties, (ii) the magnetic transition phenomenon and (iii) the emergence of high temperature austenite structure, which, upon fast cooling, gives rise to a variety of martensite and related products, make the study of physical metallurgy of ferritic steels very challenging. These phenomena are dictated by both thermodynamic and kinetic considerations. While the physical metallurgy literature on ferritic steels is ripe with many investigations devoted to kinetic aspects, the intrinsic thermodynamic stability of the ferrite matrix itself does not seem to have been investigated that extensively. A major reason for this is the absence of reliable experimental thermodynamic stability parameters which enable the subsequent use of CALPHAD or related modelling techniques to arrive at a meaningful description of the overall thermal stability of ferritic steel. In view of this situation, a study on the thermodynamic characterisation of the stability of modified 9Cr-1Mo steels has

been undertaken. The objective of this study is to generate experimental thermodynamic data for the whole temperature range of stability of the ferritic phase. In particular, the diverse phase transition points, especially the corresponding enthalpy effects etc., are characterised as a function of varying heat treatments.

As a first step, the thermal properties under normalised and tempered conditions is monitored using accurate drop calorimetry measurements in the temperature range 295 to 1300 K. The typical results are displayed in Figure 1. The experimental enthalpy results reveal two major and distinct transformation features: the first one is a smeared hump which is spread around 915 K, and the other one is fairly sharp and is placed at ~1050 K. The first transformation signifies the culmination of the complex thermal relaxation of the tempered ferrite matrix, with a measurable enthalpy jump of about 50 - 75 J/g. The lack of a sharp transformation arrest implies that the tempering of the ferritic matrix is a continuous reaction, spread over a broad temperature range. The early stages of this tempering, being characterised by small endothermic energy consumptions are not visible in the curve. However, this can be seen as a visible upward rise in the specific heat versus temperature curve. Corroboration of this result in the light of the general precipitation studies done on ferritic steels suggests that the onset of carbide precipitation in the ferrite matrix is what is responsible for this hump in the otherwise smoothly rising enthalpy that is characteristic of a pure ferrite matrix.

The second transformation arrest T_c corresponds to the transformation of magnetic ferrite to a non-magnetic state. The present experiments suggest a curie temperature of 1013 ± 5 K. The third transformation arrest, namely T_3 at 1273 ± 5 K heralds the formation of the austenite. One important observation that emerges from Fig. 1 is that the enthalpy content of ferritic steel shows a steady and pronounced upward rise with the onset of various transformation sequences. From the enthalpy data, the C_p has been estimated and with this the other thermodynamic functions of modified 9Cr-1Mo have also been generated. Thus for example, a value of 450 J kg^{-1} K^{-1} has been estimated for C_p at 323 K. At about 923 K, the typical specific heat capacity values are of the order, 760 to 780 J kg^{-1} K^{-1}. At the magnetic transformation point, the C_p is found to rise to as high as 1180 J kg^{-1} K^{-1}. A preliminary analysis revealed that in the temperature range of 273 to 973 K, the magnetic contribution to the stability of the ferrite phase is very significant.

Considering the long term and sustained interest in ferritic steels, it is planned that the data so generated will be augmented by comprehensive modelling studies that would enable the emergence of a holistic picture of the thermal stability of this steel.

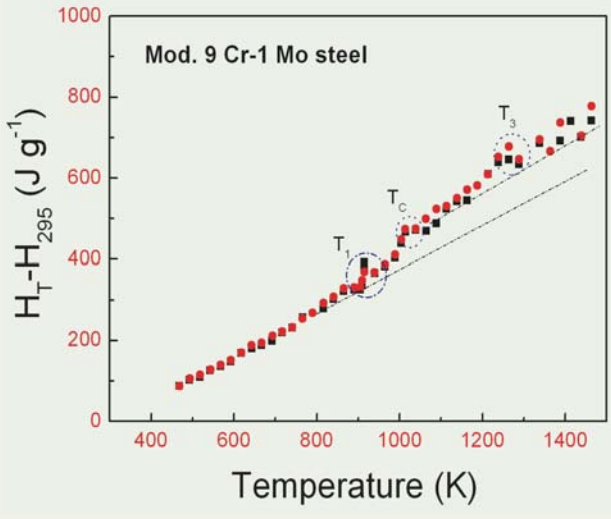

Fig. 1. Enthalpy increment vs temperature for the modified 9Cr-1Mo steel

5.4 Assessment of Structural Integrity of Components made of 2.25Cr-1Mo Steel after Long Service

Assessment of the structural integrity of high temperature components of nuclear reactors is important because of the need to avoid costly forced outages and catastrophic failures. It also enables extension of service life of the components even after completion of the original design life. Creep, tensile strength and fracture toughness are important design considerations for these components. Extension of life depends on the extent of degradation in these properties due to exposure during service. Residual mechanical properties of 2.25Cr-1Mo steel that was in service in a thermal power plant for 120,000 hours at 813 K under a steam pressure of 2.4 MPa, have been studied. Creep properties were evaluated in the temperature range 813-913 K. Fig. 1 shows the variation of creep rupture strength of service exposed and virgin steels as a function of Larson-Miller parameter (LMP) No significant degradation in the creep strength was observed due to service exposure. Figure 2 shows the variation of impact energy with test temperature for the service-exposed and virgin steels. The Charpy transition temperatures for impact energies of 68J and 110J are 264K and 278K respectively. Close proximity of Charpy upper-shelf energy of service-exposed steel to that of virgin steel and the low values of transition temperatures imply that the material has not been embrittled even after exposure to long term service at high temperature.

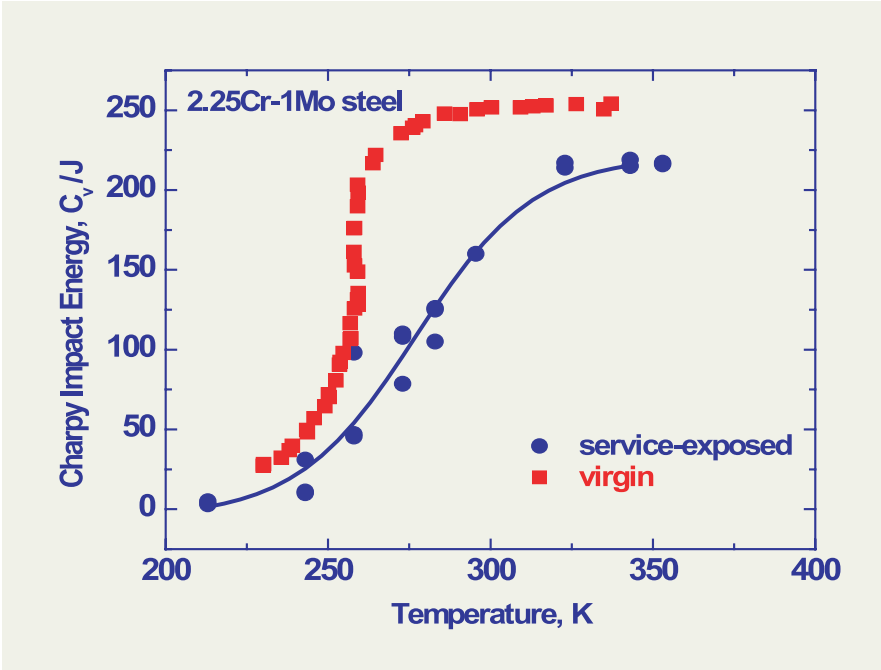

Fig. 2. Charpy transition curve for a service-exposed and virgin 2.25Cr-1Mo steel.

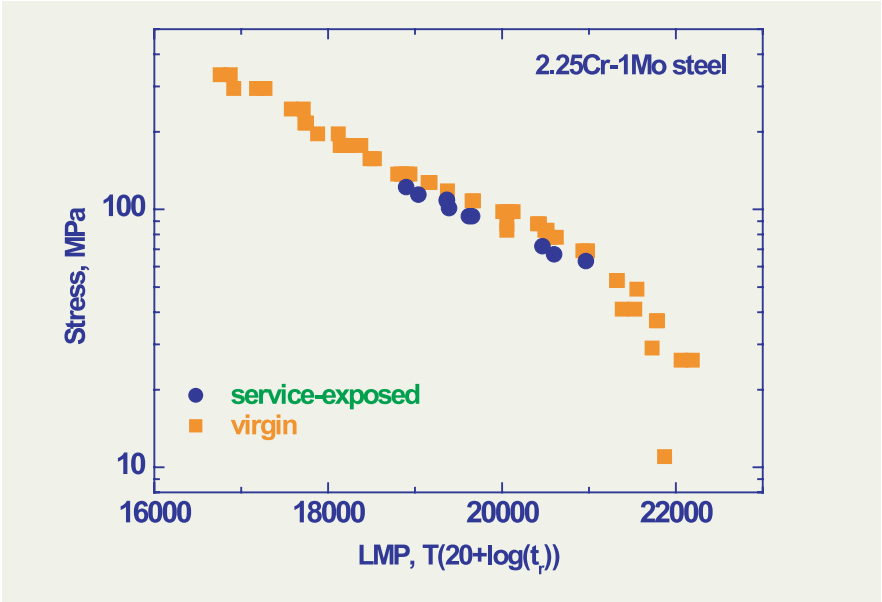

Fig. 1. Comparison of creep properties of service-exposed and virgin 2.25Cr-1Mo steel.

5.5 Evaluation of Low Cycle Fatigue Properties of Indigenous 316LN Base Metal and 316LN/316N Joints

Type 316LN austenitic stainless steel is the currently favoured structural material in the primary side of the LMFBR. Resistance to Low Cycle Fatigue (LCF) and Creep-Fatigue are important factors in the design of LMFBR components. Moreover, some of the structural components (for ex: reactor main vessel) are made in parts and integrated by welding. These weldments form one of the potential sources of Low Cycle Fatigue failure and therefore welded structures are the critical sections to be considered carefully in the design of such components. In view of this, it is necessary to understand the cyclic deformation and fracture behavior of 316LN stainless steel and its weld joints under various loading conditions representative of that encountered in service. This study focusses on the Low Cycle Fatigue behavior of indigenously developed 316LN Stainless Steel and 316LN/316N weld joints (fabricated from indigenously developed 316LN SS and 316Nelectrodes). The base material was procured from SAIL, Rourkela, and electrodes were developed at Mailam Industries, Pondicherry.

Total axial strain controlled fatigue tests were carried out in the temperature range 773 - 873 K at strain amplitudes in the range ±0.25 to 1.0%. Further, the effect of the strain rate on LCF was studied in the strain rate range 3×10^{-5} s^{-1} to 3×10^{-2} s^{-1}at 773, 823 and 873 K on weld joints.

Cyclic stress response behaviour and fatigue life variation of the weld metal and weld joints under different testing conditions were compared with that of the base metal. In general, at all test temperatures, the base metal showed an initial hardening followed by a saturated stress response while the weld metal and weld joints showed a softening regime in between. The half-life stress increased with decreasing strain rate in the weld joints. Fatigue life decreased with increase in temperature between 773 K - 873 K in both base metal and weld joints while the weld joints showed lower fatigue lives compared to base metal (Fig.1). Dynamic Strain Aging (DSA) played a considerable role in reducing the fatigue life of the base metal in the range 773 - 873 K. DSA in fatigue causes high cyclic hardening, decrease in plastic strain amplitude per cycle, negative strain rate stress response, serrations on the stress strain hysteresis loop etc. DSA results from the locking of dislocations by solute atoms. The observed lower fatigue resistance of weld joints was due to crack initiation in Heat Affected Zone (HAZ) (Fig. 2).

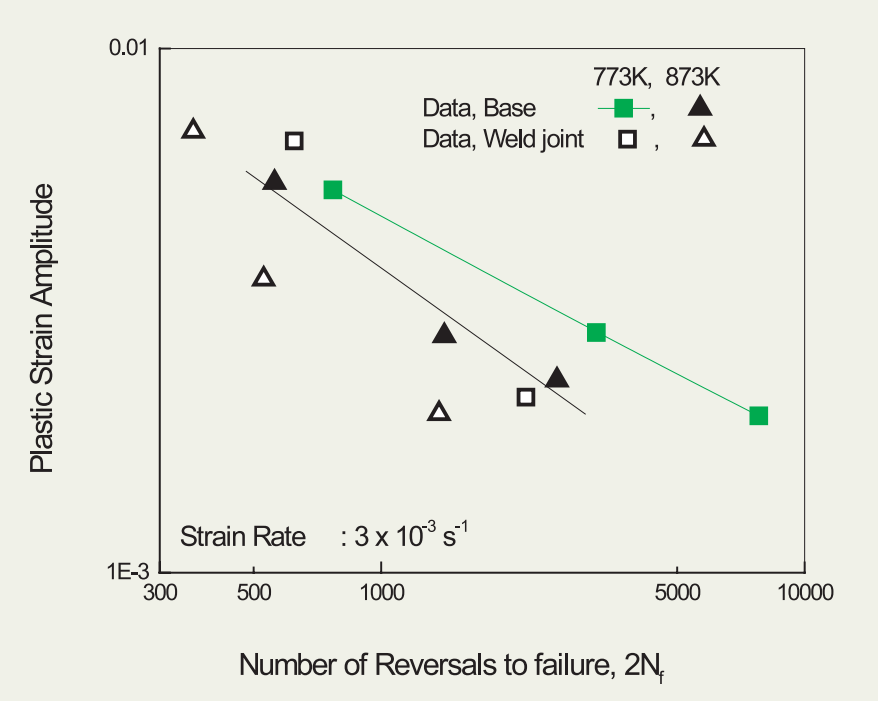

Fig. 1. Comparison of strain-life plots of 316LN SS base metal and 316LN / 316N weld joints at 773 K, 823 K and 873 K.

Further the effect of dynamic strain ageing on LCF life has been evaluated for the base, weld and weld joints. The drastic reduction in fatigue life of the weld joints with decreasing strain rate was due to deleterious effects of DSA. Fatigue-oxidation interaction has been found to be responsible for the reduction in fatigue life at 873 K. The data generated was compared with that of the joints of imported base and electrodes, and data available from the literature and the RCCMR code (Fig. 3). It is observed that the design curve for weld joint is conservative.

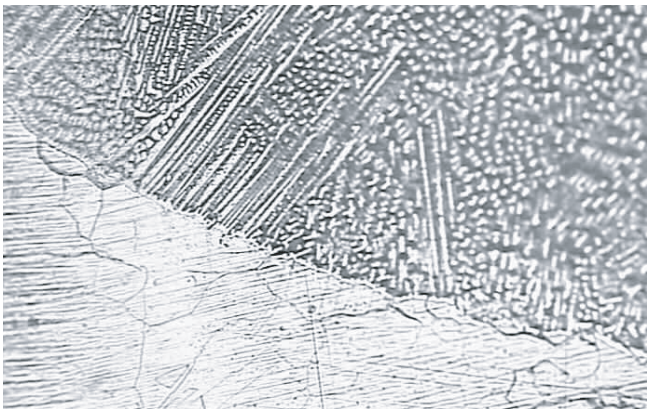

Fig. 2. Cracking near the weld and base metal interface, 823K

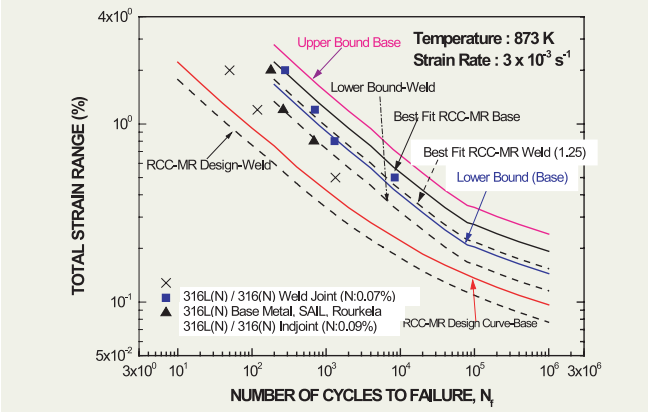

Fig. 3. Comparison of strain-life data with RCC-MR design curves at 873 K

5.6 Optimum Hot Working Domain for 316LN Stainless Steel

AISI type 316LN austenitic stainless steel is the structural material for PFBR. The processing of this material needs careful attention in order to produce defect free products with controlled microstructure. The safe processing window for hot working of the indigenous 316LN stainless steel was identified using the compression test data processed by a computer code developed and was microstructurally validated. The computer code implements the dynamic material model and the continuum instability criteria and generates the processing map from digitised load-stroke data obtained from compression tests. The map clearly identifies the "safe" and "unsafe" domains for processing of a material in the temperature and strain rate space. The "unsafe" domain corresponds to the regimes of flow instability that should be avoided during processing.

Isothermal constant true strain rate compression testing was done on cylindrical samples of 316LN stainless steel from room temperature to 1473 K and strain rate range of 0.001 to 100 s^{-1} upto an engineering strain of 0.5. The flow stress values were corrected for the adiabatic temperature rise (measured using a thermocouple embedded in the specimen) during deformation by linear interpolation of the log (*flow stress*) vs. *1/T (T* = temperature in Kelvin). The log (*flow stress*) at a particular strain versus log (*strain rate*) data at different temperatures were fitted using a cubic spline and the strain rate sensitivity (*m*) was calculated as a function of strain rate. The efficiency of dissipation of power ($\eta = 2m/(m+1)$) through microstructural changes, was then calculated as a function of temperature and strain rate and plotted as an iso-efficiency contour map. The data were also used to evaluate the instability parameter as a function of temperature and strain rate and to obtain the instability map. The power dissipation and instability maps were superimposed to obtain the processing maps at

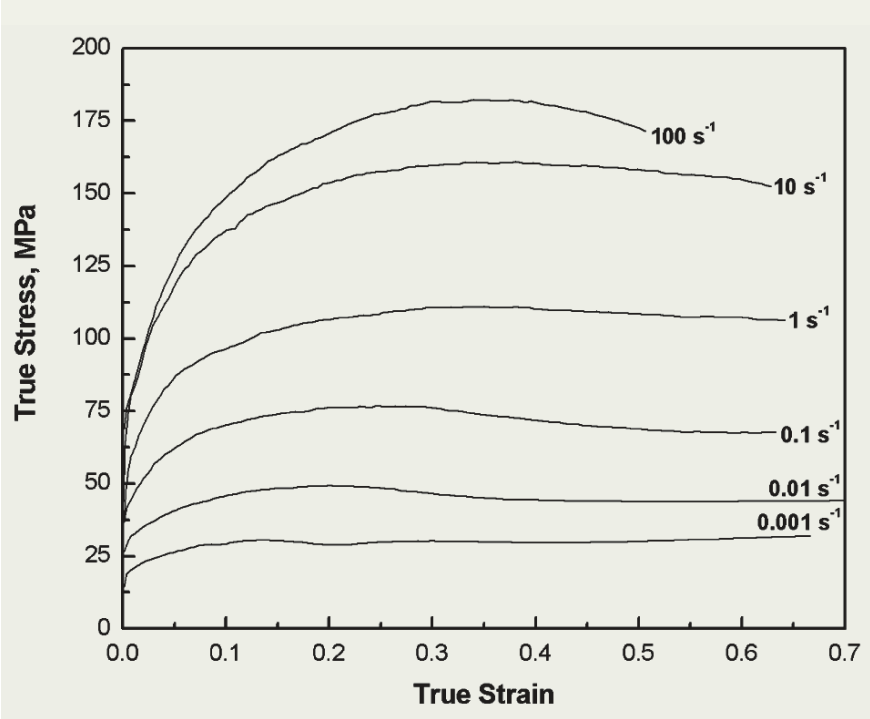

Fig. 1. Flow curves of indigenous 316LN stainless steel at 1473 K

various true strain levels up to 0.5.

The flow curves are evaluated for indigenous 316LN stainless steel from room temperature to 1473 K and in the strain rate range 0.001 s^{-1} to 100 s^{-1}. Typical flow curves at 1473 K are shown in Fig. 1. The flow curves at strain rates lower than 0.1 s^{-1} exhibited flow softening after reaching a peak stress at a critical strain and at higher strains, a steady-state flow stress is reached. The processing map in the strain rate - temperature space at a true strain of 0.5 is shown in Fig. 2. The hatched area on the map identifies the instability region. The optimum hot working domain for the indigenous 316LN stainless steel is in the temperature range of 1273 K to 1413 K and strain rate range of 0.001 s^{-1} to 0.01 s^{-1} where the efficiency of power dissipation varied in the range 34 % to 42 %. The safe domain is microstructurally characterised using optical metallography. The peak efficiency of power dissipation is found to occur at 1373 K / 0.001s^{-1}. Based on the variation of efficiency parameter and the grain size in the safe zone, it is concluded that dynamic recrystallisation is the responsible mechanism in this domain. For obtaining finer grain size in the component at the finishing stages of the operation, lower temperatures of the domain may be chosen at the strain rate corresponding to the peak efficiency. The process is safer if the temperature and strain rate ranges do not enter the instability or cracking regimes of the maps at any stage of operation.

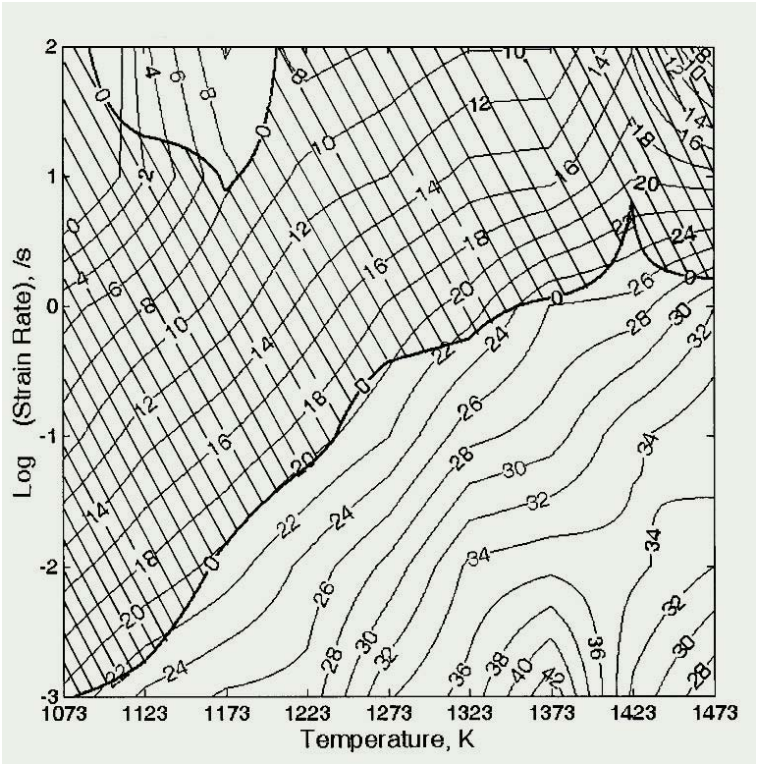

Fig. 2. Processing map of indigenous 316LN stainless steel at true strain = 0.5

5.7 Mechanistic Studies of Stress Corrosion Cracking in Type 316LN Stainless Steel using Acoustic Emission Technique

Acoustic emission (AE) is a powerful non-destructive evaluation tool for materials research. It has been used to study stress corrosion cracking (SCC), corrosion fatigue and hydrogen embrittlement, in a wide variety of materials. However, its use in the understanding of cracking mechanisms, detection of crack initiation, and other aspects of the corrosion cracking processes has been of recent interest. The AE phenomenon is the result of a transient elastic wave propagation generated by a rapid release of energy within a material due to changes in local stress and strain fields. It is a passive and non-invasive technique and remote monitoring is possible. In the present study, AE generated during SCC of AISI type 316LN stainless steel (SS) was interpreted to detect crack initiation and to pinpoint the micro-processes that caused the AE. SCC testing was carried out in 45% magnesium chloride solution at 413 K in the range of stress intensity factors (KI) of 13-26 MPa.m^{½} using the constant load testing method. The AE generated during the test were monitored with respect to time using a broad band frequency sensor. The least detectable amplitude of the system (21.6 dB) was taken as the threshold amplitude.

AE events covering a range of amplitudes ranging from 27.6 to 46.5 dB occurred during the test. Maximum AE activity of dislocation motion was observed at 31.2 dB. Fig. 1 shows a sudden increment in the AE counts and energy at the same time which was attributed to the SCC initiation, by carrying out interrupted tests. The observed AE activity in Fig. 1 was studied in detail by dividing it into four different regimes viz. start of the test (Region I), SCC initiation (Region II), early stages of SCC crack growth (Region III) and later stages of crack growth (Region IV). Fig. 2 (a) shows that during the early stages of the test (Region I), the AE was continuous. Hydrogen evolution was observed during this stage. As SCC initiation approached (Region II), the time duration between AE signals increased in (Fig. 2 b) . Hydrogen evolution ceased much before the initiation of SCC. Fig. 2 (c) and (d) show that the time interval between AE signals increased further with increasing crack growth (Regions III and IV). During crack growth, higher amplitude AE signals (> 39.8 dB) with high rise time (>120 µs) were not found to occur. Further analysis of the AE results with respect to the SCC crack

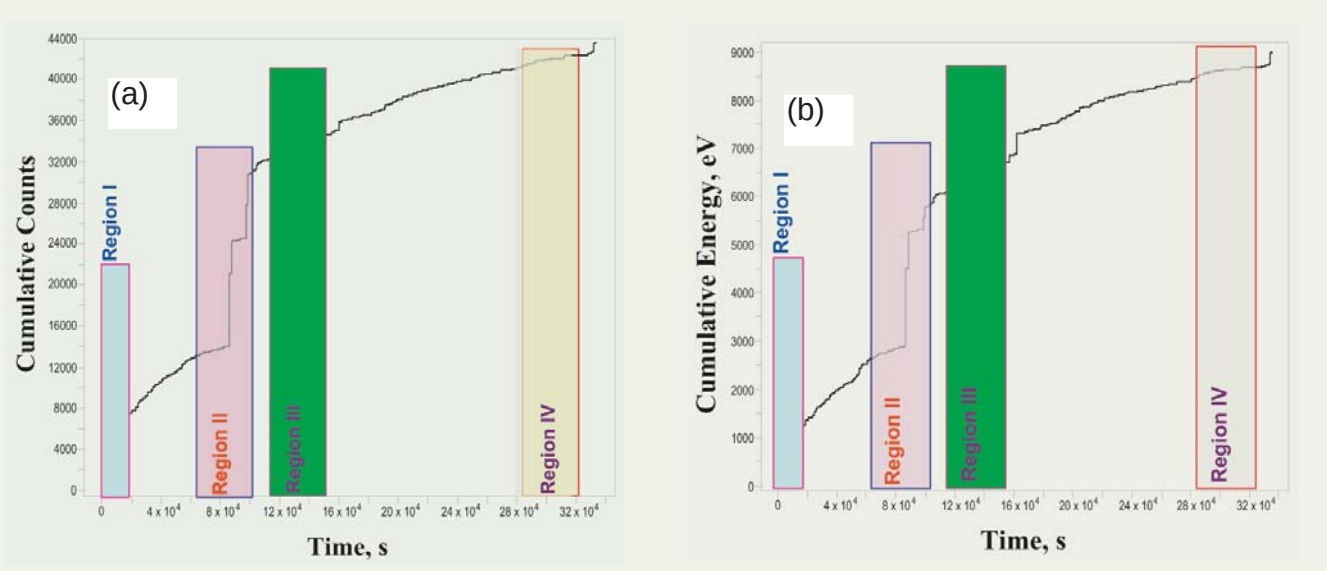

Fig.1. Sudden burst of (a) AE counts and (b) energy during initiation of SCC in type 316LN SS

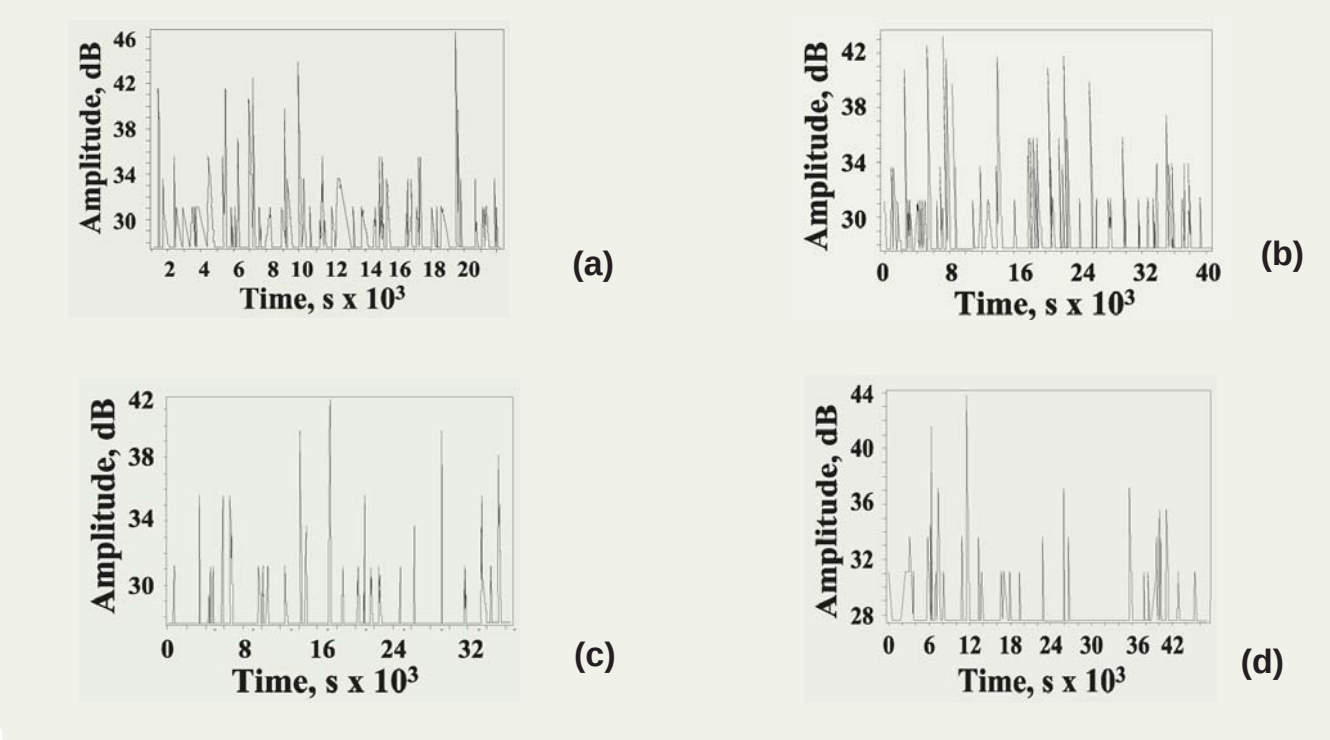

Fig. 2. The time period between two AE events increases from (a) start of test, (b) initiation, (c) early stages of crack growth and (d) later stages of crack growth

growth rate and KI was carried out. Fig. 3 shows that the rate of AE parameters decreased with increasing crack growth rate. This could be explained based on the triaxial state of the stress, ahead of the crack-tip which causes plastic deformation of the material ahead of the crack tip when the yield stress is exceeded. The plastic zone blunts the crack. As the crack length increases, the value of KI increases causing higher stress concentration and formation of larger plastic zone ahead of the crack tip, which causes greater blunting of the crack tip. Larger plastic zone requires longer times for resharpening of the crack for further crack propagation. This explains the larger time gaps between two AE events during the later stages of crack growth and the reduced AE rate with increasing crack growth rate. Each AE event could be attributed to the process of formation of a plastic zone. The time period between two AE events corresponded to the period of material dissolution that caused the crack growth. This observation was further confirmed in Fig. 4, which shows that the rates of AE counts and energy, reduced with increasing KI. Based on all the above observations, it was inferred that SCC occurred by a dissolution-controlled mechanism.

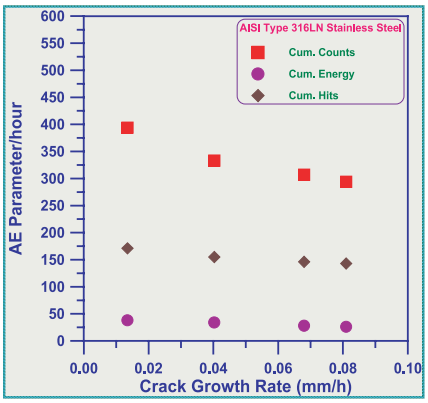

Fig. 3. Rate of AE parametersdecreases with increasing crack growth rate

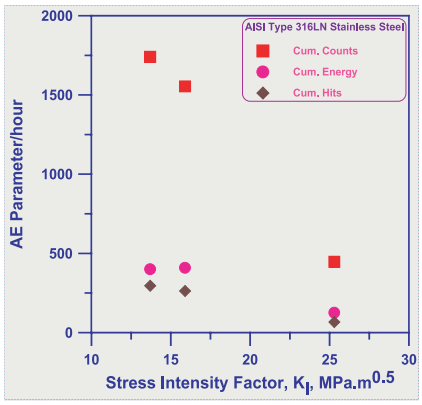

Fig. 4. Rate of AE parameters decreases with increasing KI

5.8 Stretchability of type 304 Stainless Steel Sheet: Effect of Prior Cold Work

Metastable austenitic stainless steels undergo a transformation to martensitic steel when deformed plastically at room temperature. This martensitic transformation strongly influences the mechanical properties of the material and contributes substantially to the excellent room temperature formability of the material. A study was undertaken to assess the stretchability of prior cold worked AISI type 304 sheet metal.

Stretchability is conventionally represented by its forming limit diagram which is a map in the principal strain space separating the safe strain states from the more severe states that result in failure. Failure is usually the appearance of a localised neck. In the study, the results, when plotted as forming limit diagrams, show lowering of the forming limits with increasing levels of prior strain. However when the prior cold work is also considered and the data are represented in terms of total equivalent strain as a function of strain ratio (Fig. 1), the trends are more complex. Increasing levels of cold work improves the total ductility over a wide range of strain ratios while the mill annealed and least cold worked specimens show higher limit strains in a portion of the positive minor strain region. In calculating the equivalent strain the following relation is used

$$\bar{\varepsilon} = \frac{2}{\sqrt{3}}\left[1+\rho+\rho^2\right]^{\frac{1}{2}}\varepsilon_1$$

where ε is the equivalent strain, $\rho = \varepsilon_2/\varepsilon_1$ and e_1 and e_2 are the principal strains on the plane of the sheet. Measurements of martensite just prior to the onset of flow localisation show roughly similar volume fractions forming during the stretching operations though the total volume fraction transformed increases with prior strain. This indicates a cessation of the transformation during stretching, resulting in the flow localisation. Literature indicates that the strain induced transformation is very sensitive to the temperature and exhibits a drastic decrease in the volume transformed with even a 20^0 rise in temperature. Since the stretching operations are all carried out at a strain rate of about 10^{-2} s^{-1}, it is concluded that the adiabatic heating during stretching intervenes to cause the cessation of the stain induced transformation, resulting in the lowering of the strain hardening rate and the concomitant formation of the localised neck. This is further supported by a study of the effect of forming speed on the forming limit diagrams for the same material that shows lowering of forming limits with increasing forming speed. The result also shows that the adiabatic temperature rise has

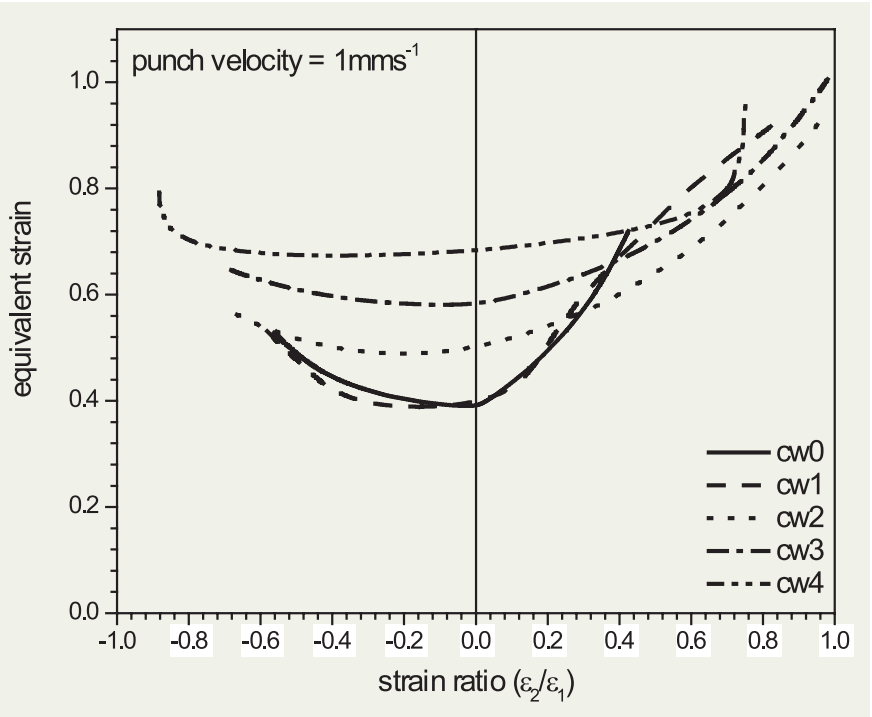

Fig. 1. Effect of prior cold work on the stretchability of type 304 sheet metal. The prior equivalent strains for cw1, cw2, cw3 and cw4 are 0.12, 0.26, 0.41 and 0.59 respectively. cw0 refers to the mill annealed condition.

a dominating influence over the positive strain rate sensitivity of the material.

The above explanation however does not account for the higher values of the total equivalent strain for the mill annealed and the least cold work conditions at strain ratios towards balanced biaxial. Experimentally it is known that the martensite forms at shear band intersections with the formation of an intersection and the probability that the intersection transforms to martensite depending on the state of stress. Application of the Olson-Cohen model for strain induced martensite modified to account for the state of stress, indicates higher incubation times followed by a increasing rate of transformation with higher saturation level as the strain ratio increases. This would result and account for the steep increase in the equivalent strains at the onset of localised necking for positive strain ratios. In the more severely cold worked material, this effect cannot be observed since prior deformation has already resulted in significant amounts of martensite.

5.9 Development of Ball-Indentation Test Techniques

Hardness tests are widely used to provide a quick measure of the flow stress of the material. Numerous investigators have developed alloy specific hardness-strength relationships which are mostly empirical in nature. Hardness tests using spherical indenters are unique because the geometry of the indentation changes with increasing penetration, corresponding to a unique stress-strain value for a particular depth. As a result, the spherical indentation test technique is a unique method for determining the complete stress-strain curve of metals using a greatly reduced volume of test material. Since the test involves indentation using very small diameters of the spherical indentor (in the range of 0.5 mm to 2 mm), the tests are nearly non-destructive in nature, and can be applied as an in-situ tool for localized zones like the welds, heat-affected zones, coatings and metallic structures while in operation.

The true stress σ during a spherical indentation is correlated to the mean pressure H, beneath the indenter which is the ratio of the applied force (P) and the projected indentation area (π $d^2/4$).

$\sigma = (H / \psi) = (4P) / (\pi d^2 \psi)$

where the parameter ψ called the constraint factor is related to the plastic zone development beneath the spherical indenter, varying from 1.01 at the initiation of the plastic zone to about 2.87 for a fully developed plastic zone beneath the indentation.

The corresponding true strain is given by the relation

$\varepsilon_p = 0.2\ d/D$

where d is the indentation diameter and D is the indenter diameter.

The complete stress-strain data from indentation tests can be generated by performing spherical indentation on a metallic sample to different penetration depths at a single location. Thus the Ball-Indentation (BI) Test involves progressive indentation of a metal surface by a spherical indenter with partial unloading performed at the same test location. The applied

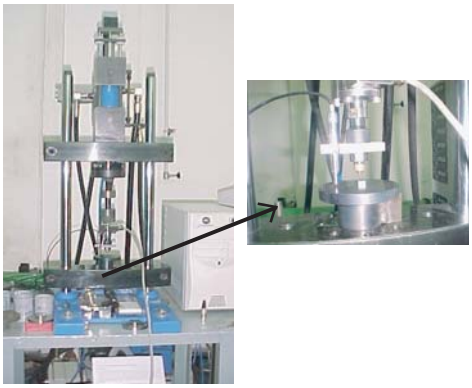

Fig. 1a. Servohydraulic test system

Fig. 1b. Motorised ball screw test system

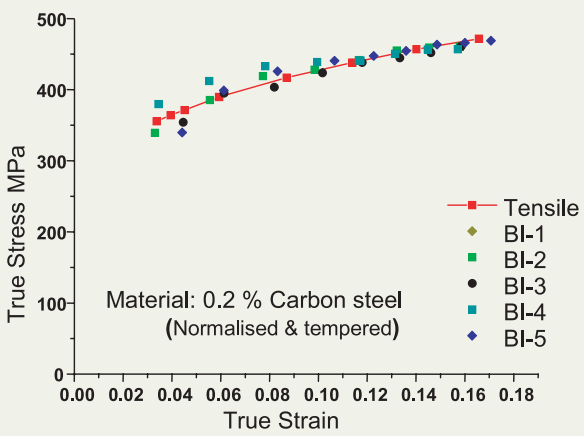

Fig. 2. Stress-strain curve from 5 repeated BI tests superimposed on tensile data

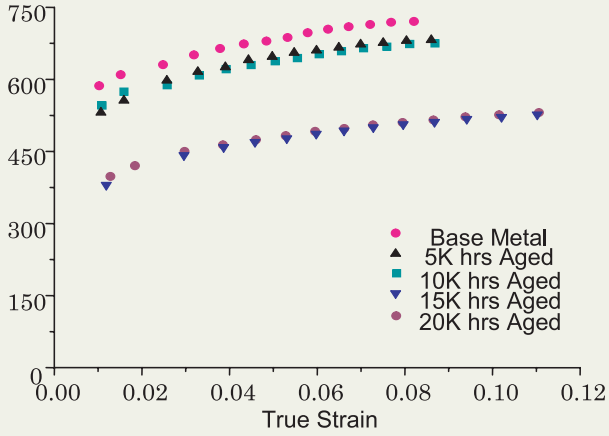

Fig. 3. True stress-strain curves obtained using BI tests on aged modified 9Cr-1Mo steel specimens

indentation loads and associated penetration depths recorded during the BI test are used to calculate true stress-strain values using the above relationships. Compared with the conventional hardness tests, this technique offers complete information during indentation loading and unloading through an analysis of the measured indentation load-depth curve.

Two test systems, namely, a servo-hydraulic test system and a miniature motorized electro-mechanical system have been designed and developed for standardizing the BI test technique. (Fig. 1) The computer controlled closed loop servo hydraulic test system consists of a light weight two-column load frame (~ 600 mm height) with two crossheads and a servo actuator driven by a compact portable servo hydraulic power supply. An integrally mounted LVDT with the actuator gives the position A of the actuator. A load cell (± 200 kg, 0.1 % linearity) mounted inline with the actuator measures the load during indentation testing. Tungsten carbide indenters of diameters ranging from 0.5 mm to 2 mm (± 2.5 μm tolerance) are used for load application. An LVDT of ± 0.25 mm range is mounted close to the indenter assembly for measuring the indentation depth with an accuracy of ± 1μm.

The servo-mechanical test system consists of a compact (500 mm height), rigid two column test frame on which a ball screw (with anti-backlash features) with a ball nut, supported by an LM shaft, is attached. A brushless AC servomotor powered by a servo drive is integrated on the test machine to drive the ball screw. A hollow shaft encoder is used for position information of the ball screw.

Both the closed loop test systems are driven by a 16-bit digital controller for signal conditioning of the different transducer outputs, control waveform generation, setting the PID gain controls and is interfaced to a PC. The salient features of the software include remote operation of the machine controls, real time data acquisition of all the transducer outputs (sampling rate of 20 readings/sec), ramping (speeds of the actuator as low as 0.05 mm/min) and cycling at pre-defined rates and real time graphics.

Extensive trials have been carried out to standardize the ball-indentation test procedure on the servo-hydraulic test system. First the servo controller was tuned to optimize the PID gain settings for a static mode of test like ball-indentation. The test procedure was then standardized on hardness calibration blocks (15 HRC, 32 HRC) to get repeatable load-depth plots. Specimen sizes of 10mm x 10mm with thickness of about 2 mm were used for the experiments. It was however ensured that the minimum thickness was at least ten times the indentation depth. Several improvements

were done in the testing fixture and in the testing procedures to get repeatable load-depth plots. Plain carbon steel material (0.2 %C) was first chosen for verification of the BI tests with the respective tensile data. Fig. 2 shows the true stress strain plot obtained from BI tests superimposed on the tensile stress-strain plot for 0.2 % carbon steel, showing very good agreement of the BI test results with the tensile results. Similarly the BI technique has been validated for several heats of modified 9Cr-1Mo steel and has been successfully applied to study the degradation in tensile properties of aged modified 9Cr-1Mo (Fig 3).

5.10 Adsorption Columns for Removal of Moisture and Oxygen from Argon Cover Gas - Experimental Results

Inert gas argon is used as cover gas for the sodium system of Fast Breeder Reactors (FBRs). The moisture and oxygen impurities in argon used for the sodium system should not exceed 5vpm each. Since moisture and oxygen present in commercial argon are above this limit (50 to 80 vpm each), they have to be removed by using adsorption columns containing molecular sieves (to remove moisture) and BASF catalyst (to remove oxygen) before supplying to the sodium system. Experiments were carried out to determine the design parameters of adsorption columns for the removal of moisture and oxygen from argon. Molecular sieves of IPCL 13X type (1/16" cylindrical pellets) and BASF catalyst of SUD Chemie India Pvt. Ltd., type C54-CS (1/4" x 1/8" tablets) were taken for the experiment. The various design parameters like breakthrough curve, adsorption capacity and minimum bed height of packing required for mass transfer were determined by the experiment.

During adsorption, argon has to flow from the top to the bottom of the adsorption column and during desorption or regeneration, argon has to flow in the reverse direction. The experiment was carried out with molecular sieves and BASF catalyst seperately with adsorption columns of bed height 5 cm and 10 cm. Moisture and oxygen meters were used at the inlet and outlet to measure the moisture and oxygen impurities in argon gas respectively. Argon from a cylinder was mixed with atmospheric air by using a trace adjustment needle valve. The amount of moisture or oxygen in argon was adjusted between 500 to 800 vpm and was passed through the adsorption column bed.

The argon sample was taken continuously from the bottom of the adsorption column bed. The readings of moisture and oxygen concentrations in argon

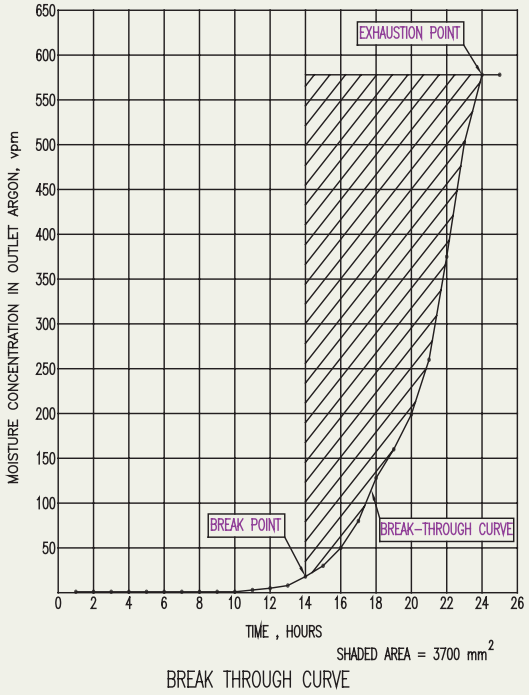

Fig. 1. Breakthrough curve for molecular-sieves

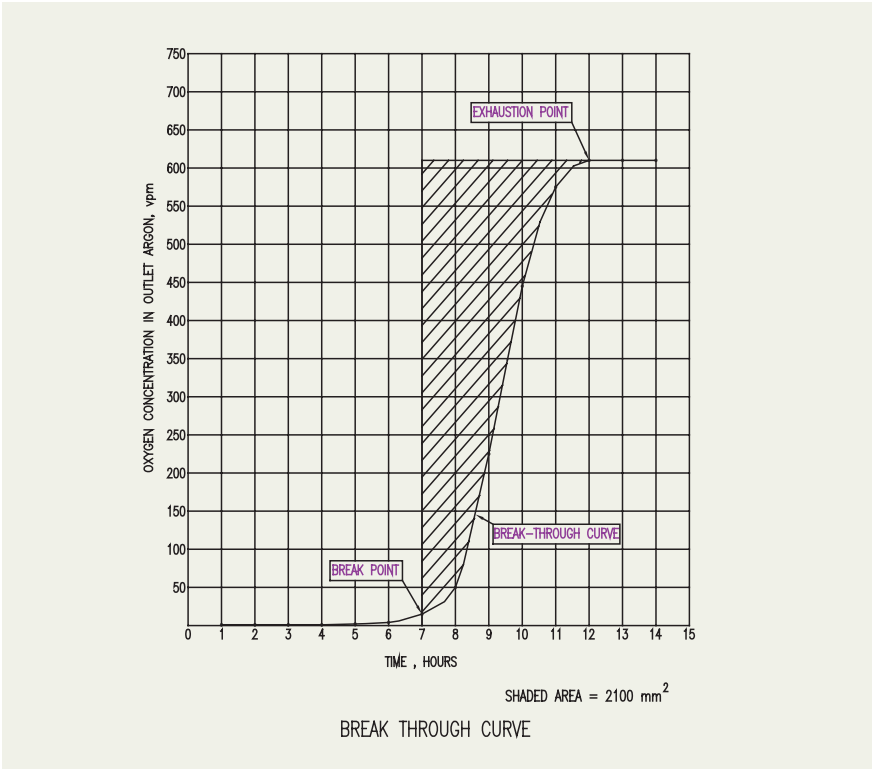

Fig. 2. Breakthrough curve for BASF catalyst

from the adsorption column bed outlet with respect to time were monitored, till the outlet impurity concentration in argon became same as that of inlet impurity concentration in argon. After saturation, the bed was regenerated. The experiment was repeated with different flow rates and also at different bed heights.

Breakthrough Curve

The upper most layer of the bed was practically saturated and the bulk of adsorption took place over a narrow mass transfer zone in which the concentration changed rapidly. After some time, the mass transfer zone reached the bottom of the bed and the oxygen concentration at the outlet increased to an appreciable value for the first time. The system was then said to have reached the break point. The breakthrough curves were plotted, outlet impurity concentration versus time as shown in Fig. 1 and 2 for molecular sieves and BASF catalyst respectively. The impurity concentration in the outlet argon was stable for some time and then started increasing to an appreciable value. The curve was termed as the breakthrough curve. The values from this graph were used for further calculations.

Adsorption Capacity

The adsorption capacity is the amount of impurity in kilograms, which can be adsorbed per kilogram of the adsorbent. The adsorption capacities of molecular sieves and BASF catalyst are found to be 4% and 2% respectively. The adsorption capacity with respect to different L/D ratios, inlet moisture concentration, flow rate and velocity were determined

Minimum Height of Adsorption Column Bed

The minimum height of the adsorption column bed for mass transfer from higher impurity concentration to lower impurity concentration is the height of the mass transfer zone obtained from the breakthrough curve. From the experiment, it was found that the minimum height of the adsorption column for molecular sieves and BASF catalyst were in the range of 20 to 37 mm and 19 to 50 mm respectively for an argon velocity of 3 to 8 cm/sec.

Adsorption Columns for PFBR

Based on the PFBR process conditions and the adsorption capacities determined from the experiment, the size of adsorption columns for PFBR were estimated for a period of six months. It was found that a column of molecular sieves of diameter of 0.32 m and length of 1.3 m and a column of BASF catalyst of diameter of 0.424 m and length of 1.727 m are adequate. Thus the design of the adsorption column for PFBR was finalized.

5.11 Weld Strength Reduction Factor in Different Grades of Cr-Mo Steels

Different grades of Cr-Mo steel are being used in the fabrication of the steam generator in power plants. The ferritic-bainitic 2.5Cr-1Mo steel has been employed in the steam generator of FBTR whereas the martensitic modified 9Cr-1Mo steel is being employed in PFBR, under construction at Kalpakkam. Under creep conditions, weld joints of these steels possess lower creep strength than their base metals due to type IV cracking. The cracking typically occurs at the intercritical region of heat affected zone (HAZ). Macroscopically the cracking appears as a typical low ductile failure but microscopically localized concentration of creep deformation along with preferential creep cavitation occurs at the intercritical region of HAZ. However, the weld strength reduction depends on the grades of the Cr-Mo steel. To assess it, creep rupture tests were carried out on the 2.25Cr-1Mo, plain 9Cr-1Mo and modified 9Cr-1Mo steels base metals and their fusion welded joints. Fig. 1 shows the variation of the creep rupture life with applied stress for the steels and their weld joints. Percentage reduction in the creep strength of the steel joints with respect to the base metal is shown in Fig. 2. The 2.25Cr-1Mo steel is most susceptible to weld strength reduction and the plain 9Cr-1Mo steel is the least.

The different weld strength reduction factors in Cr-Mo steels can be explained on the basis of their strengthening mechanisms and their vulnerability to change on intercritical exposure (between Ac_1 and Ac_3) during the weld thermal cycle. 2.5Cr-1Mo steel derives its creep strength mainly from the intragranular precipitation of Mo_2C having relatively low stability against thermal exposure. The partial dissolution / replacement of Mo_2C on intercritical exposure during the weld thermal cycle reduces the creep strength of the weld joint substantially. Plain 9Cr-1Mo steel on the other hand derives its creep strength from the solute solution hardening and dislocation sub-structure stabilized by the $M_{23}C_6$ type of carbides, which are not very much affected by intercritical heating during weld thermal cycle. In modified 9Cr-1Mo steel, in addition to the changes in plain 9Cr-1Mo steel, the coherency of the (Nb, V) (C,N) precipitates (the primary strengtheners in this steel) with the matrix is substantially reduced. These changes render more reduction in creep strength of the joint of the modified 9Cr-1Mo steel than that in the plain 9Cr-1Mo steel. Even then, the creep strength of the modified 9Cr-1Mo steel weld joint is much superior to that of plain 9Cr-1Mo steel, justifying its choice as the steam generator material for PFBR.

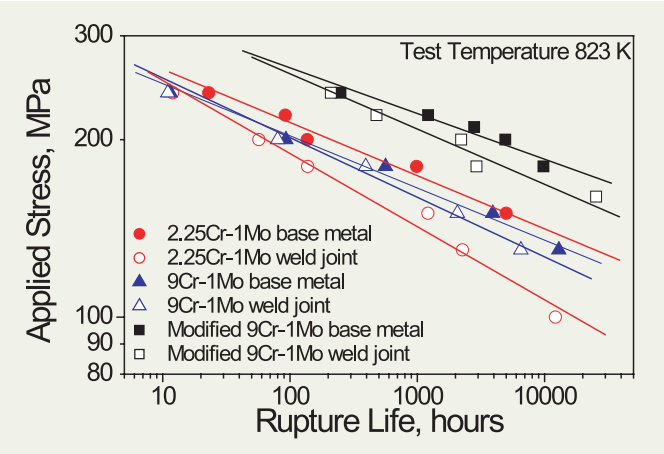

Fig. 1. Variation of creep rupture life with applied stress of different grades of Cr-Mo steel and their fusion welded joints.

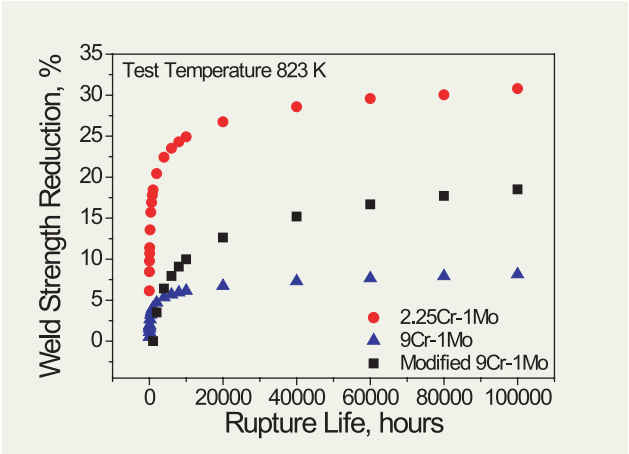

Fig. 2. Variation of weld strength reduction percentage of the different grades of Cr-Mo steel with rupture life.

5.12 Computational Model for Estimating the Solidification Modes in Austenitic Stainless Steel Welds

The most critical factor that determines the hot cracking susceptibility of austenitic stainless steel (SS) welds is the mode of solidification. Hence, the solidification mode needs to be estimated during the selection or design of welding consumables for arc welding of austenitic SS. Presently, the solidification mode is estimated by determining the Cr_{eq}/Ni_{eq} ratio from the chemical composition of the weld using the expressions:

Cr_{eq} = Cr + 1.37 Mo + 1.5 Si + 2 Nb + 3 Ti; and

Ni_{eq} = Ni + 0.31 Mn + 22 C + 14.2 N + Cu

The primary ferritic (PF) solidification mode is obtained when $Cr_{eq}/Ni_{eq} > 1.55$, while primary austenitic (PA) solidification mode is obtained with $Cr_{eq}/Ni_{eq} < 1.55$. However, these relationships do not describe the real solidification behaviour and also do not estimate the effect of individual alloying elements on the solidification mode. A more accurate approach is to use an artificial neural network. Hence, a computational model based on the Bayesian Classification Neural Network was developed for estimating solidification mode in austenitic SS welds using 204 datasets. This model shows that nickel exhibits a clear pattern in influencing the solidification mode, with the effect of other alloying elements on the solidification mode depending on the nickel content. Fig. 1 shows that the PF solidification mode is promoted when Ni < 10 wt%. Also, Fig. 2 accurately predicts that the compositions of 304LN and 316LN SS lie in the PF solidification mode region. This model predicts that for avoiding hot cracking in austenitic SS welds, by achieving PF solidification mode, the weld should have Ni < 10 wt% and Cr_{eq}/Ni_{eq} ratio > 1.55. The model predictions were validated by preparing 316LN SS electrodes with varying nickel contents.

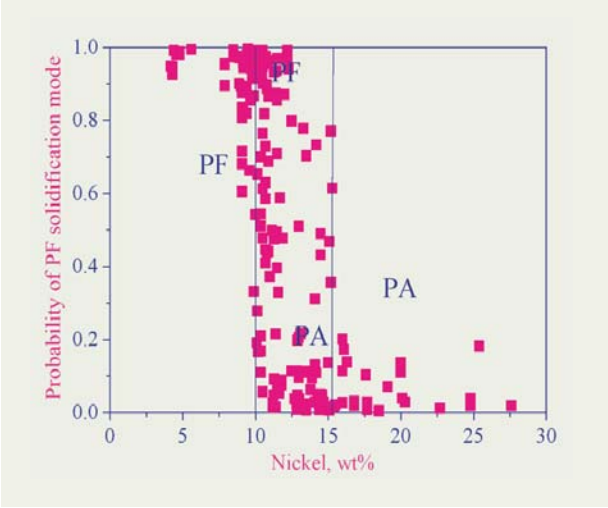

Fig. 1. Effect of nickel content on probability of PF solidification mode

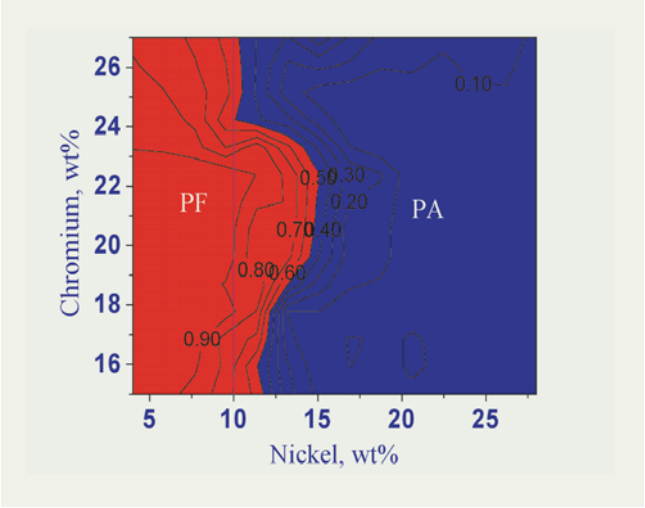

Fig. 2. Combined effect of nickel and chromium content on solidification mode

5.13 Design of D9 Pressurised Capsules for Irradiation Creep Testing of PFBR Fuel Cladding and Wrapper Tube Material by Seal and Weld Method

Pressurised capsules made of D9 alloy are being developed to carry out irradiation experiments in the FBTR to determine the in-reactor creep performance of the indigenously developed D9 alloy, which will be used as fuel cladding and wrapper tube material in PFBR. D9 tubes are closed by welding at one end and fitted with special end plugs at the other end, which enable filling of argon gas at the desired pressure into the tubes using a pressurising system. After pressurising, the gas entry path is sealed with a soft copper gasket and welding is carried out using the laser welding technique to close the special end plug with a cap. The diameter of the special end plug has been redesigned to accommodate all features within the diameter of 6.6 mm, which is same as that of the clad tube. The length of the pressurised capsule is about 70 mm. A trial capsule with an internal pressure of 65 Kg/cm^2 has been successfully developed (Fig.1). Development of capsules with higher pressures up to 120 Kg/cm^2 is in progress.

The development of instrumented irradiation capsule with heating provision has been taken up in IGCAR. This type of irradiation capsule will be useful to maintain constant temperature during the irradiation of structural material specimens in FBTR. Structural material specimens from the cladding and wrapper tube material can be tested using such an instrumented irradiation capsule to determine the change in mechanical properties due to irradiation. The instrumented capsule can be loaded in the central position of FBTR using the CIPTEX (Central Irradiation Plug for Testing and Experiments). A special fuel subassembly IF 1300 is required to be loaded in the central 0-0 position of FBTR during this experiment. This experiment is proposed to be carried out in the hybrid core of FBTR.

Fig. 1. D9 pressurised capsule with 65 kg/cm^2 pressure

Design of the irradiation capsule has been completed. The outer diameter of the instrumented capsule is 18 mm. The irradiation capsule will consist of a sub capsule concentrically located in it (Fig. 2). The structural material specimens are kept in the sub capsule with static sodium surrounding the specimens. A

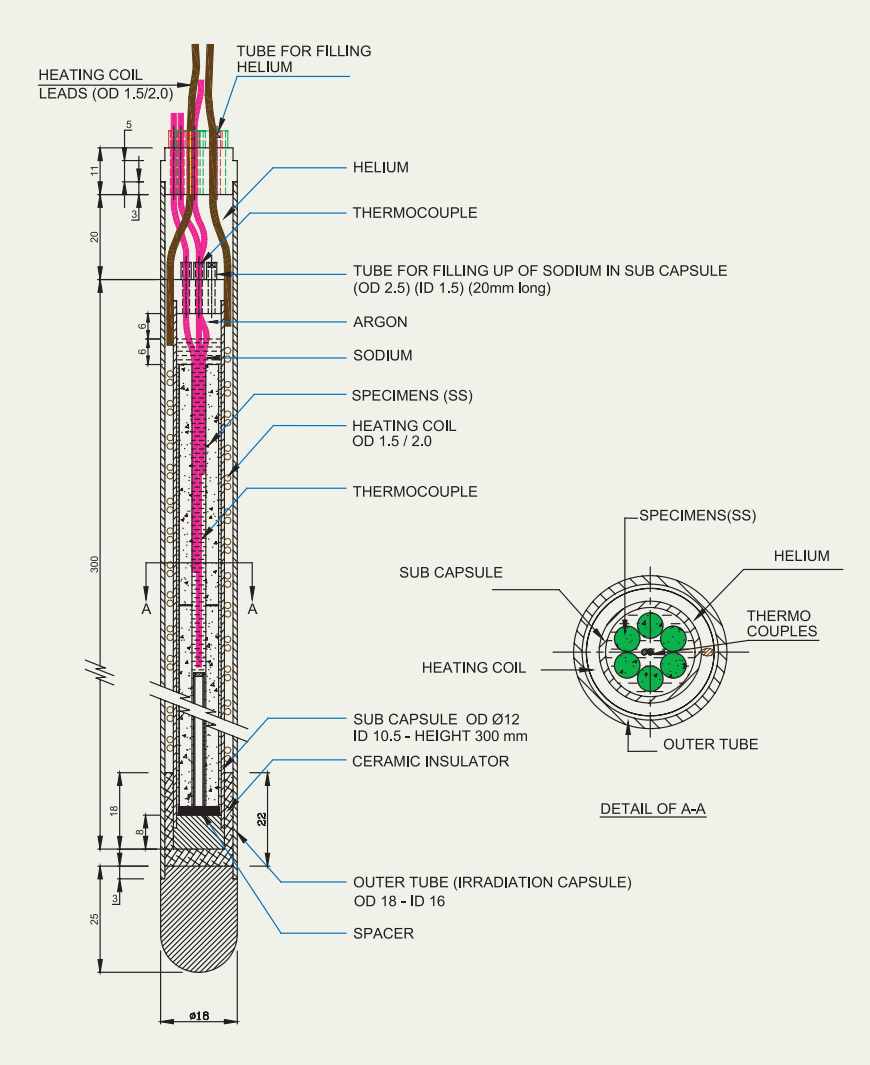

Fig. 2. Sketch of instrumented irradiation capsule with heating arrangement.

A heating coil with overall wire diameter of 1.5 mm / 2.0 mm is wound around the sub capsule to heat the specimens whenever required. Helium is filled in the annular gap between the sub capsule and the outer tube. During irradiation in the reactor, the temperature of the specimens will rise due to nuclear heating. Thermocouples are attached to the sub capsule to determine the temperature of the specimens in the sub capsule. The specimen temperature will vary during the period of irradiation due to changes in the reactor power conditions. However, the temperature of specimen will be maintained within a small range during the period of irradiation by changing the current to the heating coil. The heating coil and thermocouple will be connected to a temperature controller and thyristor. Work towards development of technology for the fabrication of instrumented capsule is in progress.

5.14 Rectification of the Heater Assembly for Surge Tanks

The surge tank is a high temperature pressure vessel that operates at a pressure of 11.25 MPa and a temperature of 565 K. The tank has been manufactured by a private vendor. During leak testing of the tank, leakage was observed between the 6 kW Heater pins and sleeves to which they are welded. The vendor could not rectify the weld. The job had been referred to Central Workshop Division (CWD) to salvage the product.

Welding of Heater pins with sleeves was a difficult task. The 150 NB class 1500 # RF Blind Flange with sleeves was replaced with 8 new "U" type Heaters. The outer diameter of the heater tube is 9.5 mm and the wall thickness varies from 0.7 to 0.8 mm. In the heater tube, around the heater element, Magnesium Oxide (MgO) is packed as the insulating material. The heater sleeve is made of AISI 316 stainless steel and has an outside diameter of 12.5 mm and is 1.35 mm thick. Welding of thin wall heater tubes with the sleeve demanded expertise in welding. During mock-up

Fig. 1. Heater assembly for surge tank

welding, it was observed that gas is produced by the insulating material (MgO) due to the high temperature reached and this resulted in pressure that leads to puncturing of the heater tube wall. A special tool that can be fitted to the end of a slow speed portable drilling machine was designed and made to remove the tightly packed hard MgO powder from heater pins over a length of 25 mm. By using the above machine, the MgO powder was successfully removed. The sleeve was welded with the blind flange and then welded with the heater tubes. After welding, a silicon compound was filled in the space from which MgO powder was removed. Finally, the heaters were sealed with ceramic sleeves (Fig. 1). The heater assembly was subjected to dimensional and liquid penetrant Inspection. The tank was successfully tested pneumatically at 7 bars and hydrostatically at 170 bars.

5.15 Manufacture of Inlet and Outlet Feeder Pipes for MAPS - I

The carbon steel inlet and outlet feeder pipe lines for the Primary Heat Transport system of the Madras Atomic Power Station (MAPS) were to be replaced due to aging (erosion/corrosion) of the existing parts. Due to non-availability of qualified vendors to carryout this job to meet the stringent quality requirements, this task was entrusted to Central Workshop Division (CWD). CWD successfully completed the bending of 1850 C.S. pipes (conforming to ASTM - A 333 Grade-6) of various diameters ranging from 1¼" to 2½" and bend radii 7½", 10" and 12" with bend angles varying from 7.5^0 to 90^0 in multiple planes. Around 30% of the pipes had double bends. This work was completed in a a short time.

The pipes supplied for carrying out the work had controlled inner diameters with varying wall thickness. The outside diameters of the pipes were varying by 2 to 3 mm. Hence, standard dies could not be used for the bend forming. Special dies, mandrels and formers were designed and fabricated to bend the pipes with varying wall thickness. The bends were formed using the Numerical Control (NC) hydraulic pipe bending machine. After bend forming to the required profile, the radii and angles were checked in a specially drawn layout. Dimensions, ovality and wall thinning were controlled and maintained within the specified limits. Dye penetrant inspection was carried out on the bend portions and found defect free.

Fig. 1. Inlet and outlet feeder pipes for MAPS-1

The complete replacement of the inlet and outlet feeder pipes is first of its kind in the Indian Pressurised Heavy Water Reactors.

5.16 6-Axis Mini-Robotic Arm

A miniature, high precision, closed loop servo-controlled six-axis robotic arm has been developed indigenously at IGCAR with active participation from the Indian industry. This arm is intended to be a platform for the development of various customized remote handling solutions ranging from handling and inspection to fabrication and assembly requiring varying degrees of freedom, end-of-arm-tooling, sensory feedback and easy maintenance. The arm with 6 joints / 6 degrees of freedom in essence, is an anthropomorphic robotic arm, which operates in a spherical work envelope of ≈ 600 mm radius, carries a payload of 3 kg and generates a maximum linear speed of 2.5 m/s at the wrist end (end-of-arm). This robotic arm is designed for positioning objects with an accuracy of 0.25 mm or better and a positional repeatability of 0.04 mm.

The robotic arm consists of a base and three major linkages i.e. waist, upper arm and forearm, which rotates with respect to each other to locate the wrist module in a desired space location. The wrist module has two minor linkages that can rotate with respect to each other and the forearm resulting in roll, pitch and yaw motions so that the end-effector can be suitably oriented to access a location or to grip / clamp an object. All the joints are actuated in a closed loop using AC servo motors, provided with resolvers and brakes. Precision, low-backlash planetary gears and harmonic precision reduction gearing are used for transmission and speed reduction in the above two cases to ensure the desirable positional accuracy of the end-effector. High strength aluminium alloy has been used as the structural material for the waist, upper arm, fore arm and wrist module. This robotic arm, which uses a pneumatically actuated two-fingered parallel-jaw gripper as the basic end-effector and has the necessary flexibility facilitating reconfigurations for a variety of applications, such as handling, inspection and precision assembly by integrating a suitable tool at the end-of-arm (EOA). The design of the arm is highly modular in nature ensuring easy maintenance and replacement of the parts. Fig.1 shows the photograph of the robotic arm and Fig. 2 shows its work envelope. Resolvers located at the motors play a dual role, providing velocity and position feedback. Simulated incremental encoder feedback derived from the resolvers by the drives, is used as the position feedback required for the servo control loop. A force transducer is provided at the gripper fingers to sense the gripping force.

Fig. 1. Mini-Robotic Arm

The robotic arm is driven and controlled (power and data communication, coordination of sensory feedbacks and motion of the axes and programming for a specific task) by custom-

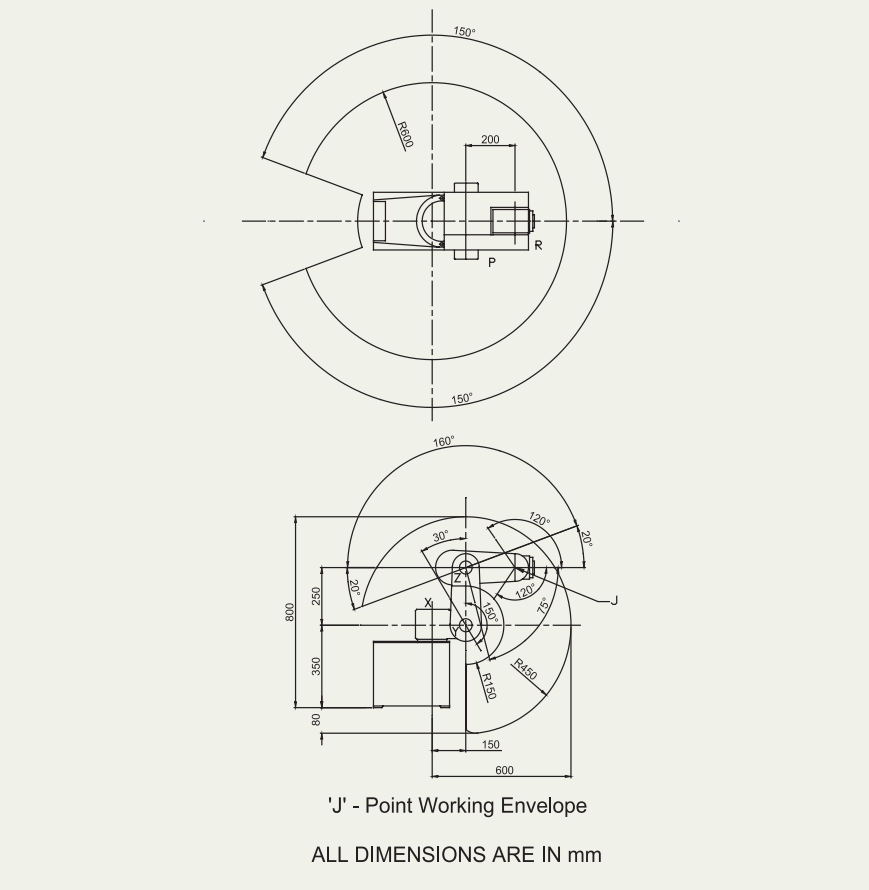

Fig. 2. Work envelope of the robotic arm

developed control software written in C++ and a PC-resident controller. The control system is based on an open architecture and distributed control. The PC provides a user friendly Windows based Graphic User Interface (GUI), which allows off-line application program development for performing complex customized tasks. Offline programming is complimented with simulation of the robotic arm which is achieved using phantom axes by giving the joint solutions to a graphic simulation software through the APIs of the software environment. The graphic simulation software also facilitates modeling of the robotic arm for online/offline simulation.

The basic process of real-time control of the robotic arm is shared by the PC and the PC resident controller. Functions such as the solution of the kinematic equations and joint solutions by inverse kinematics, motion planning / trajectory generation and supervisory functions are performed in the PC and the motion control is achieved in the controller. The control system with the C++ software facilitates appending external sensors such as vision, and range and other ancillary equipment to the architecture. Manual as well as automatic modes of control are established through a teach pendant and Man-Machine-Interface (PC). The teach pendant allows target locations to be taught and remembered by the robot. Using such taught points/locations, a new program can be created in the application development environment. The compiled program can be verified in offline mode on the graphic simulator before executing the program for running the robotic arm.

5.17 Development of Ultrasonic Transducer for Under-Sodium Scanning

The use of liquid sodium as the coolant in a liquid metal cooled fast reactor has led to a number of instrumentation issues because of the high operating temperature and the compatibility of the transducer material with sodium. In addition, the opacity of sodium precludes visual inspection of components immersed in sodium by optical means. This problem has been overcome by resorting to the ultrasonic scanning technique for under-sodium viewing. However, ultrasonic transducers working on the pulse-echo technique have to be specially developed, as the commercially available transducers are not suitable for this purpose. Therefore, a special liquid sodium- proof ultrasonic transducer has been developed and tested in sodium up to 200° C.

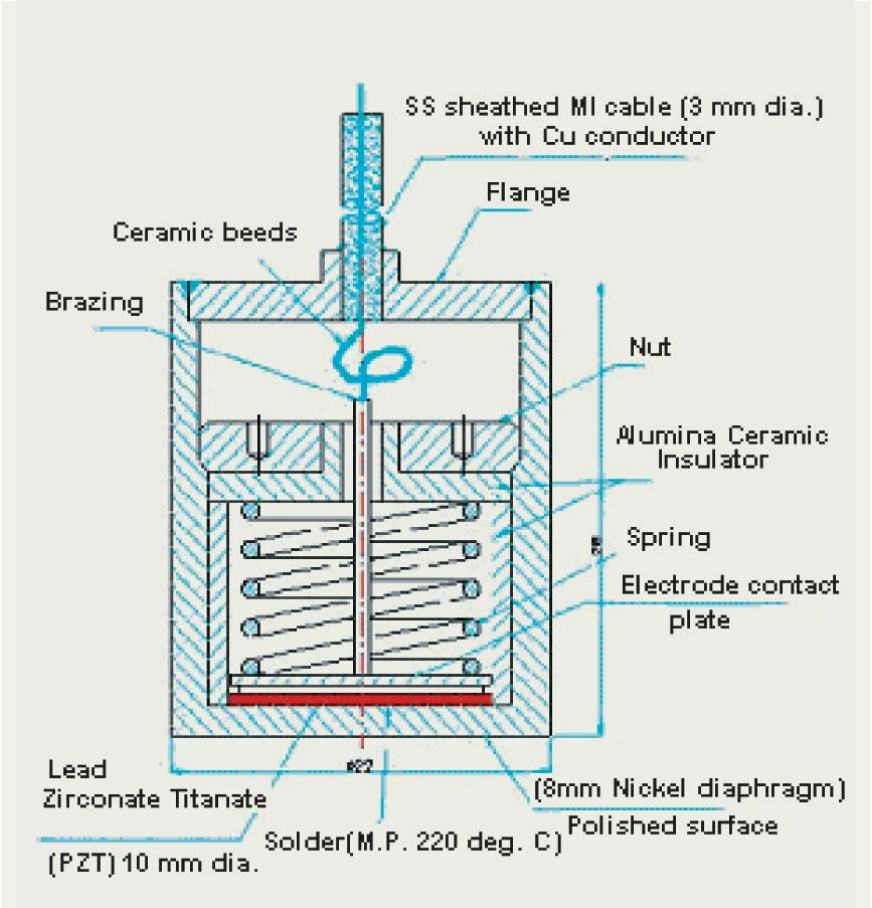

Fig. 1. Ultrasonic sodium proof transducer

Earlier, imported piezoelectric crystals (PZT-5A) in a stainless steel housing were used in FBTR. The development of a new transducer has been taken up based on an indigenous supply of piezoelectric crystals Lead Zirconate Titanate (PZT) has been selected due to its high electromechanical coupling constant (Kt) and moderate curie temperature. Two transducers were fabricated successfully with a 5 MHz frequency (for imaging) and a 1 MHz frequency (for ranging) using the piezoelectric crystal (PZT plain-A) having a Curie temperature of 380°C, which is 50°C higher than the normal PZT-5A type. This helps in developing the high temperature transducer up to 300°C by suitably selecting the solder alloys of different melting points. The bond between the crystal and the diaphragm presents a major problem in the manufacture and development of these high temperature ultrasonic transducers. The PZT crystals were soldered to the transducer inner surface made of nickel. The transducers were fabricated with a diaphragm thickness of 1.5mm instead of 0.6mm to avoid the deformation of the surface when soldering the crystal. After soldering, the crystal diaphragm thickness was reduced to 0.6mm by machining. This is a compromise between diaphragm strength and ultrasonic energy loss but, avoids transducer failure during crystal soldering. Fig.1 shows the sketch of the sodium proof ultrasonic transducer and Fig. 2 is a photo of the ultrasonic transducer .

The contact plate is brazed with the center copper conductor of the MI cable to withstand high temperature. The center conductor of the MI is insulated with small ceramic beads to avoid contact with

Fig. 2. Ultrasonic transducer

transducer body. Currently crystal soldering is carried out using a hot plate. Attempts are being made to solder the crystal in vacuum to achieve fluxless soldering which improves the life time. Development of a high temperature transducer (280°C) using lead solder alloy of melting point (304°C) is being developed.

Test results

The 5 MHz transducer was tested in water for its performance and endurance test was done in sodium for 150 hours at 200 deg. C with the target kept at a distance of 100 mm and an echo was obtained up to 500 volts of spike excitation. The test results are shown in Fig. 3 and Fig. 4. To obtain an echo amplitude in sodium equal to that of water, the instrument gain was increased by 8dB.

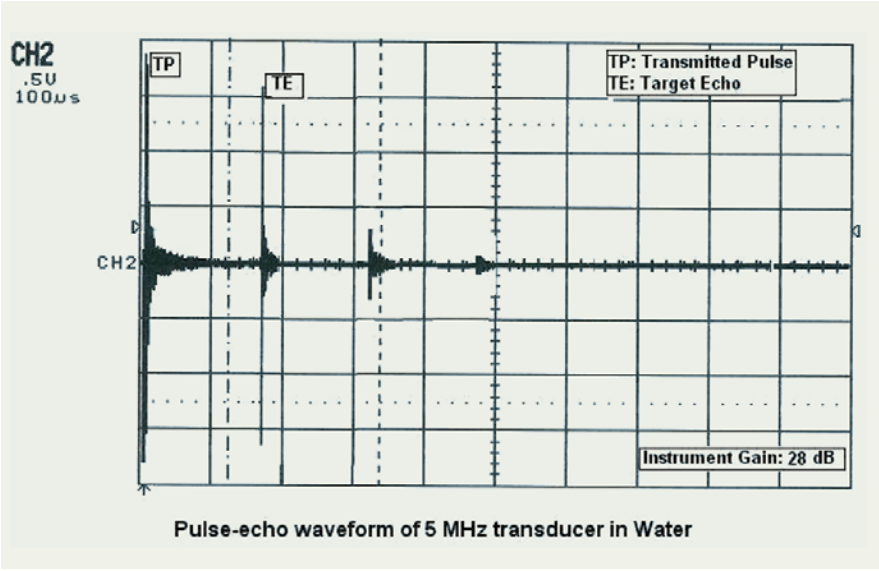

Fig. 3. Pulse-echo waveform of 5MHz transducer in water

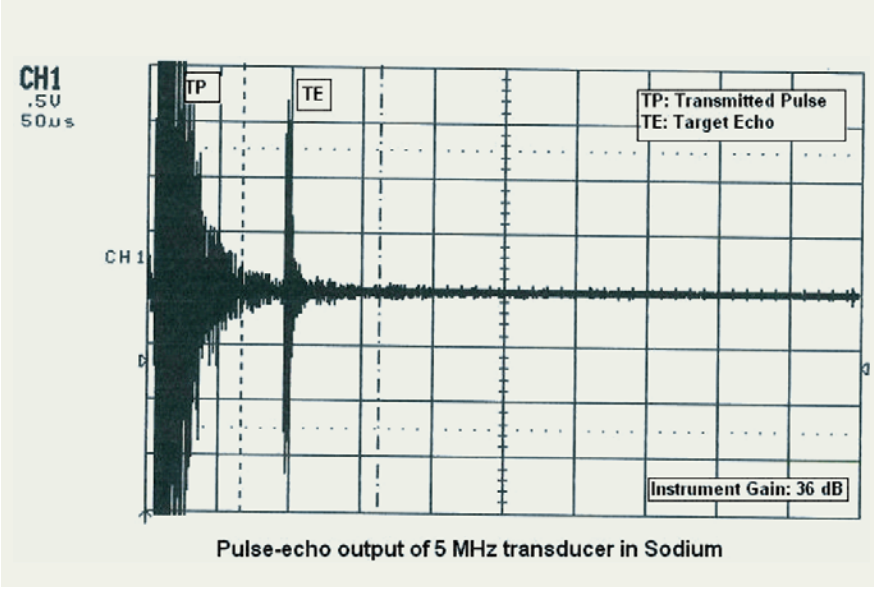

Fig. 4. Pulse-echo waveform of 5MHz transducer in sodium

5.18 Development of Multi-transducer Assembly for Subassembly Imaging

The use of ultrasound under sodium in the FBRs has two purposes. One is to detect any fuel sub-assembly projecting from its original location which may hinder the fuel-handling operation (ranging). Another is to image and locate the tops of some of the core assemblies so that estimates can be made of the bending or bowing caused by the fast neutron induced damage on the structural metal (imaging). A new device, a multi-transducer assembly has been developed to simplify the imaging method to be adopted in the reactor. Using this transducer, the technique of measuring the subassembly (SA) 'bow' has been demonstrated under water by rotating the transducer assembly. This method avoids rotation of the plug for imaging the top of the SA, thereby reducing the scanning time considerably.

The multi-transducer assembly consists of eleven, 5 MHz transducers each located at a radius ranging from 45 to 55 mm from the subassembly axis, i.e. each transducer is located at a 1mm radial difference between adjacent transducers. Each transducer's lens has been made out of a single metallic block. The advantage of this type of construction is that each transducer can be precisely located and their mounting is relatively simpler in comparison to mounting eleven transducers individually. The internal view is shown in Fig. 1.

Using this transducer, an experiment on bow measurement was conducted in a simulated condition. Fig.2 shows the 3-D model of a PFBR

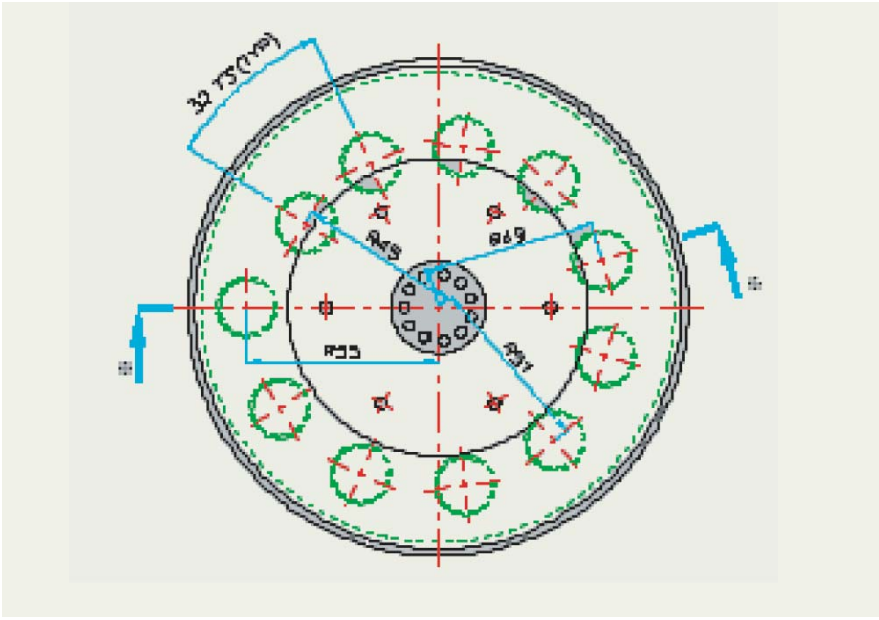

Fig. 1. Multi-transducer Assembly

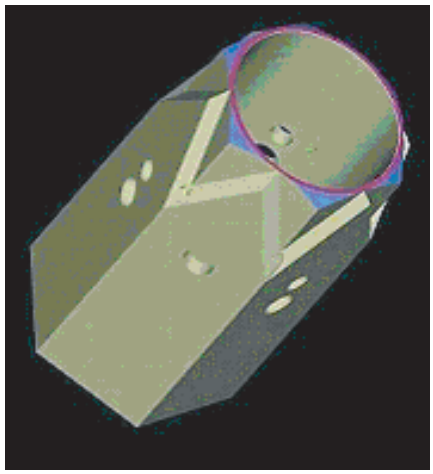

Fig. 2. 3-D model of the PFBR SA head

SA head whose top was kept as a target (pink coloured ring portion). The transducer No.10 which produces echoes of high amplitude from the target surface (a horizontal ring like surface of 3 mm wide and 108 mm mean dia.) was chosen as the reference transducer for this experiment. Initially, the axis of the target and the multi-transducers assembly were made to coincide with each other. This was confirmed by rotating the transducer-assembly about its own axis and observing uniformly high amplitude echoes from transducer No.10. Later the assembly position was shifted by 10mm horizontally with respect to the target, simulating the 'bow' of the target by the same amount. The transducer assembly was rotated about its own axis and the echo-amplitude from transducer No.10 was again observed. Whenever the transducer beam crosses the target surface, echoes were obtained. The measured

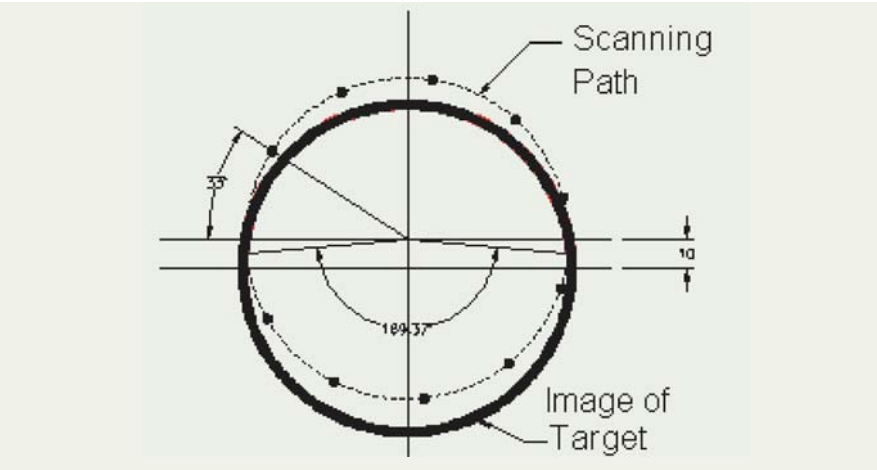

Fig. 3. Analysis of the measurement data

angles are found to agree with the calculated angle with respect to the transducer center as shown in Fig.3. From the successful results of the experiments, it is confirmed that the multi-transducer assembly is suitable for the PFBR subassembly bow measurement.

5.19 Experiences with Acoustic Leak Detection of Simulated Sodium-Water Reaction

In order to develop an acoustic leak detection system for diagnosing, characterizing and localizing leaks in the Steam Generator (SG) of PFBR, an experimental study of the behaviour of the micro leak and its propagation has been carried out at the Sodium Water Reaction Test Rig (SOWART), by injecting steam into sodium. An acoustic technique based on the Root Mean Square (RMS) level variation of the noise signal was employed to characterize the onset of the leak (steam injection into sodium). For real-time monitoring of the wide band frequency (10-100 kHz) leak signal, data acquisition and a leak alarm annunciation, an embedded system-based architecture with an in-built intelligent algorithm has been developed. The system has detected the leak signal instantaneously, which has been confirmed with frequency analysis and the hydrogen detection method.

The experiment was carried out in the Micro Leak Test Section (MLTS) in SOWART. The high-pressure steam is injected into sodium flowing at 10.0 m^3/h through the pinhole or crack in a leak simulator, which is designed and calibrated for a known leak rate. The sodium side of the crack/hole is closed by a rupture disc, which is designed to open up at a particular high pressure.

Acoustic noise is generated when steam is injected into sodium through the pin hole. Since the temperature inside the test section will be very high (~ 450°C), wave guides are welded to the test section

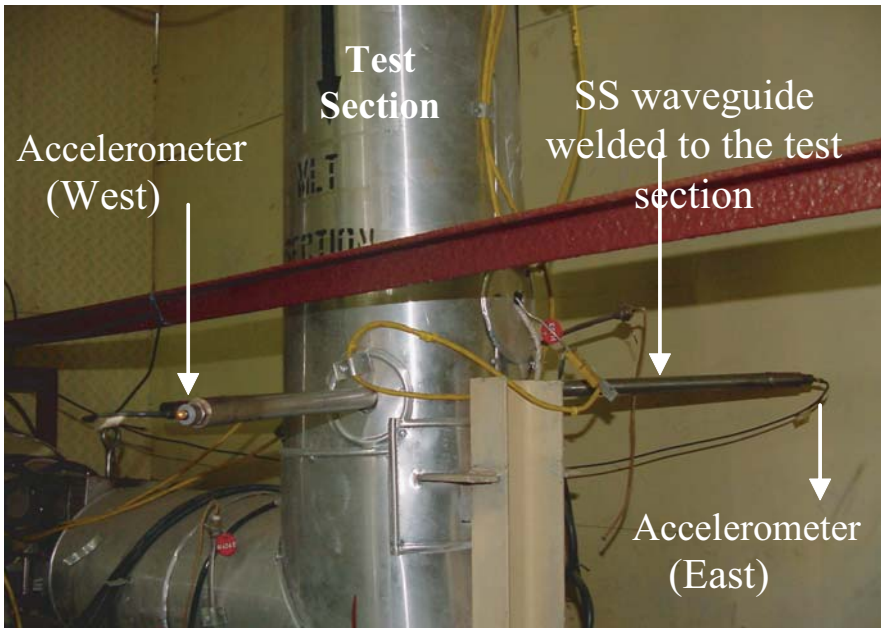

Fig. 1. Test section showing accelerometers

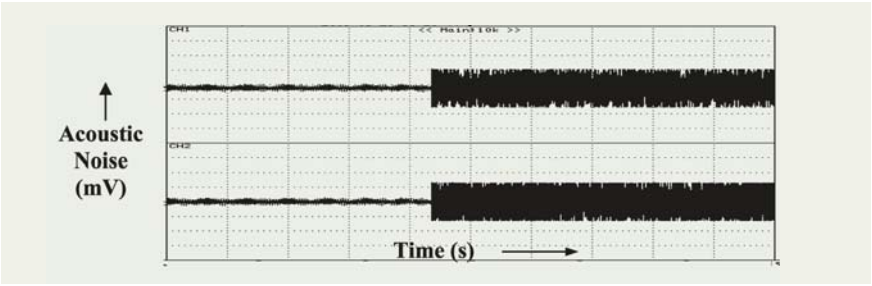

Fig. 2. Time plot during leak inception

and at the other end (cold end), piezoelectric accelerometers are installed. In the present experiments, an SS waveguide, 20 mm diameter and 1 m length is welded to the test section, and two piezoelectric accelerometers are installed on the East and West sides, as shown in Fig. 1. Continuous real-time monitoring of the acoustic signal enables the early detection of steam leak into sodium.

The acoustic signals from the accelerometer are fed to charge amplifiers. The amplified output is then filtered and fed to a 2-channel FFT analyzer for frequency domain analysis and to a digital oscilloscope for time domain analysis. In addition, this filtered signal is also fed to the Acoustic Leak Detection (ALD) unit developed at IGCAR.

This system has the capability of alarm annunciation when the leak signal persists for a pre-programmed time of 10 seconds. The system stores the real-time data with a time stamp for off-line analysis. This can give the exact leak initiation time and the duration of the leak.

Fig. 2 shows the time plot during leak inception. As can be seen, RMS of the acoustic time signal increases significantly during leak occurrence. Fig. 3 shows the variation of the RMS level of the wideband acoustic noise signal (10 kHz - 100 kHz) calculated from various spectra obtained during normal and leak condition. It has been found that acoustic noise magnitude (RMS) in the 10 kHz - 100 kHz band is most sensitive to leak inception and increases by 11 times from the background noise level.

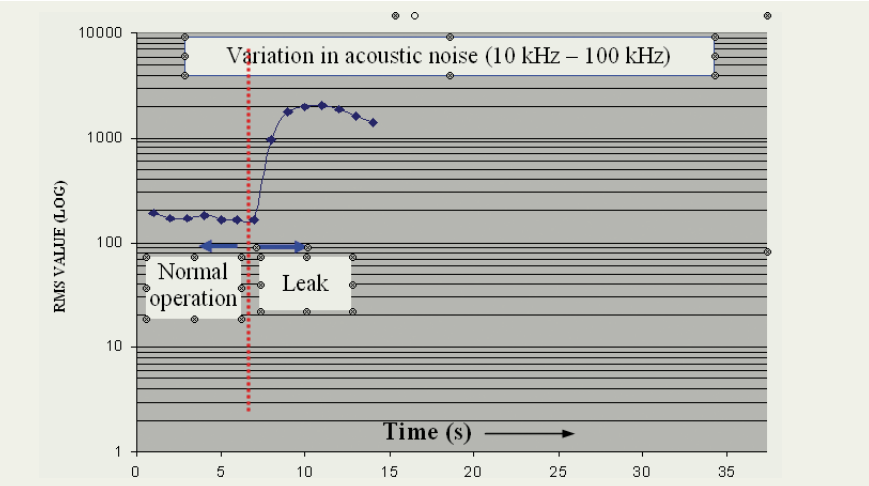

Fig. 3. Variation in noise level during leak (10 kHz - 100 kHz)

From all the present investigations, the following conclusions could be drawn:

- Increase in the overall RMS value of the wideband acoustic noise (10 kHz -100 kHz) by a factor of around 11 above the background level during leak has been observed,
- The response of the acoustic detection system has been found to be almost instantaneous and it reliably detects the initiation of leak, which has been confirmed by the hydrogen detection system, which responded with a time delay of 3-4 minutes.
- The system is designed to give an alarm indication only when the leak signal level persists for 10 seconds, so that false alarms are not generated based on spurious or transient signals.

Since in an actual running plant, the background noise in the SG from secondary sodium pumps, sodium boiling and other sources would be very high, special signal analysis and detection methods are proposed to be developed based on neural network or other similar methodologies. Our next phase of the development program is to develop an on-line leak detection system for the SG units of PFBR.

5.20 Ultrasonic Measurements for Assessment of In-Service Degradation of Wrought Inconel 625 Cracker Tubes of Heavy Water Plants at Thal and Tuticorin.

Inconel 625 tubes are extensively used in ammonia cracker units for the manufacture of heavy water. During service, the alloy is exposed to intermediate temperatures (~873 K) for prolonged periods, which leads to decrease in ductility and toughness of the alloy due to extensive precipitation of intermetallic compounds. The degraded mechanical properties of such heavily precipitated components can be regained by giving a resolution annealing heat treatment. After 120,000 h of service exposure, these tubes are generally taken out of the cracker unit to give a resolution annealing treatment at a suitable temperature to restore the toughness by dissolution of intermetallic precipitates. A non destructive methodology, based on in-situ ultrasonic and hardness measurements, has been developed and implemented at the heavy water plants at Thal and Tuticorin for the assessment of in-service degradation and the rejuvenation heat treatment of ammonia cracker tubes.

The times of flight of ultrasonic longitudinal and shear waves have been measured in-situ on cracker tubes in different conditions, such as virgin, virgin tubes service exposed for different durations, resolution annealed tubes and resolution annealed tubes service exposed for different durations. The results obtained from Poisson's ratio (derived from the measurement of time of flight of ultrasonic longitudinal and shear waves) and hardness measurements on all the tubes are presented in Fig. 1. The precipitation of intermetallic phases leads to a decrease in Poisson's ratio and an increase in the hardness. The variation in Poisson's ratio with hardness revealed that the tubes in different conditions can be represented by specific clusters in the plot. The difference in the effect of different precipitation stages on the Poisson's ratio and hardness, suggests that Poisson's ratio may be a better parameter for monitoring the degradation during the initial period, whereas, hardness may be better for the intermediate stage. Further, this would also help in deciding the inspection interval for monitoring the degradation in the tubes.

The tubes, service exposed for 1,20,000 h, exhibited a large scatter in the Poisson's ratio (0.295-0.308) and hardness (230-360 VHN) values. This clearly indicates that even though these tubes have been service exposed for the same duration (1,20,000 h), they

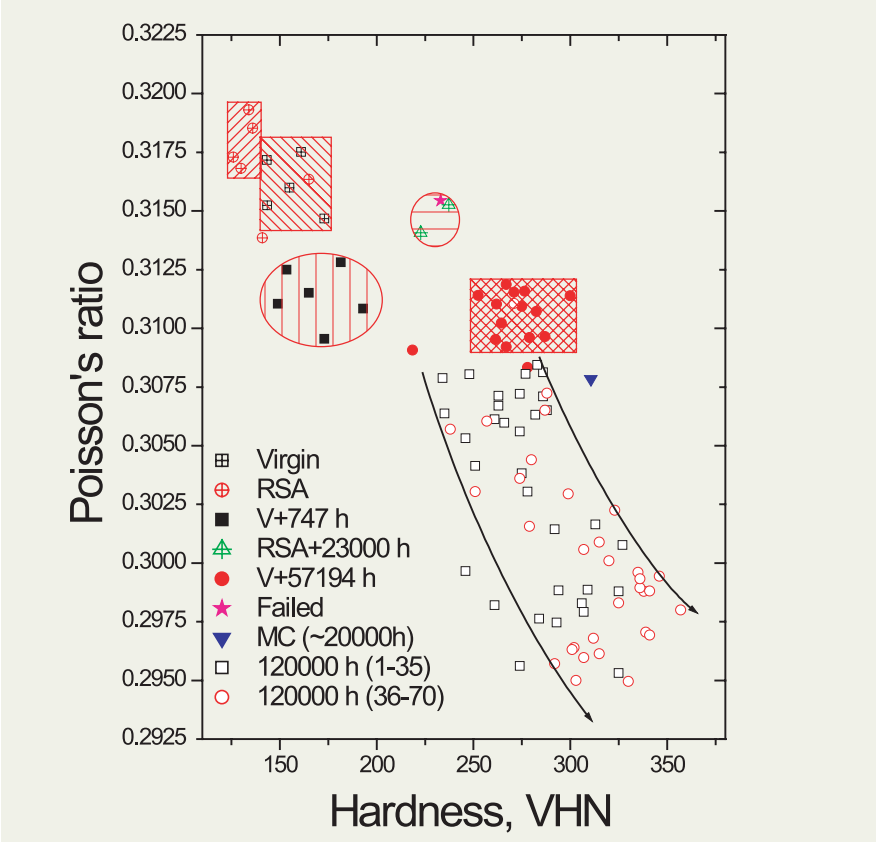

Fig. 1. Variation in Poisson's ratio with hardness for cracker tubes in different service exposed conditions at heavy water plants (V-Virgin, MC-Mini Cracker, RSA-Re-solution annealed).

exhibit different amounts of precipitation and damage. This is attributed to different operating conditions (temperature in particular) for these tubes during their operation life. Different values of hardness for the same Poisson's ratio and *vice-versa* are attributed to the difference in the relative amounts of the two precipitates, i.e. γ" and $Ni_2(Cr,Mo)$, reported to form depending upon the actual operating temperatures.

The resolution annealing of the service exposed tubes led to a decrease in the hardness (126-135 VHN) even below that for the virgin tubes. Similarly, the Poisson's ratio increased to slightly above that of the virgin tubes. This is attributed to the fact that the resolution annealing treatment leads to grain growth also, in addition to the dissolution of the precipitates in the matrix. These measurements on the resolution annealed tubes reveal that both hardness and Poisson's ratio can be used for the assessment of the adequacy of the resolution annealing treatment for rejuvenation of the mechanical properties of these tubes.

The observations on the failed tube also indicate that the measurement of the Poisson's ratio and hardness in combination can clearly bring out any anomalous change in the microstructure of the tube, such as increase in the grain size or formation of creep cracks because of abnormal service conditions such as accidental increase in temperature/load.
The study demonstrates the usefulness of Poisson's ratio in combination with hardness measurements, as an effective nondestructive tool for assessment of progress of in-service degradation of Inconel 625 cracker tubes and also for qualification of resolution annealing heat treatment for ensuring effective rejuvenation. Further, the study also reveals that by a judicious evaluation of Poisson's ratio and hardness, the life of some of these expensive tubes can be extended beyond the presently followed 1,20,000 h, before they are taken up for resolution annealing without affecting their serviceability. This is based on the observation that the extent of degradation in different tubes varies depending upon the actual service temperature experienced by the tubes during their life span.

5.21 Finite Element Modeling of Remote Field Eddy Current Phenomena

The remote field eddy current (RFEC) non-destructive evaluation (NDE) technique has been chosen for the in-service inspection of modified 9Cr-1Mo ferromagnetic steam generator (SG) tubes of PFBR. The RFEC technique uses separate exciter and receiver coils and low excitation frequencies for the NDE of tubes from the tube-side. In this technique,the induced voltage in a receiver coil placed at 2 to 3 tube diameters away from the exciter coil, is measured. Reliable detection and sizing of defects in the SG tubes requires that the excitation frequency is optimized and the receiver coil is positioned in a remote-field zone which is far away from the near-field zone of conventional eddy current testing. Finite element modeling has been carried out using the FEMLAB package to examine the near-field and the remote field zones, to optimize the receiver coil location, to optimize the excitation frequency and to get an insight into the field/defect interactions in the RFEC technique.

The governing differential equation for eddy current testing is a coupled partial differential equation (PDE) derived from the four Maxwell's equations of electromagnetism.

$$\nabla \times \frac{1}{\mu} \nabla \times \vec{A} = \vec{J}_S - \sigma \frac{\partial \vec{A}}{\partial t}$$

where A, J_s, σ and μ are magnetic vector potential, current density, electrical conductivity, magnetic permeability of the material respectively. This equation is solved using finite element method which consists of discretization (meshing) of the solution domain and

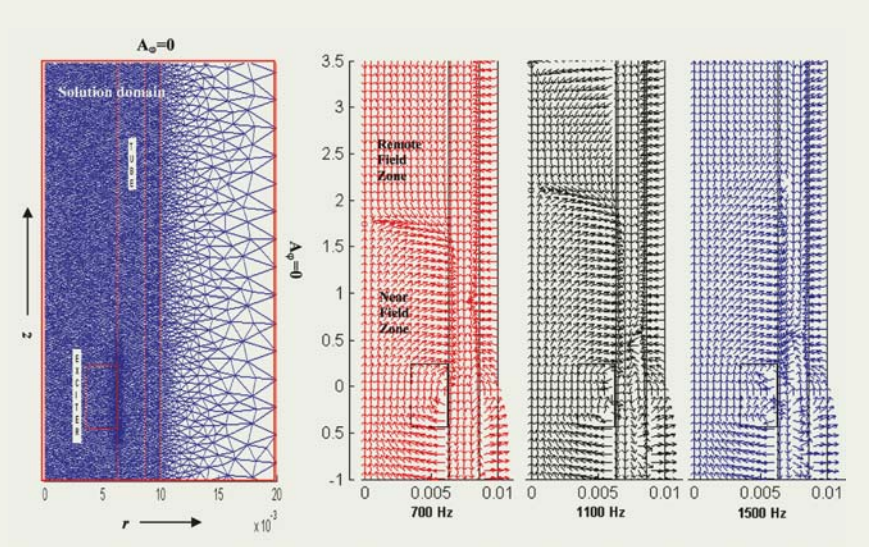

Fig. 1. Discretized triangular mesh of the solution domain comprising of exciter coil and tube and the model predicted Poynting vector plots of vector potential showing the near-field, remote field and transition zones at 700, 1100 and 1500 Hz.

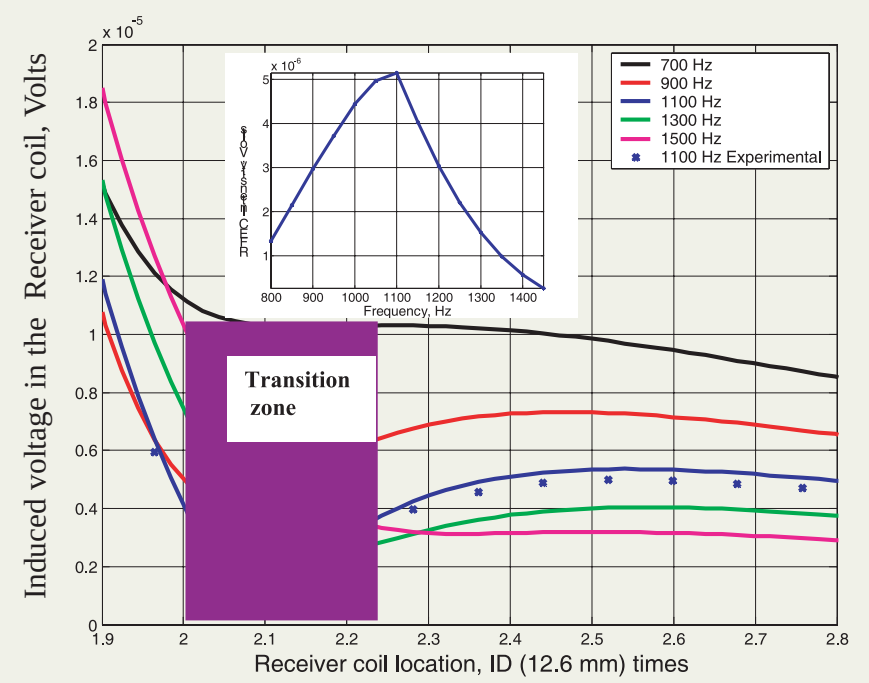

Fig. 2. Predicted induced voltage in receiver coil at 700, 900, 1100, 1300 and 1500 Hz as a function of receiver coil location and measured induced voltage at 1100 Hz. The inset shows the intensity of back entered remote field with excitation frequency.

assuming a trial solution within each element of the mesh using basis or shape functions and substituting the solution in the PDE. The error due to the assumed solution is minimised to finally arrive at the variable of interest i.e. A in each element. For the finite element modeling of the RFEC technique, the solution domain consists of a copper coil exciter (length, 7.5 mm and width, 2.8 mm) kept inside a modified 9Cr-1Mo steel tube (outer dia., 17.2 mm, wall thickness, 2.3 mm and length, 150 mm) and the magnetic vector potential values are obtained, in the time domain, at all the nodes in the discretised region to predict the induced voltage, eddy current density, magnetic flux density etc. As the coil and tube are circular, axi-symmetric modeling (*r-z*) is sufficient and the distribution and flow of eddy currents along the circumferential direction is insignificant as compared to the depth direction. As a boundary condition, the magnetic vector potential is set to zero (A_Φ=0) at a region far away from the exciter coil, without having a computational burden in terms of a larger solution region and the number of elements. An optimized uniform mesh of 50,000 triangular elements is used as shown in Fig. 1. Magnetic fields are predicted at various excitation frequencies in the range of 700 Hz-1500 Hz for the SG tubes with 10%-60% wall loss (WL) outer defects as well as without defects. The receiver coil location from exciter coil is expressed in terms of tube inner diameter (ID).

The magnetic field inside the tube does not decrease exponentially, but it increases after certain distance from the exciter with a definite transition zone. Figure 1 also shows the Poynting vector plots that show the near-field, transition and remote field zones at different frequencies. Transition zone is the region beyond which the external magnetic field (remote field)

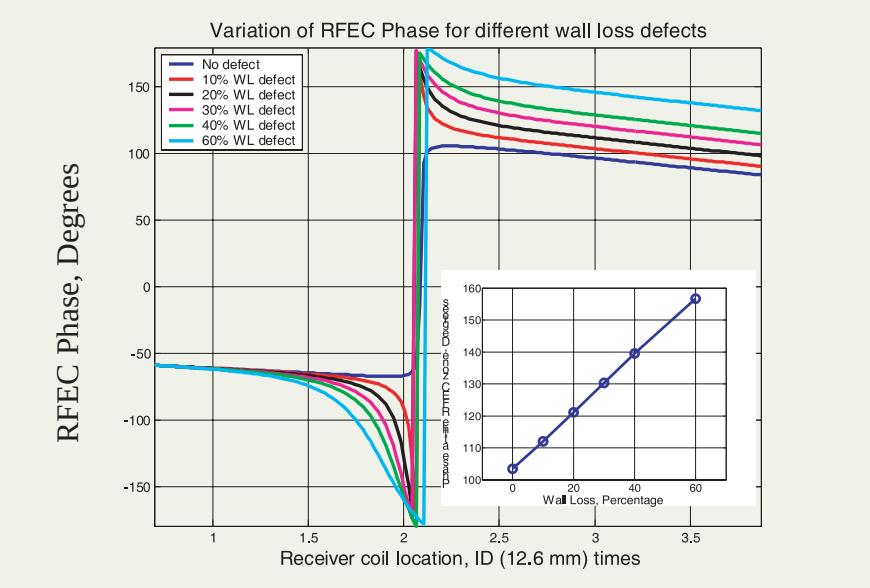

Fig. 3 Linear variation of phase lag of induced voltage in receiver coil with wall loss.

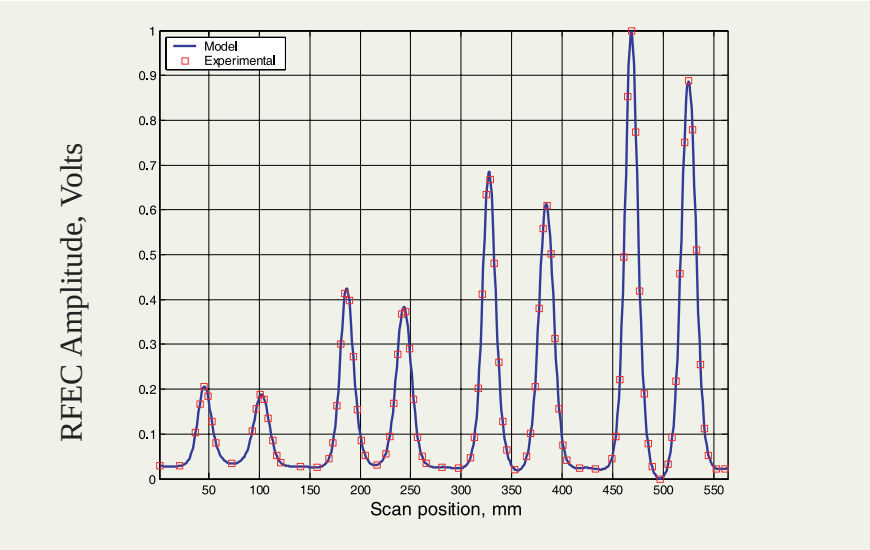

Fig. 4. FEM model predicted and experimentally obtained RFEC signals for various wall loss defects on the outer side of a SG tube at 1100 Hz.

enters back into the tube wall for pick-up by a receiver coil. With increasing frequency, the transition zone moves away from the exciter and disappears beyond 1500 Hz. The magnetic field inside the tube wall, subsequent to the double wall transit, is shown in Figure 2. As can be seen, beyond 2.1 tube diameters, the remote field intensity inside the tube increases steadily upto an axial distance of about 2.5 tube diameters, signifying the ideal location for the receiver coil for maximum pick-up of the indirect reversed magnetic fields that have the information of the defects. The intensity of the back entered remote field (with respect to the transition minimum) is maximum at 1100 Hz at 2.5 tube diameters (approximately 31.5 mm) as depicted in the inset of the Fig. 2 for the tube geometry, material properties and exciter dimensions considered in this model. The back entered magnetic field, and hence the induced voltage in the receiver coil, is also associated with a reversal in phase which has a linear relationship, with wall loss like the magnitude of induced voltage, as shown in Fig. 3. The predicted induced voltage at 1100 Hz is experimentally validated as also shown in Fig. 4. For the present case, positioning the receiver coil in the remote field zone, away from the transition zone, and using an excitation frequency of 1100 Hz in the coil ensures maximum sensitivity for the detection of defects. At the optimized conditions, RFEC signals are predicted by moving the exciter and receiver coils in tandem over wall loss defects and typical signals are shown in Fig. 4. Characteristic double peaks are observed, one when the defect is under the receiver coil and the other when the same defect is under the exciter coil. The predicted results are compared with measured RFEC signals and a very good correlation is observed as depicted in Fig. 4. In order to detect, size, and locate localized defects and corrosion wall loss, simulation of the response from a segmented receiver coil is in progress.

5.22 Evaluation of Activity of Radioactive Sources inside Shielded Containers by Surface Temperature Mapping through IR Imaging

Thermal imaging is an advanced nondestructive test technique which has been widely used at IGCAR for varied applications ranging from predicitve condition management, in-service inspection to materials charcaterisation and online weld monitoring. One of the recent novel applications, of this technique realised at IGCAR in collabration with BRIT,Vashi and Isotope Division,BARC, Mumbai has been to map the temperatures of the surface of shielded casks containing radioactive sources. It is well known that when radioactive sources with high activity are stored in a shielded container, the container gets heated up due to gamma heating. The amount of heat generated by the radiaoctive source depends on the strength of the source. This gamma heating is primarily due to absorption of the gamma rays and the conversion of photon energy, predominantly to heat energy. The rate of heat generated per unit volume at a point z in the shield is given by

$$Q(z) = \int_E \mu_a(E)\phi_\gamma(z,E)E_\gamma dE \ \text{MeV/m}^3.\text{s}$$

where $\mu_a(E)$ is the linear energy absorption for gamma rays of energy E, Eγ is the energy of the gamma ray photon in MeV. An experimental study was successfully undertaken to map the skin temperature profiles of radioactive packages and containers and for evaluating the activity of the source.

Blood irradiators containing Co-60 source (housed in a gamma chamber) with activity in the range of 700 - 800 Ci and shielded containers with Co-60 pencils and assemblies with activities ranging from 19 kCi to 97 kCi were scanned using a focal plane array based IR imaging system. After appropriate corrections for emissivity (based on the surface condition) and ambient temperature to compensate for IR radiations from other sources, the skin temperatures were quantitatively estimated. Figure 1 is a photograph of an empty gamma chamber housed inside a blood irradiator and Fig. 2 is the typical thermal image. Figure 3 is the thermal image of a shielded container with a radioactive source. Analysis of this thermal image revealed a uniform isothermal temperature distribution with skin temperatures in the range of 33.3-34.1°C, after appropriate correction. This formed the baseline data for further experimental studies to evaluate the activity level.

Thermal imaging was also carried out on shielded containers with Co-60 pencils and assemblies. Table-I summarises the temperatures mapped on the blood irradiators and shielded containers. Figs. 4(a) & (b) are the vertical and horizontal thermal line profiles of one of the casks. The temperature oscillations observed in the horizontal line profile (Fig. 4(b)) is attributed to the presence of fins of the container which represent extra thickness of material and hence have lower temperature as compared to their surroundings. One of the casks showed variation in the temperatures along the circumferential direction due to the presence of four Co-60 assemblies with different activity levels in the same cask. The peak temperatures along the circumference corresponding to the four Co-60 assemblies varied from 68-71°C. Compared to the skin temperatures of the gamma chambers, the skin temperature of the shielded casks were much higher varying from 47-72°C. Fig. 5 is the plot of the maximum

Fig. 1. Empty gamma chamber

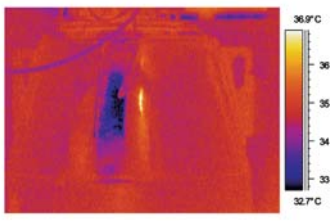

Fig. 2. Thermal image of an empty gamma chamber

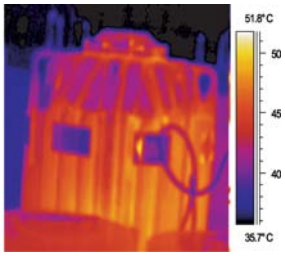

Fig. 3. Thermal image of cask 4 Model COF-100; Type B(u)Co- 60 activity - 30,000Ci

Table. 1. Skin temperatures for Co-60 sources with different activity levels.

Source	Activity (Ci)	Temperature(deg C)
Gamma Source in the Blood irradiator(Co^{60})	Empty	33.7
	700	34.7
	780	35.2
	800	36.2
Co^{60} Cask1	96,800	71.2 (max. temp at one particular direction)
Co^{60} Cask 2	18,800	47.1 (max.. temp.)
Co^{60} Cask 3	90,800	61.3 (max. Temp.)
Co^{60} Cask 4	30,000	50.5(max. Temp.)

temperature vs activity fitted by the least squares method. It can be observed from Table.1 and Fig. 5 that, as the source activity increases, the corresponding skin temperatures also increases. The relationship between the maximum skin temperature and the source activity is found to be linear for a given type of container.

This study opens up a new application of IR imaging in the nuclear industry. The experiments clearly reveal that IR imaging makes it possible to visualize the temperature variations due to gamma heating, quantitatively estimate the skin temperatures and correlate the same with the activity levels of sources contained in the packages/shielded casks. An interesting offshoot of this experimental work is that thermal imaging also provides the possibility of -detecting voids and areas with gross wall thinning that affect the effectiveness of the shielding since these areas should indicate substantial temperature difference as compared to the surrounding normal areas.

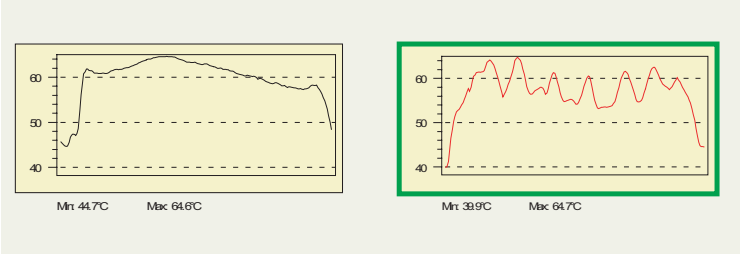

Fig. 4. (a) vertical and (b) horizontal temperature profile on the surface of cask1

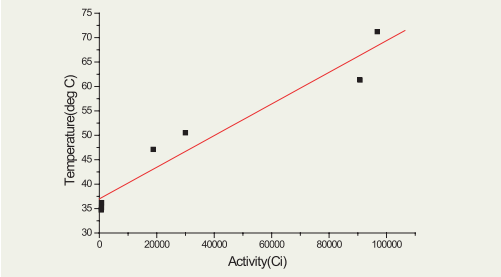

Fig. 5. Graphical plot of the maximum temperature observed for different activity levels.

5.23 Testing of Hydrogen-in-Argon Detector

Developmental activities for an on-line vacuum based hydrogen meter in the cover gas argon have been carried out. This Hydrogen in Argon Detector (HAD) employs a nickel membrane, one side of which is facing argon while other side is exposed to a high vacuum created by a sputter ion pump (SIP). Hydrogen, present in the argon, diffuses through the nickel to the vacuum side and results in a change in the sputter ion pump current which is proportional to the concentration of hydrogen. Various sensorer configurations were attempted and it was seen that maintaining the nickel temperature at 450°C in an argon atmosphere was a problem. Finally, the present configuration was arrived at. The sensor consists of an SS rod on which grooves are made (Fig 1). A nickel tube(7.2mm OD, 0.3mm WT) is wound over the grooves. Nickel in the form a coil is fixed to the SS body by a fixing ring provided at the bottom. The bottom of the tube is closed and the top is welded to the SS body where the vacuum piping is connected. A hole of 12.5mm diameter is provided in the sensor to accommodate a cartridge heater, which can heat nickel

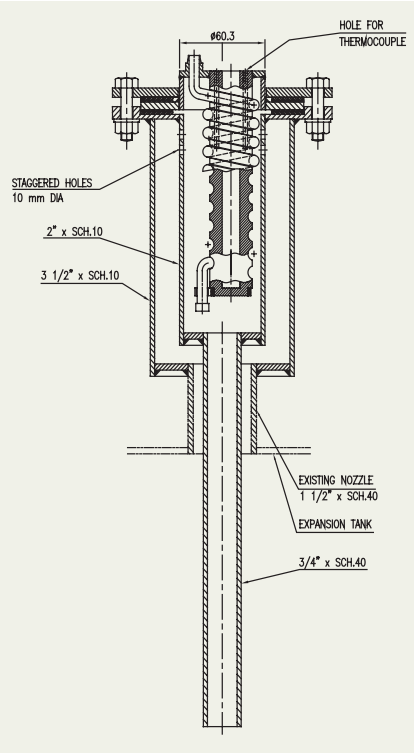

Fig. 1. HAD Sensor in the Housing

up to 450°C. A hole of 3mm diameter is provided on the rod for inserting a thermocouple, which will control the cartridge heater. The sensor is placed in a specially made housing and mounted in the expansion tank of SOWART.

Apart from this sensor, the expansion tank of SOWART houses another HAD using the thermal conductivity detector (TCD), which measures variation of thermal conductivity in argon with hydrogen concentration. Hydrogen injection tests were carried out in SOWART to study the performance of the HAD.

After starting the SIP, the nickel temperature was increased gradually to 300^{0}C. The vacuum obtained was 1x10^{-6} torr. The HAD using TCD was also put in service. Output of both the meters in volts were recorded. Hydrogen injection was done

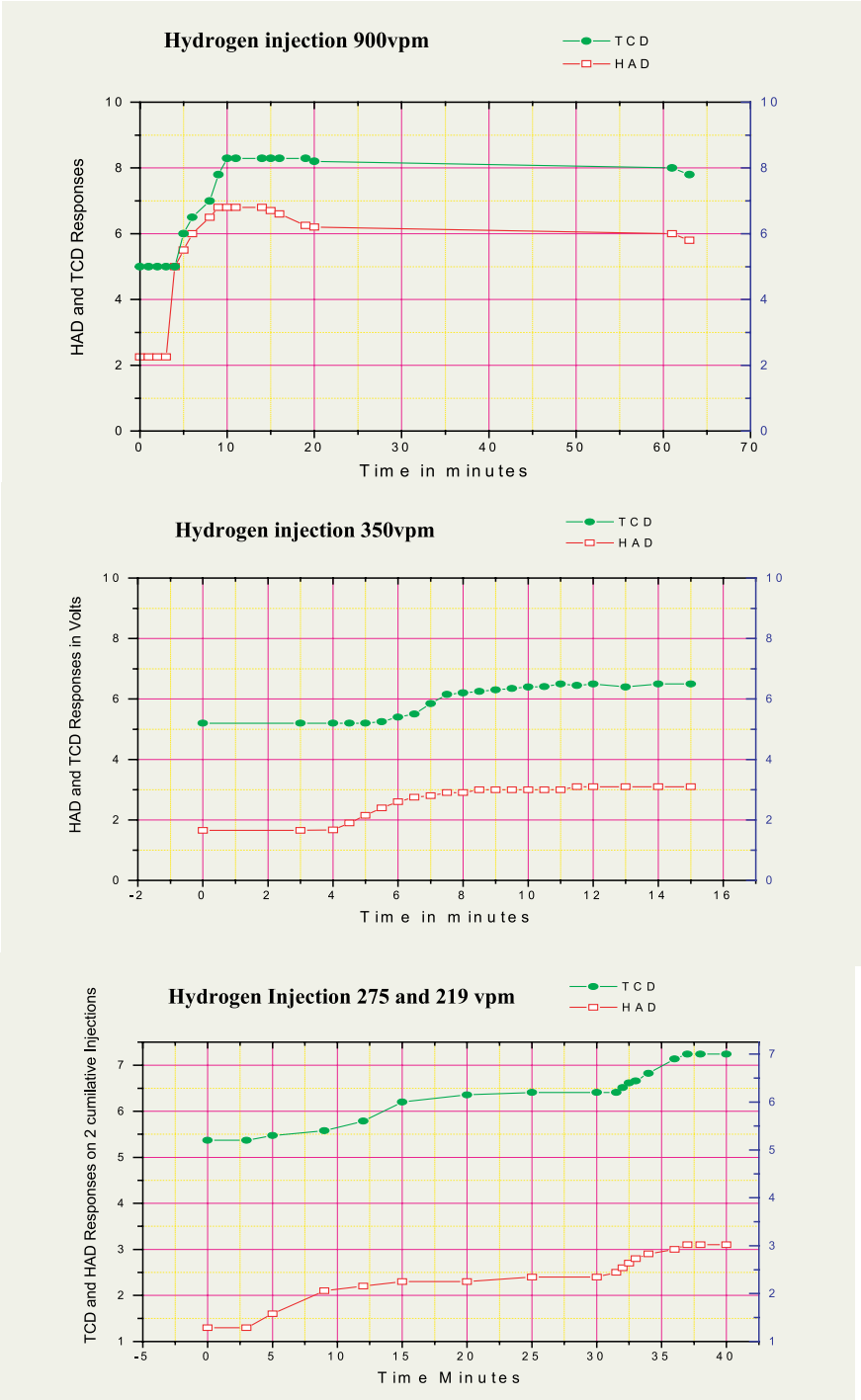

Fig.2. Responses of HAD and TCD for hydrogen Injections

on three consecutive days at a sodium temperature of 350°C. During the first and second injection, the hydrogen concentration in the cover gas was 900 vpm and 350 vpm respectively. The third and fourth were two successive injections with 275 vpm and 219 vpm respectively. The performance of both types of HAD are shown in Fig: 2.

It is observed that both meters were sensitive to all the injections. Further testing on the repeatability and optimizing the size of the sensor based on the SIP is in progress.

5.24 SQUID based System for Non-Destructive Evaluation

The Superconducting Quantum Interference Device (SQUID) is the most sensitive detector of magnetic flux available today, with an ultimate sensitivity in the range of 10fT. High quality Nb-AlO_x-Nb Josephson junctions and SQUID sensors based thereon have been developed at IGCAR using advanced micro-fabrication techniques. To linearise the periodic output response of the SQUID device, a Flux-Locked-Loop electronics has also been developed indigenously. Current efforts are directed towards harnessing the high sensitivity of the SQUID devices in a number of applications such as SQUID magnetometers and SQUID based Non-Destructive Evaluation (NDE) etc.

Fig. 1. SQUID based system for NDE.

SQUID based NDE offers the possibility of detecting deep subsurface defects which are not detectable by conventional eddy current techniques owing to skin depth limitations. A SQUID based NDE set-up, including a computer controlled precision X-Y-θ scanner has been commissioned at the Materials Science Division of IGCAR. Positioning accuracy of the scanner is 25 μm in both X- and Y- directions and better than 0.1° for θ. The sample-stage of the scanner is non-metallic and non-magnetic in construction and can support samples in the form of flat plates and cylindrical tubes while achieving scanning speeds of 1 to 50mm/sec. The SQUID sensor and the pick-up loop in the form of a first order gradiometer are located inside a liquid helium cryostat while the sample under evaluation is at room temperature and is placed on the sample stage of the X-Y scanner. The eddy currents are excited in the sample under evaluation at relatively low frequencies and the perturbations in the flow pattern of the eddy currents in the vicinity of the defects manifest as magnetic anomalies when the sample is scanned under the stationary cryostat. Alternatively, the system can be used to probe the variations in local remnant magnetization in the sample as the scanning is performed. A photograph of the system is shown in Fig.1.

As an illustration, a study was undertaken to evaluate the usefulness of the SQUID sensor for tracking variations in the magnetic content (for example, δ-ferrite) of weldment specimens when subjected to fatigue testing at elevated temperatures. 316LN stainless steel specimens were prepared by welding with 316N electrodes by the manual metal-arc welding process. Two samples were selected for SQUID based evaluation. One sample was a virgin sample while the other was a sample subjected to fatigue testing at 600°C until fracture actually occurred. The low cycle fatigue tests were conducted at a strain amplitude of ±0.4% using an Instron servohydraulic fatigue testing machine under total axial strain control mode, and a strain rate of $3x10^{-3}$ s^{-1} was employed for the test. As

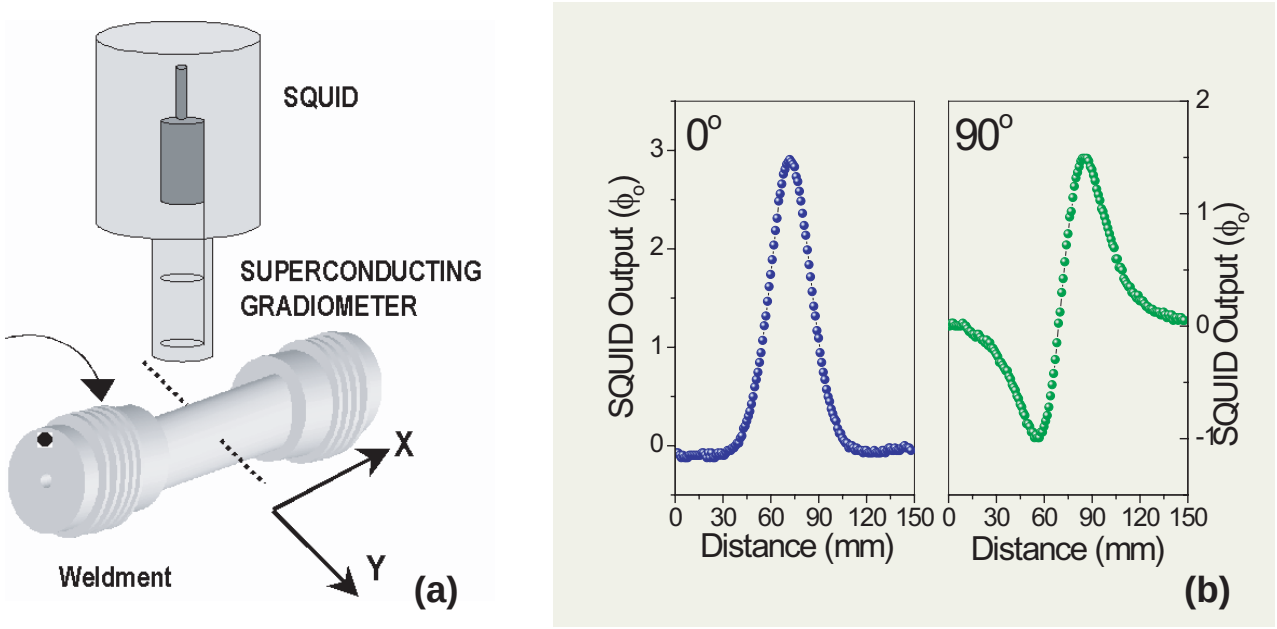

Fig. 2. (a) Schematic of the experimental arrangement and (b) Profiles of the SQUID output as the weldment was rotated about its axis with respect to a reference mark.

the samples were scanned under the cryostat, the SQUID output revealed a characteristic magnetic anomaly when the center of the gauge length of the sample passed under the pick-up loop indicating the presence of a magnetic phase at the location of the weld. As the sample was rotated about its axis, depending on the orientation of the magnetization of the sample relative to the axis of the pick-up loop, the shape of the magnetic anomaly changed from bell shaped to dipolar (fig.2). For the virgin sample, the amplitude of the magnetic anomaly was measured to be $\sim 1.78\Phi_0$, whereas for the sample which was subjected to fatigue testing at 600°C until fracture, the amplitude of the magnetic anomaly was measured to be as small as $\sim 0.05\ \Phi_0$ (Fig.3)under identical measurement conditions. (Φ_0 is an extremely small unit of magnetic flux and is equal to 2.07×10^{-15} Wb). The experiments clearly show that the magnetic phase (δ-ferrite) present in the virgin samples transforms to a nonmagnetic phase (σ or carbides etc.) when the weldment sample undergoes fatigue damage. These results demonstrate the potential of SQUID based measurements in tracking the magnetic→ nonmagnetic (ex. δ→σ) transformation in stainless steel welds when subjected to high temperature fatigue loading.

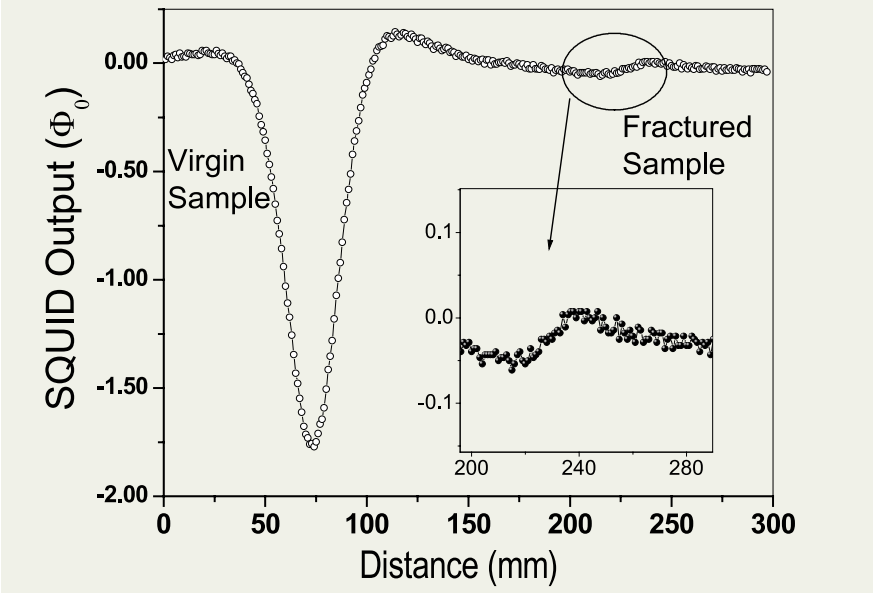

Fig. 3. SQUID output profiles of the virgin and the fractured sample. The virgin sample was rotated by 180° about its axis relative to the reference mark.

5.25 Development of Eddy Current Position Sensor for DSRDM

In the PFBR, there are three Diverse Safety Rods (DSR) in the control plug. During normal operation, they are held outside the active core region by an electromagnet. On receiving the SCRAM signal, the electromagnet de-energizes and drops the DSR, which falls under gravity in sodium. The DSR gets decelerated due to the damping action of sodium in the dash-pot after traveling the free-fall distance. The detection of the DSR at its lowest location is a safety requirement. An Eddy Current based Position Sensor (ECPS) was designed and fabricated. It was also tested in air and in sodium. The basic design was arrived at after analyzing different design options. Closed loop circuit analysis was carried out to predict its sensitivity.

A sensor having the circuit configuration as shown in Fig.1 was chosen for the design.

The primary coil, placed on the mobile assembly of Diverse Safety Rod Drive Mechanism (DSRDM) is excited with 200 mA current. A pick-up coil is also placed below the primary coil in the same axis for getting the output signal. The Secondary, signal transfer and sensor coils are placed in the hexcan. Paucity of space is a challenge for accommodating the ECPS in the DSRDM, which was overcome by arriving at a compact design using FEM analysis. Fig. 2 shows the overall arrangement of ECPS coils in the DSRDM. Table. 1 shows the diameter of the MI cable used in various coils.

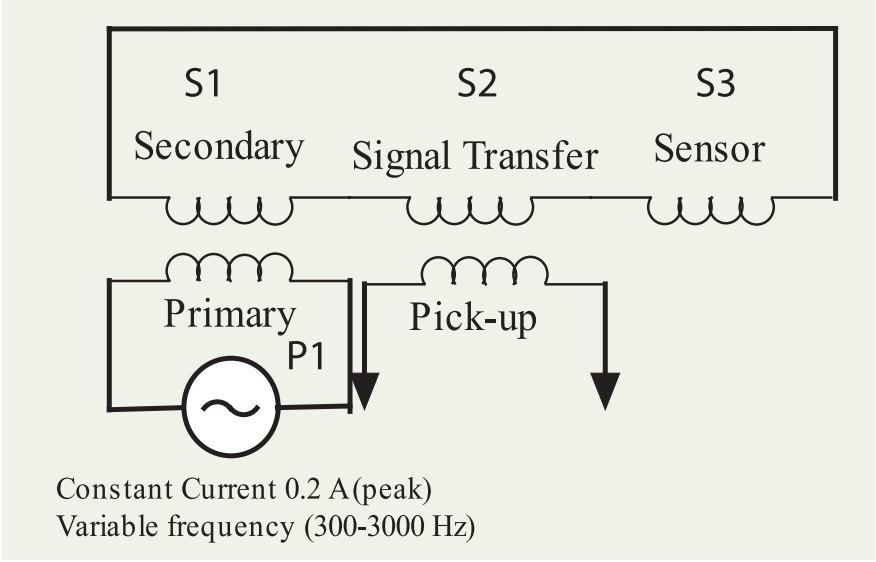

Fig. 1. Circuit diagram of prototype ECPS.

The induced voltage in the secondary would drive a circulating current in all the three coils on the secondary side. The magnitude and phase of this current depends on the total impedance of the coils on the secondary side. The impedance of the sensor coil changes when the DSR is in the deposited condition as compared to the non-deposited situation. Accordingly, the flux linkage with the pick-up coil varies, thereby changing the voltage induced in it. This indicates the presence of the DSR near the sensor coil. A parametric study was done with respect to the frequency, bobbin dimension and number of turns.

Subsequently, an ECPS model was fabricated for sodium testing. All coils were wound with MI cables. The ECPS model fabricated for sodium testing is shown in Fig.3. Before putting in sodium, it was tested in air for a functional test. The SS spacer between the primary and pickup coil was replaced with a copper spacer to reduce the cross coupling and to concentrate the flux in the intended path.

The ECPS model was put in the

Table 1. Different diametres of MI cables

Primary(P1)	1.5 mm copper core MI cable
Secondary (S1)	1.5 mm copper core MI cable
Signal transfer(S2)	1.5 mm copper core MI cable
Pick-up coil	1.0 mm copper core MI cable
Sensor Coil(S3)	1.5 mm copper core MI cable

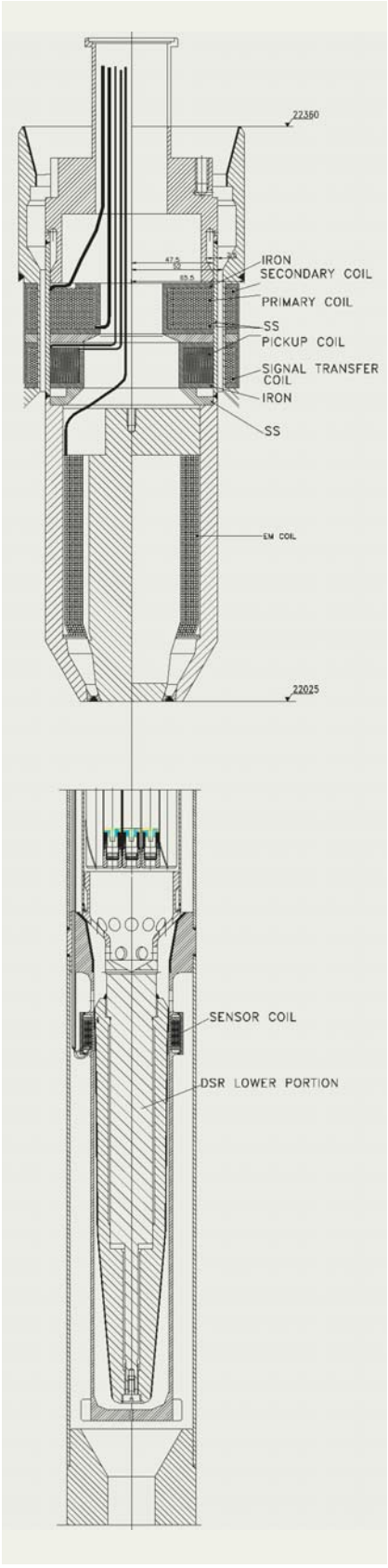

Fig. 2. ECPS coil location in DSRDM

Fig. 3. ECPS model for sodium testing.

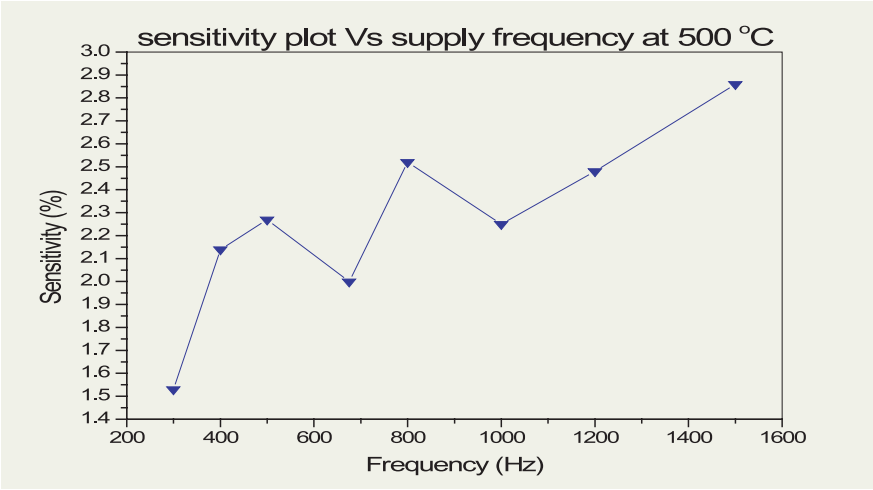

Fig. 4. Sodium test result

SILVERINA loop of FRTG for sodium testing. The tests were conducted at various temperatures. The result at 500°C is shown in Fig.4. As the frequency increases, even though sensitivity shows an increasing trend, the absolute value of pick up voltage comes down. From this point of view, an operating frequency less than 1000 Hz is preferred. In this frequency range the average sensitivity is found to be around 2%. Further design improvement will be carried out based on these experiences. The conducted test on the ECPS model gives confidence towards further development and feasibility of such a sensor.

5.26 Analytical Thermometric Facilities for Chemical Assay

Chemical reactions are associated with heat effects with consequent changes in the temperature. Quite often the temperature shifts are very small and require very costly instrumentation for extraction of chemical information from minor heat effects for quantitative work. Inexpensive high precision dielectric based temperature sensors, have been developed, which operate entirely in the digital domain starting from the generation of primary signal. This had led to a highly cost effective means for the capture of minute temperature shifts. Moreover, unlike conventional analog devices, the digital pulses as primary signal generated at the probe head can easily be transmitted over long distances.

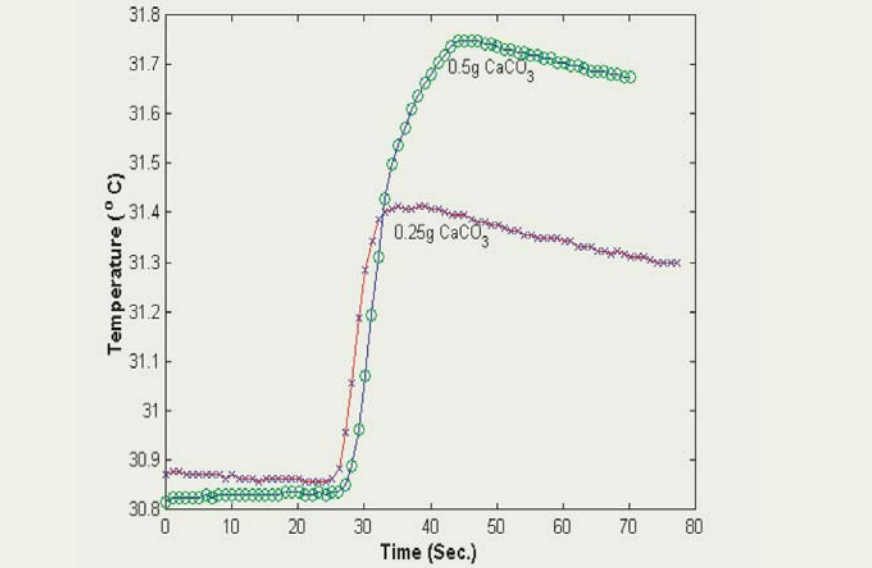

Fig. 1. Rapidly captured heat effects on reaction of 0.25 and 0.5 gm of $CaCO_3$ with 25 ml of 1N HCl in an uncovered beaker without insulation.

Highly sensitive capacitive changes caused by the strong temperature dependence of the dielectric permeability of an appropriate dielectric material, is made use of for construction of the temperature sensors. Such a sensor, when placed in the timing circuit of a suitably designed miniature oscillator, gives an output which is a train of rectangular pulses of 5V amplitude at a pulse frequency determined by the temperature of the system being sensed. A Pre-calibrated pulse frequency-to-temperature relationship in the form of polynomial of 2nd or 3rd degree is used for deriving the temperatures from the

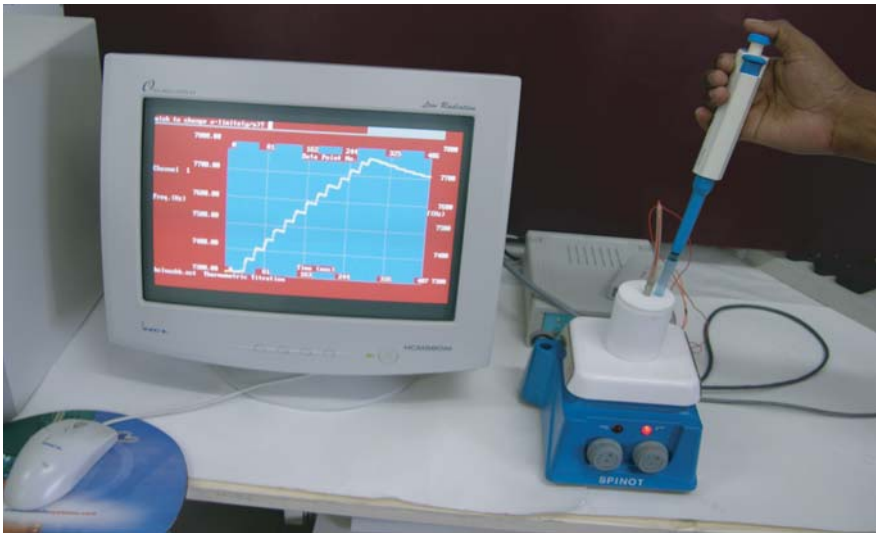

Fig. 2. Thermometric titration facility. Minor temperature shifts are being recorded during a chemical reaction which is being carried out in steps before and after completion of the reaction.

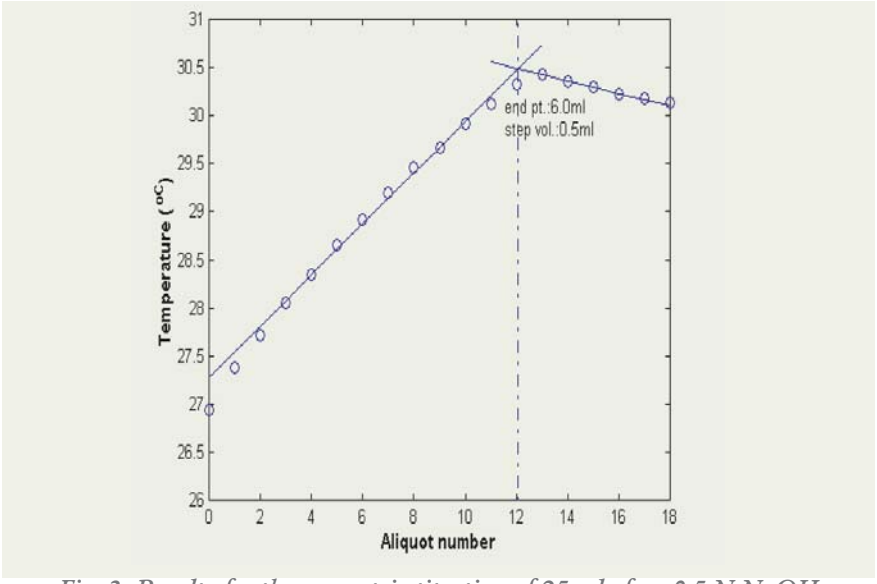

Fig. 3. Result of a thermometric titration of 25 ml of ~ 0.5 N NaOH with ~ 2N HCl added in aliquots of 0.5 ml.

measured pulse frequencies. Minor temperature shifts down to a few hundredths of a degree can be measured routinely on account of the very high precision with which the pulse frequencies are determined. Such sensors were constructed and associated hardware and software were developed for a number of applications such as the measurement of under sea temperatures at Kalpakkam coast; isotopic effects on freezing and melting points; and for the calorimetric determination of heats of dissolution and mixing; etc. A brief description follows on the application in analytical thermometry for chemical assay in aqueous solutions.

An example of the rapidly captured temperature related frequency shifts on the chemical reaction of different quantities of solid $CaCO_3$ with HCl solution in a container without thermal insulation is given in Fig. 1. The frequency shift is related non-linearly to the quantity of solid, and this is the basis for an emerging rapid thermo-analytical technique towards quick screening for the carbonate content in limestone aggregate material to be used in concrete.

The second example is with respect to thermometric titration. An inexpensive plug-and-use type PC based facility has been made for carrying out thermometric titrations within minutes using the above temperature sensor. The titration involves the recording of minor temperature shifts with the progressive stepwise addition of a solution of known concentration of one reactant A, from a micropipette at room temperature, to a solution of another reactant B of unknown concentration. The latter solution is kept in a small vessel into which the temperature sensor is placed. The rate of change in temperature during progressive addition differs before and after the end point. The point of intersection of the volume (v) versus temperature (T) fitted lines before and after the plot gives the end point. A photograph of the facility with a screen view of progressive stepwise change in temperature with successive addition of reactant A into reactant B is given in Fig. 2. A typical thermometric titration plot derived for an acid-base reaction is given in Fig. 3. These developed facilities have been and can be used for thermo-analytical work involving different types of chemical reactions.

5.27 Application of Laboratory Developed Miniature Titration Facility for Study of Electro-reduction of U(VI) to U(IV)

Use of in-situ electro-reduction of U(VI) and Pu(IV) is an advantageous choice for valency control prior to partitioning of Pu from U during reprocessing of spent FBR fuel by the PUREX process. The reduction is carried out in a bank of two-compartment flow type cells. It is necessary to study the yield of U(IV) in the cathode compartment as a function of time and current density. An in-house developed PC based rapid and automated titration facility, which is highly suitable for carrying out titrations in very small volumes of dilute solutions, was adopted for the assay of U(IV) at frequent intervals without interruption of the electro-reduction process. A photograph of the potentiometric titration set up, with built-in features for instantaneous display of titration plots with results, is given in Fig. 1.

A representative flow type electro-reduction cell is shown schematically in Fig. 2. Small volumes (100 microlitres) of samples are drawn from the cathode compartment at desired intervals and placed in a tiny titration cell, where, after a suitable chemical conditioning, U(IV) is titrated by a REDOX reaction with a standard dichromate solution by addition of the latter in steps as small drops of known volume. The change in emf as sensed by a pair of thin wire type electrodes in the titration cell, as well as the growth and fall of drops from a miniature solution dispenser as sensed by a tiny conductance sensor, are monitored and displayed as a function time in two different channels, thus providing the basic data for the generation of normal and first derivative titration plots immediately on completion of the titration.

The extent of conversion of U(VI) to U(IV), as determined by the potentiometric titration from time to time during the electrolysis at different current densities, are given in Fig. 3. Studies using the totally laboratory developed miniature potentiometric titration facility, thus, have helped in the optimisation of the conditions for efficient in-situ production of U(IV). The measurements were carried out at the Innovative Instrumentation Section (IIS) in collaboration with the Reprocessing Research and Development Division (RRDD).

Such measurements will have to be carried out later on highly radioactive samples from reduction cells in reprocessing plants. A compact signal processing cum data storage unit, instead of a PC, would add to the operational convenience during titrations in less accessible areas. The online unit would process the pulsed signals from the titration cell and the drop sensor as a function of time during the period of titration and store the data for off-line analysis using a PC elsewhere. An embedded pulse processor was designed and developed with such an application as one of the objectives.

The programmed embedded

Fig. 1. An in-house built miniature rapid potentiometric titration facility.

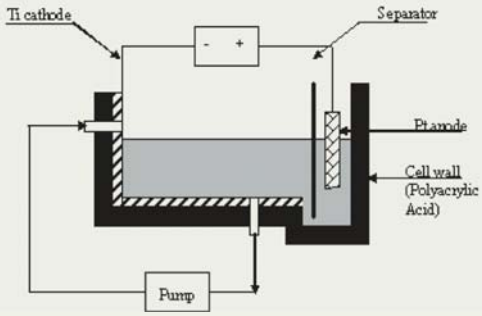

Fig. 2. Schematic representation of a typical flow type cell for electro-reduction of U(VI) to U(IV).

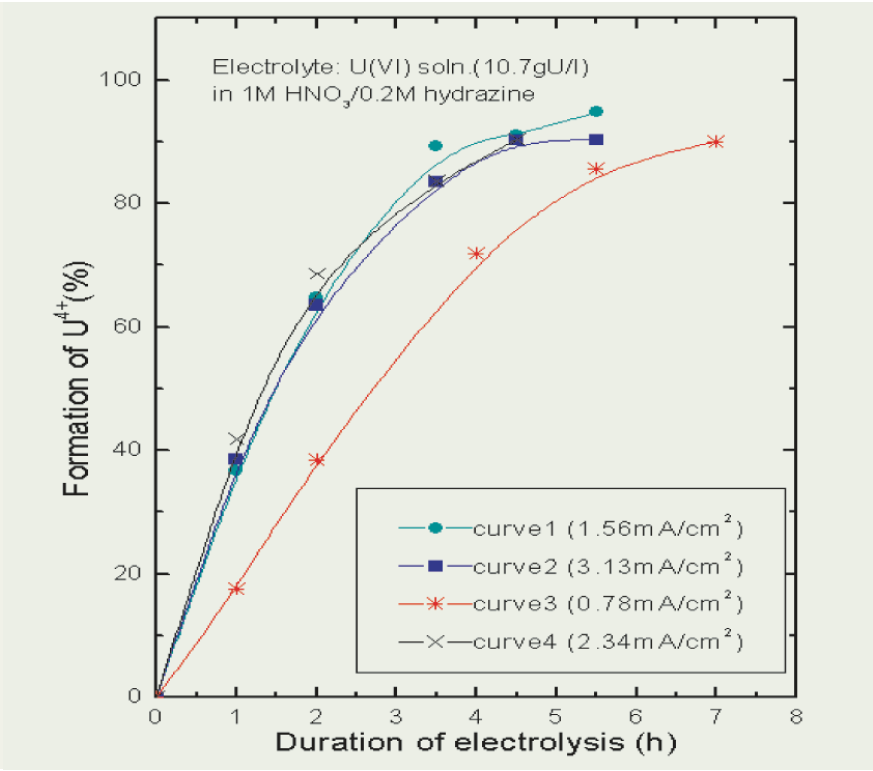

Fig. 3. Results of potentiometric assay of U(IV) on 100 microlitres of samples withdrawn from the cathode compartment at different times during electro-reduction.

Fig. 4. Embedded pulse processing unit.

device displays and stores data from three different sensors simultaneously. The unit also converts on-line measured pulse frequencies to data in the desired practical units using the preloaded calibration relationships in the form of polynomials of degree three (maximum). Besides, the embedded system can also act as a controller in all the three channels.

The unit is initially configured for a given application by interfacing it to a PC via the serial port and the communication is effected by running the HyperTerminal program in Windows. The system configuration menu prompts the user to enter the coefficients of the polynomial fitted calibration relationships for all the channels. The user has the provision to set the count duration, the interval between count cycles, and the upper and lower control thresholds for each channel. Once configured, the system can be taken to a field location where the unit can be simply powered ON to start the data acquisition. The frequency and the corresponding data value in each channel are displayed on an LCD on completion of each count cycle. The time stamped frequency values are stored in non-volatile memories and are available for further processing when required. The photograph of a laboratory developed embedded pulse processor is given in Fig. 4.

5.28 Development of a Real-time Decision Support System during a Radiological Emergency

Decision Support System (DSS) for disaster management is an explorative area of research in recent years as humanity is wreaked with increasing natural disasters on the one hand and the potential threat from technological disasters such as nuclear or radiological, chemical and biological accidents on the other hand. By integrating the state of art "3S" information technologies, namely the GIS (Geographic Information System), RS (Remote Sensing) and GPS (Geographical Positioning System) in this context, IGCAR is framing the emergency preparedness procedure in a more intelligent, user friendly manner, collaborating with expert institutions within and outside the DAE.

The system includes the following core elements:

- atmospheric dispersion models to predict the radiological impact with on-line access, assimilation and display of the field measured meteorological and radiation data;
- geographical maps showing where the crisis is and will be occurring, who is affected,;
- data management that puts plans, inventories, lists and other details, the emergency advisory information and so forth at the user's finger tips;
- the communication network for instant sharing of critical information within the organisations and for revealing relevant information to the public.

The atmospheric dispersion modelling system consists of an operational weather forecast model MM5 and a particle diffusion model. On-line access to the meteorological data as input to the regional multi-scale forecast model is established with National Centre for Medium Range Weather Forecast (NCMRWF), New Delhi and a system for real-time access is set up for the local meteorological measurements. The massively parallel code was tested for a quick run in a high performance cluster at the Institute of Mathematical Sciences and a Linux cluster is built locally using off-the-shelf server computers. The system run-time is 4h for a 24h plume forecast. The performance of MM5 has also been examined for the speedup achievable by increasing the number of computer nodes (Fig.1). The modelling system is currently operational and provides 'live' forecast of the air-borne radioactive plume direction and cross-wind spread for a hypothetical release from the Kalpakkam site.

After the spatio-temporal effect is known from the forecasted plume, the corresponding data is superimposed on the geographical maps of Kalpakkam using an indigenous GIS software developed at RRSSC, ISRO. It enables simple and expedient visual display of the disaster's effects and their integration

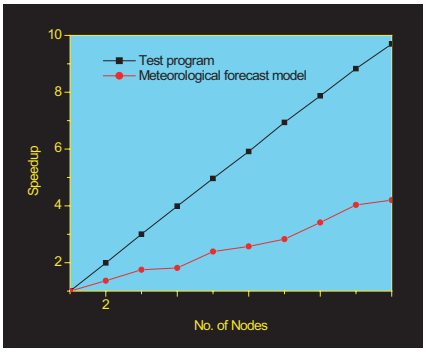

Fig. 1. Speedup diagram

with a suite of databases (population, land use/land cover, critical facilities). Subsequently, a DSS is being constructed as a quick tool to identify the areas of impact, counter measure supports and assimilation of the on-line field measured data for re-assessment of the situation. The GIS component of the Decision Support system takes the plume and the other appropriate databases, comes up with hard numbers of radioactive dose rate, collective dose, villages affected, and amounts of resources like the transport, shelter etc. required to mitigate the disaster and its aftermath. All the spatial database, dispersion simulation and the dose forecast can be integrated with facility of querying the position of interest on the maps. Sample output of a DSS for Kalpakkam is shown in Figs. 2, 3 & 4. The complete system is being tested for redundant functioning in 'live' operational mode and a thorough plan for validation of the system is in the offing.

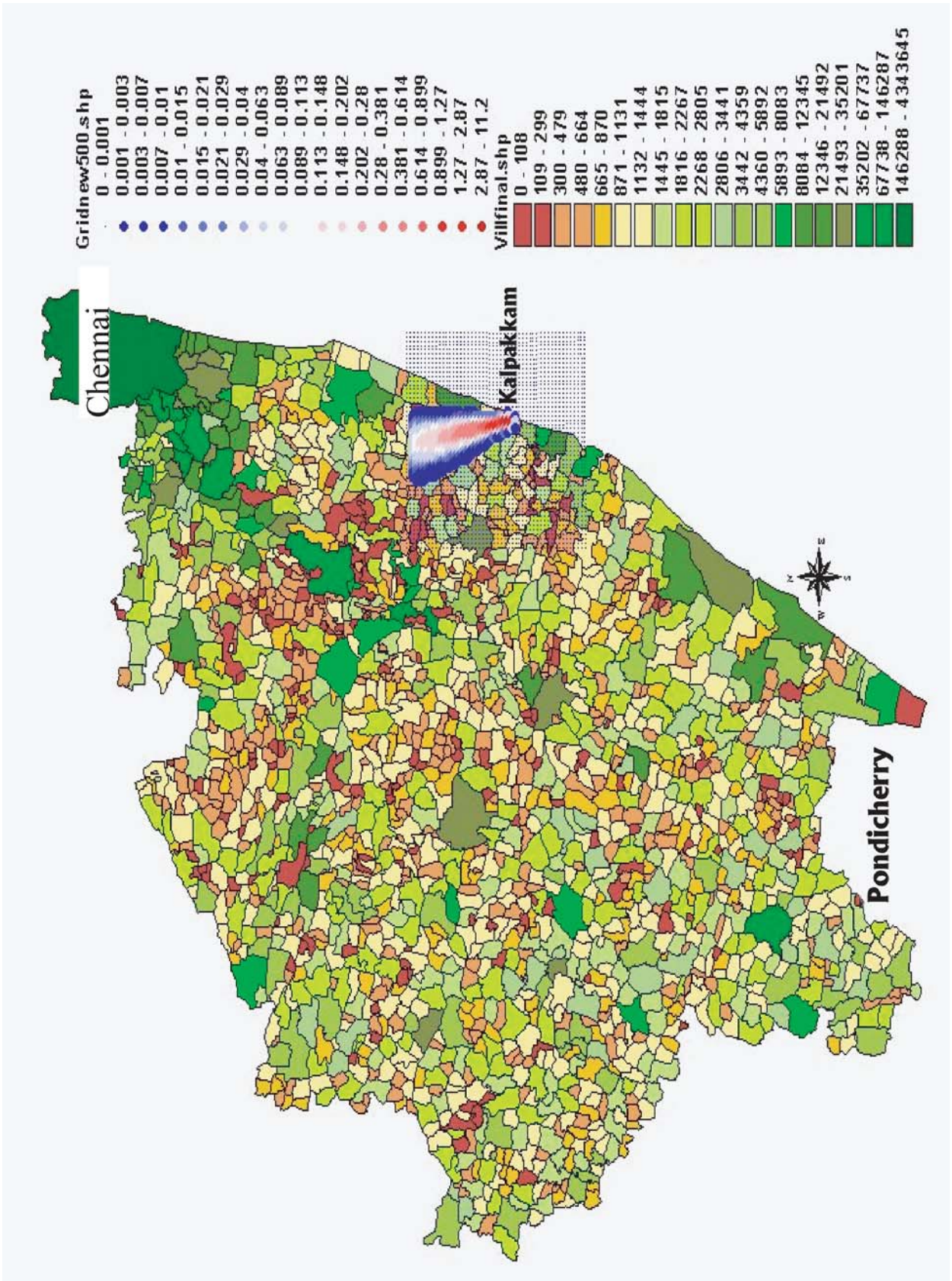

Fig. 2. Visual display of the hypothetical radioactive plume over the village map

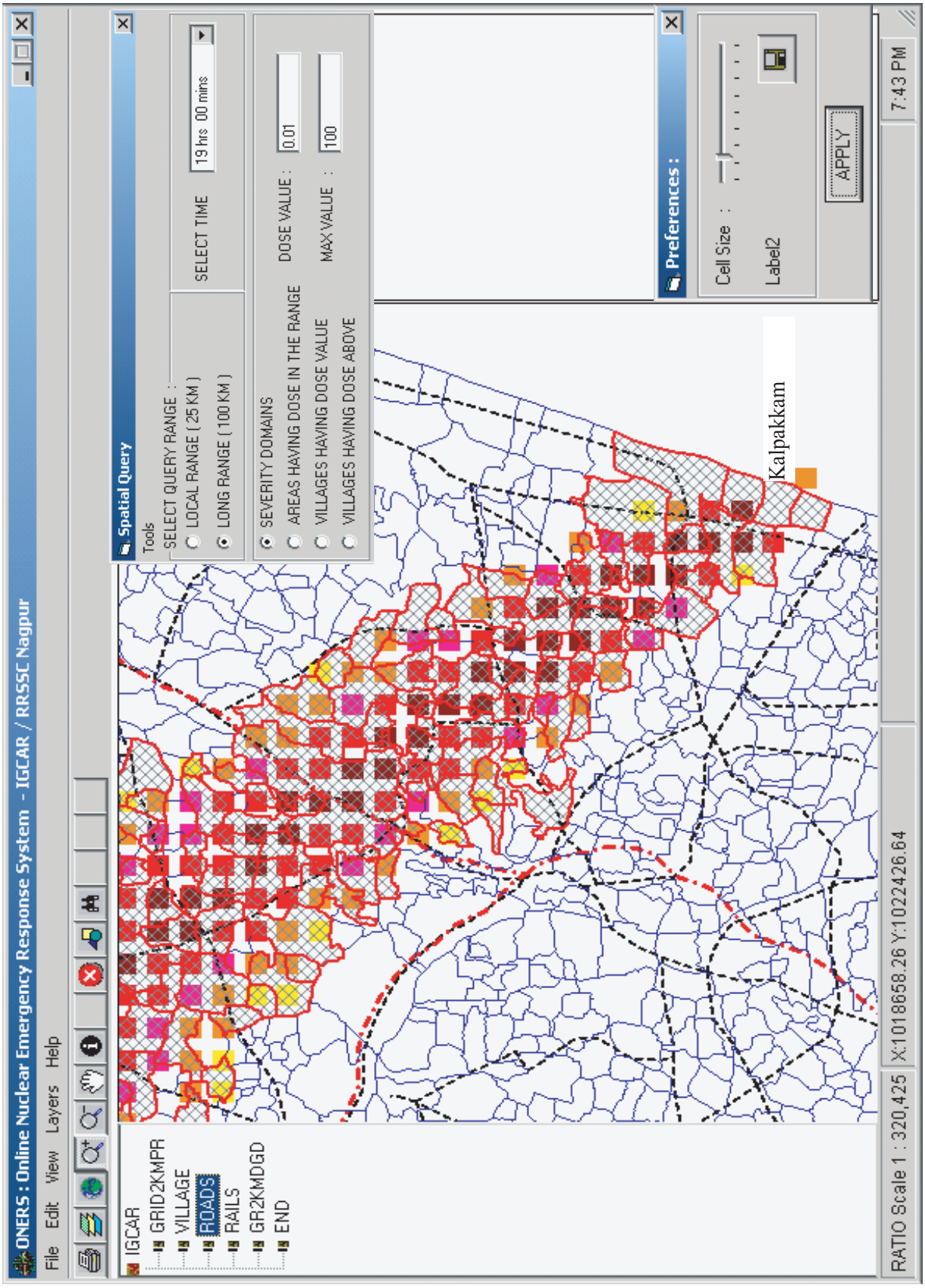

Fig. 3. Results displayed on-line upon different queries by the user.

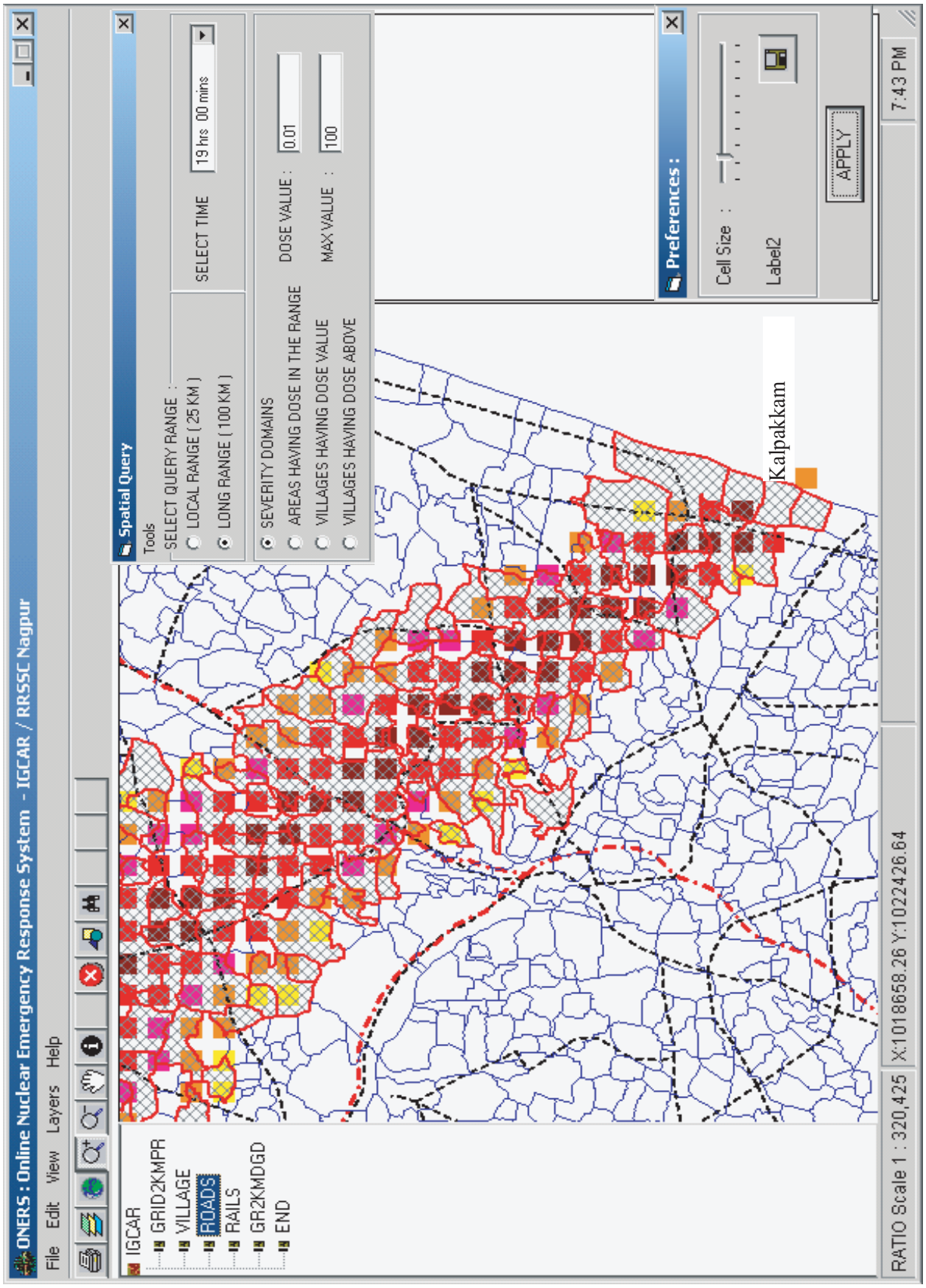

Fig. 4. Transport network, shelter points etc. shown in a high resolution (zoom-in) mode.

5.29 Software Verification and Validation

Verification and Validation (V & V) is important to demonstrate to the regulatory authority, the correctness and safety of any computer based Safety System. V & V of the software is to ensure that software conforms to its specifications. Verification is the process of determining whether or not the product of each phase like specifications, analysis, design, implementation etc. of the computer based system development process fulfills all the requirements imposed by the previous phase. The parameters like quality analysis, metrics, confirming to standards and guidelines also become part of V & V. Validation is the process of testing and evaluating the integrated computer based system (hardware and software) to ensure the compliance with the functional, performance and interface requirements.

Safety Critical Systems (SCS) play a vital role in achieving the safe operation of a Nuclear Power Plant and ensure the safety of the people and control on the environment. SCS needs to have high reliability, accuracy and availability. So, SCS needs an augmented verification processes in addition to the normal analysis and testing. The in-house developed Static Analyzer (SA) is a software tool for assessing the structural characteristics of the source code. It also analyses the code structure, including how functions and variables are defined and their dependency on each other. This improves the efficiency and reliability to achieve a high degree of confidence.

The Central Data Processing System of FBTR is the first computer based safety system and its architecture is based on a Dual Hot Standby system

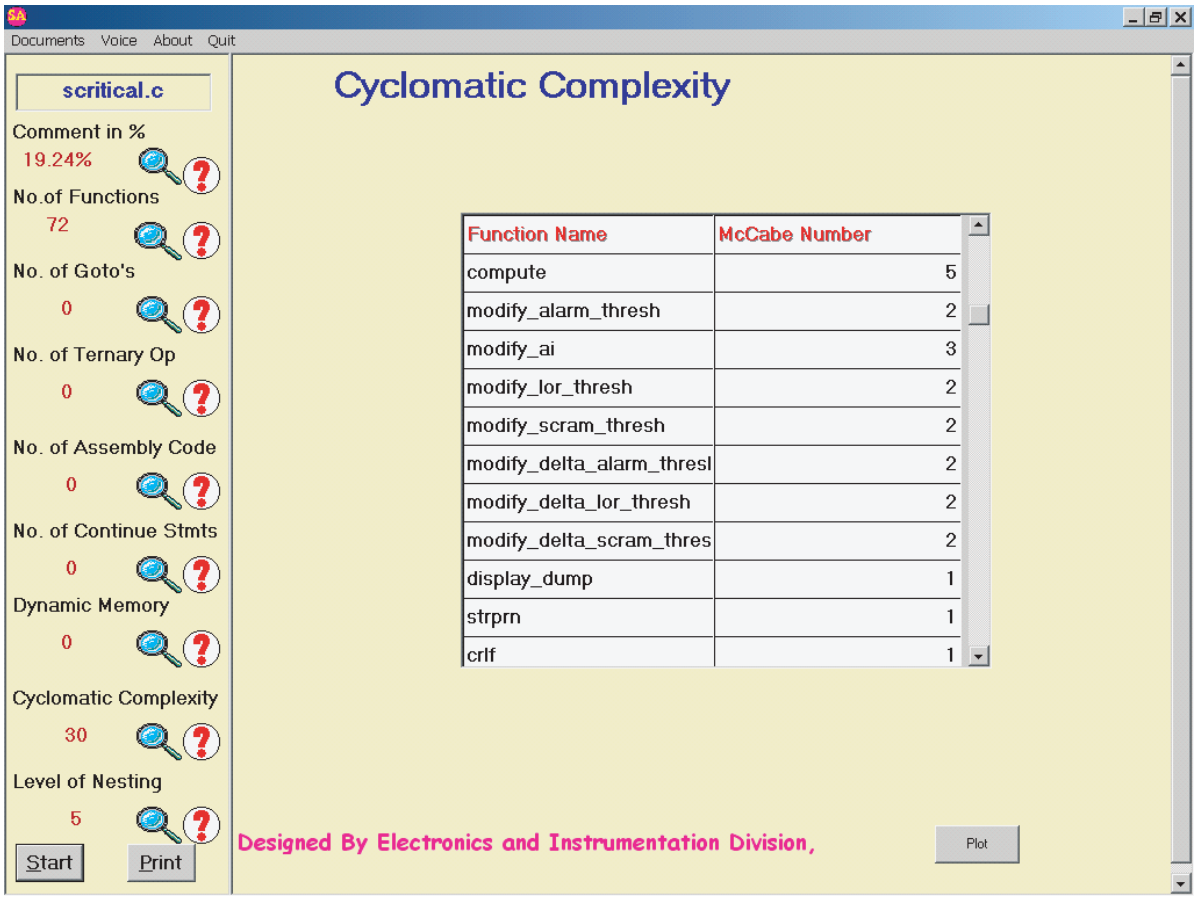

Fig. 1. Static Analyzer output on Cyclomatic Complexity of Safety Critical System

with Switch Over Logic in the case of failure of any one system. PDP 11 and UNIPOWER-30 systems were acting as dual systems, to monitor the plant signals continuously. The UNIPOWER - 30 computer system has been replaced with three in-house developed VME bus based computer systems. This system catering to the Safety Critical (SC), Safety Related (SR) and Non-nuclear Safety (NNS) functions is segregated into 3 separate distinct VME systems as per the safety criteria. The VME based computer systems are configured around a Motorola 68020 microprocessor based Central Processing Unit and input / output boards developed in-house. Hence, the old monolithic software has been functionally segregated and implemented in the three systems. It called for new software development and hence it has become mandatory for V & V of the software before commissioning the system. The V & V was carried out in all the stages of the software development which is the first of its kind in IGCAR.

The Software development was carried out using the waterfall model. Each of the following documents was prepared, verified and validated by an independent team from Electronics and Instrumentation Division (EID).

The following are the artifacts taken for the V & V:

1. System Requirement Specification
2. System Architectural Design
3. Software Requirement Specification (separately for SC, SR and NNS systems)
4. Software Design Description (separately for SC, SR and NNS systems)
5. Actual 'C' code (separately for SC, SR and NNS systems)

All the software components were written in 'C' language and targeted for the Motorola 68020 microprocessor.

The V & V reports from each of the stage was submitted to the design team. The design team incorporated the necessary changes and submitted the same for approval. The V & V team analyzed the entire 'C' code and submitted an elaborate report on the outcome.

The Static Analyzer has been extensively used for CDPS software systems. One of the outputs is shown in Fig 1. The corrections were incorporated and the software was integrated with the hardware. The systems have been already installed and functioning at the FBTR.

The V & V process of CDPS system is a prelude to the PFBR V & V. This V & V activity has given a good understanding on the process. It has also come out with useful suggestions like the need of the software design evaluation, standardization of software functional modules etc. These feedbacks are given to the respective committees and it would certainly help in producing quality, near zero-defect software and confidence for the computer based systems for PFBR.

CHAPTER 6

Basic Research

6.1 A Quadrupole Mass Spectrometric System for High Temperature Vaporization studies: Commissioning of the Apparatus and Exploratory Experiments

A high temperature mass spectrometric facility that will permit precise vaporization thermodynamic studies of air-sensitive and radioactive substances was set up in the Chemistry Group of our Centre. Fig.1 depicts this facility.

The whole vacuum envelope consisting of the Knudsen cell and ion-source chambers (specially designed for this purpose) was fabricated and installed on a glove box floor. The isolation between the two chambers is achieved through use of an indigenously designed and fabricated high- vacuum isolation valve. A quadrupole mass spectrometer system obtained from Extrel, (model C50) was aligned and tested for its ability to detect the vapor species effusing from the Knudsen cell. The Knudsen cell is heated by an electron bombardment furnace, operated in voltage control mode. A temperature of ~ 2500 K was successfully attained. An optical pyrometer is used for non-contact temperature measurements. Recognizing the possibility of vapor-condensation on the optical windows, if the orifice at the top of the Knudsen cell or a hole drilled on the side of the Knudsen cell cup were to be used as blackbody holes, a hole was drilled at the bottom of the cup and an appropriate viewing arrangement was designed, fabricated and successfully implemented. A specially designed X-Y furnace-movement piece was also fabricated for this purpose.

Exploratory investigations with elemental silver, nickel, and iron were then conducted to assess the reliability of temperature measurements and the sensitivity of the whole mass spectrometric system. Calibration experiments with pure iron, for instance, was performed on three consecutive days in the temperature range of 1505 to 1658 K. Reproducibility of the ion intensity $I(Fe^+)$ was obtained within ± 15 %. A reasonably good agreement between the mean apparent enthalpy of sublimation at 1575 K (394.9 ± 9.0 kJ/mol) with the reference value of 398.9 kJ/mol was observed.

Subsequently, vaporization of an Fe-Al alloy (40 % Al) was also studied. The ratio of the ion intensities $I(Al^+)/I(Fe^+)$ as well as the partial pressures of Al and Fe (at T ≈1550 K), deduced by using pressure calibration with pure iron, agreed well with those

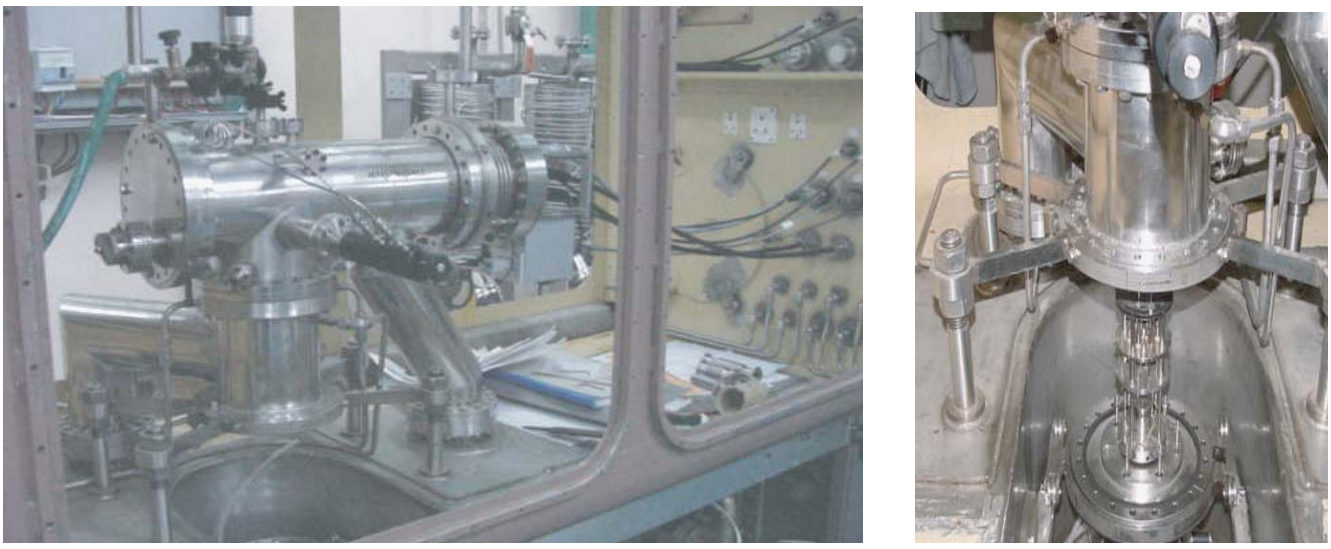

Fig. 1. A quadrupole mass spectrometric system and the electron bombardment furnace assembly for conducting vaporization thermodynamic studies of radioactive substances.

reported in the literature using magnetic sector high temperature mass spectrometers. All these experiments served to reveal (1) the absence of serious error in temperature measurements; and (2) the sensitivity of the equipment to measure vapor pressures down to ~ 10^{-3} Pa. The measured temperatures might be slightly lower than actual values (by 10 to 20 K) due to the presence of two optical elements in the path between the black body hole and the optical pyrometer. A precise determination of the temperature correction will be carried out subsequently, since at least one more optical element will be added to the set-up for the eventual closure of the glove box. Further exploratory measurements are underway.

6.2 Nanomaterials and Coatings

Recent advances in coating technology have shown that nanocrystalline coatings having grain sizes smaller than 100 nm exhibit improved mechanical, physical and chemical properties (e.g. hardness, toughness, wear and corrosion resistance) as compared to the conventional coatings. Another significant finding in this area has been the recent experimental demonstration of the improvement in hardness by several times and a corresponding increase in wear resistance for coatings in the form of nano-scale multilayers having the architecture as metal-on-ceramic or ceramic-on-ceramic, where each layer thickness is few nm to tens of nm composing a total thickness of 1-10μm, when compared to much thicker monolithic homogeneous coatings of the same material. Such nano-structured coatings have the potential for futuristic applications pertaining to the hard facing requirement of FBR components.

A multi-pronged strategy has been adopted for obtaining nano-grained monolithic coatings like CrN, TiN, TiAlN and Al_2O_3 and various nano-scale multi-layer coatings consisting of M/MN, MC/MN and MO/MN interfaces (M=Metal). The monolithic nanometric coatings are synthesized through cold spray of nanocrystalline powders obtained by soft chemical synthesis. These techniques have been successfully used to obtain monophasic CrN and TiN nanocrystalline powders. In this route, hydroxides of metallic cations are cold precipitated and calcined to yield oxides. These oxides are subjected to programmed temperature nitridation in an argon/ammonia atmosphere to give nanocrystalline nitrides. Such controlled calcinations and nitridation experiments were carried out in an in-house built Thermogravimetric Analysis - Mass Spectrometry (TGA - MS) facility. Fig.1 depicts TGA-MS profile of gas phase nitradation of Cr_2O_3. The complete conversion is achieved at 1100°C which corresponds to 16% weight loss. The HRTEM picture shows faceted nano-crystallites of CrN having a size range of 20 - 25 nm (Fig.2) The following

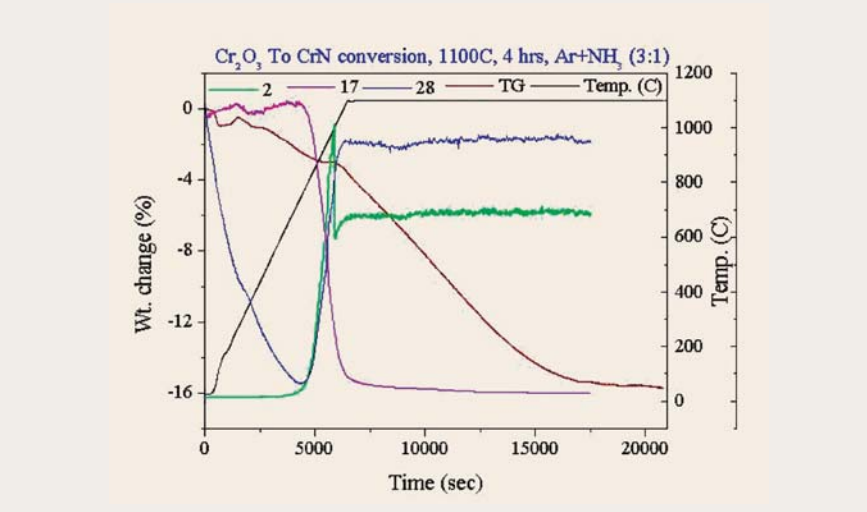

Fig. 1. Cr_2O_3 to CrN Conversion - TGA/DTA Data

mechanistic pathways have been worked out for CrN processing:

$$Cr(NO_3)_3.9H_2O \xrightarrow{Aq.NH_3} Cr(OH)_x\,yH_2O \xrightarrow{750\ ^0C} nc\ Cr_2O_3 \xrightarrow[NH_3]{1100\ ^0C} nc\ CrN$$

Apart from this, a Combustion Chemical Vapour Deposition (C-CVD) facility using principles of ultrasonic flame pyrolysis has been successfully commissioned. Nanocrystalline α-Al_2O_3 and ZrO_2 coatings are being synthesized, using this facility.

A gas-solid interaction route has been utilized to grow transition metal nitrides, carbides and carbonitride overlayers. The TG-MS facility was used to carry out isothermal nitridation and carburization experiments and to optimize the process parameters. Temperature programmed gas-phase nitridation of Cr-metal and Cr-plated steel in argon/ammonia atmosphere was carried out to grow CrN overlayers. These layers were examined by cross sectional scanning electron microscopy and also by nano-mechanical testing. Fig.3 depicts this cross sectional SEM image, the nano-mechanical test data corresponding to various regions is super imposed on it. The nitrided zone extends to a depth of 35µm for a 20-hour isothermal exposure at 900 °C. This zone is coherent and dense. The hardness and Young's modulus value of the nitrided region depicts a steep enhancement to 20 GPa and 300 GPa, respectively.

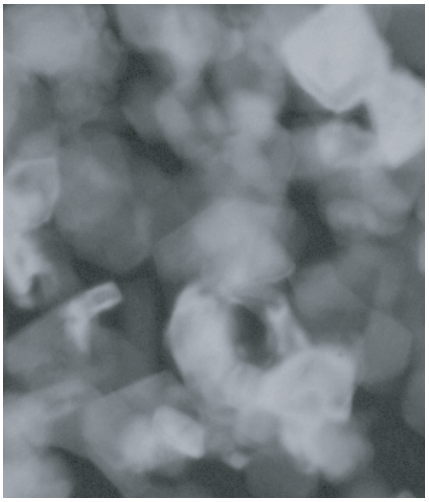

Fig. 2. TEM Image of CrN Nanoparticles

In order to enable the synthesis of nano-scale multi-layer coatings, pulsed laser deposition and magnetron sputtering facilities have been set up. TiN, AlN and Al/AlN coatings have been synthesized using these units. A versatile Scanning Probe Microscope (SPM) and a Scanning Near Field Optical Microscope (SNOM) with spectroscopy (Raman and Photoluminescence) have been set up for characterization of monolithic nano-structured coatings. The micro-chemistry at the interface is examined using a Secondary Ion Mass Spectrometer (SIMS). To evaluate the mechanical properties of these coatings, a nano-mechanical test system comprising of nano-indentation and scratch testing and a tribometer for wear measurement has been set up. Fig. 4 shows the AFM image of nano-indentation of coating on steel.

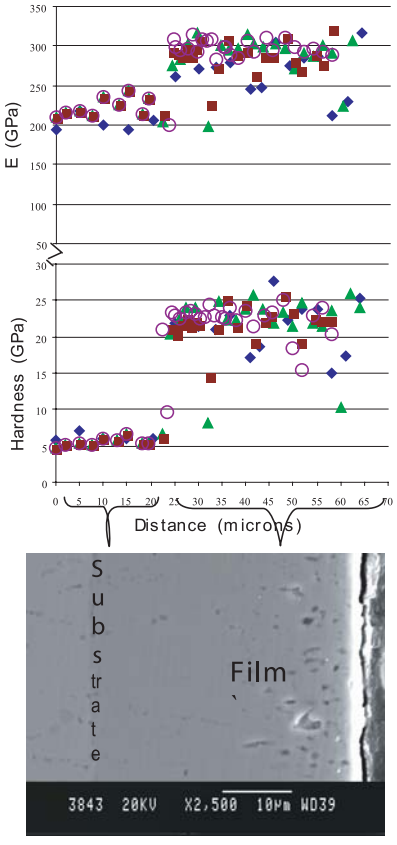

Fig. 3. Hardness and Elastic Modulus of CrN/Cr using Nano-indentation.

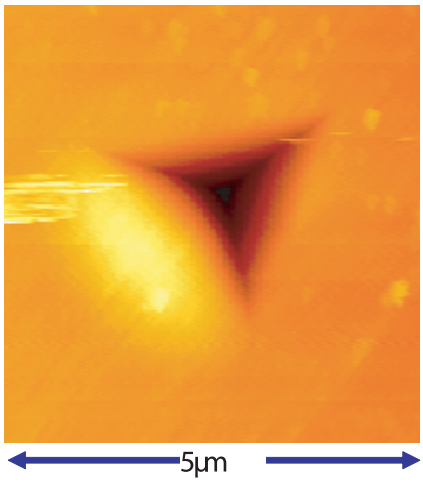

Fig. 4. AFM Image og nano-indentation of TiN coating on steel

6.3 Optical and Electronic Properties of Nanostructured Materials

Nanostructured materials are found to exhibit dramatic changes in their properties as compared to the regular polycrystalline counterparts. Almost all the properties such as mechanical, catalytic, magnetic, optical and electronic properties start exhibiting departure from the bulk values when the particle/grain size becomes smaller than a critical length-scale. These length-scales for different properties are also widely different. Extensive investigations on the electronic and optical properties of nanostructured semiconductors have been carried out to understand the nature of the phonon and carrier confinement and their consequences. The systems investigated include free-standing nanocrystalline CdS powders, silver nanoparticles dispersed in soda-glass and GaN nanostructures created by nitrogen ion implantation of GaAs.

The existence of large surface energy associated with the nanoparticles often results in the stabilization of high-symmetry metastable phases, which can transform to the stable structure upon annealing. In order to understand the kinetics of such a transformation, cubic-CdS nanocrystalline powders (average size 5 nm) were synthesized using precipitation in methanol. Structural investigations after annealing at different temperatures in argon atmosphere revealed that the zinc-blende (cubic) to wurtzite (hexagonal) transformation occurred above 300 °C. The hexagonal fraction increased monotonically and the sample was found to completely transform to the wurtzite phase at 500 °C (Fig. 1). This was also accompanied by an increase of the particle size to 38nm. Raman spectroscopic measurements exhibited peaks due to the longitudinal-optic (LO) phonon and its overtones (Fig. 2). The intensity of the 2-LO phonon, which is a measure of the electron-phonon interaction in the material, was found to increase as the particle size increased upon annealing. These results suggest that the electron-phonon interaction is weaker in the nanoparticles as compared to the bulk materials.

The GaN phases grown by ion implantation technique are significant for the formation of depth selective embedded structures and useful for optoelectronic applications. Nanocrystalline precipitates of both hexagonal wurtzite and cubic zinc-blende GaN phases were found to form in GaAs by 50 keV nitrogen ion implantation at 400°C and subsequent short duration annealing at 900°C. Crystallographic structural and Raman scattering studies reveal that the GaN phases grow for fluence values above $2x10^{17}$ cm^{-2}. Temperature-

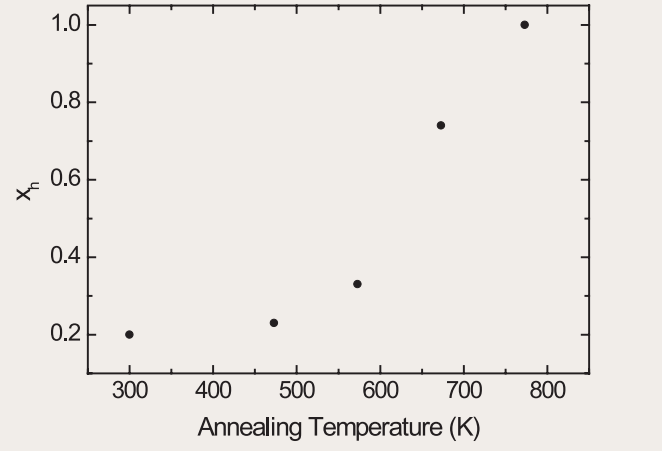

Fig. 1. Hexagonal fraction X_h of CdS nanoparticles as a function of annealing temperature.

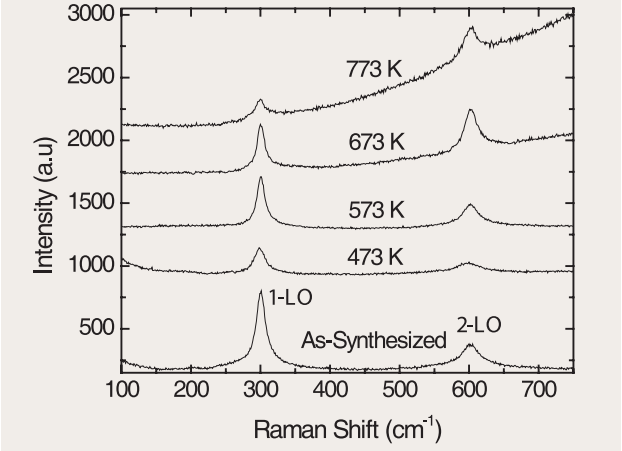

Fig. 2. Raman spectra of CdS nanoparticles after annealing at different temperatures.

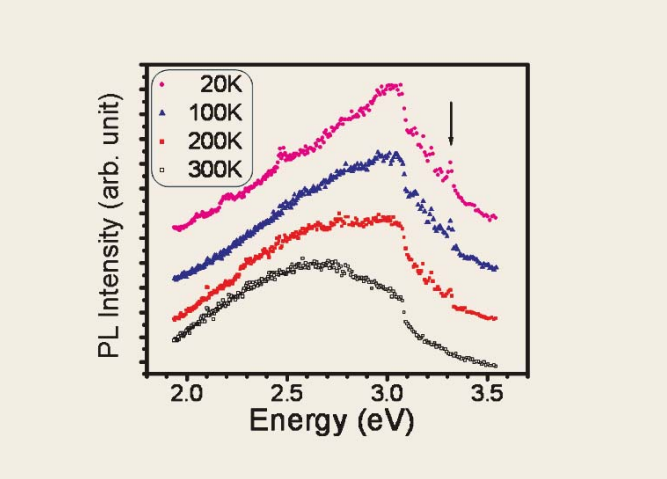

Fig. 3. Photoluminescence spectra of N^+ implanted GaAs at different temperatures

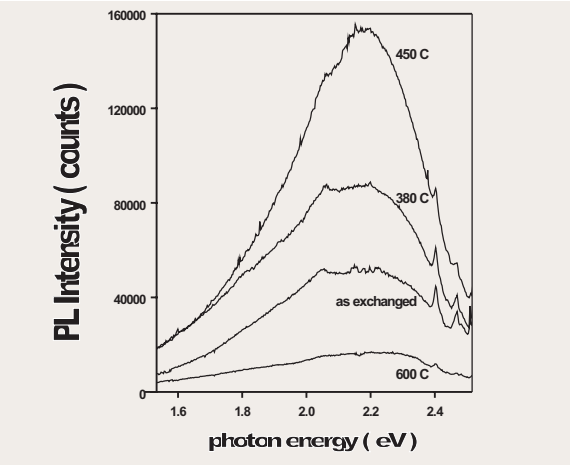

Fig. 4. Photoluminescence spectra of Ag-exchanged soda-glass after different annealing treatments. The sharp peaks above 2.4 eV correspond to the Raman spectra of glass.

dependent photoluminescence (PL) study shows a sharp direct band-to-band transition peak at 3.32 eV at temperatures lower than 200 K (Fig. 3). The value of the band gap lying between those of the hexagonal (3.4 eV) and the cubic (3.27 eV) phases of GaN, suggest the formation of mixed hexagonal and cubic phases. The broad peak at 2.6 eV, arising from nitrogen vacancy related defect, is found to become narrower and also shift to 3.0 eV at lower temperatures. This could be due to the stabilization of defects at lower temperature.

Metallic nanoparticles dispersed in silicate glasses are known to exhibit interesting optical absorption due to the surface plasmon resonance, and have immense potential as optoelectronic materials. Silver nanoparticles dispersed in soda-glass were synthesized through silver ion-exchange technique. As-synthesized samples have AgO nanoparticles, while vacuum annealing at elevated temperatures leads to their decomposition into Ag and Ag_2O. These different nanoparticles are identified by x-ray photoelectron spectroscopy, and are also found to exhibit strong photoluminescence. The dramatic changes of the photoluminescence (PL) intensity occur as a result of annealing the samples in vacuum (Fig. 4). Broad PL bands centered at 1.95 and 2.23 eV are observed in the post-annealed samples. While the emission at 1.95 eV is attributed to the presence of small silver nanoparticles, the emission at 2.23 eV is ascribed to the band-to-band radiative transition in Ag_2O. The intensity reaches the maximum after annealing at 450 ^oC and subsequently falls at higher temperatures. The initial increase of the PL intensity arises due to an increase in the volume fraction of Ag_2O nanoparticles and the subsequent decrease is attributed to the growth of large silver nanoparticles in the glass matrix. Formation of excitons (bound electron-hole pairs) in AgO nanoparticles (as-exchanged sample) has been found for the first time. Temperature-controlled growth of silver nanoparticles in the glass matrix has been further elucidated using optical absorption and Raman scattering.

6.4 A Novel Approach for Synthesis of Nanocrystalline Yttria Stabilized Zirconia Powder via Polymeric Precursor Routes

Yttria stabilized zirconia (YSZ) is a technologically important oxygen ion conducting solid electrolyte that finds applications in oxygen sensors, high-temperature fuel cells, high-temperature pH sensors, steam electrolysers and in thermochemical studies. These applications require the solid electrolyte as high-density ceramic bodies with fine-grained microstructure. Powders prepared through the conventional ceramic method are generally of large particle size (often in tens of microns); and at times are of inhomogeneous composition. Their compacts require very high sintering temperatures (~1700°C) to achieve a high density. Using powders of large size and sintering at high temperatures lead to grain growth, which in turn results in poor mechanical strength. Therefore, in recent years, many soft chemistry routes are being pursued to prepare a fine, homogeneous and sinter-active powder, which can be sintered at relatively low temperatures to yield a high-density ceramic body with desired properties.

A novel controlled-combustion technique was adopted for the synthesis of nanocrystalline YSZ powders. Normally, combustion method involves the autocombustion of the polymeric precursor powder and hence the process sometimes becomes very violent. Therefore, preparations based on this method are generally carried out in small-scale batches (typically in few gram quantities). With a view to overcome this aspect, a novel heating scheme was devised where a controlled combustion could be accomplished avoiding the violent reactions. Three different processes, namely (i) amorphous citrate process, (ii) Pechini process and (iii) polyethylene glycol (PEG) assisted process were used for synthesizing ZrO_2-5 mol% Y_2O_3 solid solutions. A systematic study of the effect of type of fuel used and its concentration on the sintering characteristics of the powders was carried out. All the three processes yielded a nanocrystalline powder of average crystallite size of 9-18 nm. Calcined powders were identified as a solid solution of yttria in zirconia essentially in the tetragonal phase. These powders yielded pellets with ≥95% of TD after compacting and sintering them at 1400°C for 2 h. A typical scanning electron micrograph of as-sintered and unpolished surface of a pellet from amorphous citrate process with citric acid to total metal ion ratio (CA/M) of 3.0 is shown in Fig.1. It is seen from the micrograph that the grains are granular with a size distributed between 200 and 700 nm range. These controlled combustion techniques can be employed for scaling up of the preparation process. Sintered densities as high as 99% of its theoretical density could be achieved with powders from (i) amorphous citrate process with CA/M ratios 2.0 and 3.0, (ii) Pechini process with EG/CA ratios 2 and 4 and (iii) PEG assisted process using PEG 400.

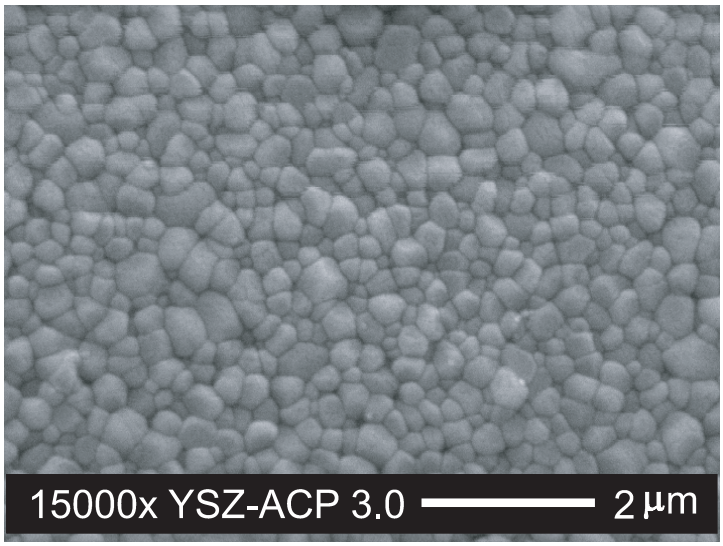

Fig. 1. Scanning electron micrograph of YSZ pellet sintered at 1400°C for 2h in air following amorphous citrate process (CA/M = 3.0).

6.5 A Novel Force Microscope for Probing Weak Forces Between Nano-particles/Drops

An effective stabilization technique that can extend the shelf life of colloidal dispersions to an infinite period is a long cherished dream of many researchers. An understanding of the nature and magnitude of forces that exist between colloidal particles is a prerequisite to tailor products with long term stability. The direct experimental techniques that are most widely used to measure weak forces are the Surface Force Apparatus (SFA) and Atomic Force Microscopy (AFM). The SFA is capable of measuring the forces between two molecularly smooth mica surfaces in vapors or liquids with a sensitivity of a few nanonewtons and a distance resolution of about 0.1nm. In AFM, the force between the tip and sample, usually less than 10^{-9} N, is measured by tracking the deflection of the cantilever within a resolution of 0.1A°. Unlike electron microscopes, AFM can image samples in air and under liquids. Though these two techniques have been widely used, the major limitation of these techniques is that they do not allow "in-situ" measurements of very weak forces between colloidal particles.

The difficulties associated with the in-situ measurement of forces between very fine objects of nanometer size have been overcome after the development of a novel force apparatus at IGCAR. The force apparatus facilitates "in-situ" measurement of weak forces (10^{-13} N to 10^{-11} N) that exist between individual colloidal droplets of the size of hundreds of nanometers. The sensitivity for the inter-space distance measurement of this apparatus is 0.1 nm. The photograph of the force apparatus is shown in Fig. 1. The force apparatus comprises of a solenoid type electromagnet and a variable current source, to subject the magnetic emulsions to variable magnetic field. By varying the magnetic field strength, the distance between the colloidal particles can be controlled. A white light source illuminates the colloidal particles. Optical fibers direct and steer the incoming and outgoing light beam and a polarizing beam splitter turns the reflected light 90^0 with respect to the incoming beam. A monochromator with holographic grating diffracts the light beam. A photodiode array with an interface card and a computer, is used for the detection of the Bragg peak position, width and intensity.

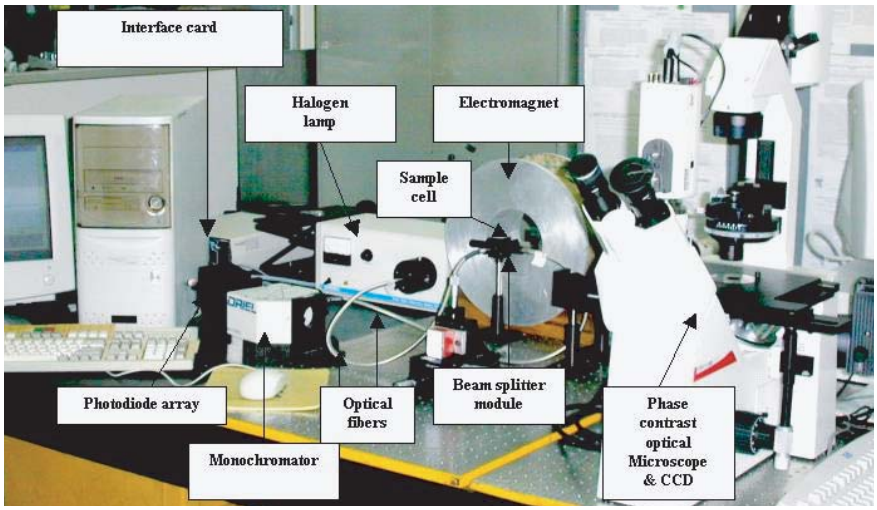

Fig. 1. The force microscope developed at IGCAR

Using this force microscope, a typical force-distance curve obtained for ferrofluid emulsion containing 200 nm size droplets in the presence of surfactant molecules (sodium dodecyl sulphate) of different concentrations, is shown in Fig. 2. The observed repulsive force profile is found to be exponentially decaying. The repulsion comes from the charges at the interface of the droplets due to the adsorption of charged surfactant molecules. The force profiles have been found to follow one of the electrostatic repulsive force equations. The intensity of the electrostatic forces is governed by the surface potential while the Debye length dictates the range of repulsion. The solid lines in the figure show the best fit obtained. The measured surface potential values are in good agreement with those values obtained independently

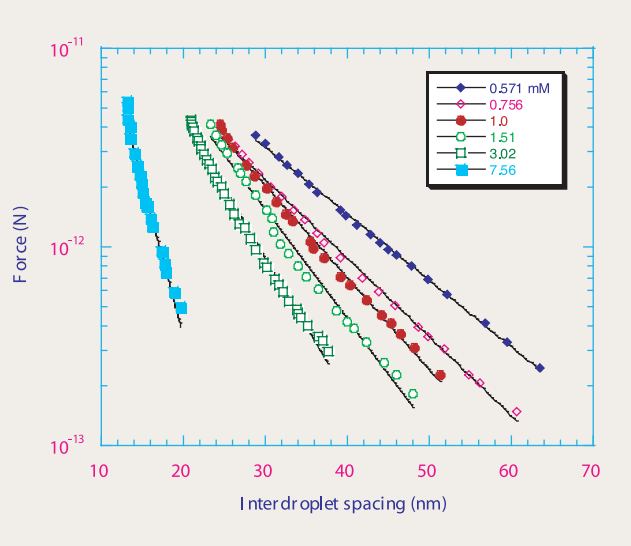

Fig. 2. Force-distance profile for 200 nm sized droplets in the presence of surfactants of different concentrations.

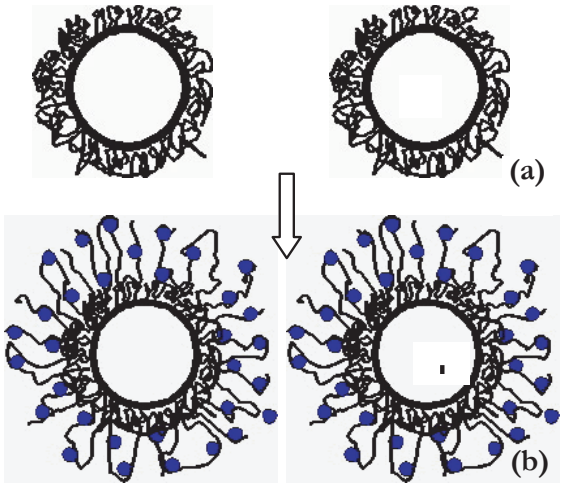

Fig. 3. Schematic representation of the conformation of adsorbed polymer on colloidal particles under (a) non-association (b) association with ionic surfactants.

from the electrophoresis mobility.

The force apparatus is being used to probe the forces between colloids in the presence of macromolecules and surfactant molecules to obtain insights into the colloidal stability. Using the force measurement technique, stretching and collapse of polymers adsorbed at the droplet interface under the influence of polymer-surfactant interaction has been demonstrated for the first time. When surfactant molecules interact with the colloidal particles pre-adsorbed with polymers, the conformation of adsorbed polymers change drastically. The charges on the polymer chain, due to bound ionic surfactant molecules, repel each other leading to the polymer chain stretching (Fig. 3), enhancing the inter-particle spacing considerably. Under such association between polymers and charged surfactants, the distance between the colloidal particles increases by hundreds of nanometers and the magnitude of force by two to three orders. Experiments also reveal that the stretched polymer brushes can be easily compressed by increasing the salt concentration. Using the molecular level understanding of the forces existing between nanometer sized emulsions, a novel methodology to enhance the long term stability of these colloidal suspensions (ferrofluid emulsion based sensors, magnetic leak free sealant for FBR applications etc.) has been developed.

6.6 A 25 kW Thermal Plasma Torch for the Generation of Submicrometer Particles

For the post-accident management of fast reactors, the knowledge on the aerosol behavior of sodium, fuel and fission products inside the containment building and the subsequent transport of aerosols into the atmosphere and their fallouts is important. In order to study the aerosol characteristics of sodium, fuel and fission products and their mixtures, an Aerosol Test facility (ATF) has been designed, fabricated, installed and tested. A 25 kW thermal plasma torch is employed for the generation of fuel equivalent fission product aerosols in the ATF. The plasma

Fig. 1. The plasma torch integrated with the aerosol chamber through plenum chamber

torch can generate aerosols from powder feeder and wire feeder. Fig.1 shows the photograph of the plasma torch system in the ATF. The aerosol formation in reactor accidents is essentially considered to be a vaporization-condensation process. To study such aerosol formation and behavior, the plasma torch method appears to be a promising technique. The plasma flame core temperature (>12000°C) is utilized to melt and evaporate the material introduced into the flame. The advantages include (i) the plasma torch based aerosol generator gives an intense and continuous aerosol source, (ii) the aerosol can be generated from metallic, ceramic and composite materials, and (iii) the aerosol generation rate and the average size can be controlled by varying the plasma torch parameters. Since the arc plasma inherently is a high turbulent discharge, it extinguishes on the slightest disturbance from equilibrium. It is therefore necessary that the arc be stabilized for the creation of a good and reliable plasma beam. The stabilization process creates and maintains boundary conditions enabling the arc in a steady state or to move in a well-defined pattern. The stabilization is achieved by (i) suitable gas flow and (ii) magnetic stabilization.

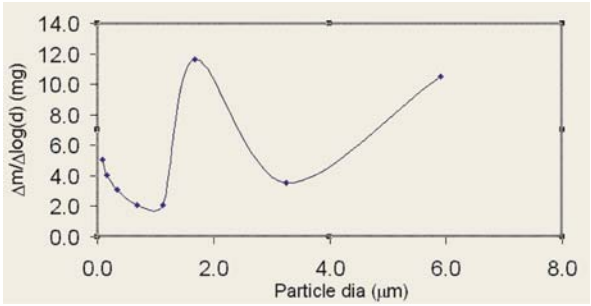

Fig. 2. Aerosol mass size distribution of Fe_2O_3 aerosols generated by the plasma torch. (fractional mass collected between size ranges (log d = log d1 - log d2)) as a function of particle diameter.)

Apart from the generation of aerosols relevant for the fast reactor safety studies, the plasma torch can generate sub-micrometer particles of various materials in large quantities. The sub-micrometer particles have varieties of industrial applications such as catalyst for water treatment plants. In one experiment, laboratory grade Fe_2O_3 powder (M/s Ranbaxy) of 40 μm size was used as primary particles and aerosols were generated using the plasma torch. The aerosol mass-size distribution was measured using a Low Pressure Impactor (LPI) and it is shown in Fig. 2. The sub-micrometer particles were collected from different stages of the LPI. The collected particles were analysed by SEM (Fig.3). The ultra-fine particles of Fe_2O_3 were used as a catalyst for UV assisted photo-discoloration of dyes.

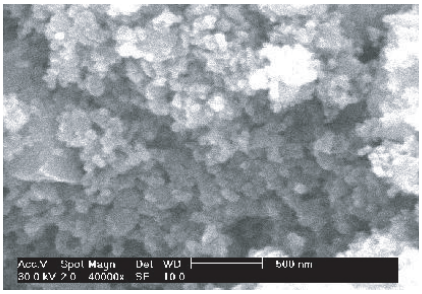

Fig. 3. SEM picture of the plasma-synthesized Fe_2O_3 sub-micrometer particles..

6.7 Calibration and Commissioning of an Indigenously Built Dilatometer for Thermal Expansion Studies on Technological Materials

A push-rod dilatometer with an LVDT transducer was set up in the Chemistry Group for the study of the high temperature thermal expansion behaviour of solid materials. The sample support and push rod are made of fused silica, and the temperature range of measurement is 300 - 1000 K. A PC based instrumentation system has been designed and developed for running the experiments in a programmed way. The generation of the thermal profile for the furnace as well as the temperature control are realized in the software and partly in the programmable hardware. This substantially reduces the hardware and brings in operational flexibility. An integrating type ADC is configured to measure the temperature and LVDT signals. The system logs the thermal expansion data in a file and also presents the same in an on-line graph.

This equipment was subjected to a rigorous regimen of testing and upgradation to ensure ease of experimentation and reliability of measurement results. The instrument has since been employed for the thermal expansion studies on several materials.

The accuracy of temperature measurement was checked by studying the temperature induced phase transformations of WO_3 with this equipment. WO_3 undergoes four known crystallographic transitions between the room temperature and 1173 K, and all these could be observed in the expected temperature ranges. The instrument was calibrated by measuring the thermal expansion of standard materials such as thoria and stainless steel in the form of 10 mm long cylinders of diameter 5 - 10 mm. The blank correction in thermal expansion was made by measuring the dimensional changes of a sample of pure fused silica. The equipment is now in regular operation. Fig. 1 shows the comparison of the measured thermal expansion of standard thoria with the recommended values at the respective temperatures, taken from the literature. Fig. 2 dispalys the experimental results on a series of D9 alloys of various Ti / C ratios, at several different temperatures in air. Fig.3 shows a photograph of the system.

Fig. 3. The indigenously built dilatometer system.

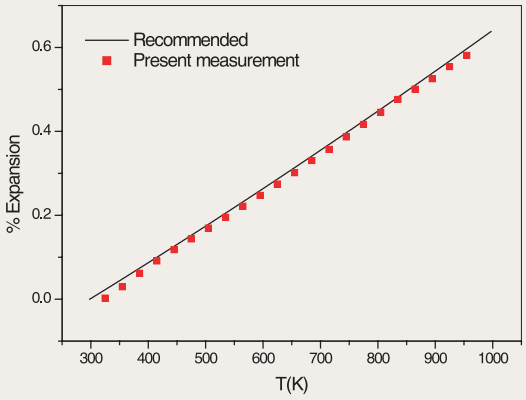

Fig. 1. Linear thermal expansion of thoria measured using the dilatometer and compared with reported values.

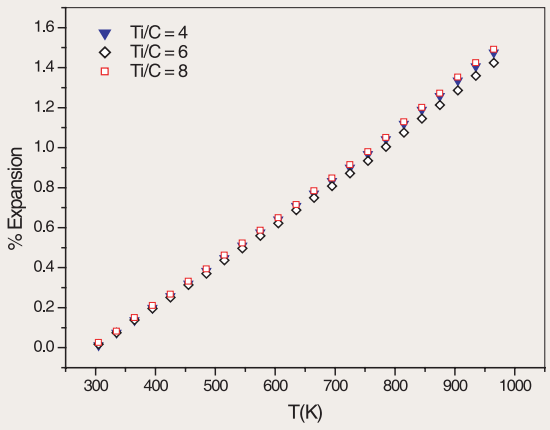

Fig. 2. Linear thermal expansion of D9 alloy with different Ti/C ratios.

6.8 Ligand Sensitized Fluorescence of Lanthanides

Development of methods to detect trace levels of lanthanides is of interest as the lanthanides serve as good models for the eventual applications of these methods to actinides. Fluorimetric methods to detect lanthanides, such as Tb^{3+}, Dy^{3+}, Eu^{3+} and Sm^{3+}, at trace levels, were therefore developed using the method of ligand sensitized fluorescence.

In the method of ligand sensitized fluorescence, the metal ion is first complexed to a ligand; the metal-ligand complex is then optically excited. The excitation energy is absorbed by the ligand, which energy is then transferred to the lanthanides. If the energy transfer from the ligand to the metal is efficient, this method turns out to be more efficient in obtaining fluorescence from the metal than a direct excitation of the metal.

Aromatic carboxylic acids were found to serve as excellent ligands for sensitizing lanthanide fluorescence, and enhancement of up to three orders of magnitude was obtained with some of these ligands. Benzene carboxylic acids enhanced the fluorescence of Tb^{3+}, Dy^{3+} and Eu^{3+}, while naphthalene carboxylic acids enhanced the fluorescence of Eu^{3+} and Sm^{3+}. As a typical case, the excitation spectrum of Tb^{3+}-benzoic acid complex is shown in Fig. 1b by monitoring the Tb^{3+} fluorescence at 544 nm. This is completely different from the spectrum shown in Fig. 1a for uncomplexed Tb^{3+}. Figs. 2a and 2b show the emission spectra of Tb^{3+} and Tb^{3+}-benzoic acid complex, respectively, both of which look identical. However, the excitation wavelengths used to record the emission spectra were different; it was 350 nm for Tb^{3+} and 273 nm for Tb^{3+}-benzoic acid complex. This observation clearly illustrates the role of benzoic acid in the sensitization process. Although the emission intensities shown in Fig. 2a and 2b are comparable, the concentrations of Tb^{3+} used to record these spectra were different. For uncomplexed Tb^{3+}, it was $3x10^{-4}$ M and for Tb^{3+}-benzoate complex it was $3x10^{-7}$M; a thosand-fold enhancement in fluorescence is thus obvious.

The fluorescence of lanthanides in the lanthanide-aromatic acid complex was further enhanced by about a factor of ten (and sometimes more), by complexation with trioctylphosphine oxide (TOPO), in the prescence of micelles. TOPO, a strongly coordinating ligand, displaces the water molecules coordinated to the emitting lanthanide ion in the aromatic acid complex and also provides an insulating layer around the lanthanide complex through its long alkyl chain. This second layer of complexation results in an enhancement of the lanthanide fluorescence (Fig. 2c) by reducing the probability of radiationless energy transfer from the lanthanides to the solvent. This fact was established by measuring both the steady state fluorescence, using a Shimadzu RF 5000 spectrofluorimeter, as well as lifetimes of the lanthanides, using a home-made time-resolved fluorimeter. The pattern of synergism displayed by TOPO was also found to vary with structure of the aromatic acid ligand. The eventual enhancement of a factor of 10,000 (and more) allow for trace determination of lanthanides (10^{-8} M - 10^{-9} M).

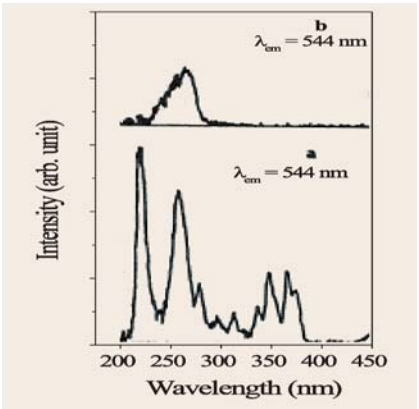

Fig. 1 Excitation spectra of (a) Tb^{3+} ($3x10^{-4}$ M) (b) Tb^{3+}($3x10^{-7}$ M)-Benzoic acid.

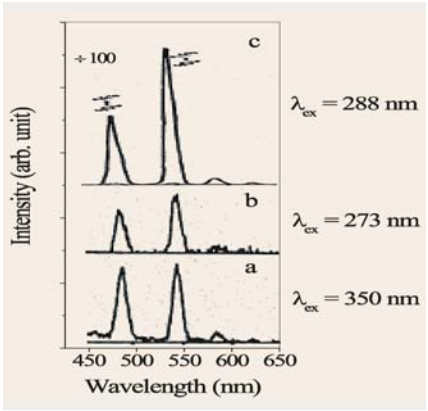

Fig. 2. Emission spectra of (a) Tb^{3+} ($3x10^{-4}$ M); (b) Tb^{3+}($3x10^{-7}$ M)-Benzoic acid; (c) Tb^{3+}($1x10^{-6}$ M)-Benzoic acid-TOPO-TritonX-100.

6.9 Matrix Isolation Infrared and *ab initio* Studies of Molecular Conformations

Studies of molecular structure and conformations form an important area of study, as they lead to a fundamental understanding of many chemical processes. It is now largely recognized that a number of functions and properties of chemical systems, ranging from chemical engineering processes to biological phenomena, are strongly influenced by molecular structure. The molecular structure itself may be modified by changes in the local environment, which results in alterations in the chemical process. In nuclear fuel reprocessing, the phenomenon such as third phase formation, which, at present, is poorly understood at the fundamental level, is probably determined by the structure of the extractant and its interactions with the diluent. A programme was therefore launched to study the conformations of organic phosphates with a view to understanding the chemical processes occurring in fuel reprocessing.

Matrix isolation infrared spectroscopy has been used for the study of the conformers of trimethylphosphate (TMP), triethylphosphate (TEP) and the phosphate of relevance to the nuclear industry, tri-n-butylphosphate (TBP). In this technique, the molecule of interest is trapped in cryogenic, inert gas solid matrices, such as those of solid Ar or solid N_2 at 12 K. At these temperatures, and in the confines of an inert environment such as those prevailing in, for example, a solid Ar matrix, many of the line-broadening mechanisms are minimized and hence the spectral peak widths in the infrared spectra of matrix isolated species, are significantly reduced. Typical line widths in matrix isolation experiments are about ~1 to 2 cm^{-1} which is significantly smaller than the ~30 cm^{-1}widths observed in neat liquid or in pressed KBr pellets. The small linewidths enable the resolution of the spectral features of the different conformers. Fig. 1 shows the infrared features of TMP in the region of the P=O stretch. *Ab intio* computations performed using the Gaussian

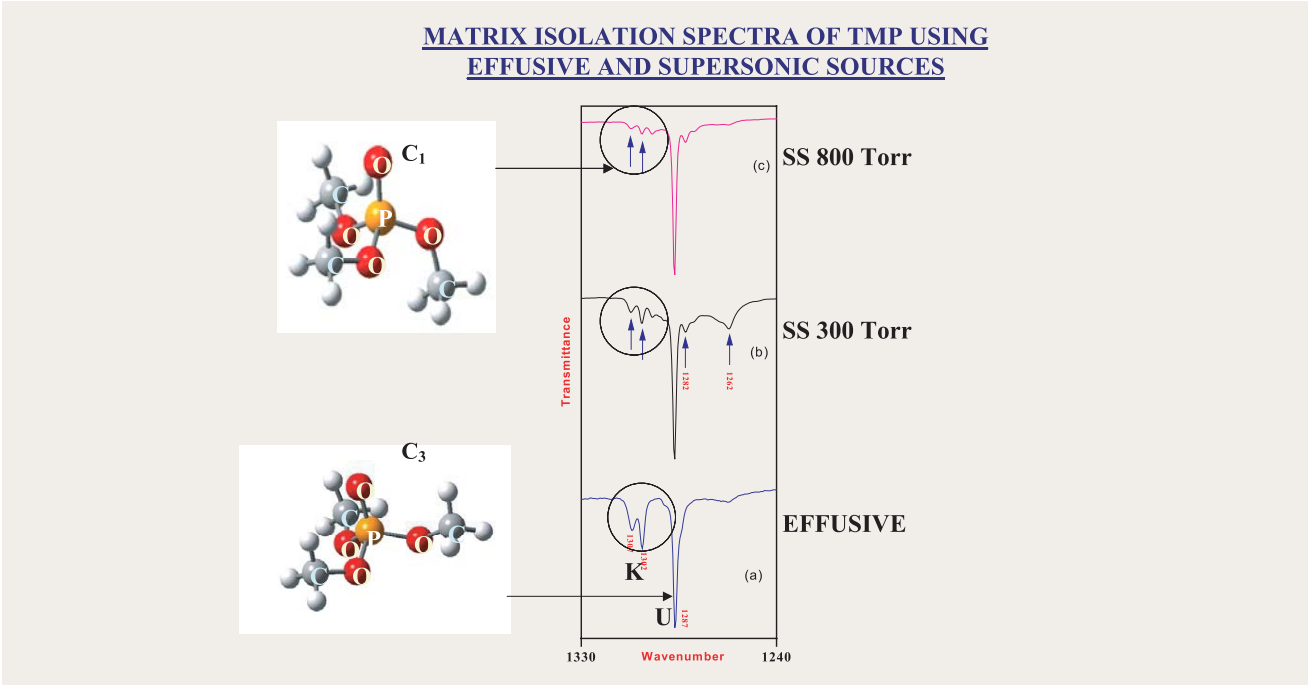

*Fig. 1. Matrix isolation infared spectra of TMP using effusive and supersonic sources. The features due to the two conformers, C_3 and C_1, are marked. The structures of the two conformers shown were computed at the MP2/6-31G** level.*

suite of programs indicate that the molecule has two stable conformers with a C3 and C1 symmetry, referred to in Fig. 1 as U and K, respectively. The 'U' conformer was determined to be the ground state conformer, while the 'K' form was a higher energy structure. It can be seen in Fig. 1, that the population of the higher energy 'K' form depleted in the cold, supersonic source, as it should, thus confirming our analysis. This study was the first to demonstrate the use of a supersonic jet as a source for depositing the matrix, to obtain unambiguously the energy ordering of the conformers. The computed frequencies for these conformers agreed well with the experimentally observed features resulting in a detailed understanding of the conformers of organic phosphates.

The studies, however, could not be extended straightforward to the study of TEP and TBP. These molecules have longer alkyl chains than TMP, which results in a significantly complex conformational picture. A need was therefore felt, not just to determine the various conformations of the phosphates, but to understand the factors that determine the conformational stabilities in these molecules. Towards this end, model compounds, such as acetals and ketals, were studied, which, being smaller molecules, were amenable to detailed computational and experimental exercises. Acetals and ketals were chosen, as these molecules had a backbone structure (C-O-C-O-C) similar to the phosphates (C-O-P-O-C). These studies pointed to the operation of the anomeric effect, (an effect that is well documented in the study of the structures of sugars), as the dominating factor in deciding the conformational stabilities in these molecules. As a result of these studies, the structure of the higher phosphates could be predicted and verified by matrix isolation experiments and *ab inito* computations.

Presently, studies are underway to understand the role of the π electrons of the P=O group in deciding the conformational stabilities. These studies are important in solvent extraction phenomena. Metal complexation in solvent extraction will deplete the p electron density and hence possibly alter conformational stabilities as a function of metal extraction. This phenomenon, we believe, may strongly influence the solvent extraction process.

6.10 Studies on MoO_3 based Compositions as Ammonia Sensor Material

Sensors for monitoring ammonia in the ambient in and around heavy water plants are required owing to the toxicity of ammonia (threshold limit value, TLV, for ammonia = 25 ppm). Earlier investigations carried out on porous pellet structures of MoO_3 have shown that MoO_3 can be a promising ammonia sensor material. The electrical conductivity of MoO_3 increases significantly in the presence of trace levels of NH_3 (in ppm) in the ambient air at 623 K. On exposure to trace

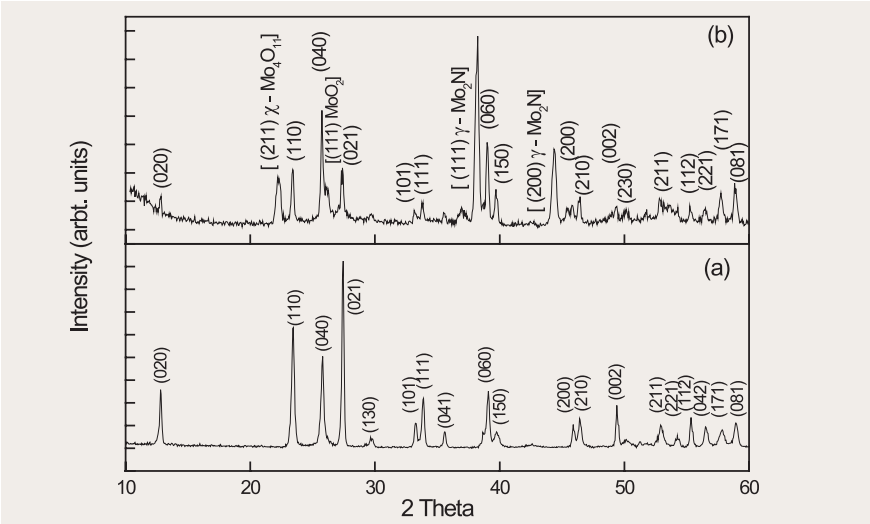

Fig. 1. XRD patterns of a) MoO_3 and b) MoO_3 pellet after exposure to air containing ammonia at 673 K

levels of NH_3 at 623 K, formation of MoO_2, Mo_4O_{11} and Mo_2N intermediates were observed in XRD and XPS studies; some of these phases are metallic, and are believed to be responsible for the appreciable increase in the electrical conductivity. Fig. 1 shows the XRD patterns of MoO_3 before and after exposure to ammonia. These intermediates quickly transform back to MoO_3 on re-exposure to air. The detection limit with MoO_3 in bulk structured form was about 500 ppm of NH_3 and has to be improved for detecting NH_3 level around the TLV. Two possible routes were adopted, viz., the use of thin film configuration of MoO_3 and the use of appropriate additives or dopants which promote the selective catalytic interaction of MoO_3 with NH_3. First, thin films of MoO_3 deposited by the pulsed laser deposition technique on alumina substrate with platinum interdigitated electrodes (Pt-IDE) were tested. Fig. 2 shows that thin film sensors are capable of sensing 100 ppm of NH_3 in air at 508 K. Secondly, among the different additives tried, namely TiO_2, V_2O_5 and Ag_2O, Ag_2O showed good promise, as this material forms silver decamolybdate ($Ag_6Mo_{10}O_{33}$), which exhibits silver ion conductivity. Electrical conductivity of this compound was measured at different temperatures and ambients and the existence of predominant silver ion conduction was found. The transport number for silver ion conduction was established at different temperatures. Fig. 3(a) to (c) show SEM micrographs of $Ag_6Mo_{10}O_{33}$ before and after exposure to NH_3. After exposure, the needle type morphology changes and bright globules start appearing. The composition analysis by EDX performed on one such globule reveals that it is primarily made up of silver [Fig. 3(d)]. In contrast to what was observed for pure MoO_3, the ammonia sensing processes of this compound was shown to involve the formation of metallic silver in addition to MoO_2, Mo_4O_{11} and Mo_2N, as confirmed by XRD studies. Preparation and characterization of thin films of $Ag_6Mo_{10}O_{33}$ are underway.

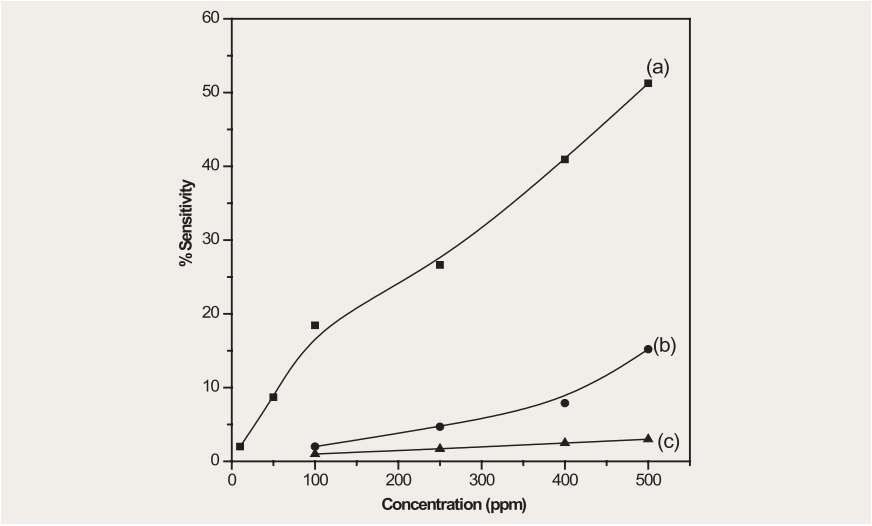

Fig. 2. Sensitivity as function of concentration of a) ammonia, b) LPG and c) hydrogen at 508 K [MoO_3 film deposited over polycrystalline alumina and annealed in air at 773 K].

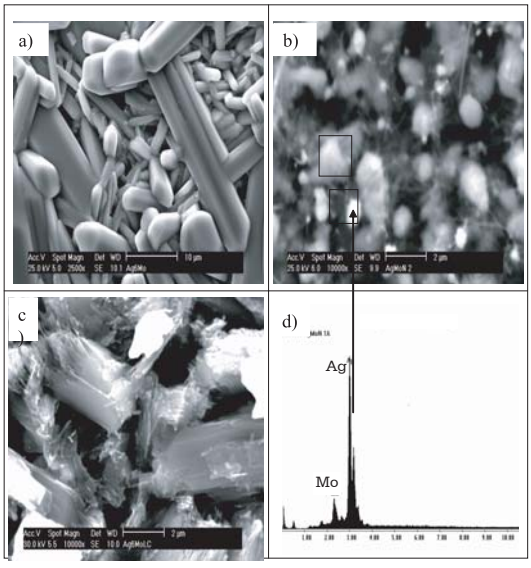

Fig. 3. Scanning electron micrographs of $Ag_6Mo_{10}O_{33}$ a) before exposing to ammonia; b) after exposing to 6.66% of ammonia at 673 K; c) after exposing to 1500 ppm of ammonia at 673 K; d) Energy dispersive x-ray analysis of the marked globule in the reduced sample.

6.11 Unusual Insulating State upon Ni Substitution in Na_xCoO_2

The sodium cobaltate system, Na_xCoO_2, is of current interest due to its high Seebeck coefficient(S) and the 4.5 K T_c in the hydrated compound having x=0.33. After the HTS cuprates and the CMR manganites, transition metal oxides involving Co-O planes have caught the attention of research workers. While for x<0.5, Na_xCoO_2 has resistivity behaviour typical of strongly correlated electron systems, higher values of x render the system with a strange Curie-Weiss kind of metallicity. Unlike the cuprates and manganites, not much substitution studies are reported in literature in the case of cobaltates. In the following, we briefly describe our results on Ni substituted series $Na_{0.75}Co_{1-y}Ni_yO_2$. Our findings had some unexpected surprises. A mere 1 at % Ni addition induced a Metal Insulator Transition (MIT) in the sample. Fig. 1 shows the resistivity vs. temperature behavior of Ni substituted sample along with the behavior in pristine $Na_{0.75}CoO_2$ sample. The temperature at which MIT occurred increased with Ni content. In the inset of Fig.1 the variation of T_{MIT} with Ni content, y, is displayed. Whereas in the insulating side, ρ(T) exhibited a correlated variable range hopping behaviour, in the metallic regime for $T>T_{MIT}$, a T^2 dependence pointed to the dominant role of *e-e* scattering in determining the resistivity changes as a function of temperature.

The lattice parameters a and c showed a non monotonic variation with y. The Fano asymmetry parameter (extracted from Infra Red (IR) measurements), a measure of the interaction strength between a phonon mode and the continuum, showed, for the in plane Co-O mode, a systematic variation with both y and T and closely tracked the ρ(y,T) evolution. The results were interpreted on the basis of thermodynamic models proposed to understand the MIT in strongly correlated electron systems. It is argued that the offsite repulsion energy (electrostatic repulsion between charges 4^+ on adjacent Co sites) combined with the large onsite repulsion energy (U, penalty for putting a charge at a site already occupied, double occupancy) facilitates the motion of charge carriers freely without costing the punitive U. This is possible and happens in pristine samples because the holes in Co^{4+} can easily hop into the degenerate empty level available on the neighbouring Co^{3+} ions and so on leading to conduction and metallicity. Such a possibility is not allowed when Ni replaces Co in the 4^+ state due to its changed electronic structure. The hole at the Ni site is rendered immobile because it occupies a higher energy level. Hence the onsite and offsite occupancies have to

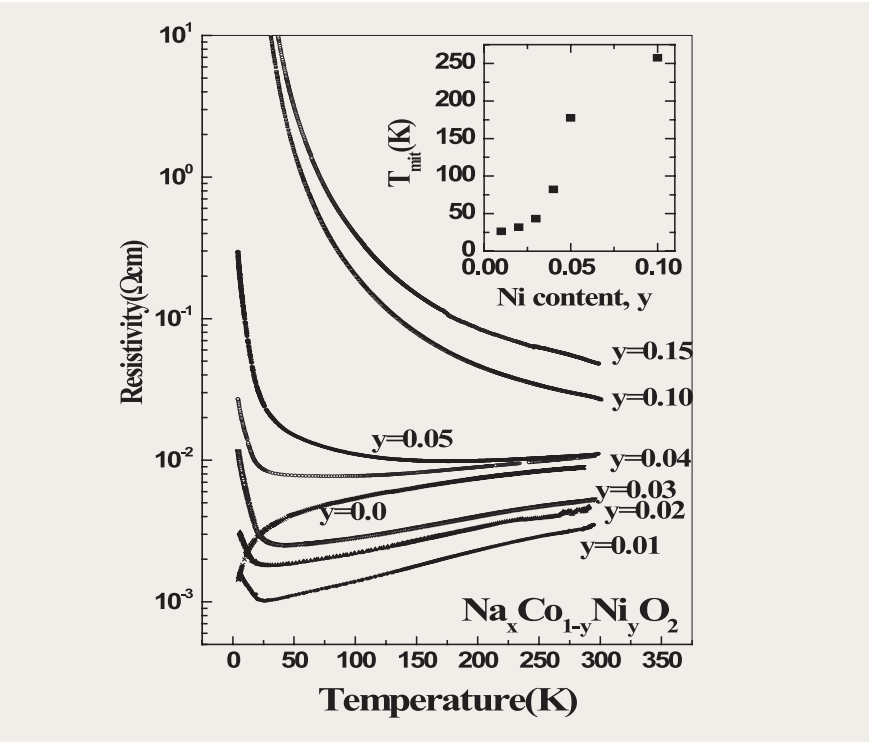

Fig. 1. Variation of R(T) with temperature for all Ni substitutions, y, indicated on the curves. Inset shows the T_{MIT} identified as the temperature at which dR/dT changes sign, as a function of Ni fraction y.

be accommodated in the system leading naturally to an insulating state at the lowest of temperatures.

Further analysis of the IR results in the case of 5 % Ni doped samples showed discontinuous changes in the intensities, mode frequencies and linewidths in the out of plane Na-O modes, at the MIT temperature (See Fig. 2). Na occupies two sites in the lattice. Area 277 represents the area under the 277 wavenumber peak and similarly for the area 297. A sudden change in the occupancy of these sites at T_{MIT} is interpreted as the signature of ordering of the Na atoms which in turn implies a charge order developing in the underlying 2D Co^{3+}/Co^{4+} ions. Such a charge ordered state has been conjectured as the insulating ground state in the Ni doped samples. Splitting of the Co-O modes and distinctive changes in the intensities of these have been observed in both pristine and 5 % Ni doped samples as a function of temperature. If following literature reports we ascribe this to Co^{4+} ordering then the intriguing possibility of pristine Na_xCoO_2 being a charge ordered metal has to be reconciled with.

Thermopower measurements have also been carried out in these samples. The Seebeck coefficient, S, increases with Ni content. Combined with the fact that the resistivity decreases with Ni addition upto 3 at%, the figure of merit has been shown to increase by a factor of three in this potential thermoelectric material. With decrease in temperature, there is a decrease in the value of the Seebeck coefficient. At ~20 K, S goes through a maximum before continuously falling to zero. The temperature at which this maximum occurs is not correlated with T_{MIT} and does not change with Ni content but rather coincides with the spin density wave transition temperature that occurs in the pristine sample. As can be seen from Fig.3, when plotted in the normalized form, S(T)/S(300 K) has a universal temperature dependence and does not depend on the Ni content in the samples. This is rather surprising considering the drastic changes in the resistivity behaviour that Ni substitution brings about in the system. It is now well established that the large thermopower in the sodium cobaltates arises from the spin entropy transport. The above results then imply that the charge and spin dynamics are unconnected in this system. This behaviour is totally different from other transition metal oxide systems undergoing MIT. In the high temperature limit, the value of S increases with Ni content in agreement with the experimental results.

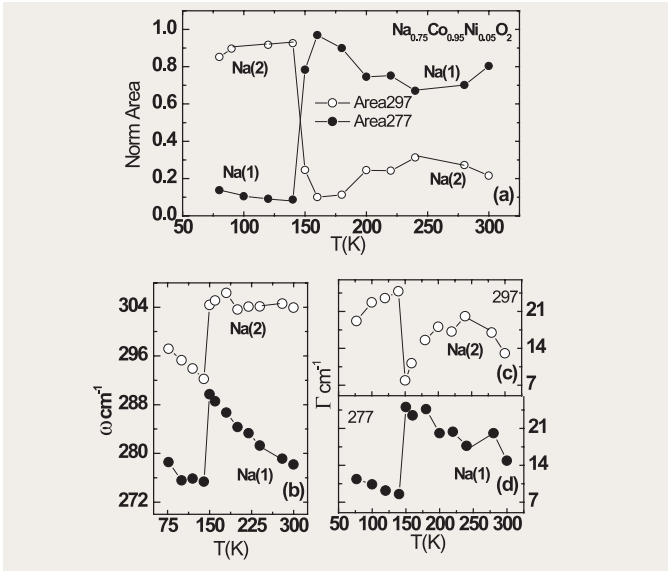

Fig. 2. (a) Dramatic flipping of the out of plane sodium mode intensities correlating with T_{MIT}. Sharp changes in line shape parameters: (b) phonon frequency corresponding to Na(1) and Na(2) sites, (c) & (d) phonon linewidths, that are seen to correlate with T_{MIT} ~150K

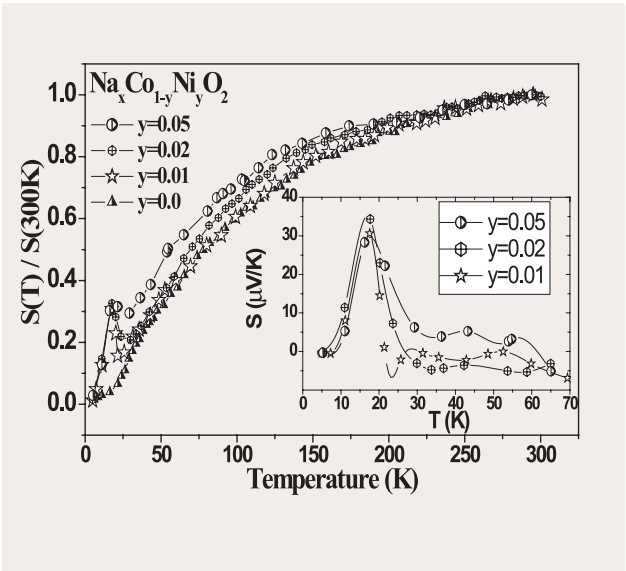

Fig. 3. Temperature dependence of S normalized to the room temperature value. Inset: S at low temperatures after subtraction of a linear background showing the peak in the substituted samples at T ~ 20K.

6.12 High Pressure Phase Stability of Actinide Materials: a High Pressure XRD study on Thorium Digallide

Study of structural stability and phase transition behaviour of materials under high pressure is an important aspect of materials research. Application of pressure leads to lattice compression and changes in the electronic structure. This leads to drastic changes in their physical and chemical properties, including phase transformations.

$ThGa_2$ stabilizes in the tetragonal structure at NTP. It was prepared and characterized in the laboratory and its lattice parameters were found to be a = 4.246±0.001 Å and c = 14.752±0.005Å. The high precision x-ray data obtained by us on this system has been accepted by the *International Center for Diffraction Data* as a standard Powder Diffraction File. Our earlier high-pressure X-ray diffraction (HPXRD) experiments on $ThAl_2$ showed interesting structural transitions from hexagonal to orthorhombic to tetragonal structures with increasing pressure. $ThGa_2$ being homologus to $ThAl_2$, is also expected to show some interesting structural transitions.

HPXRD studies on $ThGa_2$ were carried out up to ~ 62 GPa with a Mao-Bell type diamond anvil cell (DAC) using a custom-built high precision Guinier diffractometer. The DAC is a miniature high pressure device capable of generating multi-megabar (1megabar = 100 GPa) static pressures. The DAC is essentially a piston and cylinder arrangement in which two gem quality diamonds are mounted on the cylinder and piston so as to have an opposed anvil configuration. The contact area of the diamond anvils is ~ 500 μm in diameter. In between these two diamond anvils, a hard metal gasket of thickness ~ 30 - 40 μm and with a central hole of diameter ~ 100 - 200 μm is mounted. The sample in the form of powder or a small speck along with the pressure transmitting fluid and the pressure marker are placed in this tiny gasket hole. A schematic of the sample assembly for HPXRD is shown in Fig. 1. The photograph of the high pressure Guinier diffractometer system is shown in Fig. 2. The overall resolution is found to be $\delta d/d$ = 0.01-0.02. A finely powdered sample mixed with the pressure calibrant Ag was loaded into the stainless-steel gasket hole along with a mixture of methanol, ethanol and water (MEW) in the ratio of 16:3:1 as the pressure-transmitting fluid. The equation of state of Ag was used for pressure calibration.

From the observed HPXRD patterns, the pressure dependence of the d-spacings and hence the lattice parameters a and c were calculated. The cell volume was computed from these lattice parameters. The noramalised cell volume V/V_0 vs. pressure is shown in Fig. 3. It was noticed that the unit cell volume dropped by almost 4% at pressures as low as 0.2 GPa. We believe this may be due to an isostructural transition. The structure remained stable up to the maximum pressure studied. The P-V data was fitted to the Birch-Murnaghan equation of state and the bulk modulus

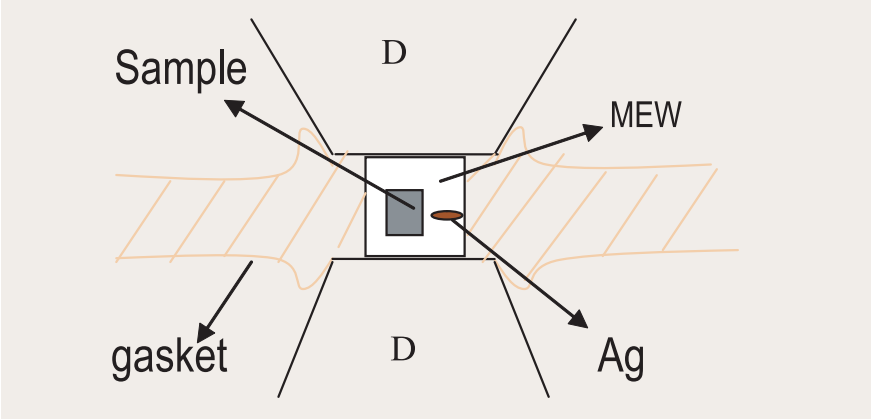

Fig. 1. Schematic of sample assembly for HPXRD. D: diamond anvils, MEW: Methanol, Ethanol and Water mixture as pressure transmitting medium. The sample and silver (pressure calibrant) are loaded in the hardened stainless steel gasket hole of F ~ 200 μm.

was found to be 169 GPa.

In order to understand the stability of the tetragonal structure of $ThGa_2$ over a large pressure range, structural stability maps were used. The structural stability regimes for various types of systems are arrived at using electron counting rules. These rules are derived from both experiments and a Hückel type theory. The observed/predicted zone of stability for tetragonal and orthorhombic structures is from 10 to 13 electrons per formula unit. $ThGa_2$ has 10 electrons per formula unit. Under pressure, the number of free electrons per formula unit is expected to increase and hence its structural stability regime may extend up to 13 electrons per formula unit. Our band structure calculations clearly show that as a function of pressure, the electron transfer among the various bands is very low. This may be the probable reason for the stability of the tetragonal structure of this compound up to 62 GPa. The density of states histograms at different compressions were also computed, and it revealed that the Fermi level remains fixed to a pseudo-gap at compressions up to 0.75 times the equilibrium volume.

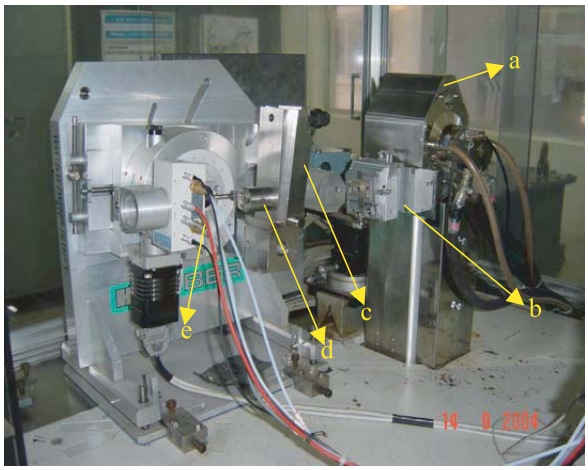

Fig. 2. High pressure Guiner diffractometer setup. a. 18 KW rotating anode X-ray generator with Mo target. b. Curved crystal monochromator c. Pressure cell holder d. Piston-Cylinder assembly of the diamond anvil cell e. Position sensitive detector

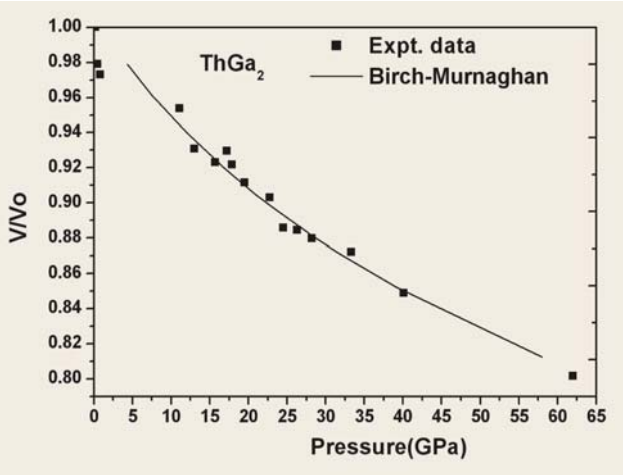

Fig. 3. V/V_0 vs pressure for $ThGa_2$. The continuous line indicates the Birch- Murnaghan equation of state fitting to the experimental data.

6.13 Electron Microscopy of Thin films of Gadolinia Doped Ceria Prepared by Pulsed Laser Ablation

Most of the oxygen ion conductors such as ZrO_2, CeO_2, and ThO_2 doped with aliovalent cations crystallize in a cubic fluorite structure with a relatively high concentration of oxygen vacancies. As compared to zirconia, the use of ceria based electrolyte presents the advantages of high ionic conductivity and compatibility with electrode materials. There is considerable interest in ceria-based solid electrolytes for applications in gas sensors, solid oxide fuel cells and oxygen membranes. The properties of the materials are often controlled by the microstructure and in particular, the grain boundaries have shown the greatest effect on the properties. Nanocrystalline oxides display unique electrical properties that are not attainable in conventional microcrystalline oxides. As a result, it is very important to understand the relationship between microstructure and electrical properties of materials in the nanocrystalline state that could enhance the reaction kinetics and electrical conductivity.

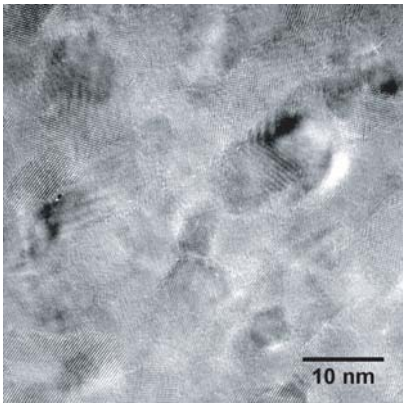

Fig. 1. TEM Image of uniformly distributed nano-crystals of Gadolinia doped Ceria deposited at 673K

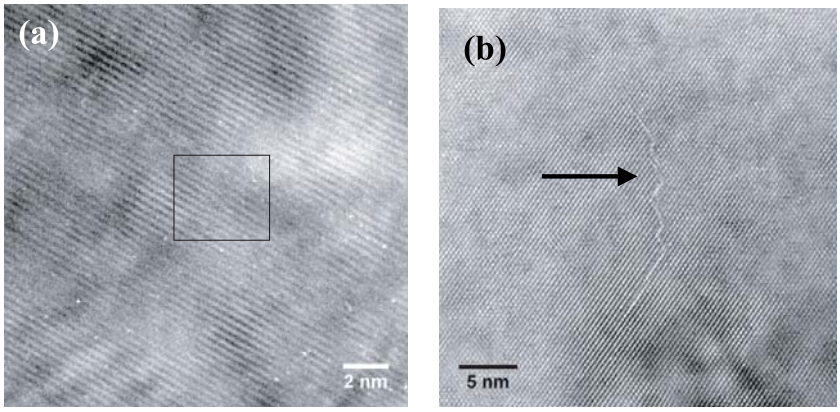

Fig. 2. Lattice images of (a)large crystalline region containing dislocations (b) Ledges

Pulsed laser ablation is a unique technique where the deposition is not only carried out at low substrate temperatures, but also the stoichiometry of the target is retained in the ablated films. The laser energy or laser fluence is an important parameter which is known to affect the deposition rate and microstructure of the films significantly. Therefore, microstructural variations in thin films of ceria doped with 5 mole % gadolinia (GDC) as a function of laser energy in the range 100-600 mJ/pulse was investigated by using the transmission electron microscopy (TEM) technique. The deposition of the films on sodium chloride crystals was carried out using a KrF excimer laser with a wavelength of 248 nm.

TEM examination of the plan view samples of the films coated on NaCl crystal, at a substrate temperature of 673 K, at various laser energies was carried out. Films deposited in the energy range 100-200 mJ/pulse have shown nanocrystalline grains of size about 7-8 nm. No segregation of Gd or formation of any secondary phase is noticed irrespective of the energy of the laser pulse. It is noted that the agglomerates of ablated particles appear at laser energy ≥ 400mJ/pulse.

Lattice images were recorded from nanocrystalline and large crystalline regions. The nanocrystalline interfaces are clean and do not contain any amorphous or secondary phases (Fig.1). On the other hand, the large crystalline area is generally defect free. However, at a few places, extended defects (Fig.2a), ledges (Fig.2b) and lattice bending could be seen in the films. The ledges shown in Fig. 2b are growth related defects which were mostly seen in grains containing (111) planes with the lattice spacing of about 0.35nm. Higher laser energy or higher deposition rate facilitates the generation of a copious amount of ablated species with reduced surface mobility, resulting in growth induced defects and agglomerates.

The results indicated a need for optimisation of laser energy for the control of defects in the films grown for technological applications. It is also noticed that phase-pure and doped cerium oxide films with uniform grains in the nanometre range could be grown using laser beam energy of about 200 mJ/pulse.

CHAPTER 7

Infrastructure Facilities

7.1 Upgradation of Campus Network from ATM to Gigabit Technology

IGCAR has a campus network based on the Asynchronous Transfer Mode (ATM) technology connecting about 50 Local Area Networks established in various laboratories. The whole network was established with single and multi-mode fibre cables. The network provides connectivity to high performance scientific computing servers, information management servers, internet, E-mail, web servers, digital library etc. and is extensively used by the scientists and engineers of the Centre.

The campus network has a three tiered architecture. It has an ATM Enterprise / Core switch with about 20 ATM (155 Mbps) ports in the first level, about 20 workgroup switches with ATM uplink in the second level and about 50 edge switches with 100 base FX / 100 base TX fast ethernet uplinks and 100 base TX fast ethernet down links in the third level of the network.

The ATM technology has become obsolete at the enterprise level and the cost of spares and maintenance is high. Further, to provide higher bandwidth, it was planned to upgrade the campus network using gigabit ethernet technology.

For upgrading the network, the gigabit switches required, the connecterisation of fibre cable to overcome the distance limitation of gigabit over multimode fibre. The sequence in which the works were to be carried out without affecting the existing network and the modalities of switching over from ATM to Gigabit were planned meticulously to ensure that the upgradation is transparent to the user and the switch over is smooth with least interruption.

The upgradation involved installation and commissioning of Non-Blocking Gigabit Core switch with 128Gbps switching bandwidth, about 75 Gigabit Workgroup switches and edge switches. Thus, the upgraded campus network has a Gigabit core switch with 24 GBIC ports in the first level and about 20 workgroup switches with GBIC ports both in the uplink as well as in the downlink, in the second level and about 50 edge switches with GBIC/1000 base T uplinks and 100 base TX fast ethernet down links in the third level. The 1Gbps backbone speed has been extended to all the buildings.

The entire upgradation was completed successfully with the least interruption in the network services. The upgraded Gigabit Ethernet network is working satisfactorily, providing high speed access to the intranet servers.

7.2 Modernisation of the Intercom Telecommunication Network at IGCAR/BARCF and at two Townships

The present intercom telecommunication network of Kalpakkam units including some of the BARCF units is being modernized with the state of the art communication system.

The IGCAR site will have 9 new exchanges and 3 new exchanges at the three townships. All these 12 exchanges will be networked and interconnected. The new IPBX intercom exchange is a private telephone switch based on an IP data network infrastructure.

The main components of the Exchange are:

- A "Call Server" that is the system control center.
- One or more (possibly none) Media Gateways supporting standard telephone equipment:
  - Wired UA or analog sets.
  - Lines to the standard public or private telephone networks.
  - DECT or PWT mobile phone base stations.

  - o the voice guides,
  - o Compressors to ensure the link between standard and IP phones.
- Wired telephone sets (UA, analog).
- IP telephone sets (IP-Phones: the e-Reflexes and IP-Touch ranges, multi-media PCs or H323 terminals).
- DECT or PWT mobile sets.

All these 12 exchanges will have 60 voice channels connectivity between them through OFC cables. Critical facilities / locations, are provided with alternate copper cable connectivity for redundancy. All the exchanges will be networked and will work as a single exchange enjoying total feature transparency between them. They will be connected to the exchanges of different makes and models at BHAVINI, MAPS and WIP also. The feature transparency between these exchanges will be limited to a few features as governed by the Q-sig limitations.

All the users in the network can receive the outstation BSNL calls on their intercom phones. The central exchange at CDO will be loaded with Unified Messaging Solutions system, which will facilitate a number of features for the entire network including Voice Mail, Voice Mail to Email, Email to Fax Mail, Fax to E Mail and Email read out facility through telephone.

The central exchange at CDO will be connected to the Anunet server. All the intercom phones in the network can receive calls through the Anunet from external installations of DAE. The CDO exchange will also be connected to the two township exchanges (Kalpakkam & Anupuram) through a redundant wireless communication system. This will co-exist along with the OFC connectivity and in case of total failure of the cable network the wireless connectivity will take over automatically.

The exchange supports IP telephony through IP Phones. The other phones supported by the exchange are ISDN phones, Proprietary Digital phones, Proprietary DECT (mobile) phones, Analogue CLIP (Caller ID) phones and plain Analogue phones. The exchanges are istalled and being tested for commissioning by the early 2006.

7.3 Automated Circulation System at SIRD

IGCAR Library currently holds a collection of around 50,000 books, 34,000 bound volumes, 13,000 standards, 1,60,000 reports and subscribes to about 900 journals every year. It has continued to grow in terms of the number of documents and number of users. Few of the challenges faced with this growth are:

- Tracking a misplaced document
- Overload at circulation counter
- Stock verification
- Pilferage of the document

Fig. 1. RFID System

As books are circulated among more patrons the work in the Circulation System increases and delay in the re-shelving arises. Also the movement and tracking of the document becomes difficult. The Scientific Information and Resources Division (SIRD) has been able to address these by implementing a Radio Frequency Identification (RFID) Circulation System (Fig. 1)

RFID tags can be read and written to at distances of up to several feet, while in motion, in any orientation regardless of soiling or smudges, and through intervening objects such as paper, plastic, cardboard, or wood. The most significant fact is that many RFID tags can automatically and simultaneously be read or written to, contrary to bar codes, which must be scanned one-by-one.

Fig. 2. The RFID anti-theft system

An antitheft function is built into the RFID tag, specifically for library applications to protect the documents(Fig. 2). The main benefits of the RFID tag are to improve the speed and ergonomics of library document processing; improve the management of the collection utilising the re-programmable memory of the chip for recording information such as Accession Number, the location of the book in the library, statistics, etc; streamline and make easier the inventory of the collection by allowing a fast RFID shelf inventory, instead of a one by one scanning of books / shelves.

With the implementation of RFID, multiple books can be issued and returned at the transaction counter, thus saving the valuable time of the users and the SIRD staff.

The RFID based circulation system has been commissioned and all the circulation transactions are being carried out through this. In the first phase, the tagging and automation of the book holdings have been effectively implemented.

7.4 Independent Water Supply Scheme

Water is one of the precious resources on the earth and its demand for water is continuously growing. All DAE units and Kalpakkam Township depend mainly on the Palar river for water. Ground water potential of the Palar riverbed has gone down over the years due to insufficient rainfall coupled with excessive extraction for the past four decades. Non supply of water from Panankattuchery (Palar river) for few days in the year 2003 due to shortage resulted in the forced shutdown of chiller units in CWCP resulting in disruption of air conditioning for entire IGCAR campus and disruption of normal functioning of many laboratories for want of process water.

Realising the gravity of problems due to shortage of water supply, it was decided to identify and develop local water sources within IGCAR campus. One of the sites identified was the Poyyakarai pond near the western side of the main gate. Water from the pond has all the properties required for drinking purposes. The groundwater potential and its sustainability near Poyyakarai pond was assessed by a team of scientists from Central Ground Water Board, Chennai. Suggestions from experts were implemented while developing the pond.

To enhance the water retaining capacity, desilting and strengthening of banks of the pond were carried out. Besides development of the pond, a water supply scheme was developed and linked with the existing water supply schemes at IGCAR and Anupuram Township (ATS). For this, 8 bore wells, located on the banks of the pond were drilled to a depth of 6 to 7 m below ground level depending on the depth of water bearing strata. Water from these bore wells is collected in an underground sump near the main gate. A water conveying PVC line of 160 OD, and 4 kms length was built. This line connects the main gate under ground sump with IGCAR under ground sump.

Water from Poyyakarai pond is being used as a standby source to meet the shortfalls in water supply from Panankattuchery water line. From this developed source, so far 46 million gallons of water was consumed by IGCAR, ATS and BARCF. Since the commissioning of this pond, there were no AC shutdowns and water scarcity in IGCAR

7.5 Commissioning of State-of-the-Art New Chillers

IGCAR requires for all its R&D activities uninterrupted, reliable and satisfactory Air Conditioning and Ventilation services at its various facilities, round the clock. Four 500 TR capacity R-11 Centrifugal chillers were installed in the year 1978 and two more machines of 550 TR capacities were added in the year 1985 to augment the plant capacity at Central Water Chilling Plant (CWCP). One 500 TR capacity, CFC 11, HS 17 chiller was replaced in 1996. Three R-11 chillers were replaced in 2000 with eco-friendly Chillers (HFC 134a) due to obsolescence, non-availability of spares, deterioration of performance and as well as to meet the requirement of the Montreal protocol, which has mandated that CFCs have to be phased out

Two 550 TR capacity, state-of-the-art, energy efficient, eco-friendly chillers were installed and commissioned in place of old machines, which had been operating since 1985 and logged over 60,000 hrs with CFC as refrigerant. The new chillers use environment friendly refrigerant having zero Ozone Depletion Potential and also help in substantial energy savings as these machines consume about 0.653 kW/TR against 0.85 kW/TR of the old machines. (Fig. 1) The new chillers are not only energy efficient but also operator friendly and operate at very low sound levels.

Fig. 1. Photograph of CWCP Layout

Awards & Honours

- Dr. A. K. Arora of MSD has been awarded the Prof. Y. T. Thathachari Memorial Research Award, Mysore for the year 2005 in the area of physical sciences.

- Dr. Baldev Raj has been awarded the Lifetime Achievement Award for the year 2004 by the Indian Welding Society for his contributions to the field of Welding, during February 2005. He has also been awarded the Jaeger Lecture Award by the International Institute of Welding during the International Welding Congress at Mumbai. Dr. Baldev Raj has also been awarded the Indian Nuclear Soceity (INS) Award for the year 2004. He has been elected President of Indian Institute of Metals. He has also been elected Fellow of The Indian National Science Academy (INSA), New Delhi. He has been conferred with a Honorary Doctorate by Sathyabama Deemed University, Chennai. He has been conferred with the prestigious 14th Nayudamma Memorial Award, instituted by Dr. Y. Nayudamma Memorial Trust, Tenali, Andhra Pradesh for the year 2005.

- Dr. U. Kamachi Mudali of CSTD was awarded the INS Medal for the year 2004. He has been awarded the Metallurgist of the year award for 2005 by Ministry of Steels & Mines. He has also been awarded the Homi Bhabha Science & Technology Award for the year 2004.

- Dr. K. G. M. Nair of MSD has been selected for the Materials Research Soceity of India (MRSI) Medal Lecture for the year 2006.

- Dr. S. Venugopal of MTD has been elected as a Fellow of Indian National Academy of Engineering (INAE).

- Dr. C. Anand Babu, Dr. B. K. Sharma and Shri. G. Mohanakrishnan of FRTG were awarded the Indian Chemical Institute (ICI), India IIChE Award for Excellence in Process or Product Development for the year 2005 for their work on "Ion exchange chromotographic separation of isotopes of boron".

- Dr. Baldev Raj, Shri R. Natarajan, Dr. S. B. Koganti, Shri M. Venkataraman, Shri V. Sundararaman and Shri A. Ravisankar of RpG were jointly chosen for the Award for Excellence in Design or Development of Process Plant and equipment for the year 2005 for their work on "*Fuel Reprocessing of Unique Plutonium based Carbide Fuel*".

INDIRA GANDHI CENTRE FOR ATOMIC RESEARCH

ORGANIZATIONAL CHART AS ON 01-01-2006

DIRECTOR, IGCAR
Dr. BALDEV RAJ

IGC COUNCIL

DIRECTOR'S ADVISORY COMMITTEE [DAC]

IGC SCIENTIFIC COMMITTEE [IGCSC]

DIVISIONS & HEADS

CHEMISTRY GROUP
DIRECTOR
Dr. P.R. VASUDEVA RAO

- LIQUID METALS & STRUCTURAL CHEMISTRY — Dr. T. GNANASEKARAN
- MATERIALS CHEMISTRY — Dr. G. PERIASWAMI
- CHEMICAL FACILITIES — Shri K.C. SRINIVAS
- FUEL CHEMISTRY — Dr. T.G. SRINIVASAN

INSPECTION TECHNOLOGY GROUP
ASSOCIATE DIRECTOR
Shri P. KALYANASUNDARAM

- PIE, IN-SERVICE INSPECTION, REMOTE HANDLING & ROBOTICS — Shri K.V. KASIVISWANATHAN
- NON-DESTRUCTIVE EVALUATION — Dr. T. JAYAKUMAR

METALLURGY & MATERIALS GROUP
DIRECTOR
Dr. S.L. MANNAN

- MATERIALS TECHNOLOGY — Dr. S.K. RAY
- MECHANICAL METALLURGY — Dr. K. BHANUSANKARA RAO
- MATERAIALS SCIENCE — Dr. C.S. SUNDAR

MATERIALS CHARACTERISATION GROUP
ASSOCIATE DIRECTOR
Dr. V.S. RAGHUNATHAN

- CORROSION SCIENCE & TECHNOLOGY — Dr. H.S. KHATAK
- PHYSICAL METALLURGY SECTION — Dr. M. VIJAYALAKSHMI
- IDEAS SECTION — Shri P.V. KUMAR, **PROJECT MANAGER, FRFCF**

ELECTRONICS & INSTRUMENTATION GROUP
DIRECTOR
Shri P. SWAMINATHAN

- ELECTRONICS & INSTRUMENT., — Shri S.ILANGO SAMBASIVAM
- COMPUTER — Shri S. ATHINARAYANAN
- MEDICAL — Dr. A. VIJAYA

ENGINEERING SERVICES GROUP
DIRECTOR
Shri Y.C. MANJUNATHA
CHIEF ENGINEER

- ELECTRICAL SERVICES — Shri A. JYOTHIS KUMAR
- A/C & VENTILATION SYSTEM — Shri S. KESHAVAMURTHY RAO
- CENTRAL WORKSHOP — Shri A.S.L.K. RAO
- QUALITY ASSURANCE — Shri B. VENKATARAMAN
- CIVIL ENGINEERING — Shri C. SIVATHANU PILLAI, ACE (CIVIL)
- TECH. COORDINATION AND QUALITY CONTROL SECTION — Shri N. VIJAYAN VARIER*

PLANNING DIVISION — Shri S. SUBRAMANIAN

CHIEF ADMINISTRATIVE OFFICER
Shri V. DAYALAN

- ADMINISTRATIVE OFFICER (R&SR) — Shri JOSEPH DORAIRAJ
- ADMINISTRATIVE OFFICER (P) — Shri V.M. THOMAS

REACTOR OPERATION & MAINTENANCE GROUP
DIRECTOR
Shri P.V.RAMALINGAM

ADVISOR — Shri V.S. KRISHNAMACHARI

DIVISIONS & HEADS

- TECHNICAL SERVICES — Shri G. SRINIVASAN
- TRAINING & HRD — Shri K. RAVISHANKAR

OPERATION & MAINTENANCE GROUP
ASSOCIATE DIRECTOR
Shri B. RAJENDRAN

- REACTOR OPERATIONS — Shri B. RAJENDRAN, REACTOR SUPERINTENDENT
- REACTOR MAINTENANCE — Dr. V. RAMANATHAN
- COMPONENTS & INSTRUMENT., DEVELOPMENT — Shri K. SWAMINATHAN
- SEPARATION TECHNOLOGY & HYDRAULICS — Dr. C. ANAND BABU

FAST REACTOR TECHNOLOGY GROUP
DIRECTOR
Shri G. VAIDYANATHAN

SODIUM TECHNOLOGY GROUP
ASSOCIATE DIRECTOR
Shri P. KALYANASUNDARAM

- SODIUM FACILITIES — Shri K.K. RAJAN

REACTOR ENGINEERING GROUP
DIRECTOR
Shri S.C. CHETAL

- REACTOR PHYSICS — Dr. P. MOHANA KRISHNAN
- SODIUM CIRCUITS & COMPONENT HANDLING — Shri S.C. CHETAL
- CIVIL ENGINEERING — Shri C. SIVATHANU PILLAI (FOR PFBR DESIGN)
- INSTRUMENTATION & CONTROL — Shri C.PARAMASIVAN PILLAI
- POWER PLANT ENGINEERING — Shri T.K. SHANMUGAM

NUCLEAR ENGINEERING GROUP
ASSOCIATE DIRECTOR
Dr. P. CHELLAPANDI

- REACTOR COMPONENTS — Shri P. PUTHIYAVINAYAGAM
- MECHANICS & HYDRAULICS — Dr. P. SELVARAJ

REPROCESSING GROUP
DIRECTOR
Shri R. NATARAJAN

- FUEL REPROCESSING PROCESS — Shri V. SUNDARA RAMAN
- REPROCESSING PLANT OPERATIONS — Shri M. VENKATARAMAN
- REPROCESSING R&D — Dr. S.B. KOGANTI
- REPROCESSING PROJECTS & SERVICES — Shri P. RAMKUMAR
- REPROCESSING PLANT DESIGN — Shri A. RAVISANKAR

SAFETY GROUP
DIRECTOR
Shri M. RAJAN

- SAFETY ENGINEERING — Shri N. KASINATHAN
- RADIOLOGICAL SAFETY — Dr. R. INDIRA
- SCIENTIFIC INFORMATION & RESOURCES — Shri M. SOMASEKHARAN

JOINT CONTROLLER (FINANCE & ACCOUNTS)
Shri V. JAYARAJ

- DEPUTY CONTROLLER OF ACCOUNTS — Shri R. SATHYAMURTHY
- SENIOR ACCTS., OFFICER (PAO) — Shri J. VINCENT SUNDARAKUMAR

* STATIONED AT MUMBAI

Colloquia, Seminars, Conferences - 2005

Special Lectures

1. Vikram Sarabhai Lecture: "Science for our Future" by Prof. C.N.R. Rao, Linus Pauling Research Professor, Honorary President, JNCASR, Bangalore and Chairman, Scientific Advisory Committee to Prime Minister of India, on January 20.

2. Prof. Brahm Prakash Memorial Lecture: "Pursuit of Science-The Fascinations and Excitements of a Materials Scientist" by Dr. Baldev Raj, Distinguished Scientist and Director, IGCAR to the participants of Prof. Brahm Prakash Memorial Materials Quiz-2005 on September 30.

IGC Colloquia

1. "Interaction of Hydrogen with Internally Oxidised Palladium Alloys" by Prof. R. Balasubrmanian, Department of Materials and Metallurgical Engineering, IIT Kanpur on February 2.
2. " Earth Quakes: Space borne techniques for monitoring" by Dr. C.D. Reddy, Indian Institute of Geomagnetism, Mumbai on February 4.
3. "Technology Foresight and Innovation" by Dr. R. Chidambaram, Homi Bhabha Professor and Principal Scientific Advisor, Government of India on February 23.
4. " Indian Space Program" by Dr. C.B. Kartha, Deputy Director, VSSC, Trivandrum on March 7.
5. " Chemical Issues in Nuclear Fuel Waste Management" by Prof. G.R. Choppin, Emeritus Professor, Florida State University on March 21.
6. " Earth quakes and Tsunami" by Dr. G. J. Nair, Head, Seismology Division, BARC on June 10.
7. " SLOW POKE-2 Reactor Facility at Dlahousie University" by Dr. A. Chatt, Director, SLOWPOKE-2 Reactor Facility, Dalhousie University, Haifox, Canada on November 7.
8. " Sensor Networks: Recent Advances" by Prof. Dharma P. Agarwal, University of Cincinnati, USA on December 15.

Seminars, Workshops and Meetings

1. Seminar on Safety Handling of Plutonium, a seminar covering all aspects from design of Plutonium- handling laboratories to waste management of plutonium and internal dosimetry, February 22-23.
2. Recent Advances in Information Technology READIT-2005, July 14-15.
3. IAEA Workshop on external flooding of Nuclear Power Plants, August 29 - September 2.
4. 5th Quality Circle Awareness Day-2005, QC Program, September 6,8.
5. Seminar on the Occasion of 2 decades of FBTR Operation on October 18.
6. Theme Meeting on Mass Spectrometry in Nuclear Fuel Cycle, December 21-23
7. Seminar on Physics of Fast Breeder Reactors , December 28.

Nurturing activites

1. Summer Training in Physics and Chemistry (STIPAC 05), a six weeks summer training programme in Physics and Chemistry for final year M.Sc (Physics/Chemistry) students from May 27 - July 8.
2. Professor Brahm Prakash Memorial Materials Quiz-2005, an annual event of materials quiz organized for students of Classes XI and XII participating from across the country as well as from neighbouring countries, on September 30.

Peer Review of research activities in Chemistry and Chemical Engineering

A peer review of the research and development activities in Chemistry and Chemical Engineering was conducted on April 7-8, 2005. The review was conducted by a panel of eminent experts consisting of Prof. M. M. Sharma (Chairman), Former Director, UDCT, Mumbai, Dr. S. Sivaram, Director, National Chemical Laboratory, Pune, Dr. K. V. Raghavan, Chairman, Recruitment and Assessment Centre, Defence Research & Development Organization, Delhi, Dr. T. Ramaswami, Director, CLRI, Chennai, Prof. P. T. Manoharan, Honorary Professor (JNCASR), Sophisticated Analytical Instrumentation Facility, IIT, Chennai and Shri B. Bhattacharjee, Special Advisor to Chairman, Atomic Energy Commission. To help in the review process, a detailed document "Report on the Research and Development Activities over the last five years in the areas of Chemistry and Chemical Engineering", was sent to the committee prior to the review. This document provided an overview of the various activities of the Centre in the above areas. The review consisted of presentations by various researchers, followed by in-depth deliberations. It covered diverse areas of both basic research and applied technology conducted in the Chemistry Group, Reprocessing Group, Metallurgy Group and Fast Reactor Technology Group. The review committee also visited the relevant laboratories to aid in their assessment.

The peer review process was a very useful exercise as it helped us to obtain independent, critical and constructive suggestions on the research work and its directions. While the appreciation received from the experts served as a great source of motivation, their suggestions will certainly help the programmes to attain greater heights.

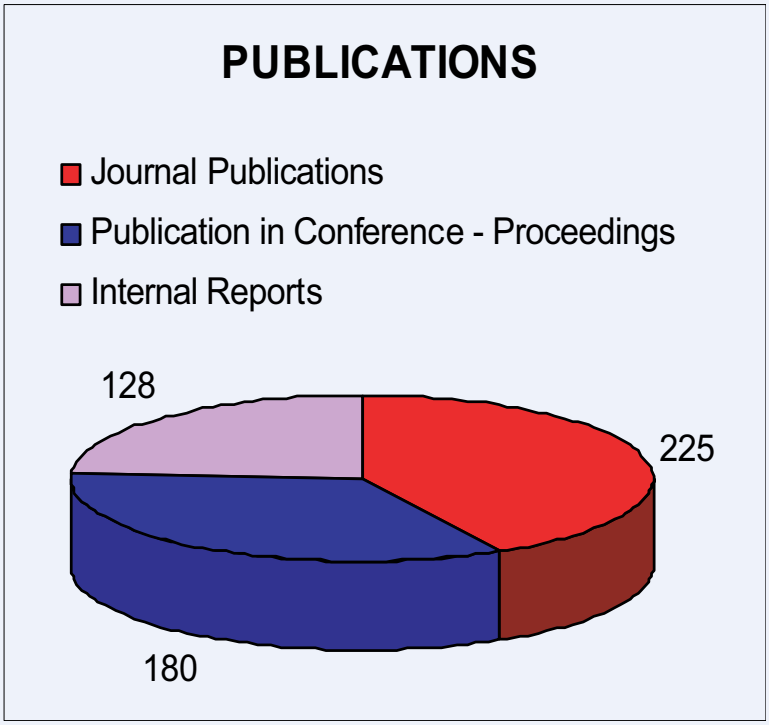

News and Events

A function to commemorate twenty years of successful operation of FBTR was held at SRI Guest House on November 2, 2005. Staff members of FBTR participated with families. Photo shows Dr. Anil Kakodkar, Chairman, AEC and Secretary, DAE partcipating in the function. Also seen in the picture are (L to R) Shri B. Rajendran, Associate Director, (O&M), Dr. Baldev Raj, Director, IGCAR and Shri P. V. Ramalingam, Director, ROMG.

CORAL (COmpact factility for Reprocessing Advanced fuels in Lead cells) has achieved a remarkable feat of reprocessing mixed carbide fuel with 100,000 MWd/t burn-up. To commemorate this event, which was achieved for the first time in the world, a family get together was organised on June 11, 2005 at SRI Guest House, Anupuram. Seen in the photo are (L to R) Shri V. R. Raman, former Associate Director, RpG, Shri G. R. Balasubramanian, Former Director, RpG, Dr. Anil Kakodkar, Chairman, AEC and Secretary, DAE, Dr. P. Rodriguez, Former Director, IGCAR, Dr. Baldev Raj, Director, IGCAR and Shri R. Natarajan, Director, RpG during the function.

A French delegation led by Dr. Andre-Claude Lacoste, Director General, DGSNR visited IGCAR on October 26, 2005. This was the fifth session of the Indo-French dialogue on Nuclear Safety. Seen in the photo are the French delegation and the Indian counterparts led by Dr. Baldev Raj, Director, IGCAR.

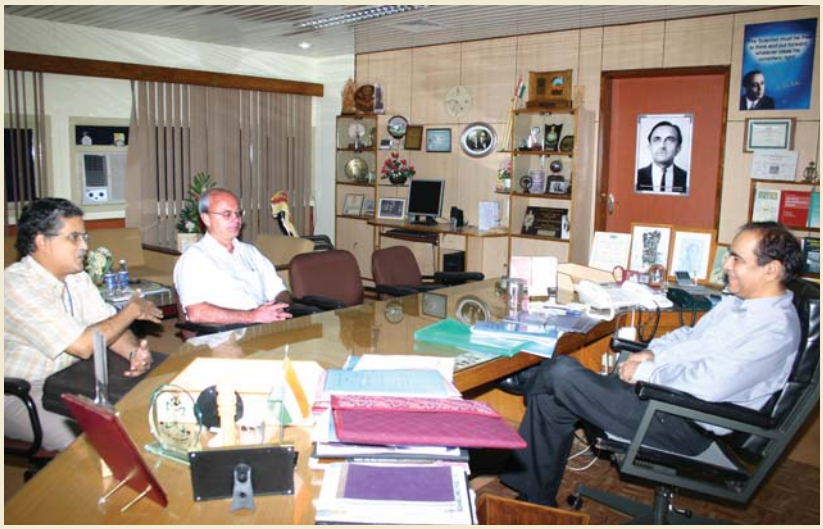

Dr. Y. A. Sokolov, Deputy Director General and Head of the Department of Nuclear Energy, IAEA, Vienna visited IGCAR on November 11, 2005. Photo shows Dr. P.R. Vasudeva Rao, Dr. Sokolov and Dr. Baldev Raj.

IGC Council

Chairman

Dr. Baldev Raj is a Distinguished Scientist and the Director of Indira Gandhi Centre for Atomic Research. His specializations include materials characterization, testing, and evaluation using nondestructive evaluation methodologies; materials development and performance assessment; and technology management. He is a fellow of the Indian National Academy of Engineering, Indian National Science Academy, Indian Academy of Sciences, The National Academy of Sciences and Tamil Nadu Academy of Sciences. He has won many awards including Sir C.V. Raman Award, Keith Hartley Memorial Award, VASVIK Award, AEWG Gold Medal, G.D. Birla Gold Medal, SAIL Gold Medal, MRSI-ICSC Superconductivity and Materials Science Annual Prize, Lifetime Achievement Award of the Indian Society for Nondestructive Testing, Indian Welding Society, Jaeger Lecture Award of International Institute of Welding, International Researcher Award of International Committee on Nondestructive Testing, Indian Nuclear Society Award, NOCIL Award of Indian Institute of Chemical Engineering, etc. He has more than 640 publications, 5 Indian Standards and 16 patents to his credit. He is co-author of 10 books and monographs and co-editor of 22 books and special issues of journals. He is on the editorial boards of national and international journals and is a reviewer of proposals and publications from prestigious bodies in India and abroad.

His interests include religion, philosophy, culture and education. He is an acclaimed specialist in the area of archeometallurgy and education at all levels.

Members

Dr. C.V. Ananda Bose, IAS, is presently the Joint Secretary (Research and Development), Department of Atomic Energy. Coming from the Kerala Cadre, he has held several positions in Kerala including the Principal Secretary to Chief Minister of Kerala. He is a visiting Professor of the Birla Insititute of Technology and Science, Pilani and has authored eight books and about a hundred papers and articles in the fields of Habitat, Architecture, Environment and Land Reforms. He is a recipient of several National and International Awards that include the Jawaharlal Nehru Fellowship, Bremen Partnership Award and Rajiv Gandhi National Asward for Excellence in Management. He has received more than a hundred prizes and medals and is a member of several International and National Expert Groups.

Shri S.C. Chetal, B.E.(Mech), is a Distinguished Scientist and the Director, Reactor Engineering Group at IGCAR. Since 1971, he has been engaged in the field of fast reactor engineering. He has made significant contributions towards design of FBTR sodium systems and components. He has also contributed to the material selection, manufacturing technology, R&D and design of the 500 MWe Prototype Fast Breeder Reactor. He is a member of many professional institutions and a Fellow of the Indian National Academy of Engineering. He has received the National Technology Award 2000 from DRDO for significant contributions in the field of high purity titanium sponge production and the Indian Nuclear Society Award 2003 for contributions towards nuclear related high technology. His interests include pressure vessel and materials technology. He has to his credit 300 publications in Journals/Symposia/Conferences.

Shri S.C. Hiremath, a Distinguished Scientist, is the Chairman and the Chief Executive of Heavy Water Board (HWB). He has been working as a key member of DAE's Heavy Water Programme right from its inception i.e. conceptualisation, application oriented R&D, including development of process equipment/ machinery, technology development and setting up of the first totally indigenous H_2S based plant besides being a member of "Think Tank" of maturing NH_3 based plants. He is well known for laying an emphasis on maximising the production of heavy water and making the process energy efficient. He is actively pursuing diversification into production of other stable isotopes including enrichment of Boron-10 through alternative routes, high end solvents required for self sufficiency in the 2nd stage of India's nuclear power programme besides many other high technology issues like development of an industrial scale cryo-cycle operating at around 20 K. He was on the board of Directors of M/s KRIBHCO, New Delhi as non Executive Director. He is currently as the board of Management of NFC, Hyderabad and Member of AERB's Advisory Committee on Nuclear Safety (ACNS).

In recognition of his outstanding contributions, Shri Hiremath has been awarded the INS Award-2001 by the Indian Nuclear Society. He has also been awarded Management Excellence Award-2002 and Maharana Mewar Award-2003 for his devotion/commitment beyond the call of duty.

Shri R.Kalidas is presently the Chairman and Chief Executive of the Nuclear Fuel Complex, Hyderabad. He is a Mechanical Engineer from the 11th batch of the BARC Training School. He has to his credit, design, installation and operation of the first Stainless Steel Seamless Tube Plant in the country. He played a key role in developing tubular products in a variety of materials for critical applications in atomic energy, defence, aerospace, aeronautical, chemical and engineering industries. He was responsible for preparation of a Technology Report, which served as a road map for the creation of sophisticated manufacturing plants for zirconium alloy tubes and components for the enhanced nuclear power programme. He served NFC for the last 33 years in various capacities in different departments and has gained rich experience in Project Engineering, Production, Maintenance and Marketing Management. Shri Kalidas besides being a member of IGC Council, is also on the board of UCIL and IREL.

Shri H.S. Kamath, B.E (Metallurgy), is a Distinguished Scientist and Director of the Nuclear Fuels Group in BARC. He has been associated with the development of plutonium bearing nuclear fuels for the last 35 years, which started with the fabrication of fuel for 'PURNIMA' in 1970-1972. His main area of work is in the development of uranium-plutonium mixed oxide (MOX) fuels for the nuclear power programme. He has made important contributions in this field, both in the laboratory scale as well as the industrial scale activities. His most important contribution has been the setting up of the industrial scale MOX fuel fabrication plant at Tarapur. Shri Kamath is the recipient of the Indian Nuclear Society Award for the year 2003 in recognition of his outstanding contributions in the field of nuclear fuel fabrication.

Dr. M. B Kurup, MSc, Ph.D, is a Professor and Dean in the Faculty of Natural Sciences of the Tata Institute of Fundamental Research (TIFR), Mumbai. His areas of specialisation are the application of Ion beams for study of atomic physics, materials science and biological systems and the science and technology of accelerators. He has guided a lot of Doctoral Scholars and has a large number of publications besides prestigious honours in his field.

Shri H.S. Kushwaha, B.Sc., M.Tech.(IIT, Kanpur), is presently the Director of Health, Safety and Environment Group at BARC. He has made significant and important contributions in the design and analysis of nuclear structures, components and piping of Indian Pressurised Heavy Water Reactors (PHWR). He has done pioneering work in the area of seismic design and analysis of the 500 MWe PHWR being built at Tarapur, Maharashtra. He has developed several finite element computer programmes in the field of structural mechanics, heat transfer and fluid mechanics. He has developed an improved finite element method using upwinding schemes to solve the three dimensional advection-diffusion equation. He is an active member of the Project Design Safety Committee of PHWRs/FBR, Civil Engineering Safety Committee and Safety Review Committee for Operating Plants (SARCOP) constituted by AERB, Mumbai. He has published around 400 papers/reports in national and international journals.

Shri S.D. Misra, B.E. (Electrical and Mechanical Engineering), is presently the Director of Nuclear Recycle Group at BARC. Right from joining BARC from the 13th Batch of Training School, he has been involved in the development of radioactive waste management technologies. He was a member of a team that pioneered setting up of the first vitrification plant in the country at Tarapur and also was responsible for design and construction of Waste Immobilisation Plants at Trombay and Kalpakkam. He also served as Director of the Directorate of Purchase and Stores of DAE. In this capacity he has successfully used his vast experience of managing large projects that involved procurement of various types of materials, in overcoming several challenging situations. As Director of NRG, he is holding the responsibility of setting up and operation of reprocessing and waste management plants at various sites in the country.

Shri R.K. Sinha, B.E (Mechanical Engineering), is presently a Distinguished Scientist and Director of the Reactor Design and Development Group at BARC. He is a nationally and internationally recognised expert in the area of nuclear reactor technology. He has handled several major assignments relating to the Indian research and power reactors. In particular, he has specialised in the design, development and safety related activities relating to coolant channels of heavy water reactors. He is currently guiding the design and development of the innovative Advanced Heavy Water Reactor and Compact High Temperature Reactor. Shri Sinha has received several awards and honours including the Homi Bhabha Science and Technology Award, VASWIK Award and the Indian Nuclear Society Award.

Shri Umesh Chandra, B.Tech (IIT, Kanpur), is currently the Senior Executive Director (CA and R&D) in NPCIL. He has been responsible for establishment of R&D facilities for nuclear and electronic systems in NPCIL. These facilities are located at R&D Centre, Tarapur and R&D Lab., NUB, Mumbai. He is also directing development and deployment of Computer Based Systems in nuclear power plants for Control and Instrumentation Systems, Main Control Rooms and Training Simulators for PHWR and LWRs. He is also guiding establishment of IT infrastructure and applications in the organisation. He was responsible for Control and Instrumentation of TAPP-4 nuclear power plant, which achieved criticality within 5 years of start of construction. He is directing the Knowledge Management activities in NPCIL. Earlier at Reactor Control Division, BARC, he has been engaged in the development of computer based control and operator information systems for nuclear power plants. He was responsible for computerized control system for on-power refuelling machines of PHWRs from NAPS onwards and Dual Processor Hot Standby (DPHS) based - Processs Control System and Reactor Regulating System for Kaiga-1,2 and RAPP-3,4 reactors. He participated in activities of AERB as a member of several safety committees and Advisory Committee for Code, Guides and manuals for safety in design for nuclear power plants. He was Head, Reactor Control Division and Associate Director, Automation and Manufacturing Group, BARC before joining NPCIL.

Dr. V. Venugopal, M.Sc.,Ph.D, is presently an Outstanding Scientist and the Director of Radio Chemistry and Isotope Group at BARC, Mumbai, and Head, Nuclear Material Accounting and Control (NUMAC) cell of DAE. He is a specialist in the field of thermal/ thermodynamics of plutonium based fuels at high temperatures, chemical quality control of fuel, X-ray and solid state chemistry. He has to his credit more than 300 publications out of which 145 are published in reputed international journals. Widely acclaimed as an expert in the area of thermodynamics, he is currently the regional editor of the Journal of Thermal analysis and Calorimetry. Dr. Venugopal is the president of the Indian Association of Nuclear Chemists and Allied Scientists (IANCAS) and the Indian Thermal Analysis Society (ITAS). He is also a member of several professional bodies like INS, NAARRI, ISAS,ISEAS,MRSI and Hindi Vigyan Parishad. He has received many awards including the Netzsch-ITAS award in 2001, ISCAS silver medal in 2002 and MRSI medal for 2003-04.

Members of Indira Gandhi Centre Scientific Committee (IGCSC) and Activities of Various Groups

Reactor Engineering Group

Shri S. C. Chetal
Director

Dr. P. Chellapandi
Associate Director, NEG

Dr. P. Mohanakrishnan
Head, RPD

Shri T.K. Shanmugam
Head, PPED

Shri P. Puthiyavinayagam
Head, RCD

Shri C. Paramasivan Pillai
Head, ICD

Shri C. Sivathanu Pillai
Head, CED

Dr. P. Selvaraj
Head, MHD

Mrs. Uma Seshadri
Head, PIS

Reactor Engineering Group (REG) is responsible for the design of the 500 MWe Prototype Fast Breeder Reactor (PFBR). Design of the Nuclear Steam Supply System is carried out in-house. For balance of the Plant, design coordination is carried out by REG while the consultants are assigned the design work. REG is responsible for getting the design clearance of 500 MWe FBR from AERB. R&D coordination towards FBR and execution of R&D for structural mechanics is the responsibility of the Group. As the PFBR is primarily based on indigenous technology, the manufacturing technology development of important nuclear components was undertaken by REG with the active participation of Indian industries and has been successfully completed. The components include the main vessel, inner vessel, grid plate, roof slab, shutdown mechanisms, steam generator and the largest size sodium service valve. REG provides the design support to FBTR. REG has acquired expertise in the design of fast reactors. As a spin-off, structural mechanics expertise is being provided for non-reactor activities.

Metallurgy and Materials Group

Dr. S. L. Mannan
Director

Dr. V. S. Raghunathan
Associate Director, MCG

Shri P. Kalyanasundaram
Associate Director, ITG

Dr. H. S. Khatak
Head, CSTD

Dr. S. K. Ray
Head, MTD

Dr. K. Bhanu Sankara Rao
Head, MMD

Dr. C. S. Sundar
Head, MSD

Shri K. V. Kasiviswanathan
Head, PIRD

Dr. T. Jayakumar
Head NDED

Shri P. V. Kumar
Head, IDEAS

The Metallurgy and Materials Group has the mandate for a comprehensive materials R & D programme focussed towards FBR technology. This requires multifaceted and multidisciplinary approaches that include development of special alloys, welding consumables, optimisation of fabrication schedules, characterisation of mechanical properties under sustained as well as varying loads at elevated temperatures over a wide ranges of strain rates, comprehensive characterisation of corrosion, concrete corrosion and bio-fouling, development and application of specialised NDE techniques, innovative designs, and robotics for remote handling. This has been backed by fundamental studies in basic science that includes studies on microstructure dependence of the various properties, radiation damage, positron annihilation, thermo-physical properties and mathematical modelling. Some significant contributions of the group include PIE of FBTR fuel pins that has led to enhancement of target burn up, and development of indigenous structural steels and welding consumables for PFBR applications. At the same time, the outstanding research contributions have brought international recognition in fields as diverse as life prediction under creep and creep-fatigue conditions, characterisation of microstructures by NDE techniques, welding science and technology and materials science.

Fast Reactor Technology Group

Shri G. Vaidyanathan
Director

Shri. P. Kalyanasundaram
Associate Director, STG

Shri C. Anand Babu
Head, ST & HD

Shri K. Swaminathan
Head, CIDD

Shri K. K. Raja
Head, SFD

The Fast Reactor Technology Group is involved in the heat and mass transfer studies in the cover gas above sodium free levels, development and testing of sodium components like cold trap, plugging indicator, filters, heaters, valves etc., development and testing of sodium sensors for level and flow, leak detection sensors for sodium , sodium pump development, testing of control rod mechanisms, inflatable seals, fuel and other subassemblies for pressure drop and cavitation, reactor assembly flow patterns, vibration testing of steam generator and intermediate heat exchanger etc., instability measurement in steam generators, testing of full scale fuel handling machines in air and sodium. To achieve the above, the group has many water and sodium rigs. The biggest rig is the Steam Generator Test Facility (5.5 MWt). The R&D and testing activities for the 500 MWe Fast Breeder Reactor (FBR) are presently in progress.

Important contributions during the year include development and testing of prototype Eddy Current Flowmeter for Primary Sodium Pump of PFBR, testing of devices to reduce gas entrainement in reactor hot pool, acoustic leak detection of sodium water reaction, performance testing of hydrogen in argon detector and continuos production of 65% enriched Boric Acid for PFBR. The experiences with testing of Eddy Current Position Sensor in air and sodium was highly rewarding.

Reactor Operation and Maintenance Group

Shri P. V. Ramalingam
Director

Shri B. Rajendran
Associate Director

Shri G. Srinivasan
Head, TSD

Shri K. Ravishankar
Head, THRDD

Shri V. Ramanathan
Head, RMD

ROMG is responsible for the safe operation of the Fast Breeder Test Reactor (FBTR) and KAMINI reactor within the limits given in the technical specification documents. The group takes part in the operational safety review of the 500 MWe Prototype Fast Breeder Reactor (PFBR) Project documents. The Training and Human Resources Development Division of the group, besides training the O&M staff of FBTR and KAMINI, is also responsible for training the O&M staff of FBR. Introducing innovations and new features in FBTR to increase its availability, enhancing safety, and gaining newer experience for incorporation of inferred ideas in FBR construction and operation, represent a part of ROMG's activities.

During the current year, FBTR completed the 13th irrdiation campaign with the mission to irradiate the test fuel simulating the PFBR Fuel composition. The test fuel has achieved a burn-up of 59 GWd/t at a linear heat rating of 450 W/cm, as against the target burn-up of 100 GWd/t. The Mk-1 carbide driver fuel itself has reached a burn-up 155 GWd/t without any failure. This is a record for the carbide fuel and among the deft international records for any Fast Reactor driver fuel. The various modifications and the refurbishments carried out earlier resulted in a record campaign availability factor of 94.8% during the 13th irradiation campaign. FBTR completed 20 Years of operation on 18th October, 2005. This event was celebrated with a technical seminar in Tamil for the staff, an open house for the family members and a get together under the auspices of INS Kalpakkam Chapter. FBTR is now due for periodic safety review by AERB. For this, the Plant life assessment is in progress and preliminery indications are that FBTR has a residual life exceeding 15 effective full power years. Since sufficient experience has now been obtained with the carbide fuel including its reprocessing, it is now planned to expand the core by adding high- Pu MOX fuel (44%, PuO_2) surrounding the carbide fuel. Safety clearance, has in principle been obtained for this hybrid core of 30nos of Mk-1 fuel and 54 nos of MOX fuel capable of generating 31MWth/10.7 MWe.

Reprocessing Group

Shri R. Natarajan
Director

Dr. S. B. Koganti
Head, RRDD

Shri P. Ramkumar
Head, RPSD

Shri A. Ravisankar
Head, RPDD

Shri M. Venkataraman
Head, RPOD

Shri V. Sundararaman
Head, FRPD

The Reprocessing Group (RpG) of IGCAR is responsible for the development of fast reactor fuel reprocessing technology and construction of the reprocessing plants.
Various developmental works related to fast reactor fuel reprocessing are carried out at the Reprocessing Development Laboratory (RDL). This Laboratory has hot cell facilities and the associated analytical laboratory. In one of the hot cell facilities, U-233 was recovered from irradiated thorium rods on campaign basis and used as fuel in the KAMINI reactor and in FBTR (as PFBR test fuel). In the other hot cell facility, called, CORAL, (COmpact facility for Reprocessing Advanced fuels in Lead cells) (formerly known as LMC) commissioned in 2003, is a test bed for validating the process flow sheet and scaling up of the equipment designs for fast reactor fuel reprocessing, by reprocessing the FBTR fuel. LMC has already reprocessed mixed carbide fuels irradiated in FBTR with 25, 50 and 100 GWd/t burnups. This has provided valuable experience to the Demonstration Fast reactor fuel Reprocessing Plant, DFRP, in which the FBTR fuels will be regularly reprocessed, which is currently under construction. The scope of DFRP is being expanded for experimental reprocessing demonstration of PFBR fuel subassemblies also. Till DFRP is commissioned, FBTR spent fuel will be reprocessed at CORAL.

The engineering scale testing of equipment and systems are done at RDL. The Chopper, dissolver, feed clarification equipment and centrifugal extractors are few of the important equipment developed here. Apart from equipment development, research is undertaken for understanding and solving various process and chemistry problems of fast reactor fuel reprocessing such as, mathematical modeling of solvent extraction of the complex U-Pu system, efficient solvent management, development of online monitoring of Pu for process control, liquid flow metering in high radioactive fields etc.

Chemistry Group

Dr. P. R. Vasudeva Rao
Director

Dr. G. Periaswami
Head, MCD

Dr. T. G. Srinivasan
Head, FChD

Dr. T. Gnanasekaran
Head, LMSCD

Shri K.C. Srinivas
Head, FICD

The Chemistry Group is responsible for carrying out R & D to provide inputs with respect to all the chemistry aspects of the fast reactor and its fuel cycle. In addition, it also takes up R&D programmes which would have a long term impact on the reactor programmes. Besides the R&D activities, the Chemistry Group also provides extensive analytical support using a wide range of analytical techniques to all the programmes in the Centre. The Chemistry Group has also specialized in setting up of facilities for experiments with radioactive or air-sensitive materials, and in indigenous development of chemical instrumentation.

The areas of R & D in Chemistry Group include sodium chemistry, chemistry of un-irradiated as well as irradiated fuel materials, development of the fuel cycle, analytical chemistry, spectroscopy and more recently, boron chemistry. Development of sensors for PFBR and sensors for environmental applications, cover gas purification system for PFBR, development of Laser Induced Breakdown Spectroscopy and X-ray absorption based techniques for on-line monitoring of Pu streams in reprocessing plants, development of technology for production of Pu rich fuels and minor actinide containing fuels through the sol-gel route and development of sodium bonding for metallic fuels are some of the R & D programmes on the anvil.

Safety Group

Shri M. Rajan
Director

Shri N. Kasinathan
Head, SED

Dr R. Indira
Head, RSD

Shri M. Somasekharan
Head, SIRD

Safety Group consists of Safety Engineering Division, Radiological Safety Division and Scientific Information and Resources Division.

Safety Engineering Division is engaged in the simulated experimental studies and development of mathematical models for FBR accident scenarios such as core subassembly flow blockage, molten fuel relocation, core debris cooling in core catcher, mitigation of consequences of sodium fires and radioactivity transport and deposition in sodium circuits.

Radiological Safety Division is mainly responsible for the research and development activities in radiation safety. The Division provides health physics services for all the radioactive facilities in IGCAR. Studies on criticality safety, radiological safety analysis of Beyond Design Based Accident (BDBA) in PFBR, radiation detector development, biodosimetry with reference to low level radiation exposure effects, development of a neutron generator for actinide assay in wastes, studies on thermoluminescence studies and radioactivity transport in media are some of the major research work being carried out presently.

The group also organizes public awareness programmes for radiation awareness and carries out industrial training programme to increase safety awareness.

The Scientific Information Resource Division is taking care of the Library and Information Services at the Centre. Work is in progress towards creation of a digital library for the FBR literature and making it available for campus wide access using the IGC Network. All the IGC publications will also be made available in full text electronic form.

Electronics and Instrumentation Group

Shri P. Swaminathan
Director

Shri S. Athinarayanan
Head, CD

Shri S. Ilango Sambasivan
Head, EID

Shri B. Saha
Head, IIS

Dr. A. Vijaya
Medical Superindent,
DAE Hospital

The Electronics and Instrumentation Group is actively engaged in the development of Strategic Safety and Innovative Instrumentation Systems for Fast Breeder Reactor Programme such as VME based Real Time Computer systems, Safety Logic Systems, Application specific Systems etc. Highly reliable Instrumentation systems are developed using VLSI design, thermal design and EMI/EMC design tools. The technology of the Safety Instrumentation System is transferred to M/s ECIL for production of Industrial grade system. Application software packages are being developed using modern CASE TOOLS. A Full scope Replica Type Training Simulator is being developed for training the operators of the Plant. Both normal operation of the plant such as start-up, power raising as well as incidents such as station black-out, tripping of pumps etc are simulated. Walk-through of different areas of the reactor are being developed using PDMS packages. Innovative digital sensors and signal processing systems are being developed for the measurement of temperature, flow, level and pressure of nuclear process systems. This group provides the state-of-the-art electronic security to the strategic installations.

The DAE hospital provides cost effective diagnostic and healthcare facilities for the employees and their family members residing in the Townships. Health care facilities are also extended to retired employees and their families.

Engineering Services Group

Shri Y. C. Manjunatha
Director

Shri A. Jyotish Kumar
Head, ESD

Shri A.S.L.K. Rao
Head, CWD

Dr. B. Venkatraman
Head, QAD

Shri S. Keshvamurthy Rao
Head, AC&VSD

Shri N. Vijayan Varier
Head, QC & CS

Engineering Services Group is responsible for providing quality services pertaining to Civil Engineering, Electrical Engineering, Voice Communication Systems, Air-conditioning & Ventilation Systems, Material Handling Equipments, Central Workshop activities, Quality Control & Quality Assurance and Testing. The Group also coordinates the telecommunication requirements of the centre. The Group has a mandate to establish additional infrastructure requirements so as to meet Design, R&D and operational objectives of IGCAR. The Group has expert teams with capability to design, engineer and execute systems under their jurisdiction. Electricity, water, quality-air and other services are being extended to other units of DAE located at Kalpakkam. The nature of work involves interaction with several State-Government and Central Government - organizations.

Planning Division

Shri S. Subramaniam,
Head, PD

Administration & Accounts

Shri V. Dayalan,
Chief Administrative Officer

Shri Joseph Doriaraj,
Adminstrative Officer (R&SR)
Member Secretary, IGCSC

Shri V. Jayaraj,
Joint Controller
(Finance & Accounts)

Madras Regional Purchase Unit

Shri K. Balachander,
Regional Director, MRPU

LIST OF IMPORTANT ABBREVIATIONS

AERB	Atomic Energy Regulatory Board
BARC	Bhabha Atomic Research Centre
BARCF	BARC Facilities
BHAVINI	Bharatiya Nabhikiya Vidyut Nigam Limited
BHEL	Bharat Heavy Electricals Limited
CD	Computer Division
CDO	Central Design Office
CDPS	Central Data Processing System
CERMON	Continuous Environmental Radiation Monitoring Network
CG	Chemistry Group
CORAL	Compact facility for Reprocessing Advanced fuels in Lead cell
CSTD	Corrosion Science and Technology Division
CWD	Central Workshop Division
ED	Eletronics Division
EIG	Eletronics and Instrumentation Group
ESG	Engineering Services Group
FBR	Fast Breeder Reactor
FBTR	Fast Breeder Test Reactor
FChD	Fuel Chemistry Division
FRFCF	Fast Reactor Fuel Cycle Facility
FRTG	Fast Reactor Technology Group
IDEAS	Innovative Design, Engineering and Synthesis
IIS	Innovative Instrumentation Section
IIT	Indian Institute of Technology
IMSc	Institute of Mathematical Sciences
ITG	Inspection Technology Group
LMFBR	Liquid Metal Cooled Fast Breeder Reactor
MAPS	Madras Atomic Power Station
MCD	Materials Chemistry Division
MMD	Mechanical Metallurgy Division
MMG	Metallurgy and Materials Group
MSD	Materials Science Division
MTD	Materials Technology Division
NFC	Nuclear Fuel Complex
NICB	Nuclear Island Connected Buildings
NPC	Nuclear Power Corporation
NSSS	Nuclear Steam Supply System
PFBR	Prototype Fast Breeder Reactor
PHWR	Pressurised Heavy Water Reactor
REG	Reactor Engineering Group
RHS	Remote Handling Section
ROMG	Reactor Operation and Maintenance Group
RPD	Reactor Physics Division
RpG	Reprocessing Group
RRDD	Reprocesssing Research and Development Division
RSD	Radiological Safety Division
SED	Safety Engineering Division
SG	Safety Group
SGTF	Steam Generator Test Facility
SIRD	Scientific Information and Resources Division
SOWART	Sodium Water Reaction Test facility

FAST BREEDER REACTORS
Towards Energy Security for the Nation

IGC Annual Report 2005